

DISSERTATION

**Entwicklung und Anwendung der *in vivo* abdominalen  
Magnetresonanzelastographie**

**Development and application of *in vivo* abdominal  
magnetic resonance elastography**

zur Erlangung des akademischen Grades  
Medical Doctor - Doctor of Philosophy (MD/PhD)

vorgelegt der Medizinischen Fakultät  
Charité – Universitätsmedizin Berlin

von

Mehrgan Shahryari

Erstbetreuung: Prof. Dr. rer. nat. Ingolf Sack

Datum der Promotion: 30.06.2024



## Table of content

<b>List of figures</b> .....	iii
<b>List of tables</b> .....	iv
<b>List of abbreviations</b> .....	v
<b>List of symbols</b> .....	vii
<b>Abstract</b> .....	1
<b>Zusammenfassung</b> .....	3
<b>1 Introduction</b> .....	5
<b>1.1 Manual palpation</b> .....	5
<b>1.2 Magnetic resonance elastography</b> .....	6
<b>1.3 Applications of abdominal MRE</b> .....	6
<b>1.4 Objective of this work</b> .....	8
1.4.1 Study 1: “Tomoelastography distinguishes noninvasively between benign and malignant liver lesions” <sup>87</sup> .....	9
1.4.2 Study 2: “Reduction of breathing artifacts in multifrequency magnetic resonance elastography of the abdomen” <sup>88</sup> .....	10
1.4.3 Study 3: “On the relationship between metabolic capacities and <i>in vivo</i> viscoelastic properties of the liver” <sup>89</sup> .....	11
<b>2 Theoretical background</b> .....	13
<b>2.1 Viscoelasticity</b> .....	13
<b>2.2 Technical basis of magnetic resonance elastography</b> .....	15
2.2.1 Mechanical excitation.....	15
2.2.2 Image acquisition.....	17
2.2.3 Inversion algorithms.....	18
<b>3 Methods</b> .....	21
<b>3.1 Subjects</b> .....	21
<b>3.2 Experimental procedure</b> .....	24
<b>3.3 Data processing</b> .....	30

---

3.4	Statistical analysis .....	32
4	Results .....	35
4.1	Study 1 - Patient study .....	35
4.2	Study 2 - Participant study .....	41
4.3	Study 3 – Animal study .....	45
5	Discussion .....	51
5.1	Interpretation of results .....	51
5.2	Limitations .....	56
5.3	Future research .....	57
6	Conclusion .....	59
	References .....	61
	Statutory declaration .....	77
	Declaration of contribution to the publications .....	78
	Publications .....	81
	<b>Publication 1: Tomoelastography Distinguishes Noninvasively between Benign and Malignant Liver Lesions</b> .....	81
	<b>Publication 2: Reduction of breathing artifacts in multifrequency magnetic resonance elastography of the abdomen</b> .....	91
	<b>Publication 3: On the relationship between metabolic capacities and <i>in vivo</i> viscoelastic properties of the liver</b> .....	105
	Curriculum vitae .....	119
	Publication list .....	121
	Acknowledgment .....	125

## List of figures

<b>Figure 1:</b> Illustration of small bottle-shaped 3D printed actuator in abdominal MRE.....	16
<b>Figure 2:</b> Encoding scheme of different time steps of a vibration frequency.....	18
<b>Figure 3:</b> Flow chart of included patients for Study 1 – Patient study. ....	22
<b>Figure 4:</b> Experimental setup for abdominal MRE for humans and rabbits.....	25
<b>Figure 5:</b> Wave fields of 40 Hz frequency in a patient with a liver tumor.....	27
<b>Figure 6:</b> Simplified scheme of image acquisition timing of the four multifrequency MRE protocols conducted in Study 2 - Participant study. ....	29
<b>Figure 7:</b> Quantitative tomoelastography maps of stiffness, based on shear wave speed ( <i>SWS</i> ), and fluidity, derived from the phase of the complex shear modulus $\varphi$ , for four patients with malignant liver tumors.....	36
<b>Figure 8:</b> Quantitative tomoelastography maps of stiffness, based on shear wave speed ( <i>SWS</i> ), and fluidity, derived from the phase of the complex shear modulus $\varphi$ , for four patients with benign liver tumors. ....	37
<b>Figure 9:</b> Box plot and ROC curves of <i>SWS</i> and $\varphi$ of tumor and liver tissue. ....	40
<b>Figure 10:</b> Representative tomoelastography maps illustrating breathing artifacts and motion reduction strategies investigated in Study 2 – Participant study. ....	41
<b>Figure 11:</b> Box plots of displacement <i>U</i> (in mm and pixel) grouped by the different MRE acquisition paradigms. ....	43
<b>Figure 12:</b> Box plots of stiffness <i>SWS</i> (in m/s) grouped by the different acquisition paradigms for the abdominal organs. From Shahryari et al., 2021 <sup>88</sup> . ....	44
<b>Figure 13:</b> Box plots of relative improvement of image sharpness $\xi$ in percent due to motion correction by image registration. ....	45
<b>Figure 14:</b> Representative rabbit liver images in a PET/MRI scanner.....	46
<b>Figure 15:</b> Box plots of metabolic capacities and imaging parameters of the two metabolic cluster.....	47
<b>Figure 16:</b> Box plots of metabolic capacities and imaging parameters of stiff and soft livers ( <i>SWS</i> cutoff 1.6 m/s).....	48
<b>Figure 17:</b> Linear correlation of imaging parameters and metabolic capacities. ....	49

---

**List of tables**

<b>Table 1:</b> Characteristics of subjects investigated in Study 1, Study 2 and Study 3. ....	23
<b>Table 2:</b> MRE sequence parameters for Study 1, Study 2 and Study 3.....	25
<b>Table 3:</b> Quantitative parameters of tumor and liver tissue of Study 1.....	38

**List of abbreviations**

1D	One-dimensional
2D	Two-dimensional
3D	Three-dimensional
AC	Attenuation and scatter correction
acac	Acetylacetone
ARRIVE	Animal Research: Reporting of In Vivo Experiments
AUC	Area under the receiver operating characteristics curve
BH	Breath-hold
CCA	Cholangiocarcinoma carcinoma
CI	Confidence intervals
EASL	European Association for the Study of the Liver
EPI	Echo planar imaging
FB	Free-breathing
FDA	Food and Drug Administration
FDG	Fluorodeoxyglucose
FELASA	Federation of Laboratory Animal Science Association
FNH	Focal nodular hyperplasia
G	Gated
GF	Gated and navigator-based slice block adjustment
GLMM	General linear mixed-effect models
HCA	Hepatocellular adenoma
HEM	Hepatic hemangioma
ICG	Indocyanine green
IRB	Institutional Review Board
<i>k</i> -MDEV	Wavenumber-based multifrequency-dual elasto-visco
LAGESO	Landesamt für Gesundheit und Soziales
LC-MS	Liquid chromatography–mass spectrometry
LiMAx	Liver maximum function capacity test
LMM	Linear mixed effect models
MDEV	Multifrequency-dual elasto-visco
MEG	Motion-encoding-gradients
MET	Liver metastasis

---

MRE	Magnetic resonance elastography
MRI	Magnetic resonance imaging
PET	Positron emission tomography
QIBA	Quantitative Imaging Biomarker Alliance
RF	Radio frequency
RSNA	Radiological Society of North America
SD	Standard deviation
SE	Spin-echo
SNR	Signal-to-noise ratio
tag	Triacylglycerol
USE	Ultrasound elastography
vldl	Very low-density lipoprotein
VOI	Volumes of interest

## List of symbols

$\sigma$	Shear stress
$\varepsilon$	Shear strain
$\mu$	Shear modulus
$\dot{\varepsilon}$	Shear strain rate
$\eta$	Viscosity
$G^*$	Complex valued shear modulus
$G'$	Storage modulus
$G''$	Loss modulus
$ G^* $	Magnitude of the complex valued shear modulus
$\varphi$	Phase of the complex valued shear modulus
$\mathbf{u}$	Complex valued shear wave displacement vector field
$\ddot{\mathbf{u}}$	Second temporal derivate of the complex valued displacement vector field
$c^*$	Complex valued wave speed
$\Delta$	Laplace operator
$\rho$	Material density
$u_{h,n}$	Complex valued shear wave displacement field of the $h^{\text{th}}$ cartesian components and $n^{\text{th}}$ frequency
$u_{h,d,n}$	Complex valued plane wave displacement field of the $h^{\text{th}}$ cartesian components, $d^{\text{th}}$ direction and $n^{\text{th}}$ frequency
$k'_{h,d,n}$	Real part of the plane wave of the $h^{\text{th}}$ cartesian components, $d^{\text{th}}$ direction and $n^{\text{th}}$ frequency
$k''_{h,d,n}$	Imaginary part of the plane wave of the $h^{\text{th}}$ cartesian components, $d^{\text{th}}$ direction and $n^{\text{th}}$ frequency
$SWS$	Shear wave speed
$PR$	Penetration rate
$W_{h,d,n}$	Weighting factor based on the plane wave displacement magnitude of the $h^{\text{th}}$ cartesian components, $d^{\text{th}}$ direction and $n^{\text{th}}$ frequency
$\xi$	Image sharpness based on the variance of the Laplace operator $\Delta$
$M$	Mean magnitude image of $m_i$ individual images
$U$	Mean displacement of respiratory motion in the $x$ and $y$ directions
$SUV$	Standardized uptake values



## Abstract

Magnetic Resonance Elastography (MRE) is a well-established non-invasive imaging technique used to quantify the mechanical properties of tissues *in vivo* for the diagnosis of liver fibrosis. However, MRE is limited by its spatial resolution, sensitivity to motion artifacts, and insensitivity to metabolic function. Therefore, three studies of abdominal MRE were conducted to improve the quality of mechanical maps for characterizing liver tumors, to correct for motion artifacts induced by breathing, and to implement MRE on a PET/MRI scanner to correlate mechanical liver properties with metabolic functions in small animals through technical improvements in image acquisition and post-processing.

High-resolution stiffness (shear wave speed in m/s), wave penetration (penetration rate in m/s), and fluidity (phase of the complex shear modulus in rad) maps were generated using multifrequency MRE, novel actuators, and tomoelastography post-processing. The first study characterized the stiffness and fluidity of a total of 141 liver tumors in 70 patients. The second study analyzed the motion of abdominal organs and its effect on their stiffness using different acquisition paradigms and image registration in 12 subjects. The third study examined the relationship of liver stiffness and wave penetration to central metabolic liver functions in 19 rabbits.

Malignant liver tumors were distinguished from the surrounding liver (stiffness area under the curve [AUC]: 0.88 and fluidity AUC: 0.95) and benign tumors (stiffness AUC: 0.85 and fluidity AUC: 0.86) due to their increased stiffness and fluidity. In the second study, no significant differences in stiffness were observed despite significant differences in examination time, organ motion, and image quality with different image acquisition paradigms. Motion correction by image registration increased image sharpness, so that no significant difference was measurable between MRE in free breathing and breath-hold. Healthy rabbit livers showed heterogeneous liver stiffness, such that division into low and high stiffness (>1.6 m/s) groups resulted in significant differences in central metabolic functions.

Stiffness and fluidity measured by multifrequency MRE hold promise as quantitative biomarkers for the diagnosis of malignant liver tumors. Abdominal MRE with free breathing, followed by image registration, is recommended as the best balance between fast examination time and good image quality. Additionally, the applicability of abdominal

MRE in small animals in a clinical MRI was demonstrated, and correlations between mechanical liver properties and metabolic functions were found.

This study demonstrates improvements in the quality of maps of biophysical parameters for both clinical and preclinical studies, making an important contribution to the clinical translation of multifrequency MRE as a non-invasive imaging modality for abdominal organs and pathologies.

## Zusammenfassung

Die Magnetresonanzelastographie (MRE) ist eine nichtinvasive Bildgebungsmethode zur Quantifizierung mechanischer Gewebeeigenschaften *in vivo* bei der Diagnose von Leberfibrose. Limitationen bestehen aufgrund örtlicher Bildauflösung, Bewegungsempfindlichkeit und Insensitivität zu metabolischen Funktionen. Aufgrund technischer Verbesserung in der Bildaufnahme und der Bildauswertung wurde daher anhand von drei Studien zur abdominellen MRE die Bildqualität mechanischer Karten zur Charakterisierung von Lebertumoren verbessert, atmungsinduzierte Organbewegungen korrigiert und die MRE an klinischen PET/MRT implementiert, um an Kleintieren die mechanischen Lebereigenschaften mit metabolischen Funktionen zu korrelieren.

Mittels multifrequenter MRE, neuartiger Aktoren und tomoelastographischer Auswertung wurden hochaufgelöste Karten der Steifigkeit (Scherwellengeschwindigkeit in m/s), Wellenpenetration (Wellenpenetrationsrate in m/s) und Fluidität (Phase des komplexen Schermoduls in rad) generiert. Die erste Studie charakterisierte die Steifigkeit und Fluidität von insgesamt 141 Lebertumoren an 70 Patienten. Eine zweite Studie analysierte die Bewegung und den Einfluss auf die Steifigkeit abdomineller Organe mittels unterschiedlicher Aufnahme-Paradigmen und Bildregistrierung in 12 Probanden. In einer dritten Studie wurde der Zusammenhang von Lebersteifigkeit und Wellenpenetration zu zentralen metabolischen Leberfunktionen an 19 Kaninchen untersucht.

Maligne Lebertumoren können durch erhöhte Steifigkeit und Fluidität (Steifigkeit AUC: 0.88 und Fluidität AUC: 0.95) gut von gutartigen Tumoren (Steifigkeit AUC: 0.85 und Fluidität AUC: 0.86) unterschieden werden. In der zweiten Studie wurden trotz verschiedener Aufnahme-Paradigmen und Unterschiede in Untersuchungsdauer, Organbewegung und Bildqualität keine signifikanten Unterschiede in der Organsteifigkeit festgestellt. Die Bildregistrierung verbesserte die Bildschärfe, sodass kein signifikanter Unterschied zwischen freier Atmung und Atempause messbar war. Kaninchenlebern zeigten heterogene Steifigkeiten, sodass eine Zweiteilung in niedrige und hohe Steifigkeit (>1.6 m/s) signifikante Unterschiede in zentralen metabolischen Funktionen zeigte.

Steifigkeit und Fluidität, die mittels der Mehrfrequenz-MRE gemessen werden, stellen vielversprechende quantitative Biomarker für die Diagnose maligner Lebertumoren dar. Abdominelle MRE in freier Atmung mit Bildregistrierung ist der beste Kompromiss aus

schneller Untersuchungsdauer und guter Bildqualität. Die Anwendbarkeit an Kleintieren in einem klinischen MRT wurde gezeigt, inklusive Korrelationen zwischen mechanischen Lebereigenschaften und metabolischen Funktionen.

Diese Arbeit konnte somit die Bildqualität mechanischer Karten sowohl für klinische als auch präklinische Untersuchungen verbessern und damit einen wichtigen Beitrag zur Translation der Multifrequenz-MRE als klinisch angewandte nichtinvasive Bildgebungsmethode abdomineller Organe und Pathologien leisten.

# 1 Introduction

## 1.1 Manual palpation

Manual palpation is an essential part of a physical medical examination.<sup>1</sup> By moving tissue layers with the palpating fingers, force is applied to the human body, resulting in deformation of the tissue. The palpating fingers feel resistance to the deformation. This subjective perception provides information about mechanical tissue properties, which are altered in many pathological processes.

For example, liver fibrosis is associated with a stiffening of the liver.<sup>2</sup> Chronic hepatic stress and inflammation of different etiology (e.g. chronic toxins, viral inflammation, etc.) leads to fibrosis of the liver accompanied by metabolic dysfunction.<sup>3,4</sup> As the disease advances, hepatic fibrosis increases, resulting in decreased liver function.<sup>4-7</sup> This change in tissue mechanics during disease progression can be used for diagnosis and screening.<sup>8,9</sup> Therefore, palpation of the liver margins to determine liver size and induration is part of a clinical abdominal examination.<sup>7,9</sup> Moreover, in cancer mechanical properties have an important role.<sup>10</sup> For example, bimanual breast palpation is the first indication of a malignant breast tumor in most cases.<sup>11</sup> Therefore, manual breast palpation as a secondary screening measure is an integral part of annual cancer screening in women over 50 years of age in Germany.<sup>12</sup> Similarly, in men over 45 years of age, digital rectal palpation of the prostate is recommended as a routine annual examination for secondary prevention of prostate cancer.<sup>13</sup> A rough, asymmetric lump can raise suspicion of prostate cancer even before the first symptoms appear.<sup>14</sup> Early diagnosis of cancer allows adequate therapy, which increases the chances of cure.

However, traditional palpation is limited to superficial tissue accessible to the hand. Palpation of tumors located within the liver is therefore not possible. The accuracy of palpation depends on the sensitivity of the fingertips, and no precise, quantitative information is obtained. Furthermore, the examination is subjective and dependent on the clinical experience of the physician.<sup>15</sup> Thus, the evaluation of suspicious nodules in the context of cancer screening may vary between physicians.<sup>15</sup> Therefore, the subjective nature of manual palpation does not allow for long-term observation or monitoring of disease progression or treatment success.

## 1.2 Magnetic resonance elastography

Various medical imaging methods of elastography have been developed to overcome the limitations of manual palpation and quantitatively determine mechanical properties of tissues *in vivo*.<sup>16</sup> Typical elastography methods are ultrasound elastography (USE), and magnetic resonance elastography (MRE).<sup>17-21</sup> MRE is based on three basic principles: i) mechanical harmonic excitation and deformation of tissue, ii) acquisition of mechanical deformation fields, and iii) calculation of tissue mechanical properties based on deformation.<sup>22,23</sup> For MRE, harmonic vibrations of a single or multiple frequencies (multifrequency MRE) are applied to the region of interest.<sup>22-24</sup> The vibrations cause deformation of the tissue with propagating shear waves. The propagating shear waves are encoded in a snapshot-like fashion at different time points using a motion-encoding, phase-sensitive MRI sequence.<sup>22-24</sup> Image acquisition of the displacement fields requires only a few minutes and can therefore be integrated into a clinically indicated MRI examination.<sup>22-24</sup> The encoded displacement fields can be transformed into a complex shear wave field using physical models.<sup>22-24</sup> By applying physical inversion algorithms to the shear wave field, two quantitative parameter maps related to elasticity and viscosity or shear wave speed and shear wave penetration are typically generated.<sup>22-24</sup> MRE can thus quantify the mechanical properties of organs and deep tissues that were previously inaccessible and present them in spatially resolved maps (termed elastograms) that allow quantification and characterization of the mechanical properties of healthy and diseased tissues.

## 1.3 Applications of abdominal MRE

Recently, MRE has been used for the mechanical characterization of various diseases in abdominal organs.<sup>25-31</sup> Meta-analyses have shown that liver fibrosis can be diagnosed noninvasively, *in vivo* by MRE with a very high sensitivity and specificity allowing diagnostic staging of liver fibrosis that outperforms other elastography methods<sup>32,33</sup> Based on these excellent results, MRE was approved by U.S. Food and Drug Administration (FDA) for the diagnosis of liver fibrosis.<sup>34,35</sup> The distribution pattern of liver stiffness appears to differ between primary sclerosing cholangitis and viral hepatitis.<sup>36</sup> Increased liver stiffness in conjunction with increased splenic stiffness may provide information about portal hypertension and esophageal varices.<sup>37-40</sup> Pancreatitis increases pancreatic stiffness.<sup>30,41-43</sup> Initial studies have shown that renal stiffness is reduced in

patients with chronic kidney disease.<sup>44</sup> Furthermore, as recent results show, MRE may be useful for therapy monitoring and prediction of complications.<sup>45-48</sup> In particular, in the liver, the most important metabolic organ, decompensation in patients with liver cirrhosis could be predicted by MRE.<sup>49-54</sup>

Because tumor diseases can lead to marked mechanical tissue changes but are often located deep within organs, they are a particular focus of MRE research.<sup>10,19</sup> For instance, increased matrix deposition occurs in the tumor environment with increased protein fiber linkage.<sup>55-57</sup> Cancer induces neoangiogenesis, leading to the formation of perforated blood vessels that increase fluid pressure within the tissue.<sup>55,58</sup> In addition, tumor cell proliferation with cellular unjamming increases solid stress on the surrounding tissue.<sup>55,58-60</sup> Preliminary MRE studies in liver tumors have indicated that the stiffness of tumors is increased, especially in malignant liver tumors.<sup>61</sup> Renal and in pancreatic tumors have also shown an elevated stiffness in preliminary studies.<sup>26,42,62-64</sup> With regard to tumor disease, preclinical animal experiments are essential in basic research. Therefore, MRE, which was first developed for use in humans in 1995, has been extended to various preclinical animal models.<sup>24,59,65-68</sup> An increase in liver tumors stiffness after laser ablation has been demonstrated in pigs.<sup>69</sup> Human colon cancer cells subcutaneously transplanted into mice showed a decrease in stiffness after drug administration.<sup>70</sup>

In addition to pathological alterations, MRE is also sensitive to physiological effects. An increase in liver stiffness after food or water ingestion was reported.<sup>71-76</sup> In rats, liver stiffness increased due to cell hypertrophy during pregnancy.<sup>77</sup> However, to date, there is no information on the relationship between metabolic functions and mechanical tissue properties measured with MRE.

Despite the promising studies, abdominal *in vivo* MRE has been limited by insufficient mechanical excitation of shear wave amplitudes, extended acquisition times and low spatial resolutions, which overall compromise MRE reproducibility.<sup>35,76,78-82</sup> For example, the FDA-approved commercially available MRE device uses only a single actuation unit and is therefore limited in providing sufficient shear wave amplitudes.<sup>23,28,35,83</sup> However, sufficient mechanical excitation with high wave amplitudes in the organs of interest is required to apply wave inversion algorithms, which is challenging for organs that are deeply located in the body, such as the kidneys and pancreas.<sup>28,83</sup> In addition, due to its large diameter, the commercial actuation unit is not suitable for studies of small animals

such as rabbits. MRE image acquisition usually takes several minutes being susceptible to motion artifacts, i.e., caused by breathing.<sup>23,84,85</sup> This can lead to image blurring and reduce image quality.<sup>23</sup> Motion artifacts also occur in examinations with breathing commands, which, on the one hand, prolong examination time and, on the other hand, are not feasible in animals and some patients.<sup>28,86</sup> These limitations are particularly relevant for the characterization of small lesions such as tumors and in preclinical animal studies.

#### **1.4 Objective of this work**

The focus of this work was on the application and improvement of *in vivo* abdominal MRE for tumor characterization and preclinical animal studies. To this end, adaptations in mechanical excitation, image acquisition, and data processing were made. Novel three – dimensional (3D)-printed actuators in a small bottle shape were utilized.<sup>87-89</sup> These actuators were attached to a custom-made belt placed around the abdomen, allowing for the generation of sufficiently high amplitudes of harmonic displacement fields.<sup>87-89</sup> The use of multiple actuators was possible due to their small size.<sup>87-89</sup> In combination with tomoelastography, a novel noise-robust inversion algorithm, maps with high spatial resolution could be generated.<sup>87-90</sup> The aim of the first study was to apply tomoelastography for the first time in patients with liver tumors, with the goal of obtaining high spatial resolution images for the delineation and mechanical characterization of liver lesions as small as 1 cm.<sup>87</sup> The benefit of using tomoelastography for the diagnosis of liver tumors was investigated.<sup>87</sup> Due to the degradation of image quality caused by respiratory motion during MRE image acquisition, strategies to reduce breathing-induced organ motion were investigated in the second study.<sup>88</sup> To this end, different image acquisition sequences and image registration were implemented for post-processing of the image data to provide the best compromise in terms of image quality, parameter consistency, and examination time.<sup>88</sup> The third study aimed to demonstrate that technical advancements have enabled the *in vivo* examination of small animals such as rabbits, which do not fit into an animal scanner, using a human MRI. Multifrequency MRE was implemented on a human PET/MRI scanner to acquire MRE and PET measurements simultaneously.<sup>88</sup> This enabled the correlation of high-resolution maps of the viscoelastic properties of the liver with metabolic liver functions.<sup>87</sup> The three studies were conducted

using MRI scanners of varying field strengths and located at different sites to showcase the versatility of MRE for both clinical and preclinical studies of the abdomen.<sup>87-89</sup>

In the following, the essence of the presented studies of this work is described in more detail.

#### 1.4.1 Study 1: “Tomoelastography distinguishes noninvasively between benign and malignant liver lesions”<sup>87</sup>

In the first study, the mechanical properties of primary and secondary liver tumors of different entities were investigated in 70 patients using tomoelastography based on multifrequency MRE.<sup>87</sup> Liver tumors are the third most common cause of cancer deaths as of 2020, with early diagnosis leading to improved survival.<sup>91-96</sup> An increase in liver stiffness due to fibrosis increases the likelihood of HCC occurrence by approximately 4%.<sup>54</sup> Preliminary single-frequency MRE studies in a small study population have demonstrated that liver tumors are associated with increased elasticity and viscosity.<sup>97-99</sup> However, these studies were limited in their spatial resolution and image quality.<sup>87</sup> Data on mechanical fluidity, which in MRE denotes the proportion of elastic-solid to viscous-fluid material properties, are scarce.<sup>87</sup> There is evidence that malignant tissue is associated with higher fluidity<sup>97,100</sup> rendering the further development and application of MRE for the mechanical characterization of liver tumors important. Therefore, the aim of this study was to investigate the potential of multifrequency MRE for the diagnosis of liver tumors by characterizing stiffness and fluidity of liver tumors and non-tumor liver.<sup>87</sup> For this purpose, multiple novel compressed-air actuators, multifrequency excitation, and tomoelastography reconstruction methods were, for the first time, combined to generate maps of stiffness and fluidity in patients with liver tumors.<sup>87</sup> To calculate the delineation capability, the tumor’s mechanical properties were compared with those of the non-tumorous liver.<sup>87</sup> Differences in stiffness and fluidity between different tumor entities were analyzed and the separability between benign and malignant liver tumors was calculated.<sup>87</sup> This study will be referred to as *Study 1 - Patient study* - in the rest of the manuscript.

#### 1.4.2 Study 2: "Reduction of breathing artifacts in multifrequency magnetic resonance elastography of the abdomen"<sup>88</sup>

The second study focused on strategies to reduce breathing-induced motion in abdominal organs of 12 healthy participants.<sup>88</sup> The rising clinical application of MRE in abdominal pathologies has prompted the development of numerous novel MRE techniques.<sup>22</sup> However, one limitation that all existing MRE techniques have in common, is their sensitivity to breathing motion causing to imaging artifacts.<sup>23</sup> The motion induced by respiration during image acquisition can displace organs, resulting in blurred images and image artifacts, such as "ghosting".<sup>101</sup> "Ghosting" is caused by artefactual signal variation along the phase-encoding direction and is characterized by the presence of noisy and duplicated versions of the primary object in the MRI image.<sup>101</sup> This phenomenon is also relevant for phase contrast imaging, such as MRE.<sup>102</sup> Together, motion induced blurring and ghosting, can significantly degrade image quality, which can hinder the accurate detection of small lesions, making it unacceptable for precise diagnosis.<sup>19,23,35,84,85,88</sup> Therefore, the Quantitative Imaging Biomarker Alliance (QIBA) of the Radiological Society of North America (RSNA) recommends MRE examinations with breath hold at end-expiration.<sup>35</sup> However, there are reasons why image acquisition in breath-hold of the subject is not always appropriate.<sup>88</sup> Patients with abdominal disease cannot always hold their breath for up to 20 seconds multiple times, which is required for the multi slice acquisition of commercially available MRE.<sup>28,35</sup> In pediatric and geriatric patients, compliance with breathing commands may be challenging or not possible in all cases.<sup>88</sup> Breathing commands cannot be followed by animals investigated in preclinical studies. Breath-hold in expiration can lead to pressure and perfusion changes of abdominal organs, which may have influence on organ stiffness.<sup>103,104</sup> Furthermore, breathing commands prolong the overall examination time.<sup>88</sup> Breath-hold commands in a multifrequency MRE, such as tomoelastography, which allows a high image quality despite respiratory motion, prolong the examination time by a factor of 4.<sup>105</sup> Therefore, multifrequency MRE has been performed in free breathing mostly.<sup>44,106-108</sup> The aim of this work was to provide guidance for handling breathing-induced motion in future abdominal MRE applications.<sup>88</sup> To achieve this goal, reduction strategies were analyzed during both the image acquisition and post-processing stages.<sup>88</sup> The different image acquisitions paradigms included MRE during breath-hold, during free-breathing, and during free-breathing with respiratory navigators.<sup>88</sup> Image registration on unprocessed data quantified and corrected motion of liver, kidneys, spleen, and pancreas in the different

acquisition paradigms.<sup>88</sup> The different methods were compared in terms of the best compromise between image quality and examination time.<sup>88</sup> This study will be referred to as *Study 2 - Participant study* - in the rest of the manuscript.

#### 1.4.3 Study 3: “On the relationship between metabolic capacities and *in vivo* viscoelastic properties of the liver”<sup>89</sup>

In the third study, the applicability of multifrequency MRE in a clinical hybrid PET/MRI scanner and the relationship between rabbit liver function and mechanics were investigated *in vivo* in 19 rabbits.<sup>89</sup> Determination of liver function to estimate the risk of post hepatectomy liver failure plays a crucial role for curative liver resection, especially in patients with severe intrahepatic tumor load.<sup>109-117</sup> Metabolic liver functions are also altered in chronic progressive liver diseases such as NAFLD, the hepatic manifestation of metabolic syndrome.<sup>118-122</sup> However, noninvasive quantification of liver functions remains a major clinical challenge.<sup>89</sup> Static liver function assessment, such as the Child-Turcotte-Pugh score that is based on relevant serum or plasma metabolites for assessment hepatic synthesis capacities, are insensitive in early disease stages.<sup>123-126</sup> Dynamic labeling measurements such as the liver maximum function capacity test (LiMAx) are time-consuming, expensive and only assess specific pathways.<sup>127,128</sup> PET is a functional imaging technique that uses radiotracer labeled metabolites, such as <sup>18</sup>F-fluorodeoxyglucose (FDG), which indicates glucose metabolism.<sup>129</sup> It can be used to diagnoses various diseases with associated with high metabolic activity, such as tumors and neurodegenerative processes.<sup>129-134</sup> Nevertheless, PET is limited by its high cost, ionizing radiation and specific metabolic pathways of the injected metabolites.<sup>135-137</sup> Central metabolic liver functions can be assessed by computational modeling based on proteomics data.<sup>138-143</sup> However, this requires the collection of liver tissue samples, which cannot be routinely obtained from patients due to the invasiveness.<sup>144,145</sup> Although the liver is the only organ for which MRE is FDA-approved in the U.S., there is no information on the relationship between mechanical liver properties and specific metabolic functions, which would be of particular interest in early stages of NAFLD in which measurable fibrosis has not yet occurred.<sup>89</sup> Additionally, to date, MRE has not been applied on a PET/MRI scanner to allow simultaneous measurements of MRE and i.e., glucose metabolism.<sup>89</sup> Therefore, the aim of this study was to investigate the relationship between mechanical liver properties, as assessed by high-resolution viscoelastic maps, and metabolic capabilities determined by PET imaging and computational modeling based on

proteomics data from post-mortem liver samples.<sup>89</sup> To achieve this, multifrequency MRE was implemented on a human PET/MRI scanner to acquire MRE and PET measurements simultaneously on rabbits, which do not fit in an animal MRI due to their size.<sup>89</sup> Novel small bottle-shaped actuators were attached to a custom-made belt for rabbits, and the MRE sequence parameters, mechanical excitation frequencies, and inversion post-processing were adjusted for small animals to generate high-resolution viscoelastic maps.<sup>89</sup> This study serves as the first reference investigating mechanical liver properties with metabolic capabilities.<sup>89</sup> In addition, this study demonstrates that high-resolution images in small animals are feasible in clinical MRI and offers the possibility of performing MRE imaging simultaneously with PET imaging for clinical and preclinical purposes in the future.<sup>89</sup> This study will be referred to as *Study 3 - Animal study* - in the rest of the manuscript.

## 2 Theoretical background

### 2.1 Viscoelasticity

In addition to histological and functional characterization of biological tissue, mechanical properties can also be used to describe the tissue. In general, by applying stress  $\sigma$  on a biological tissue leads to strain  $\varepsilon$ , whereas the material property that resists to the deforming stress is the elastic modulus and denotes the proportionality between  $\sigma$  and  $\varepsilon$ .<sup>146</sup>

In an incompressible and purely linear-elastic material (e.g. spring) the proportionality between shear stress and shear strain is described by the shear modulus  $\mu$ . In an isotropic material with small deformation a linear relationship between shear stress and shear strain can be assumed, which is why Hooke's law can be applied:<sup>22</sup>

$$\sigma = 2 \mu \varepsilon . \quad (1)$$

In purely viscous material (e.g. water), the stress is proportional to strain rate  $\dot{\varepsilon}$ .<sup>22</sup> Instead of a instant deformation as in a elastic material, a flow process is occurring.<sup>22</sup> In case of laminar flow the material can be described as a Newton fluid and is characterized by the viscosity  $\eta$ :<sup>22</sup>

$$\sigma = 2 \eta \dot{\varepsilon} . \quad (2)$$

Biological tissue can be considered as viscoelastic material.<sup>146</sup> Viscoelastic materials exhibit both elastic and viscous behavior, combining the characteristics of elastic solids and viscous fluids.<sup>146</sup>

Viscoelastic biological tissue can be represented by a complex number:<sup>22</sup>

$$G^* = |G^*| e^{i\varphi} = G' + i G'' , \quad (3)$$

$$\sigma = 2 G^* \varepsilon , \quad (4)$$

with  $|G^*|$  being the magnitude of the complex valued shear modulus and  $\varphi$  the phase of the complex valued shear modulus. In particular,  $\varphi$  ranges from 0 (pure elastic material) to  $\frac{\pi}{2}$  (pure viscous material).<sup>22</sup> In the following,  $\varphi$  is termed fluidity.  $|G^*|$  and  $\varphi$  can be

expressed by the storage modulus  $G'$  and loss modulus  $G''$  by  $|G^*| = \sqrt{G'^2 + G''^2}$  and  $\varphi = \arctan\left(\frac{G''}{G'}\right)$ , respectively.

The Helmholtz equation for complex-valued shear waves in viscoelastic materials can be derived from the incompressible, isotropic, and homogeneous version of the Navier equation under linear deformation, using the Helmholtz decomposition:<sup>22</sup>

$$\ddot{\mathbf{u}} - \frac{G^*}{\rho} \Delta \mathbf{u} = \mathbf{0}, \quad (5)$$

where  $\mathbf{u}$  represents the shear wave displacement vector field,  $\ddot{\mathbf{u}}$  represents the corresponding second time derivative,  $\rho$  denotes the density of the material and  $\Delta$  represents the Laplace operator.

Comparing eq.5 with the wave equation  $\ddot{\mathbf{u}} - c^{*2} \Delta \mathbf{u} = \mathbf{0}$ , allows to determine the complex wave speed  $c^*$ :<sup>22</sup>

$$c^* = \sqrt{\frac{G^*}{\rho}}. \quad (6)$$

To quantitatively assess the viscoelastic properties of biological tissue, the real valued shear wave speed (*SWS*) and penetration rate (*PR*) can be determined.<sup>90</sup> Both can be represented by  $c^*$  or respectively by  $G^*$ .<sup>90</sup>

$$SWS = \frac{1}{\operatorname{Re}\left\{\frac{1}{c^*}\right\}} = \sqrt{\frac{2|G^*|}{\rho(1+\cos\varphi)}}, \quad (7)$$

$$PR = \frac{1}{-2\pi \operatorname{Im}\left\{\frac{1}{c^*}\right\}} = \frac{1}{2\pi} \sqrt{\frac{2|G^*|}{\rho(1-\cos\varphi)}}. \quad (8)$$

Overall, three stiffness related parameters can be derived: the magnitude of the complex shear modulus  $|G^*|$ , the storage modulus  $G'$  associated with elasticity and the shear wave speed *SWS*. Conversely, three viscosity-related parameters can be obtained: the phase of the complex shear modulus  $\varphi$ , also referred to as fluidity, the loss modulus  $G''$  and the wave penetration rate *PR* associated with inverse damping properties.<sup>22,90</sup> All parameters are dependent on the frequency of vibration.<sup>22,90</sup>

## 2.2 Technical basis of magnetic resonance elastography

In the following section, the fundamental principles of MRE shall be elucidated.

### 2.2.1 Mechanical excitation

Motion generating actuators introduce shear waves into the body via harmonic vibrations. Over the last two decades, numerous actuator systems have been designed, differing in their principle of motion generation and transducing.<sup>22</sup> Actuator systems that use pressurized air are cost-effective and have proven to be practical for both clinical and scientific purposes in patients. Therefore, they are currently the most commonly used.<sup>22,23,147,148</sup> These actuators are attached to the region of interest on the body surface and vibrate at a specific frequency. A detailed analysis of different actuator types can be found in the book *Magnetic Resonance Elastography* by Hirsch et al.<sup>22</sup>. Figure 1 illustrates a novel bottle-shaped 3D printed actuator system for MRE measurement of abdominal organs, which is powered by compressed air. In comparison to the most common actuator systems, several of these small bottle-shaped actuators can be attached around the patient's abdomen to generate shear waves with high amplitudes.<sup>87,88</sup>

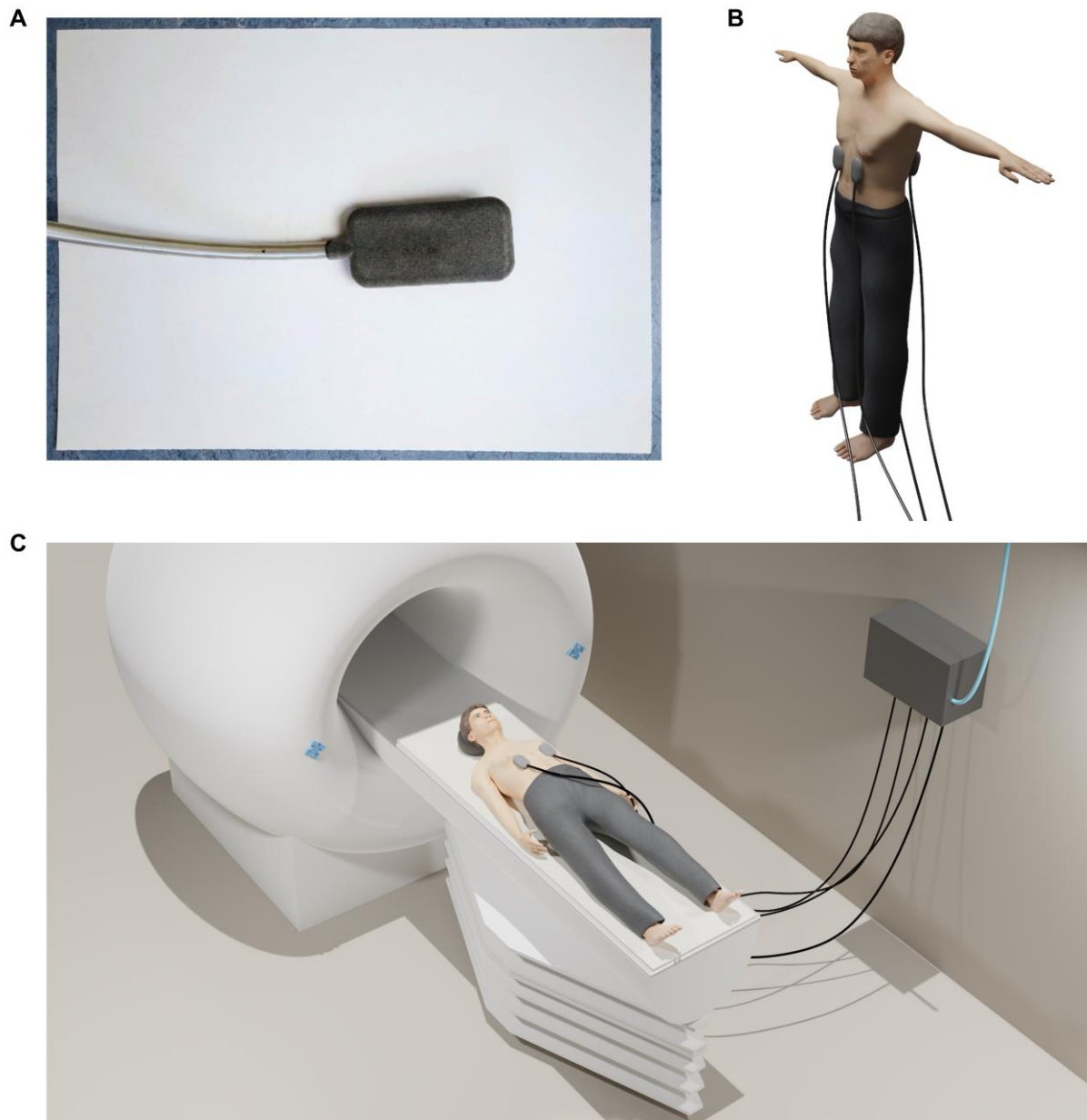


**Figure 1:** Illustration of small bottle-shaped 3D printed actuator in abdominal MRE.

A newly designed 3D-printed actuator system, shaped like a small bottle and equipped with tubing for the flow of compressed air is presented. A standard Din-A4 page is provided for size comparison. B Two dorsal and two ventral actuators are placed on the upper abdominal region. C The patient is positioned in a supine orientation on the MRI scanner table, while the actuators are affixed to their body. Pressurized air with a specific frequency and amplitude generated by the pneumatic control unit at the flows via the tubes to the actuators and transduces shear waves into the abdominal region. Own figure.

Lower vibration frequencies result in longer spatial wavelengths, leading to greater tissue displacement with less wave attenuation.<sup>22</sup> Thus, they can penetrate the tissue more easily. Higher vibration frequencies allow for a better spatial resolution of elastograms due to smaller spatial wavelength, but are limited in penetration depth and displacement of tissue.<sup>22</sup> Therefore, the size and location of the tissue of interest must be considered when choosing a vibration frequency. In a multifrequency approach, the advantages between low and high mechanical frequencies are compromised. This allows for higher spatial resolution and better signal to noise ratio (SNR), while ensuring depth penetration.<sup>22</sup> In addition, standing waves can be accounted for.<sup>22</sup> Typically, frequencies between 20 and 100 Hz are used for MRE in humans and small animals, leading to tissue displacement usually in the  $\mu\text{m}$  range.<sup>149-151</sup>

### 2.2.2 Image acquisition

The propagating shear waves in the tissue lead to harmonically oscillating tissue displacement. The displacement is encoded with a phase-contrast MRI sequence.<sup>22,24</sup> The sequence has bipolar trapezoidal, motion-encoding-gradients (MEGs) that encode displacement into the phase of the complex MRI signal, whereas the magnitude captures the signal intensity and provides anatomical information.<sup>22</sup> The MEG has a fixed amplitude and duration.<sup>22</sup> The MEG frequency is in the range of the mechanical frequency and displacement encoding occurs along the MEG direction.<sup>22,152</sup> To acquire a 3D wave field, MEGs are repeated for all three Cartesian motion fields, which usually match the direction of imaging gradients of the MRI.<sup>22</sup> Only moving spins accumulate a net phase signal due to the shape of the MEG (0<sup>th</sup> gradient moment nulling).<sup>22</sup> Motions with a constant velocity such as rigid body motion or laminar blood flow, can be eliminated by a 1<sup>th</sup> gradient moment nulling approach adding extra gradient lobes.<sup>22</sup>

The displacement is encoded in the phase, which ranges from  $-\pi$  to  $\pi$ .<sup>22</sup> When the accumulated phase signal exceeds these limits, phase discontinuities occur.<sup>153</sup> The phase values are then wrapped with opposite sign, which is called phase wraps. Phase wraps occur, for example, when the amplitude of the mechanical driving frequency or the MEG is high.<sup>22</sup> There are several phase unwrapping algorithms for correcting phase discontinuities.<sup>154,155</sup> Usually, MRE phase images are smoothed prior to phase unwrapping to increase data stability.<sup>22</sup>

To acquire a harmonic oscillating displacement, at least 3 different phases with equidistant time steps ( $\Delta t$ ) have to be acquired.<sup>22</sup> Usually, six to eight time steps are acquired.<sup>22</sup> Therefore, the acquisition of the time steps by the MRE sequence has to be synchronized with the driving frequency.<sup>22</sup> Subsequently, the temporal Fourier transformation allows the fundamental driving frequency to be extracted, neglecting unwanted signals and noise occurring naturally during the measurement.<sup>22</sup> Figure 2 illustrates the sampling scheme of an MRE sequence. Several MRE magnitude and phase images are acquired, which are composed of the different time steps, MEG directions and frequencies.

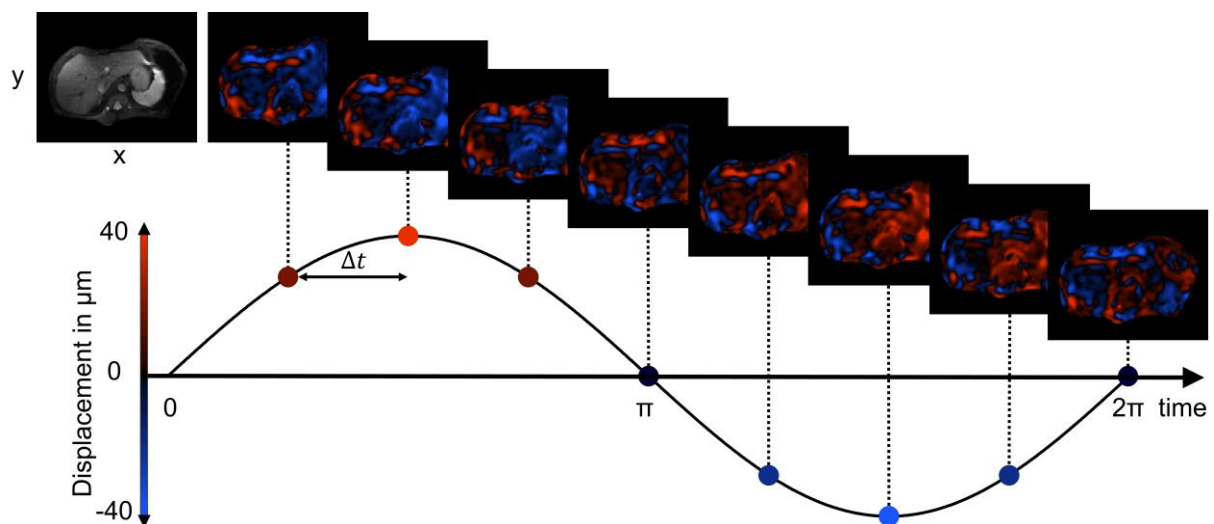


**Figure 2:** Encoding scheme of different time steps of a vibration frequency.

Shown is the transverse plane of time-harmonic displacement (in  $\mu\text{m}$ ) in the  $x$ -direction of a 60 Hz frequency. The harmonic displacement is sampled at different phases with equidistant time steps ( $\Delta t$ ). Blue denotes values below and red values above  $0 \mu\text{m}$ . Own figure based on data from Shahryari et al., 2019<sup>87</sup>.

### 2.2.3 Inversion algorithms

After image acquisition, spatial smoothing, phase unwrapping and temporal Fourier transformation a displacement field  $\mathbf{u}$  is generated, which contains the shear and compression wave.<sup>22</sup> In MRE, only the shear wave is relevant, necessitating the removal

of the compression wave.<sup>22</sup> The application of a high-pass k-space filter allows the differentiation between compression and shear waves, as the former exhibit longer wavelengths compared to the latter.<sup>22</sup> There exist various inversion algorithms that can reconstruct distinct mechanical parameters based on the propagation of shear waves to characterize the viscoelastic properties of tissues.<sup>22</sup> The algorithms used in this work are the multifrequency-dual elasto-visco (MDEV) and the wavenumber-based MDEV (*k*-MDEV) inversion methods, respectively.<sup>90,105</sup>

MDEV is an inversion method that directly solves the Helmholtz equation (5) and reconstructs  $|G^*|$ , and  $\varphi$  independently.<sup>105</sup> It omits the frequency dependency of  $|G^*|$  and  $\varphi$  and therefore, simply averages over the MEG components of the shear wave displacement  $u_{h,n}$  with 3 cartesian components  $h$  and  $N$  vibration frequencies  $f_n$ , respectively:<sup>105</sup>

$$\varphi = \text{acos} \left( - \frac{\sum_{n=1}^N \sum_{h=1}^3 |u_{h,n}|' |\Delta u_{h,n}|' + |u_{h,n}|'' |\Delta u_{h,n}|''}{\sum_{n=1}^N \sum_{h=1}^3 |u_{h,n}| |\Delta u_{h,n}|} \right), \quad (9)$$

$$|G^*| = \rho \left( \frac{\sum_{n=1}^N \sum_{h=1}^3 (2 \pi f_n)^2 |u_{h,n}|}{\sum_{n=1}^N \sum_{h=1}^3 |\Delta u_{h,n}|} \right). \quad (10)$$

As it uses the Laplacian  $\Delta$ , being a second order spatial derivate operator and is thus, susceptible to noise.<sup>105</sup> The density  $\rho$  was defined as constant with  $1 \frac{\text{g}}{\text{cm}^3}$ , which describes the average density of soft biological soft tissue very well.<sup>105</sup>

For tomoelastography, *k*-MDEV is used in combination with multifrequency MRE driven by the proposed multiple small bottle-shaped actuators (Figure 1).<sup>90</sup> One advantage of *k*-MDEV is its utilization of a first order spatial derivative inversion approach, which makes it more resistant to noise when compared to MDEV.<sup>90</sup> Unlike MDEV, *k*-MDEV reconstructs primary the real and imaginary wave number  $k'$  and  $k''$ , respectively, of the complex wave number  $k^*$ .<sup>90</sup> For *k*-MDEV, plane waves are required, which are extracted through directional filtering of the shear wave field using 8 directions  $d$ :<sup>90</sup>

$$k'_{h,d,n} = \|\nabla \arg(u_{h,d,n})\|, \quad (11)$$

$$k''_{h,d,n} = \left\| \frac{\nabla |u_{h,d,n}|}{|u_{h,d,n}|} \right\|. \quad (12)$$

$SWS$  and  $PR$  can be calculated using a weighted averaging over all MEG components, frequencies and plane wave directions of  $k'_{h,d,n}$  and  $k''_{h,d,n}$ , respectively:<sup>90</sup>

$$\frac{1}{SWS} = \frac{\sum_{h,d,n} \frac{k'_{h,d,n}}{2\pi f_n} W_{h,d,n}}{\sum_{h,d,n} W_{h,d,n}}, \quad (13)$$

$$\frac{1}{PR} = \frac{\sum_{h,d,n} \frac{k''_{h,d,n}}{f_n} W_{h,d,n}}{\sum_{h,d,n} W_{h,d,n}}. \quad (14)$$

A weighting factor based on the wave amplitude  $W_{h,d,n} = |u_{h,d,n}|^4$  is utilized to prioritize waves with high amplitude and thus improve the SNR.<sup>90</sup>

### 3 Methods

#### 3.1 Subjects

*Study 1 – Patient study* and *Study 2 – Participant study* investigated multifrequency MRE in patients and healthy participants.<sup>87,88</sup> These studies were in accordance with the World Medical Association Declaration of Helsinki and were approved by the Institutional Review Board (IRB) of the Charité – Universitätsmedizin Berlin (EA1/261/12 and EA1/076/17).<sup>87,88</sup> All study subjects were older than 18 years and had no contradiction to MRI or risk factors related to the experimental study examination.<sup>87,88</sup> All volunteers gave their written informed consent to participate in the study prior to enrollment.<sup>87,88</sup>

*Study 1 - Patient study:* The source population consisted of patients with focal liver lesion presenting for diagnosis and therapy at the Charité Universitätsmedizin Berlin, Campus Virchow Klinikum. Inclusion criteria were patients with previously diagnosed focal liver lesion and no tumor therapy prior to study participation.<sup>87</sup> Between March 2015 and August 2017, eligible patients were screened via the radiology and surgery electronic scheduling system in a single-center study.<sup>87</sup> In a consecutive sampling scheme patients were approached and informed about the content, form and aim of the study.<sup>87</sup> The study sample consisted of 70 patients with focal liver lesions.<sup>87</sup> A total of 105 malignant and 36 benign tumors of various entities were studied.<sup>87</sup> 3 malignant entities (hepatocellular carcinoma [HCC], cholangiocarcinoma [CCA], and liver metastasis [MET]), as well as 3 benign entities: hepatocellular adenoma [HCA], focal nodular hyperplasia [FNH], and hepatic hemangioma [HEM]) were studied.<sup>87</sup> Tumor entity conformation was made by histopathology in all patients with malignant and in 7 of the 16 patients with benign tumors.<sup>87</sup> In the other cases, the diagnosis was made by clinical contrast enhanced MRI according to the European Association for the Study of the Liver (EASL) guidelines.<sup>156,157</sup> A flowchart of the patients and tumor entities studied is shown in Figure 3.

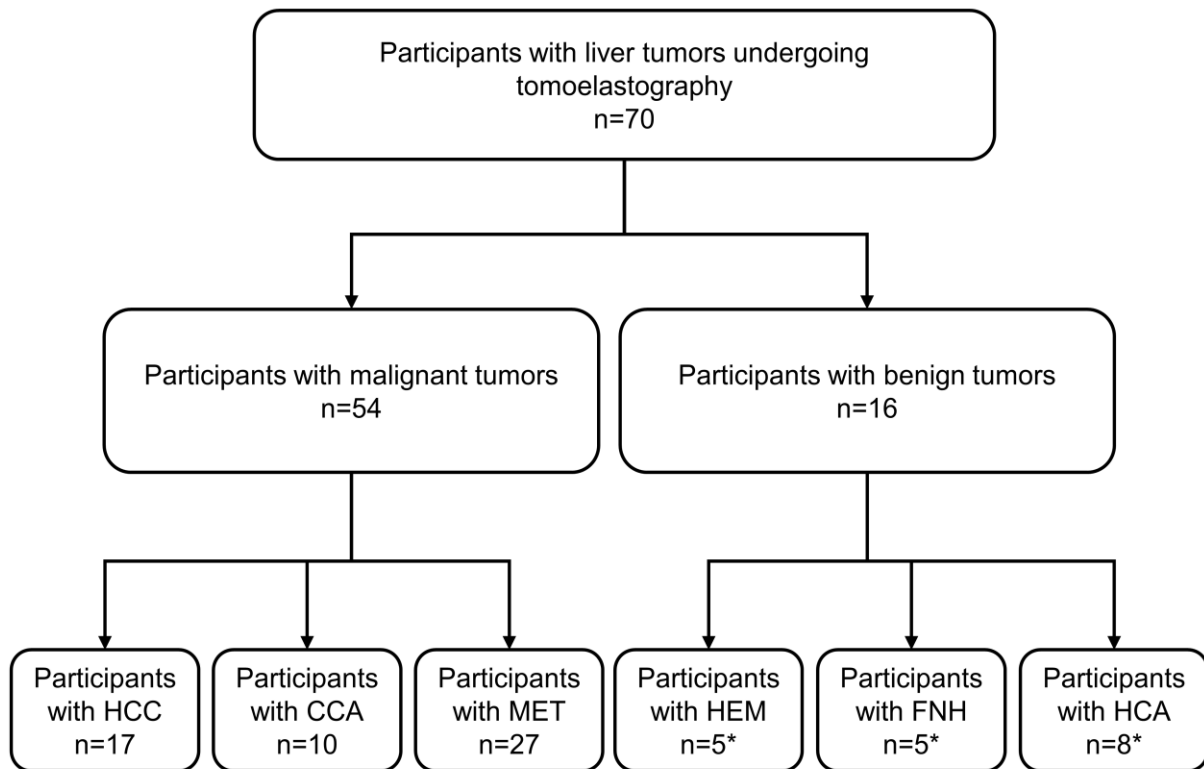


**Figure 3:** Flow chart of included patients for Study 1 – Patient study.

A total of 70 patients were studied by multifrequency MRE. 16 patients had a benign liver tumor disease and 54 a malignant liver tumor disease. Twenty-seven patients had multiple liver tumors. \*Two patients had lesions of different tumor entities, one had a focal nodular hyperplasia (FNH) and a hepatic adenoma (HCA) and the other had a hemangioma (HEM) and a FNH. HCC; hepatocellular carcinoma; CCA, cholangiocarcinoma; MET, metastasis. Modified from Shahryari et al., 2019<sup>87</sup>.

**Study 2 - Participant study:** Eleven healthy male participants with no history of pulmonary or abdominal disease were acquired at Charité - Universitätsmedizin Berlin, Campus Mitte.<sup>88</sup>

**Study 3 – Animal study:** Nineteen healthy female New Zealand white rabbits (Charles River Laboratories, Sulzfeld, Germany) were included.<sup>89</sup> The local authority, Landesamt für Gesundheit und Soziales (LAGESO) Berlin, approved the study protocol (Reg. No. 0178/17).<sup>89</sup> All experimental procedures were in accordance with the Federation of Laboratory Animal Science Association (FELASA) and the Animal Research: Reporting of In Vivo Experiments (ARRIVE) guidelines and regulations.<sup>89</sup> All rabbits were accommodated in a controlled laboratory setting, specifically in a pathogen-free animal

facility at the Charité Campus Virchow Klinikum with laminar airflow systems, where the rooms maintained a consistent temperature and humidity.<sup>89</sup> The rabbits were between 11 and 15 weeks old and had an average weight of  $3.22 \pm 0.27$  kg on the day of measurement.<sup>89</sup>

The descriptive characteristics of the subjects from *Study 1*, *Study 2* and *Study 3* are given in Table 1.

**Table 1:** Characteristics of subjects investigated in *Study 1*, *Study 2* and *Study 3*.

The total number of subjects in each entity, along with their corresponding proportions, as well as the total number of female subjects and their proportion among the total subjects, are provided. Age is presented as the mean value and range, while BMI is given as the mean value  $\pm$  standard deviation. Furthermore, the total number of tumor lesions and their proportion among the subjects are provided for *Study 1*. HCC, hepatocellular carcinoma; CCA, cholangiocarcinoma, MET, metastasis; HEM, hemangioma; FNH, focal nodular hyperplasia; HCA, hepatic adenoma; BG, blood glucose. Own table based on data from Shahryari et al., 2019<sup>87</sup>, 2021<sup>88</sup>, 2023<sup>89</sup>.

	Entity	Subject numbers (%)	Woman (%)	Age in years (range)	BMI (kg/m <sup>2</sup> )	Number of tumors (%)
Study 1	HCC	17 (24.3)	4 (5.7)	67 (43-81)	26.1 $\pm$ 3.4	22 (15.6)
	CCA	10 (18.6)	5 (7.1)	70 (56-76)	25.9 $\pm$ 4.1	12 (8.5)
	MET	27 (38.6)	10 (14.3)	61 (30-85)	25.2 $\pm$ 4.0	71 (50.4)
	HEM	5 (7.1)	5 (7.1)	52 (38-74)	24.0 $\pm$ 4.2	11 (7.8)
	FNH	5 (7.1)	3 (4.3)	38 (29-66)	25.2 $\pm$ 5.2	10 (7.1)
	HCA	6 (8.6)	8 (11.4)	39 (22-52)	25.0 $\pm$ 5.0	15 (10.6)
	Total	70 (100)	35 (50%)	57 (22-81)	25.12 $\pm$ 3.88	141 (100)

Study 3	Healthy	11 (100)	0 (0)	28 (23-38)	23 ± 2	0 (0)
Study 3	<b>Entity</b>	<b>Subject numbers (%)</b>	<b>Female (%)</b>	<b>Age in weeks (range)</b>	<b>Weight in kg</b>	<b>BG in mg/dL</b>
	Healthy	19 (100)	100 (100)	13 (11-15)	3.23±0.26	153.06±24.1

### 3.2 Experimental procedure

The novel small bottle-shaped 3D-printed actuators powered by pressurized air pulses were used for the three studies, as presented in 2.2.1.<sup>87-89</sup> To generate and control the harmonic vibrations by pressurized air, a control unit was used.<sup>87-89</sup> The control unit was synchronized with the internal clock of the MRI scanner.<sup>87-89</sup> For *Study 1 – Patient study* and *Study 2 – Participant study* two drivers were placed bilateral ventrally on the midclavicular line and two drivers were attached dorsally on the scapular line.<sup>87,88</sup> The ventral and dorsal actuators were running with 0.4 and 0.6 mbar, respectively.<sup>87,88</sup> Shear waves were induced in the abdominal organs using the attached actuators, which were powered by mechanical frequencies of 30, 40, 50, and 60 Hz generated by the control unit and transmitted through tubes (Figure 1).<sup>87,88</sup> For *Study 3 – Animal study* two drivers were attached laterally on the upper abdomen of the rabbits and frequencies of 40, 50, 60, 70 and 80 Hz were applied at 0.2 mBar.<sup>89</sup> A belt around the transpyloric plane containing the drivers was fastened to increase a better coupling of the harmonic vibrations.<sup>87-89</sup> A frequency forerun of 3 seconds prior to image acquisition (see 2.2.3) was conducted, to achieve harmonic oscillation of the abdominal organs.<sup>87-89</sup> In *Study 1 – Patient Study* and *Study 2 – Participant study* volunteers were lying supine on the examination table,<sup>87,88</sup> whereas in *Study 3 – Animal study* rabbits were in prone position.<sup>89</sup> Figure 4 illustrates the setup for three studies.

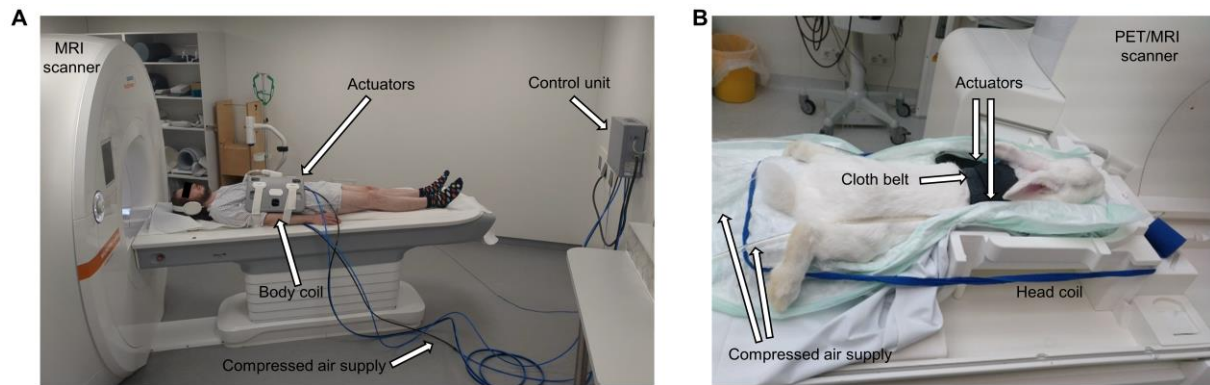


**Figure 4:** Experimental setup for abdominal MRE for humans and rabbits.

**A** Volunteer lying supine head-first on the MRI scanner table. Four actuators, consisting of two located dorsally and two ventrally, are affixed to the upper abdominal area and secured with a cloth strap that is obscured from view by the body coil. Pressurized air with a specific frequency and amplitude generated by the control unit flows via the tubes to the actuators and transduces shear waves into the abdominal region. Own figure. **B** Rabbit lying prone head-first on the PET/MRI scanner table. Two actuators are placed laterally on the upper abdominal region. A head coil is used for imaging. Modified from Shahryari et al., 2019<sup>89</sup>.

A single-shot, spin-echo (SE) echo planar imaging (EPI) multi-slice sequence with flow-compensated (1<sup>th</sup> moment nulling) MEGs (see 2.2.3 Image acquisition) was used in all studies.<sup>87-89</sup> Eight equidistant phase steps over a whole vibration period were acquired for each vibration frequency for all three Cartesian motion field directions.<sup>87-89</sup> Further MRE imaging parameters for all three studies are shown in Table 2.

**Table 2:** MRE sequence parameters for Study 1, Study 2 and Study 3.

A spin-echo, echo planar imaging sequence with integrated motion encoding gradient (MEG) was used for all studies. It is noteworthy that the measurement time for Study 2 was solely listed for free-breathing MRE. Own table based on data from Shahryari et al., 2019<sup>87</sup>, 2021<sup>88</sup> and 2023<sup>89</sup>.

Study 1	Study 2	Study 3
---------	---------	---------

<b>Scanner</b>	Magnetom Aera, Siemens Healthineers	Magnetom Sonata, Siemens Healthineers	Magnetom Biograph mMR, Siemens Healthineers
<b>Magnetic field strength (T)</b>	1.5	1.5	3
<b>Time of echo (ms)</b>	59	55	40
<b>Time of repetition (ms)</b>	2050	1200	1000
<b>Matrix size</b>	128 × 104	104 × 128	104 × 60
<b>Field of view (mm<sup>2</sup>)</b>	384 × 312	284 × 350	161.2 × 93
<b>Voxel size (mm<sup>3</sup>)</b>	3 × 3 × 5	2.7 × 2.7 × 5	1.55 × 1.55 × 5
<b>Number of slices</b>	15	9	6
<b>Slice orientation</b>	transversal	coronal	transversal
<b>Mechanical frequencies (Hz)</b>	30, 40, 50, 60	30, 40, 50, 60	40, 50, 60, 70, 80
<b>MEG frequencies (Hz)</b>	43.48 for 30, 40, and 50 Hz and 44.88 Hz for 60 Hz	43.48 for 30, 40, and 50 Hz and 44.88 Hz for 60 Hz	78.61
<b>MEG amplitude (mT/m)</b>	30	30	42
<b>Acquisition time (minutes)</b>	3.5	2 for free-breathing	8

*Study 1 - Patient study:* MRI and MRE acquisitions were conducted in a 1.5 T clinical MRI scanner (Magnetom Aera, Siemens Healthineers, Erlangen, Germany) at the Charité – Campus Virchow Klinikum, using the spine-array coils, which are integrated into the examination table and a 12-channel phased-array surface body coil.<sup>87</sup> For anatomical

lesion localization, localizer, transversal T<sub>2</sub>-weighted and T<sub>1</sub>-weighted sequences were conducted prior to MRE. Multifrequency MRE was conducted in a transversal slice orientation and the center of the slice block was placed on the center of the liver lesion.<sup>87</sup> MRE was conducted in free breathing of the patient.<sup>87</sup> Figure 5 shows wave fields of a 40 Hz frequency for all three MEG directions, as well as a clinical T<sub>2</sub>-weighted sequence as anatomical reference of a patient with a liver tumor.<sup>87</sup>

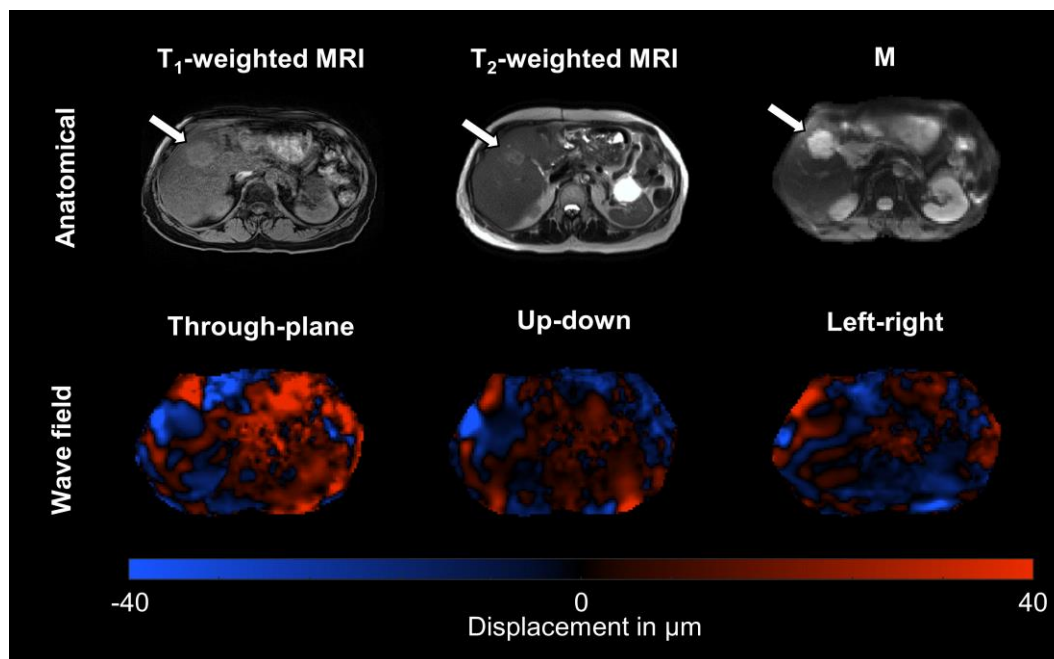


**Figure 5:** Wave fields of 40 Hz frequency in a patient with a liver tumor.

Shown are an anatomic T<sub>2</sub>-weighted image and the MRE wave field for the three motion encoding gradients (MEGs) with a vibration frequency of 40 Hz in a patient diagnosed with hepatocellular carcinoma (HCC). The arrow points to the liver tumor. Own figure based on data from Shahryari et al., 2019<sup>87</sup>.

**Study 2 - Participant study:** Multifrequency MRE and MRI was performed at the Charité – Campus Mitte in a 1.5 T clinical Scanner (Magnetom Sonata, Siemens Healthineers, Erlangen, Germany) using the spine-array coils and a 12-channel phased-array surface body coil.<sup>88</sup> For anatomical localization of organs, a localizer, transversal T<sub>2</sub>-weighted and T<sub>1</sub>-weighted sequences, as well as a coronal T<sub>2</sub>-weighted sequence were acquired prior to MRE.<sup>88</sup> Multifrequency MRE was performed in a coronal slice orientation to cover multiple abdominal organs. Four different multifrequency MRE acquisitions paradigms

were conducted to investigate motion reduction strategies related to respiratory during abdominal MRE in each participant:<sup>88</sup>

(i) Acquisition of repeated breath-holds (BH-MRE): Each MEG component and frequency was acquired with separate breath-holds, resulting in 12 acquisitions (3 MEG components × 4 frequencies) of approximately 10 seconds each. This imaging protocol can therefore be regarded as a block acquisition. The 12 acquisition blocks were merged afterwards to a full dataset of 96 consecutive images consisting of 8 time steps × 3 components × 4 frequencies.

(ii) Free-breathing (FB-MRE) of the participant: Image acquisition was performed continuously during free-breathing of the participant without accounting for respiratory motion artifacts.

For the (iii) and (iv) protocol a pencil beam navigator echo was integrated into the EPI sequence of the MRE prior to slice block acquisition.<sup>158</sup> The navigator consists of a 30° flip angle radio frequency (RF) pulse of 20 mm diameter, which was placed craniocaudally through the center of the right diaphragm. The readout axis was parallel along the RF pulse. Real time Fourier transformation of pencil beam navigator signal yielded a one-dimensional (1D) line, illustrating respiratory motion based on the position of the right diaphragm. Based on this 1D signal an acceptance window was determined. Image slice blocks were continuously excited by RF pulses. However, if the position of the diaphragm was outside of the acceptance window, no images were acquired.

(iii) Gated (G-MRE) MRE with an acceptance window of 5 mm. Data outside of the acceptance window due to respiratory motion led to interruption of the image acquisition.

(iv) Gated MRE with an acceptance window of 20 mm and a slice block position adjustment according to the depicted navigator signal (GF-MRE). The slice block was moved craniocaudally according to the position of the right diaphragm. Only if respiratory motion led to data outside of the acceptance window image acquisition was interrupted similar to G-MRE. Figure 6 illustrates a scheme of the different multifrequency MRE protocols conducted in this study.

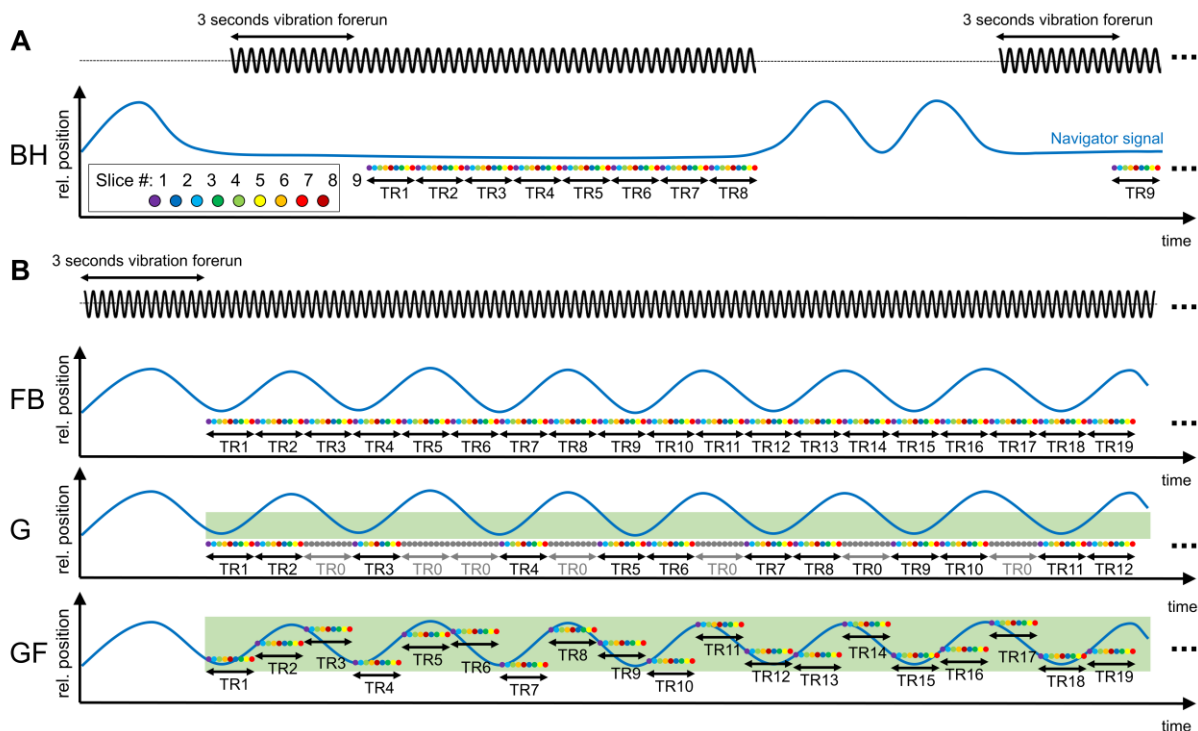


**Figure 6:** Simplified scheme of image acquisition timing of the four multifrequency MRE protocols conducted in Study 2 - Participant study.

**A** shows block acquisition of breath-hold MRE protocol. **B** shows continuously acquired free-breathing (FB), gated based on navigator signal of the diaphragm (G) and gated and automated slice block adjustment based on navigator signal of the diaphragm (GF) MRE paradigms. Mechanical vibration is shown as black sine wave. Respiratory motion indicated by the navigator signal is shown as blue line on the relative (rel.) position axis. Vibration frequency forerun of 3 seconds was performed prior to image acquisition to achieve steady state harmonic oscillation of the abdominal organs. MRE slice blocks consists of 9 slices, which are shown by colored circle within the different repetition times (e.g., TR1, TR2, etc.). Slices are acquired in an interleaved manner, 1,3,5,7,9,2,4,6,8 as indicated by the different colors. Relative position and automated adjustment of slice blocks are shown by the relative position of TRs on the rel. position axis. For G and GF, image acquisition interruption caused by navigator signal outside of the acceptance window due to respiratory motion is shown as grey TR0. Of note, RF excitation was performed continuously. From Shahryari et al., 2021<sup>88</sup>.

**Study 3 – Animal study:** Prior to imaging, blood glucose level and animal weight were measured. MRI, MRE and PET were conducted in a 3 T clinical hybrid PET/MRI scanner (Magnetom Biograph mMR, Siemens Healthineers, Erlangen, Germany) at the Charité –

Campus Virchow Klinikum using the 20-channel head coil.<sup>89</sup> The rabbits were deeply sedated during the experiments with subcutaneously administered medetomidin hydrochlorid (Cepetor, 200 mg/kg body weight).<sup>89</sup> For anatomical reference, transversal T<sub>1</sub>-weighted fat-saturated Dixon sequence was acquired.<sup>89,159,160</sup> In a subgroup of 12 rabbits, PET using intravenously injected <sup>18</sup>F-FDG as radiotracer was performed.<sup>89</sup> PET covered the entire thorax and abdomen after an acquisition time of 60 minutes.<sup>89</sup> Ordered-subset expectation maximization with 3 iterations and 21 subsets was used for reconstruction of PET images.<sup>89,161,162</sup> An image matrix of 512 × 512 with 127 slices and an image resolution of 1 × 1 × 2 mm<sup>3</sup> was calculated.<sup>89</sup> Attenuation and scatter correction (AC) was performed by a vendor implemented ultrashort echo-time sequence.<sup>89,163</sup> Immediately after imaging experiments, euthanasia was performed using intravenously injected phentobarbital sodium (Narcoren, 300 mg/kg body weight) and liver tissue samples were dissected and immediately frozen with liquid nitrogen and stored at -80° for proteomics analysis by liquid chromatography–mass spectrometry (LC-MS).<sup>89,164</sup> Further information about proteomics analysis can be found in Shahryari et al., 2023<sup>89</sup>.

### 3.3 Data processing

Data processing was conducted in MATLAB versions: 9.5.0 (R2018a) and 9.8.0 (R2020a).<sup>165</sup> A mean magnitude image  $M$  was computed from the individual images  $m_i$  obtained from a MRE scan, and was averaged across the number  $n$  of frequencies, components, and time steps:<sup>87-89</sup>

$$M = \frac{1}{n} \sum_{i=1}^n m_i . \quad (15)$$

In *Study 1* and *Study 2*, a total of  $n = 96$  images were averaged (obtained from 8 time steps × 3 components × 4 frequencies).<sup>87,88</sup> In *Study 3*,  $n = 104$  images were averaged (obtained from 8 time steps × 3 components × 5 frequencies).<sup>89</sup>

*Study 1 - Patient study:* MDEV and  $k$ -MDEV were used and maps of  $SWS$  in m/s as surrogate for stiffness and the phase angle of the complex shear modulus  $\varphi$  in rad as surrogate for fluidity were generated.<sup>87,90,105</sup> Using information from clinical MRI examination, as well as anatomical T<sub>2</sub>-weighted sequence, volumes of interests (VOIs) covering tumor and non-tumorous liver were drawn manually on MRE mean magnitude (M) slices.<sup>87</sup> Large blood vessels were excluded from the VOIs.<sup>87</sup>

*Study 2 - participant study:* Multifrequency data processing consisted of 3 steps:<sup>88</sup> i) motion estimation and correction of tissue displacement by image registration, ii) inversion of motion corrected and uncorrected MRE data, iii) tissue stiffness and image sharpness quantification of motion corrected and uncorrected MRE.

i) The open-source Elastix toolbox was used to perform two-dimensional (2D) rigid body image registration.<sup>166</sup> Separate region of interests (ROI) defining liver, kidneys, spleen and pancreas were manually delineated on  $M$ .<sup>88</sup> ROIs covered the whole organ, as well as a tolerance area of ca. 5 pixels for possible displacement due to respiratory motion.<sup>88</sup> For each slice, 95 of the overall 96 images (8 time steps  $\times$  3 components  $\times$  4 frequencies) were registered to the first acquired image, which served as reference.<sup>88</sup> Advanced Mattes mutual information with 32 histogram bins and stochastic gradient descent were used as similarity and optimizer metric, respectively.<sup>88</sup> A pyramid scheme with 3 different resolutions and a maximum 100 iterations was performed.<sup>88</sup> For each iteration 200 random coordinates were sampled to calculate the similarity metric.<sup>88</sup> Consequently, for each organ  $n = 95$  matrices with relative  $x$  and  $y$  displacement to the reference image were generated.<sup>88</sup> The mean displacement  $U$  was calculated by the magnitude of  $x$  and  $y$  displacement:<sup>88</sup>

$$U = \frac{1}{n} \sum_{i=1}^n \sqrt{(\bar{x} - \vec{x})^2 + (\bar{y} - \vec{y})^2} . \quad (16)$$

ii)  $k$ -MDEV was used to generate maps of  $SWS$  in m/s of motion corrected and uncorrected MRE. ROIs of liver, kidneys, spleen and pancreas were drawn on  $M$ .<sup>88</sup> Large blood vessels were excluded from the ROIs.<sup>88</sup>

iii) By applying a  $3 \times 3$  Laplacian derivate Kernel  $\Delta$  maps of image sharpness for motion corrected and uncorrected  $M$  were generated.<sup>88,167</sup> Image sharpness  $\xi$  of organs was calculated using the variance of the Laplacian  $\Delta$  maps and organ ROIs for image registration, which included the tolerance margin of organ boundaries.<sup>88</sup>

*Study 3 – Animal study:*  $k$ -MDEV was adapted to account for the applied higher frequencies and reduced liver size in rabbits.<sup>89</sup> A third order Butterworth low-pass filter with  $250 \text{ m}^{-1}$  for noise suppression was implemented.<sup>89</sup> A spatial third order Bandpass filter with a threshold of 15 and  $300 \text{ m}^{-1}$ , respectively, for directional filtering was used.<sup>89</sup> All frequencies were weighted equally for calculating maps of  $SWS$  in m/s and  $PR$  in m/s.<sup>89</sup> Maps of  $M$ ,  $SWS$ ,  $PR$  and AC PET images were converted to NIFTI file format.<sup>89</sup> Liver

VOIs were manually drawn in ITK-SNAP on  $M$  and AC PET, respectively.<sup>89,168</sup> Standardized uptake values ( $SUV$ ) were calculated for liver VOI for each rabbit.<sup>89</sup> Shotgun proteome profiling was conducted on LC-MS data.<sup>89,164</sup> HEPATOKIN1 was used on proteomics data to calculate metabolic liver capacities of central metabolic liver functions, such a lipid, amino acid, and carbohydrate metabolisms.<sup>89,169</sup> A range of physiological states by changes of particular plasma metabolites (e.g. plasma glucose between 3-12 mM) was used to assess maximum capacities of physiological functions by personalized kinetic modelling.<sup>89,169-173</sup> Further information about the metabolic modelling can be found in Shahryari et al., 2023<sup>89</sup>.

### 3.4 Statistical analysis

All statistical analyses were performed in R versions 3.4.3, 3.6.2 and 4.0.2 using "lme4", "lsmeans", "pROC," and "ggplot2" packages.<sup>87-89,174</sup> Unless stated otherwise,  $P < 0.05$  was considered statistically significant.

*Study 1 - Patient study:* Mean  $SWS$  and  $\varphi$  values were calculated for tumor and liver tissue VOIs. Data were grouped by tumor entity and means  $\pm$  standard deviations (SD) are given.<sup>87</sup> The two different tumor entities in two patients were regarded as independent samples.<sup>87</sup> Nonparametric Kruskal-Wallis test with a Bonferroni corrected Tukey's post-hoc test was performed to identify differences of  $SWS$  and  $\varphi$  between tumor entities.<sup>87</sup> To account for the dependency of multiple lesions within a subject, a random intercept general linear mixed-effect models (GLMM) was used with the categorical outcome variable "tumor" or "liver", the fixed effect  $SWS$  and  $\varphi$ , respectively.<sup>87</sup> Patients were treated as a random effect.<sup>87</sup> Receiver operating characteristic curves based on the predicted probabilities of the GLMMs were used to estimate the separability of tumor and liver.<sup>87,175</sup> DeLong's methods were used to compare ROCs.<sup>87,176</sup> ROC was also performed for separation of malignant and benign liver lesions based on  $SWS$  and  $\varphi$ .<sup>87</sup> For this purpose, values of multiple lesions of the same entity within a subject were averaged.<sup>87</sup> ROC analysis was repeated excluding hepatic hemangioma due to their uncomplicated diagnostic in clinical MRI by strong  $T_2$ -hyperintensity.<sup>87,177</sup> Sensitivity, specificity and area under the receiver operating characteristics curve (AUC) are provided.<sup>87</sup> Youden index was used to derive cutoff values for  $SWS$  and  $\varphi$ .<sup>87,178</sup> 95% confidence intervals (CI) are given for the statistical tests.

*Study 2 - Participant study:* Total image acquisition time was calculated for each MRE acquisition paradigms.  $U$  of liver, kidneys, spleen and pancreas was calculated for all four acquisition paradigms.<sup>88</sup> Mean  $SWS$  and  $\sigma$  was computed for all four MRE acquisition paradigms with and without motion correction.<sup>88</sup> To estimate differences in  $U$  and  $SWS$  of organs between the different acquisition paradigms random intercept linear mixed effect models (LMMs) were performed.<sup>88</sup>  $U$  and  $SWS$  were set as numerical outcome variables, the different acquisition paradigms and abdominal organs, as well as their interaction were set as fixed effects.<sup>88</sup> Participants were defined as a random effect.<sup>88</sup> Statistical significant differences of the fixed effects on the outcome variables were analyzed by Bonferroni corrected Tukey's post-hoc test.<sup>88</sup> Differences in  $SWS$  and  $\xi$  between motion corrected and uncorrected MRE for all organs and acquisition paradigms was tested by paired two-sided Student's t-test or Wilcoxon signed-rank test, respectively.<sup>88</sup> Additionally, difference in motion uncorrected BH-MRE were tested against motion-corrected FB-MRE in all organs.<sup>88</sup>

*Study 3 – Animal study:* Mean liver  $SWS$ , PR and  $SUV$  were calculated for each rabbit.<sup>89</sup> Rabbits were grouped in two groups based on unbiased cluster analysis by the clustergram function in MATLAB version 9.10.0 (R2021a)<sup>165</sup> using the bioinformatics toolbox.<sup>89</sup> In addition to metabolic clustering, livers were divided into a “soft” and “stiff” according to their mechanical properties, with a  $SWS$  cutoff value of 1.6 m/s.<sup>89</sup> Statistical differences between the two metabolic cluster groups, as well as stiffness group were analyzed by unpaired two-sided Student's t-test or paired Wilcoxon signed-rank test, depending on whether normality assumption was met.<sup>89</sup> Correlation of parameters was analyzed by linear regression models.<sup>89</sup>



## 4 Results

### 4.1 Study 1 - Patient study

The proposed tomoelastography, based on multifrequency MRE, was successfully performed in all patients without any dropout or technical failure.<sup>87</sup> Viscoelastic maps of  $SWS$  and  $\varphi$  were generated, enabling quantification of both tumor and liver tissue.<sup>87</sup> Representative maps of malignant liver tumors are shown in Figure 7 (HCC, CCA and MET). Figure 8 displays representative maps of benign liver tumors (HCA, FNH and HEM). The smallest tumor had a diameter of 9 mm (Figure 7A).<sup>87</sup> Quantitative values of tissue parameters are given in Table 3.

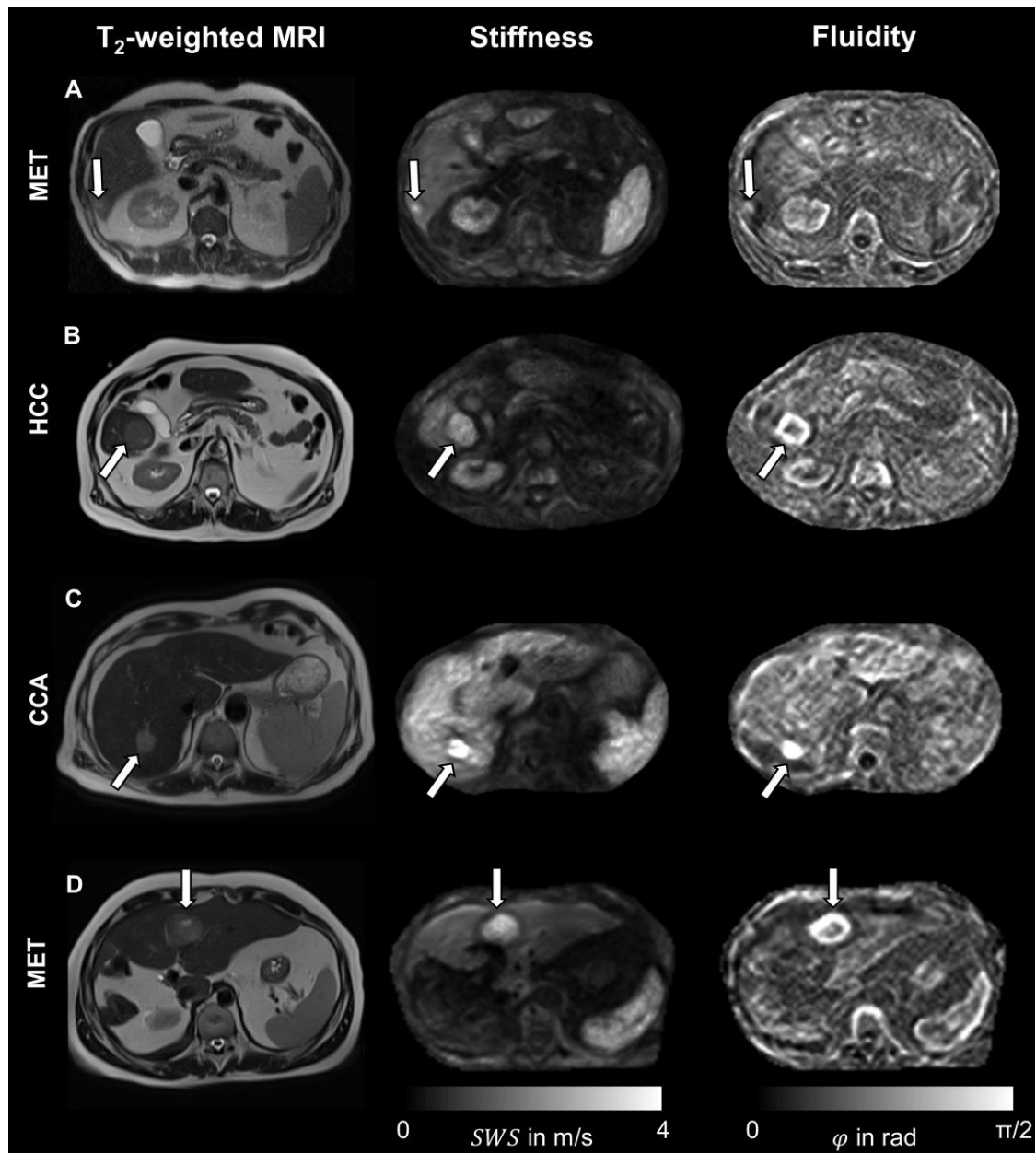


**Figure 7:** Quantitative tomoelastography maps of stiffness, based on shear wave speed (SWS), and fluidity, derived from the phase of the complex shear modulus  $\varphi$ , for four patients with malignant liver tumors.

An anatomical reference  $T_2$ -weighted image is provided, with the tumor indicated by a white arrow. **A** A 66-year-old male patient with a 9-mm diameter urothelial metastasis (MET) was found to have higher shear wave speed (SWS) and complex shear modulus phase ( $\varphi$ ) values in the tumor compared to non-tumorous liver tissue. **B** In a 78-year-old male patient with hepatocellular carcinoma (HCC) surrounded by fibrotic liver, elevated SWS was observed in the fibrotic liver. The tumor showed higher SWS and  $\varphi$  values than the fibrotic liver. **C** Cholangiocarcinoma (CCA) was detected in a 72-year-old male patient

with cirrhotic liver.  $SWS$  and  $\varphi$  values of CCA were higher than those of the surrounding non-tumorous liver, although the liver exhibited increased  $SWS$  due to cirrhosis. **D** In a 50-year-old male patient post hemihepatectomy, neuroendocrine tumor metastasis had elevated  $SWS$  and  $\varphi$  values compared to surrounding liver tissue. Edited from Shahryari et al., 2019<sup>87</sup>.

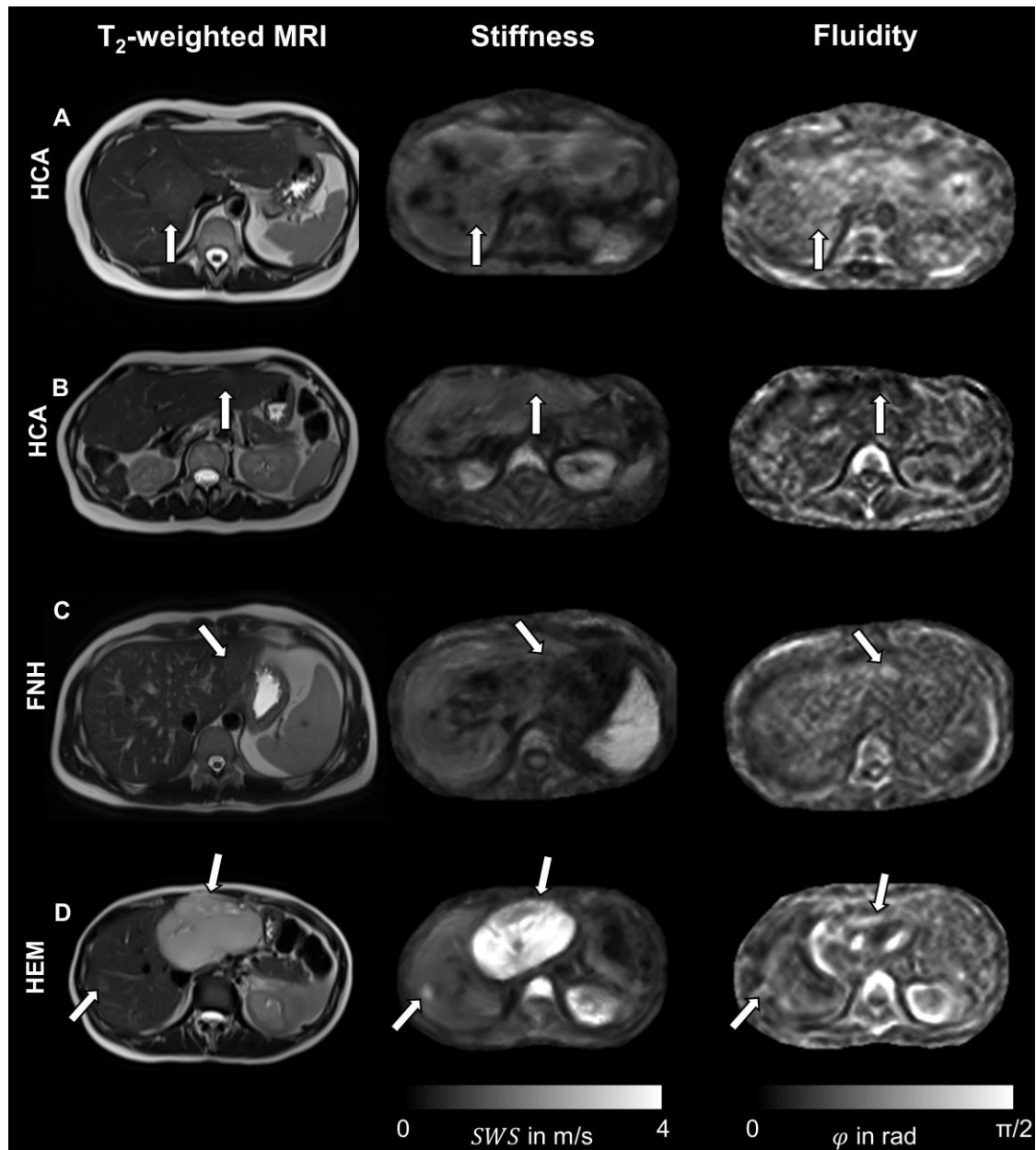


**Figure 8:** Quantitative tomoelastography maps of stiffness, based on shear wave speed ( $SWS$ ), and fluidity, derived from the phase of the complex shear modulus  $\varphi$ , for four patients with benign liver tumors.

An anatomical reference  $T_2$ -weighted image is provided, with the tumor indicated by a white arrow. **A** A 40-year-old woman presented with benign hepatocellular carcinoma (HCA), which showed similar SWS and  $\varphi$  values as the surrounding non-tumorous liver tissue. **B** In a 52-year-old woman who underwent partial hepatic resection, hepatic adenoma was observed with SWS and  $\varphi$  comparable to those observed in non-tumorous liver tissue. **C** Focal nodular hyperplasia (FNH) was detected in the liver of a 22-year-old man, where  $\varphi$  was slightly elevated compared to surrounding liver tissue, while SWS showed similar properties. **D** A 42-year-old woman with two hepatic hemangiomas (HEM) presented with elevated  $T_2$ -weighted intensity, as well as elevated SWS and  $\varphi$  values compared to surrounding liver tissue. Edited from Shahryari et al., 2019<sup>89</sup>.

**Table 3:** Quantitative parameters of tumor and liver tissue of Study 1.

Tumor diameter is reported as median with range, while tumor and liver volume of interest (VOI) are reported as median with interquartile range (IQR). Tumor and liver shear wave speed (SWS) and phase angle of the complex shear modulus  $\varphi$  are reported as mean  $\pm$  standard deviation. Edited from Shahryari et al., 2019<sup>89</sup>.

Tumor entities	Tumor diameter in mm (range)	Tumor VOI in cm <sup>3</sup> (IQR)	Tumor SWS in m/s	Tumor $\varphi$ in rad	Liver VOI in cm <sup>3</sup> (IQR)	Liver SWS in m/s	Liver $\varphi$ in rad
HCC	30 (12-150)	9.0 (1.7-33.8)	2.54 $\pm$ 0.64	1.20 $\pm$ 0.29	180 (100-344)	1.97 $\pm$ 0.49	0.81 $\pm$ 0.16
CCA	53 (16-124)	11.3 (3.9-164.4)	2.57 $\pm$ 0.90	1.24 $\pm$ 0.25	252 (156-453)	1.72 $\pm$ 0.29	0.66 $\pm$ 0.10
MET	25 (9-175)	5.7 (2.0-12.1)	2.34 $\pm$ 0.48	1.14 $\pm$ 0.28	210 (104-308)	1.61 $\pm$ 0.23	0.65 $\pm$ 0.08

HEM	23 (12-87)	1.8			260		
		(1.0-3.6)	1.97±0.45	0.95±0.30	(241-329)	1.37±0.13	0.60±0.03
FNH	21 (9-95)	2.9			372		
		(1.5-7.6)	2.08±0.96	0.78±0.24	(329-497)	1.40±0.12	0.66±0.04
HCA	30 (14-90)	5.3			226		
		(2.3-22.8)	1.41±0.21	0.66±0.12	(143-316)	1.38±0.12	0.66±0.06

*Delineation tumor vs. liver:* GLMM showed that *SWS* and  $\varphi$  could significantly predict malignant liver tumors and non-tumorous liver (*SWS* :  $\beta=3.62$  [95% CI 2.42, 5.73],  $P<0.001$ ;  $\varphi$ :  $\beta=10.64$  [95% CI 7.02, 16.35],  $P<0.001$ ).<sup>87</sup> ROC analysis revealed that malignant liver tumors could be delineated from liver tissue based on both *SWS* and  $\varphi$ , with a significantly higher AUC for  $\varphi$  than *SWS* (0.95 [95% CI 0.92, 0.98] vs. 0.88 [95% CI 0.83, 0.94],  $P < 0.01$ ).<sup>87</sup> Regarding benign lesions, only *SWS* predicted tumor and non-tumorous liver (*SWS*:  $\beta=3.2$  [95% CI 0.8, 6.55],  $P<0.05$ ;  $\varphi$ :  $\beta=3.32$  [95% CI 0.34, 7.14],  $P=0.051$ ).<sup>87</sup> No significant difference was observed between *SWS* and  $\varphi$  in AUC for delineating benign tumors from liver tissue (0.71 [95% CI 0.57, 0.84] vs. 0.66 [95% CI 0.51, 0.80],  $P=0.057$ ).<sup>87</sup> Results of GLMM based ROC analysis with AUC, sensitivity and specificity are provided in Figure 9A.

*Separation malignant vs. benign tumor:* A significant difference between the tumor entities was observed for *SWS* and  $\varphi$  ( $P<0.001$ ).<sup>87</sup> HCA showed reduced *SWS* and  $\varphi$  compared to all malignant tumor entities (*SWS*: all  $P<0.001$ ;  $\varphi$ :  $P<0.001$  for HCA vs. MET and  $P<0.01$  for HCA vs. HCC and CCA), whereas no significant difference was observed to other benign tumor entities.<sup>87</sup> Box plots of tumor entity grouped *SWS* and  $\varphi$  of tumor and liver tissue are shown in Figure 9B. Separation of malignant from benign liver lesion based on *SWS* and  $\varphi$  was excellent with an AUC of 0.85 (95% CI: 0.72, 0.98) and 0.86 (95% CI: 0.77, 0.96), respectively, with no significant difference between the AUC.<sup>87</sup> A *SWS* cutoff value of 1.75 m/s provided an outstanding sensitivity of 94% (95% CI: 87, 100) with an acceptable specificity of 78% (95% CI: 56, 94) for the separation of malignant and benign tumors.<sup>87</sup> For  $\varphi$ , a cutoff value of 0.91 rad provided and an excellent sensitivity of 83% (95% CI: 72, 93), with an acceptable specificity of 78% (95% CI: 56, 94).<sup>87</sup> By

excluding patients with hemangioma ROC analysis reveal higher AUC, sensitivity and specificity for both  $SWS$  and  $\varphi$  ( $SWS$ : AUC 0.88 [95% CI 0.73, 1.00], sensitivity 94% [95% CI 89, 100], specificity 85% [95% CI 62, 100] and  $\varphi$ : AUC 0.92 [95% CI 0.85, 0.99], sensitivity 83% [95% CI 72, 93], specificity 92% [95% CI 77, 100]).<sup>87</sup> A strong correlation between tumor and liver  $SWS$  was observed ( $R=0.74$ ,  $P<0.001$ ), whereas tumor  $SWS$  and liver  $\varphi$  were only weakly correlated ( $R=0.34$ ,  $P<0.01$ ).<sup>87</sup> ROC curves with AUC, sensitivity and specificity are provided in Figure 9C.

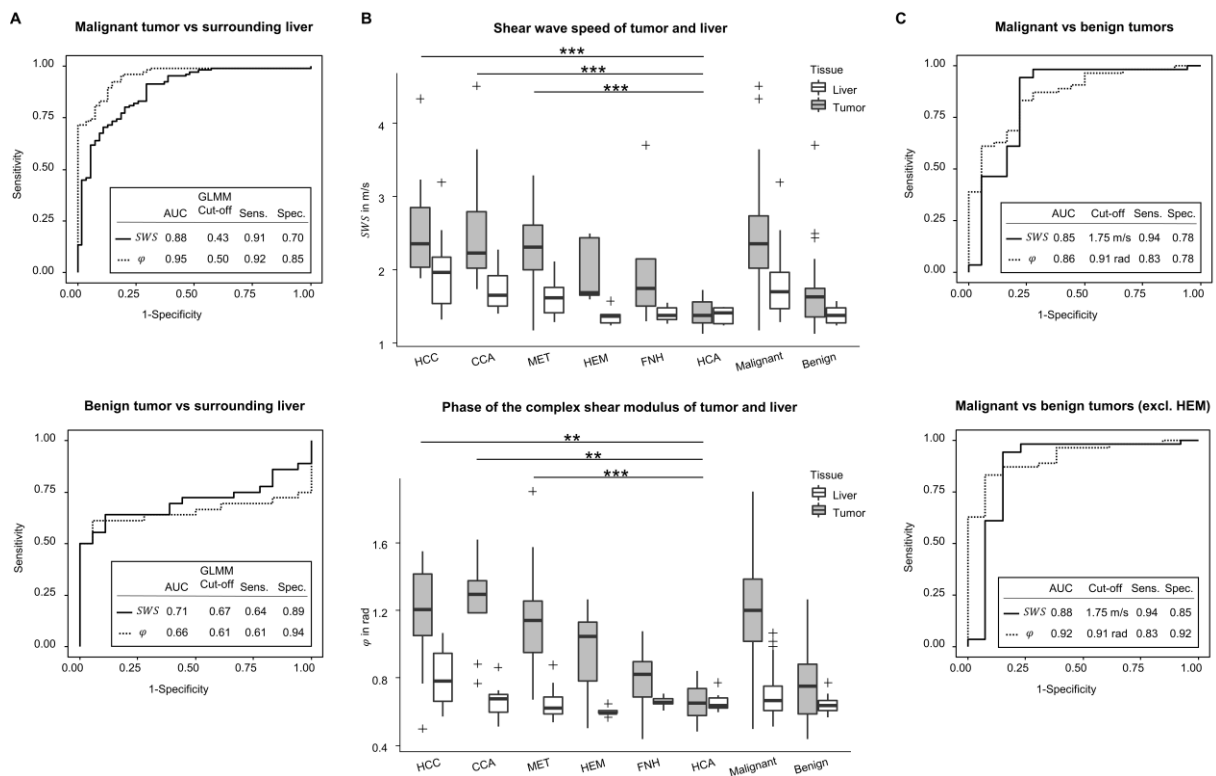


**Figure 9:** Box plot and ROC curves of  $SWS$  and  $\varphi$  of tumor and liver tissue.

**A** ROC analysis based on predicted probabilities of the generalized linear mixed models (GLMMs) delineating malignant and benign tumor, respectively, from non-tumorous tissue liver. **B** Box plots of tumor and non-tumorous liver tissue grouped by tumor entities. Asterisks denote the significant difference of Bonferroni corrected post-hoc test with \*\*  $P<0.01$  and \*\*\*  $P<0.001$ . **C** ROC analyses separating patients with malignant from patients with benign liver tumors. The analyses were also performed excluding patients with hemangioma (HEM). HCC, hepatocellular carcinoma; CCA, cholangiocarcinoma; MET, metastasis; FNH, focal nodular hyperplasia; HCA, hepatic adenoma;  $SWS$ , shear

wave speed;  $\varphi$ , phase of the complex shear modulus. Edited from Shahryari et al., 2019<sup>89</sup>.

## 4.2 Study 2 - Participant study

The examination time or MRE varied across different paradigms.<sup>88</sup> The time required for acquiring a complete multifrequency magnetic resonance elastography (MRE) dataset was  $376 \pm 68$  seconds for BH-MRE, 120 seconds for FB-MRE,  $166 \pm 117$  seconds for G-MRE, and  $128 \pm 17$  seconds for GF-MRE.<sup>88</sup> Furthermore, the mean time required for respiratory navigator adjustment prior to image acquisition in G- and GF-MRE was 168 seconds (range 18 to 413 seconds).<sup>88</sup>

*Displacement U*: Figure 10 presents representative images that demonstrate the impact of respiratory motion on liver and kidney measurements obtained through various MRE acquisition paradigms, both with and without motion correction.<sup>88</sup>

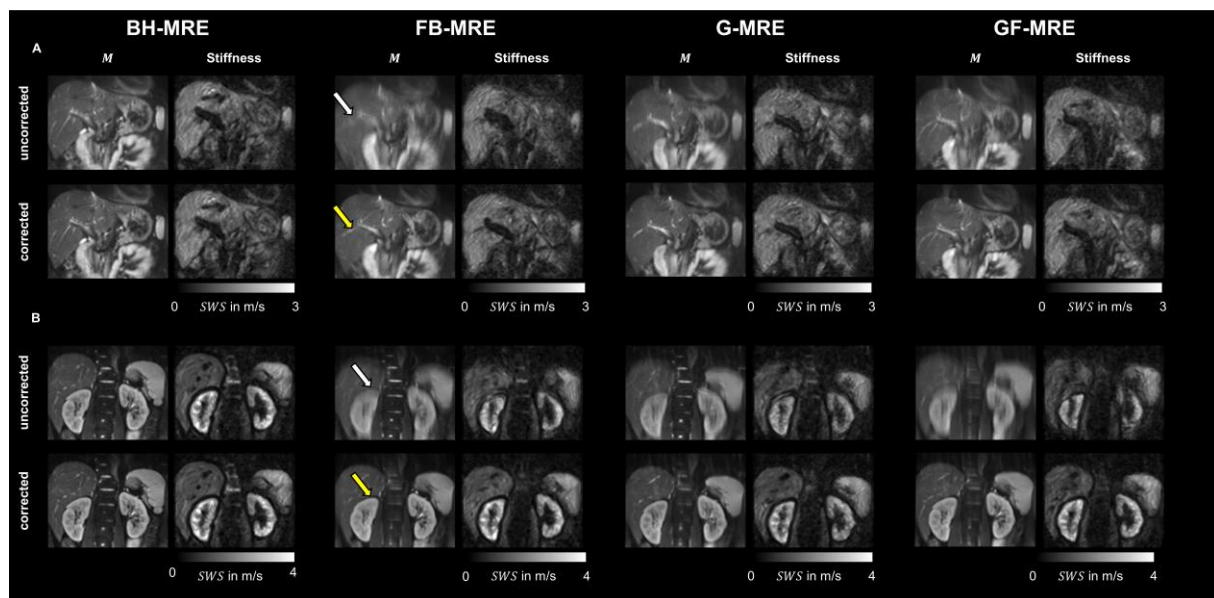


**Figure 10:** Representative tomoelastography maps illustrating breathing artifacts and motion reduction strategies investigated in Study 2 – Participant study.

Representative mean MRE magnitude ( $M$ ) and shear wave speed ( $SWS$ ) images of the liver **A** and kidneys **B** of a healthy participant measured using four acquisition paradigms with and without motion correction by 2D rigid body image registration. The white arrow indicates a blurred organ boundary, while the yellow arrow highlights an improvement in

*image sharpness, as observed by the naked eye, due to the application of motion correction. Edited from Shahryari et al., 2021<sup>88</sup>.*

Overall, due to breathing, abdominal organs varied significantly in  $U$  (Figure 11).<sup>88</sup> BH-MRE revealed smallest  $U$  without significant differences between the organs (liver:  $0.7 \pm 0.2$  mm, kidneys:  $0.4 \pm 0.2$  mm, spleen:  $0.5 \pm 0.2$  mm and pancreas  $0.7 \pm 0.5$  mm,  $P > 0.05$ ).<sup>88</sup> Liver yielded significant larger  $U$  compared to kidneys in FB ( $P < 0.01$ ), whereas no statistical significance was observed between the other organs (liver:  $4.7 \pm 1.5$  mm, kidneys:  $2.4 \pm 2.2$  mm, spleen:  $3.1 \pm 2.4$  mm, pancreas:  $3.4 \pm 1.4$  mm,  $P > 0.05$ ).<sup>88</sup> Conducting MRE without a breath-hold paradigm led to larger  $U$  for all organs (all  $P < 0.05$ ), except for kidneys measured in G ( $P > 0.05$ , G-MRE liver:  $3.5 \pm 1.4$  mm, kidneys:  $2.0 \pm 1.7$  mm, spleen:  $3.0 \pm 1.8$  mm and pancreas  $3.0 \pm 1.3$  mm).<sup>88</sup> Liver measured in FB had a significantly larger  $U$  in comparison to GF ( $P < 0.5$ ), whereas kidneys and spleen showed a significant smaller  $U$  ( $P < 0.001$ , GF-MRE liver:  $2.6 \pm 1.4$  mm, kidneys:  $5.6 \pm 2.6$  mm, spleen:  $5.9 \pm 3.8$  mm and pancreas  $5.0 \pm 2.6$  mm).<sup>88</sup> Interestingly, GF had significant larger  $U$  compared to G for kidneys and spleen ( $P < 0.001$ ), as well as pancreas ( $P < 0.05$ ).<sup>88</sup> Figure 11 shows box plots of  $U$  grouped by acquisition paradigms for the abdominal organs.

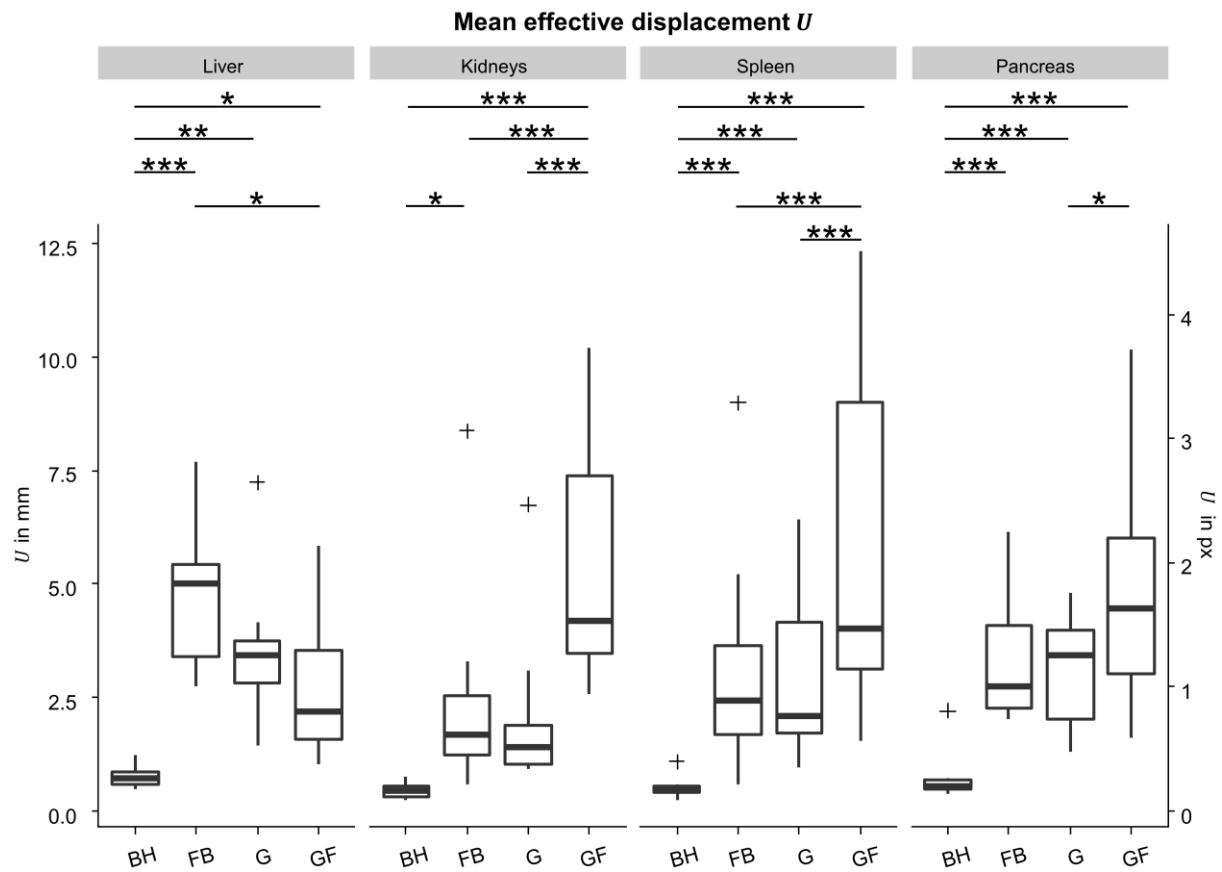


**Figure 11:** Box plots of displacement  $U$  (in mm and pixel) grouped by the different MRE acquisition paradigms.

Asterisks denote statistical significance of Bonferroni corrected Tukey's post hoc test of the linear mixed model (LMM) with \*  $P < 0.05$ , \*\*  $P < 0.01$  and \*\*\*  $P < 0.001$ . From Shahryari et al., 2021<sup>88</sup>.

**Stiffness  $SWS$ :** There was no statistical difference in  $SWS$  between the four acquisition paradigms for the organs.<sup>88</sup> Figure 12 shows box plots of  $SWS$  of the different organs grouped by acquisition paradigms.

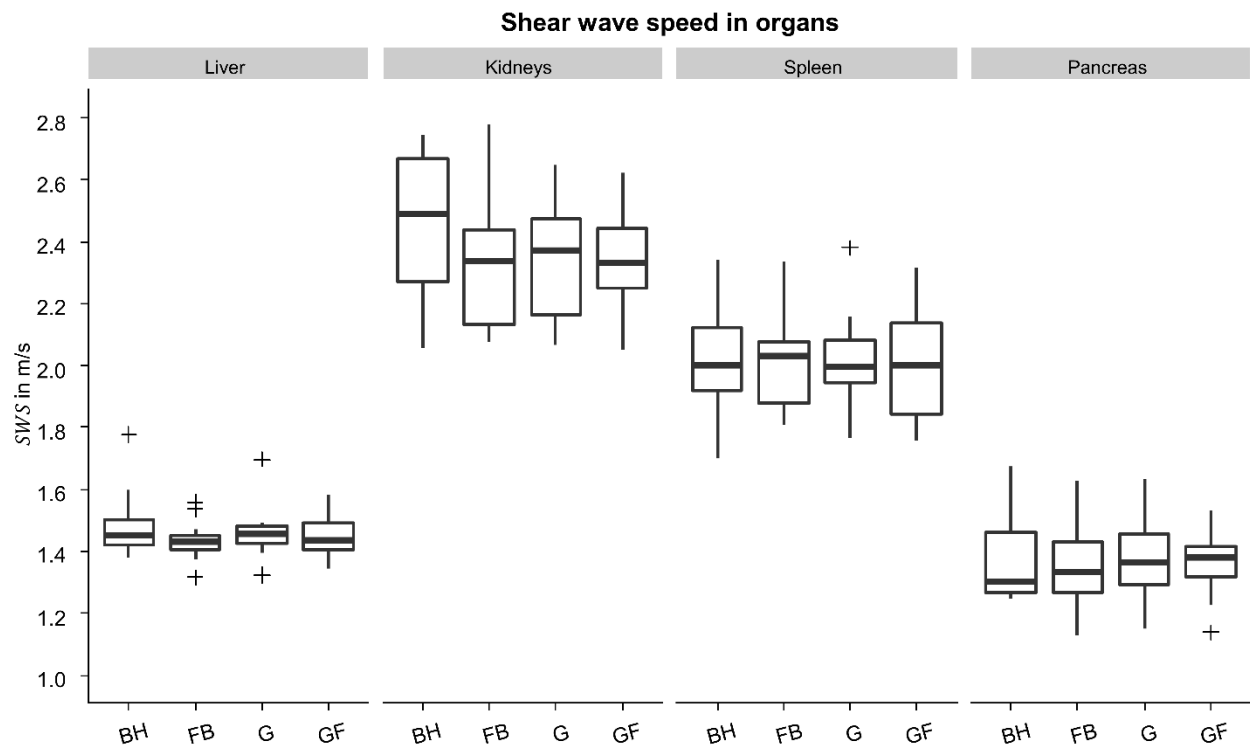


**Figure 12:** Box plots of stiffness  $SWS$  (in m/s) grouped by the different acquisition paradigms for the abdominal organs. From Shahryari et al., 2021<sup>88</sup>.

*Image sharpness  $\xi$* : Motion correction by image registration led to noticeable improvement in image sharpness  $\xi$  of  $M$ , which was already visible by the naked eye (Figure 10).<sup>88</sup> Except for liver measured in BH and GF and spleen measured in BH, image sharpness  $\xi$  was significantly higher for all abdominal organs and paradigms after motion correction ( $P < 0.05$ ).<sup>88</sup> Figure 13 shows box plots of  $\xi$  grouped by the different acquisition paradigms for the abdominal organs.

Motion corrected FB-MRE showed no significant difference of  $\xi$  in liver, spleen and pancreas compared to BH-MRE ( $P > 0.05$ ), whereas  $\xi$  in kidneys of corrected FB-MRE was significantly lower compared to uncorrected BH.<sup>88</sup>

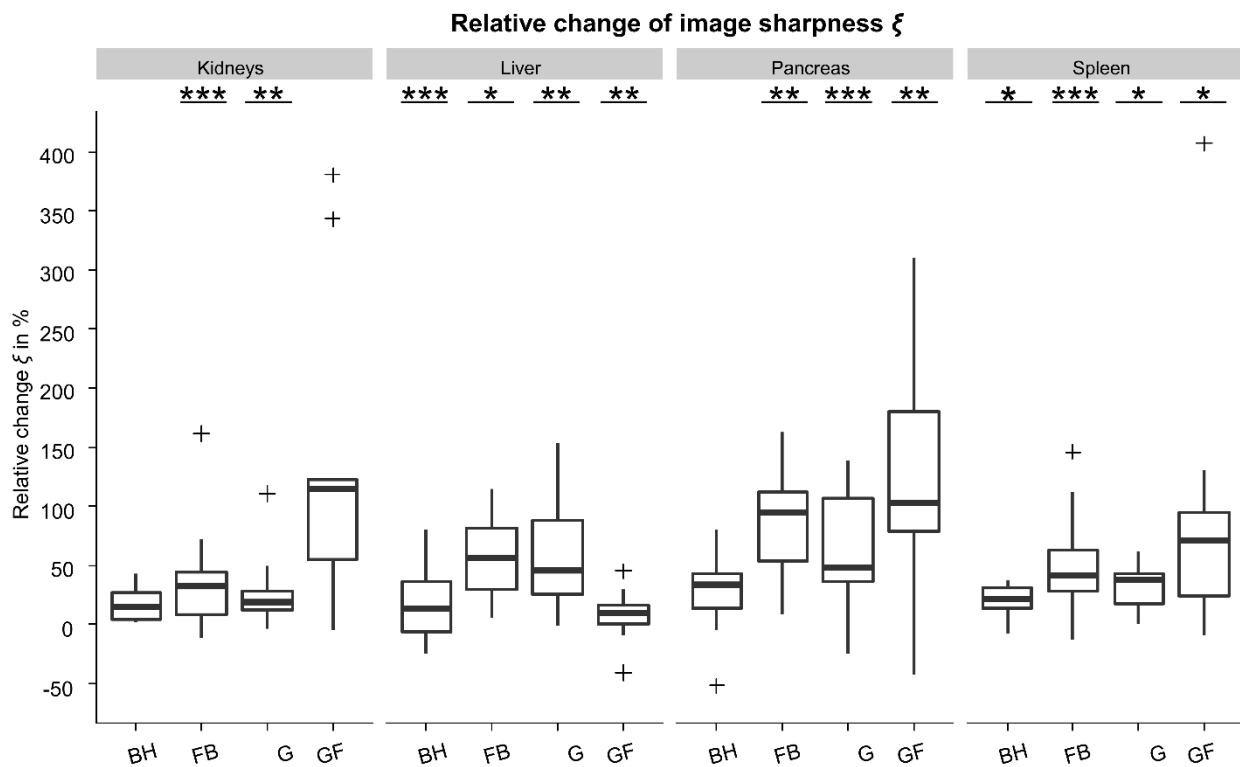


**Figure 13:** Box plots of relative improvement of image sharpness  $\xi$  in percent due to motion correction by image registration.

Sharpness improvement is quantified by the variance of the Laplacian  $\Delta$  of mean MRE magnitude image  $M$  and calculated by  $100 \left( \frac{\xi_{corrected} - \xi_{uncorrected}}{\xi_{uncorrected}} \right)$ . Asterisks denote statistical significance of two-tailed paired student's  $t$ -test with \*  $P < 0.05$ , \*\*  $P < 0.01$  and \*\*\*  $P < 0.001$ . Edited from Shahryari et al., 2021<sup>88</sup>.

### 4.3 Study 3 – Animal study

Multifrequency MRE in a clinical hybrid PET/MRI scanner was successfully performed in rabbits.<sup>89</sup> Multifrequency MRE was simultaneously performed with PET imaging and viscoelastic liver maps of  $SWS$  and  $PR$ , as well as AC PET images were obtained.<sup>89</sup> Figure 14 shows a representative case of rabbit liver maps in a PET/MRI scanner.

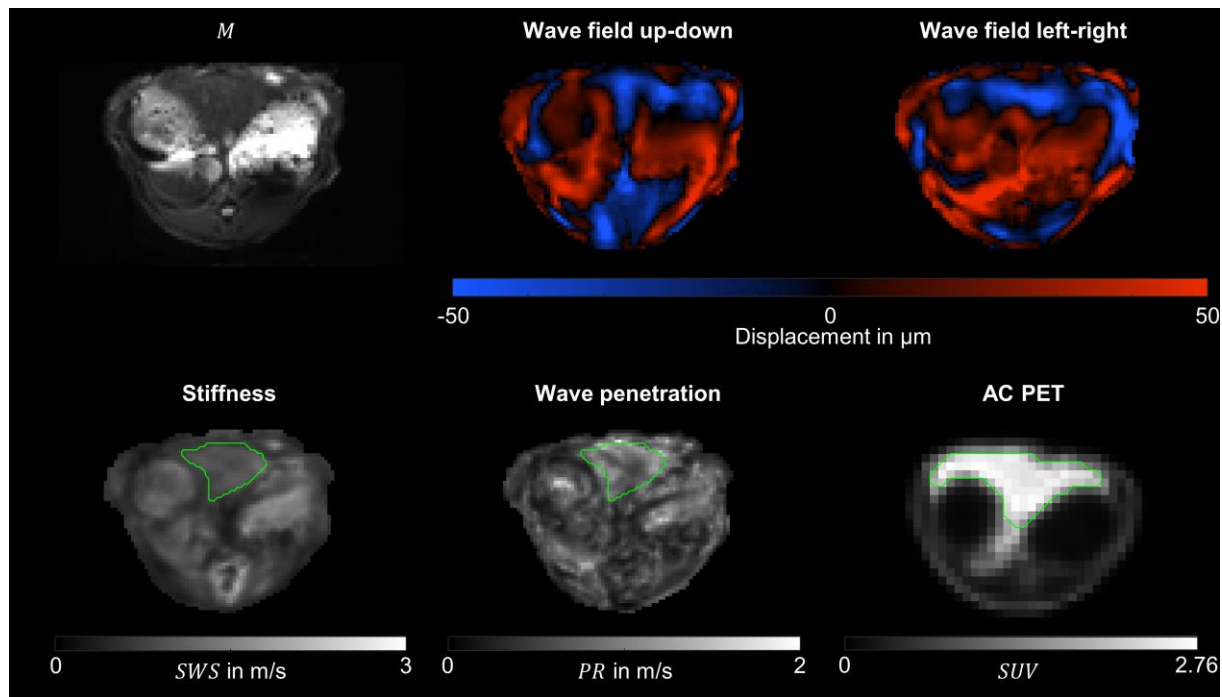


**Figure 14:** Representative rabbit liver images in a PET/MRI scanner.

The upper row shows mean MRE magnitude image ( $M$ ) and a 60 Hz wave field in up-down and left-right direction. The lower row shows shear wave speed ( $SWS$ ) and penetration rate ( $PR$ ), as well as attenuation corrected positron emission tomography (AC PET) images. Green contour delineates liver region of interest.  $SUV$ , standardized uptake value. Edited from Shahryari et al., 2023<sup>89</sup>.

Proteomics-based computational modeling of central liver function revealed heterogeneous metabolic capabilities of healthy rabbit livers, which allowed clustering of the rabbit livers in two groups.<sup>89</sup> Clustering based on metabolic capacities revealed significant metabolic difference in fatty acid uptake ( $P < 0.01$ ), very low density (vldl) export ( $P < 0.01$ ), cholesterol synthesis ( $P < 0.05$ ), triacylglycerol (tag) synthesis ( $P < 0.01$ ) and content ( $P < 0.05$ ), ketone body production ( $P < 0.01$ ), acetylacetone (acac) production ( $P < 0.001$ ), ammonia uptake ( $P < 0.05$ ), glutamine exchange ( $P < 0.01$ ) and urea production (all  $P < 0.01$ , Figure 15).<sup>89</sup> Although the viscoelastic properties of the liver did not differ significantly between metabolic groups, a trend of higher  $PR$  was observed in metabolic cluster 1 ( $P = 0.065$ ).<sup>89</sup>

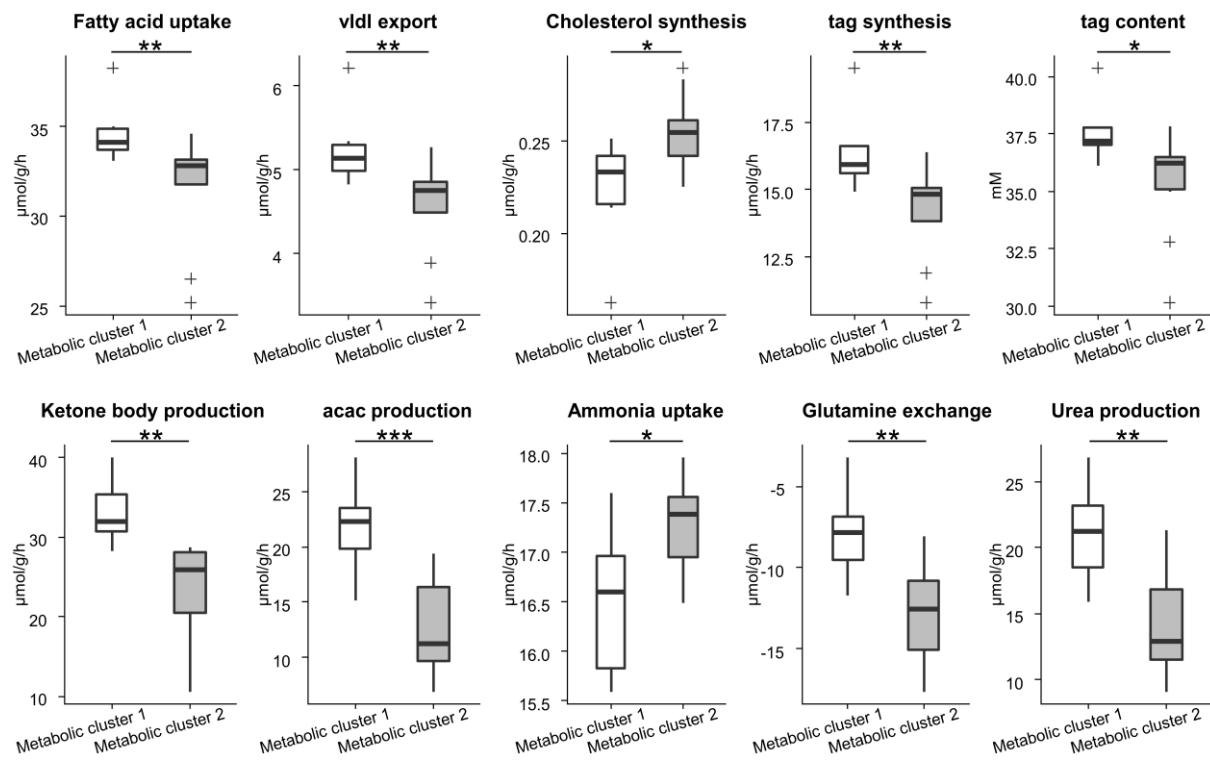


**Figure 15:** Box plots of metabolic capacities and imaging parameters of the two metabolic cluster.

Asterisks denote statistical significance of two-tailed unpaired student's *t*-test or Wilcoxon signed-ranked test, respectively with \*  $P < 0.05$ , \*\*  $P < 0.01$  and \*\*\*  $P < 0.001$ . tag, triglyceride; vldl, very low-density lipoprotein; acac, acetylacetone. Edited from Shahryari et al., 2023<sup>89</sup>.

Classifying rabbit liver based on *SWS* cutoff value of 1.6 m/s revealed significant difference in gluconeogenesis, cholesterol synthesis and tag content (all  $P < 0.05$ ).<sup>89</sup> Interestingly *PR* was significantly higher in the stiff liver cluster ( $P < 0.01$ ).<sup>89</sup> Significant differences are presented as box plots in Figure 16.

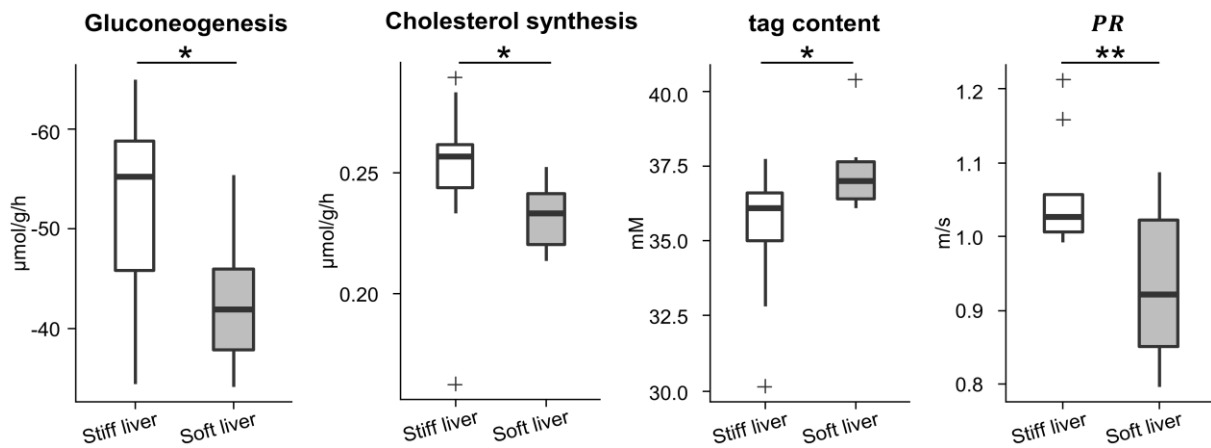


**Figure 16:** Box plots of metabolic capacities and imaging parameters of stiff and soft livers (*SWS* cutoff 1.6 m/s).

Asterisks denote statistical significance of two-tailed unpaired student's *t*-test or Wilcoxon signed-ranked test, respectively with \*  $P < 0.05$ , \*\*  $P < 0.01$  and \*\*\*  $P < 0.001$ . tag, triglyceride; PR, penetration rate. Edited from Shahryari et al., 2023<sup>89</sup>.

Linear correlation revealed a negative association of correlation of *SWS* with gluconeogenesis ( $R = -0.5$ ,  $P < 0.05$ ), as well a negative association of PR with urea production ( $R = -0.5$ ,  $P < 0.05$ ) and glutamine exchange ( $R = -0.47$ ,  $P < 0.05$ ).<sup>89</sup> A positive association of between *SWS* and PR was observed ( $R = -0.59$ ,  $P < 0.01$ ).<sup>89</sup> Scatter plots of linear correlation analysis are given in Figure 17.

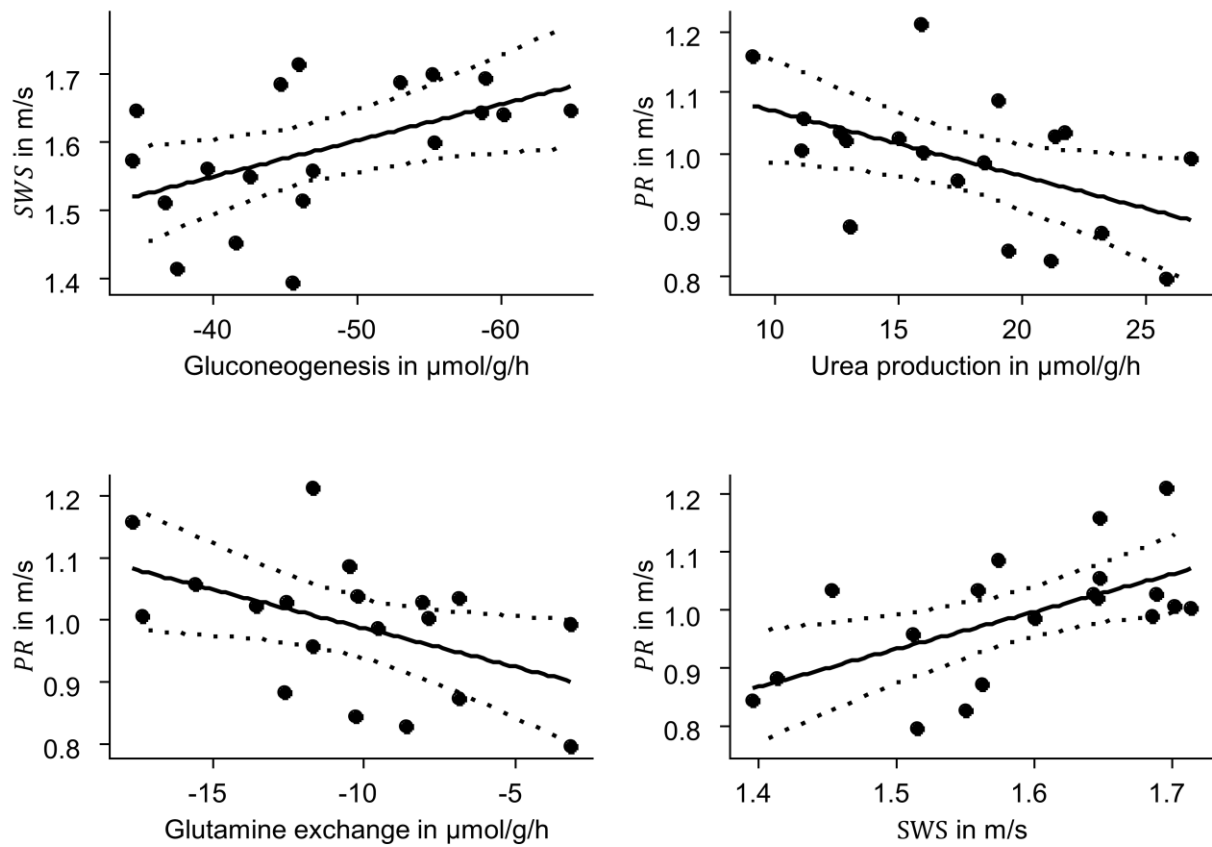


**Figure 17:** Linear correlation of imaging parameters and metabolic capacities.

Solid line illustrates regression line; dashed line illustrates the 95% confidence interval.

PR, penetration rate; SWS, shear wave speed. Edited from Shahryari et al., 2023<sup>89</sup>.



## 5 Discussion

Achieving reliable mechanical values with high spatial image resolution is challenging in abdominal MRI, but essential for its clinical applications. The novel 3D-printed bottle-shaped actuators and the tomoelastography based on multifrequency MRE pipeline enabled generation of high-resolution quantitative viscoelastic maps *in vivo* in the three presented studies.<sup>87-89</sup> This technique facilitated the first-ever delineation of liver tumors as small as 9 mm in diameter and differentiation between malignant and benign liver tumors based on tissue stiffness and fluidity.<sup>87</sup> These technical advancements enabled imaging of small animals' livers, such as rabbits, which do not fit in an animal MRI due to their size, using a human PET/MRI scanner.<sup>89</sup> For the first time, it was demonstrated that metabolic liver capacities are correlated with liver stiffness and viscosity.<sup>89</sup> Correction of respiratory motion by image registration improved image quality and robustness in abdominal MRE and therefore, is recommended for its use in clinical applications.<sup>88</sup>

### 5.1 Interpretation of results

*Study 1 - Patient study:* To the best of my knowledge, this is the first study using multifrequency MRE to investigate fluidity as a tumor marker for liver tumors.<sup>87</sup> Tomographic imaging of the stiffness and fluidity of the entire transverse slice of an abdomen to visualize multiple lesions in the same organ is of great clinical importance.<sup>87</sup> In this work, 27 out of 70 patients had more than one lesion within their livers including two patients with different entities.<sup>87</sup> Furthermore, the high spatial resolution enabled the delineation of small lesions. In this study, 3 lesions were smaller than 10 millimeter in diameter which falls below the detection limit of previous MRE work.<sup>87,97,99,179</sup> Although the detection of small lesions is not the primary task of MRE, characterization depends on the precise depiction of tumor boundaries.<sup>87</sup> Therefore, tumor delineation is important for an accurate characterization of liver lesions by MRE.<sup>87</sup> The fact that tumor stiffness strongly correlated with liver stiffness, indicates malignant liver tumors tend to grow in a stiff liver environment.<sup>54</sup> However, due to the weak correlation of tumor and liver fluidity, delineation of tumor and liver was better with fluidity than stiffness for malignant tumors.<sup>87</sup>

This study showed that malignant tumors can be distinguished with a high accuracy by an elevated of stiffness and fluidity with a *SWS* cutoff value of 1.75 m/s and  $\varphi$  cutoff value

of 0.91 rad, respectively.<sup>87</sup> Of note, as the cutoff value of  $\varphi$  of 0.91 rad is above  $\frac{\pi}{4}$  it indicates that malignant liver tumors are characterized predominantly by fluid than solid tissue properties.<sup>87</sup> Considering previous work from Garteiser et al.<sup>97</sup>, which showed that malignant tumors have an elevated  $|G^*|$  and  $G''$ , whereas  $G'$  was not different between the tumor entities, it is highly possible that the increase in stiffness  $SWS$  and fluidity  $\varphi$  is predominantly determined by an increase of  $G''$  (see 2.1).<sup>87</sup>  $G''$  can be described as viscosity (see 2.1).<sup>87</sup> In malignant tumors viscous dissipation is increased due to high interstitial pressure and fluid content, which might be caused by neovascularization with leaky blood vessels and necrosis with release of cytoplasm into the ECM forming debris.<sup>58,60,87,180,181</sup> Additionally, cell proliferation, as well as abundant accumulation of proteins, such as collagen, and their mechanical interaction increase internal mechanical friction and bulk stiffness, leading to an increase of tissue stiffness and fluidity.<sup>10,56,87,182</sup> Interestingly, in colon and brain cancer, it has been shown that an increase in microvascular density leads to an increase in stiffness and viscosity.<sup>59,183</sup>

In this work, hepatic hemangioma, which is a benign tumor originating from the vascular system, was characterized by an elevated fluidity  $\varphi$ , supporting the hypothesis of the increase of viscous dissipation due to accumulation of blood vessels.<sup>87,184</sup> As the diagnosis of HEM poses no challenge in radiology using contrast-enhanced MRI, HEM was excluded for the separation analysis of malignant and benign liver lesions.<sup>87,177</sup> This increased the specificity of stiffness  $SWS$  and fluidity  $\varphi$  to 85 % and 92 %, respectively.<sup>87</sup> The delineation of MET and their distinction from HCA and FNH based on mechanical properties as demonstrated Figure 7 could be of special clinical relevance towards an improved quantitative image-based diagnosis in radiology.<sup>87</sup> Tumor stiffness showed high sensitivity, whereas tumor fluidity showed high specificity for distinguishing malignant from benign lesions, highlighting the complementary utility of the two parameters for diagnostic purposes.<sup>87</sup> A meta-analysis of ultrasound-based shear-wave elastography in 2017 reported mean sensitivity and specificity values for differentiating malignant and benign liver lesions of 0.82 (95% CI: 73.4–88.5) and 0.80 (95% CI: 73.3–85.7), respectively.<sup>61</sup> In comparison tomoelastography outperforms current elastography methods for liver tumor characterization, most probably as result of full organ coverage with high spatial resolution and good image quality.<sup>87</sup> Thus, tumor stiffness and fluidity pose promising non-invasive quantitative biomarker for liver tumor diagnosis based on imaging.<sup>87</sup>

*Study 2 - Participant study.* So far, this is the first study that quantitatively analyzed motion of abdominal organs in MRE.<sup>88</sup> This work showed that the liver and pancreas are the abdominal organs most displaced by respiratory motion in MRE, whereas the kidneys are displaced the least.<sup>88</sup> Unsurprisingly, breath-hold MRE resulted in the least abdominal organ displacement in participants compared with navigator-based and free-breathing MRE.<sup>88</sup> A previous study analyzing the movement of a single participant's kidneys showed that the kidneys were displaced less when breathing was shallow and free in comparison to breath-hold MRE.<sup>108</sup> In contrast, the systematic analysis on 12 subjects in this work showed that breath-hold MRE resulted in less renal displacement.<sup>88</sup>

Performing MRE with an implemented respiratory navigator reduced the displacement of organs in the first acquired slices of the slice block, whereas organs acquired in slices at the end of the slice block acquisition showed increased displacement.<sup>88</sup> This is due to the fact that only a single navigator signal is taken prior to the acquisition of each slice block, resulting in precise estimates of diaphragm position for the first acquired slices, but inaccurate estimates for slices acquired later (Figure 6).<sup>88</sup> In this work, single slice analyses were performed.<sup>88</sup> The liver, which was always analyzed in the first acquired slice, showed the least displacement in the navigator-based sequences G and GF.<sup>88</sup> In contrast, the spleen and kidneys, which were evaluated in slices acquired later, showed the greatest displacement (Figure 11).<sup>88</sup> To account for this latency, the first slice of the slice block should cover the tissue of interest when performing such a navigator-based MRE sequence.<sup>88</sup>

Free-breathing MRE examination was on average 3 times faster than BH-MRE and twice as fast as navigator-based G- and GF-MRE, which can be attributed to the breathing commands and the preparation of the navigator signal, respectively.<sup>88</sup> Therefore, breath-hold examination poses a challenge in patients who cannot lie down for long periods of time or have difficulty following breathing commands.<sup>88</sup>

Stiffness values of the different organs acquired by the different MRE paradigms are in agreement with previously published  $SWS$  and  $|G^*|$  values.<sup>76,88,108,185</sup> Although the mean magnitude images acquired in free-breathing looked blurry to the naked eye and therefore indicated that  $SWS$  of organs might be altered by breathing motion, stiffness values were not affected.<sup>88</sup> This highlights the reproducibility and noise-robustness of

tomoelastography based on multifrequency MRE, since alterations in actuator position and wave amplitude caused by breathing did not seem to affect the mechanical values.<sup>88</sup> As the spatial wavelength is analyzed locally in the inversion algorithm, boundary artifacts caused by breathing might have a minor influence on the final mechanical parameter maps.<sup>22,88,90</sup> Additionally, the eight acquired time points are Fourier transformed (see 2.2.3) and only the fundamental frequency of the harmonic actuation frequency is used for further calculation in the inversion algorithm.<sup>22,88,90</sup> Therefore, shear wave alterations caused by respiratory motion do not affect the inversion algorithm unless they overlap with the fundamental frequency.<sup>88</sup>

Interestingly, previous studies using single-frequency gradient-echo MRE showed no statistical difference in liver stiffness between breath-hold, navigator and free-breathing MRE.<sup>86,88,186</sup> In these studies breath-hold MRE had twice the measurement time, whereas navigator-based MRE had five times the measurement time.<sup>86,88,186</sup> Free-breathing MRE reduced the measurable areas of the livers.<sup>86</sup> Based on this work, this limitation could be overcome by retrospective motion correction.<sup>88</sup>

Rigid body image registration after image acquisition could successfully correct motion of abdominal organs caused by breathing.<sup>88</sup> The time-averaged mean magnitude and stiffness images were less blurred and had significantly higher image sharpness quantified by  $\xi$  (Figure 13).<sup>88</sup> In particular, organ boundaries are sharper to delineate and anatomical structures such as the renal cortex and medulla are more visible to the naked eye in stiffness maps (Figure 10).<sup>88</sup> Remarkably, even MRE performed in participant's breath-hold showed a significant increase in image sharpness.<sup>88</sup>

Motion-corrected free-breathing MRE had comparable image sharpness to uncorrected breath-hold MRE, which is the recommended acquisition method according to QIBA, while having three times longer acquisition time.<sup>35,88</sup> Therefore, based on this work, MRE under free breathing combined with motion correction based on rigid body image registration is recommended for multifrequency abdominal MRE because it provides the fastest acquisition time while ensuring high image quality and sharpness.<sup>88</sup>

*Study 3 – Animal study:* This work was the first to demonstrate the feasibility of MRE in a clinical hybrid 3 T PET/MRI scanner.<sup>89</sup> Tomoelastography based on multifrequency MRE allowed to successfully generate mechanical maps of stiffness and wave penetration with

high spatial resolution in rabbit livers, while  $^{18}\text{F}$ -FDG in PET could simultaneously be acquired.<sup>89</sup> The relationship of mechanical liver properties to various metabolic liver functions assessed by computational modeling performed on proteomics data and  $^{18}\text{F}$ -FDG uptake in PET was also investigated first-ever.<sup>89</sup>

Interestingly, although the rabbits had the same genotype and were fed the same diet, they showed a wide variation in their different metabolic capacities.<sup>89</sup> This allowed classifying the livers into two clusters, whereas cluster 1 was defined by decreased biosynthetic and increased fatty-acid metabolism capabilities.<sup>89</sup> An ultrasound elastography study by Qiu et al.<sup>187</sup> in rabbits examining liver function by an indocyanine green (ICG) elimination test in fibrotic liver showed a similarly high variation in liver stiffness (1.91-8.53 kPa) and metabolic functions (ICG retention after 15 minutes 4.8%-15.6%) in the non-fibrotic (F0) control group.<sup>89</sup> Although not statistically significant, a trend towards higher wave penetration indicating more viscous tissue properties was observed in cluster 1.<sup>89</sup>

The *SWS* cutoff value of 1.6 m/s for dividing rabbit livers into two groups is consistent with the stiffness of healthy human livers at 1.4 m/s, when the frequency dependency (see 2.1) is taken into account.<sup>89,188</sup> Multifrequency MRE in humans typically uses 30 to 60 Hz, similar to *Study 1* and *Study 2* in this work, whereas the frequencies for *Study 3* were increased to 40 to 80 Hz to account for the smaller livers of rabbits.<sup>87-89</sup> This highlights the comparability of abdominal tomoelastography based on multifrequency MRE across species, MRI scanners, as well as MRI field strengths.<sup>87-89</sup>

Soft livers have decreased cholesterol synthesis, whereas gluconeogenesis and tag content are increased.<sup>89</sup> This is in agreement with a study from Abuhattum et al.<sup>189</sup>, showing that excessive accumulation of lipids is associated with a stiffness decrease in adipocytes.<sup>89</sup> Previous studies investigating liver functional reserve in cirrhotic and liver tumor patients showed a negative correlation of liver stiffness and function.<sup>190-193</sup> This is mainly due to chronic liver injury, which induces fibrogenesis with the accumulation of ECM proteins, alteration of the vasculature and perfusion with the reduction of substrate availability and hepatocellular damage.<sup>89,194</sup> A study by Berndt et al.<sup>141</sup> that analyzed liver microperfusion and structure showed the alteration of glucose metabolism by changing structural components that affected substrate availability, thus indirectly built a link between liver mechanics and metabolism.<sup>89</sup> However, in this work healthy livers were

studied and although it is tempting to discuss the relationship of metabolic function and liver mechanics, causality cannot be proven.<sup>89</sup> To account for confounding physiological factors that may alter mechanical properties, such as liver perfusion and prandial state, animals were fasted for 2 hours before imaging.<sup>89</sup> These physiological factors influence the mechanical properties within minutes and hours as shown in previous work, whereas metabolic capacity alterations occur within days or even longer.<sup>71,72,74,76,89</sup> A direct association between gluconeogenesis and stiffness, as well as urea production and glutamine exchange and wave penetration was observed.<sup>89</sup> Considering a study by Hudert et al.<sup>107</sup> of pediatric NAFLD, which showed that fibrosis is associated with an increase in stiffness, whereas steatosis leads to a decrease in wave penetration, it could be hypothesized that an alteration in hepatic gluconeogenesis and urea production could serve as an early biomarker of NAFLD – especially considering that the effects are stronger in diseased livers than in healthy ones.<sup>89</sup>

In summary, this study demonstrated that technical advancements have enabled the use of multifrequency MRE on small animals such as rabbits in a clinical PET/MRI scanner.<sup>89</sup> The study highlights the potential of MRE for non-invasively imaging metabolic liver functions by revealing correlations between liver mechanical properties and metabolic capabilities.<sup>89</sup>

## 5.2 Limitations

Although the presented studies are encouraging, they have limitations. First, only a few subjects were included in all studies.<sup>87-89</sup> For example, *Study 1 – Patient study* measured only a few patients with benign tumors.<sup>87</sup> This was because only patients with known liver lesions who were treated for further diagnosis and therapy were included in the study.<sup>87</sup> In most cases of benign liver tumors, further diagnosis or follow-up is usually not required.<sup>87</sup> Therefore, the patient population is biased towards malignant liver tumors, which reflects the patient distribution in radiology of a tertiary care facility such as Charité – Universitätsmedizin Berlin.<sup>87</sup> Possible solutions to overcome this include oversampling of patients with known benign liver tumors or performing MRE as an additional sequence on abdominal MRI examination in clinical routine measurements.<sup>87</sup> This would prolong the overall measurement time by only a few minutes.<sup>87</sup> In some patients with benign liver tumors, the diagnosis was not made by histopathology but by imaging findings based on

contrast-enhanced clinical MRI.<sup>87,156</sup> Furthermore, histologic subtypes of the different tumor entities were not analyzed.<sup>87,195-197</sup>

*In Study 2 – Participant study*, organ displacement caused by respiratory motion was analyzed and corrected only in 2D (craniocaudal and lateral) in a coronal MRE sequence because the craniocaudal direction is the main component in which displacement occurs.<sup>88,198</sup> For through-plane displacement, a 3D rigid body motion correction must be performed.<sup>88</sup> This would be of particular interest for a transversal MRE sequence.<sup>88</sup> In addition, the navigator signal in G- and GF-MRE was analyzed only once before acquiring an entire slice block.<sup>88</sup> The later the slice was acquired within the slice block, the greater was the latency between the navigator signal and the slice.<sup>88</sup> Hence, motion correction by the navigator-based MRE sequences worked well for the first acquired slices and poorly for the slices acquired later.<sup>88</sup> This limitation can be overcome by adjusting the position of the first slices of the slice block to the organ of interest.<sup>88</sup>

*In Study 3 – Animal study*, not all rabbits received PET imaging due to the high financial cost of the examination.<sup>89</sup> Unfortunately, the *SUV* samples of metabolic cluster 1 consisted of only 4 data points and statistical power was low.<sup>89</sup> Proteomic analysis was performed on only a small piece of liver tissue, whereas MRE analyzed the entire liver in at least two slices.<sup>89</sup> Although heterogeneous liver tissue could affect the proteomics data, no large heterogeneity of the liver tissue was assumed because the livers were healthy.<sup>89</sup>

### 5.3 Future research

Using the multifrequency MRE technique proposed in this work, future studies can answer novel research questions and fill research gaps based on the results of the three studies presented.

Based on *Study 1 - Patient Study*, which demonstrated that liver tumors can be accurately differentiated from the liver and that patients with malignant liver tumors can be distinguished from benign ones by multifrequency MRE, it would be interesting to conduct a diagnostic accuracy study in the form of a prospective cohort study with randomized groups and in accordance with the STARD guidelines.<sup>87,199</sup> To this end, the diagnostic accuracy of clinical contrast-enhanced MRI, which is commonly performed in radiology to diagnose liver tumors, can be compared in one group to the examination that includes MRE in the other group to demonstrate an improvement in the accuracy of liver tumor

diagnosis based on imaging. Ideally, such a study should be multicenter and use different MRI scanners or field strengths to ensure external generalizability and applicability.<sup>87,200</sup> The fluidity parameter  $\varphi$  seems promising as an indicator of malignancy, and its usefulness has already been demonstrated in studies on prostate and brain tumors.<sup>87,201,202</sup> Further research could investigate individual tumor entities and analyze different histologic features in more detail, for example, in ADE or HCC, and correlate histopathologic features with mechanical properties. Interestingly, after the publication of *Study 1*, multifrequency MRE studies revealed that mechanical parameters improve the prediction of mitotic rate and proliferation classes in HCCs.<sup>148,203</sup>

Based on *Study 2 - Participant study*, it is recommended to perform abdominal MRE in free-breathing subjects and then correct for respiratory motion in the images using image registration techniques.<sup>88</sup> Because the analyses and motion correction strategies were only 2D, 3D rigid body correction should be performed in future studies to account for motion through the imaging plane.<sup>88</sup> The findings of this study may also be applicable to other organs such as the uterus and could potentially be used to improve image quality and reproducibility in future applications.<sup>88</sup>

Since *Study 3 - Animal study* investigated the association of mechanical properties with metabolic functions of a healthy liver in a PET/MRI scanner, it would be interesting to investigate these associations in liver disease such as NAFLD and liver fibrosis.<sup>89</sup> Differences in liver metabolism within each fibrosis grade should be analyzed separately and correlated with mechanical properties.<sup>89</sup> Accurate determination of liver reserve function before liver resection in patients with cirrhosis and liver tumors is still a major problem in surgery.<sup>111,112,204</sup> A recent study by Lin et al.<sup>191</sup> showed that liver reserve capacity estimated based on the ICG clearance test was positively correlated with liver stiffness and fluidity in patients with HCC. A future study analyzing metabolic pathways and mechanics in cirrhotic livers prior to partial liver resection may shed further light on this issue. In addition, the multifrequency MRE method presented here can be used for preclinical studies of liver tumors in small animals in a clinical PET/MRI scanner so that MRI, PET, and MRE studies can be performed simultaneously to investigate the relationship between tumor imaging parameters, mechanical properties, and metabolism.<sup>89</sup> Furthermore, the presented methods can be extended to human pathologies.<sup>89</sup>

## 6 Conclusion

Assessment of tissue mechanical properties for detecting and characterizing disease is an important procedure in medicine.<sup>1</sup> Quantitative mechanical parameters measured by MRE can be used as biomarkers to aid diagnosis and monitoring of diseases.<sup>45-48,87</sup> However, to date, MRE has only been approved for the diagnosis of liver fibrosis and has not been clinically established for other organs or diseases.<sup>34,35</sup> To be approved for clinical use on other abdominal organs and in other diseases, the technology must be continuously improved and its utility for specific applications must be demonstrated.<sup>87-89</sup> The studies in this work improved the multifrequency MRE technique for clinical and preclinical use by producing highly resolved maps of reproducible biophysical parameters using novel actuators, motion correction techniques, and robust inversion algorithms.<sup>87-89</sup> The utility of MRE for liver tumor characterization, the stability against organ motion together with image registration and metabolic liver function *in vivo* has been demonstrated.<sup>87-89</sup>

In the first study, tomoelastography based on multifrequency MRE was successfully applied to 70 patients with overall 141 liver tumors and provided high-resolution maps of stiffness and fluidity of the liver and embedded liver tumors.<sup>87</sup> This allowed lesions to be delineated from liver tissue based on their mechanical properties, with the smallest lesions measuring approximately 9 mm in diameter.<sup>87</sup> Due to their increased stiffness and fluidity, malignant liver tumors could be distinguished from benign ones with high sensitivity and specificity, respectively.<sup>87</sup> Thus, tomoelastography provides noninvasive quantitative biomarkers for liver tumor characterization and lays a foundation for clinical diagnosis and therapy monitoring.<sup>87</sup>

In the second study, the displacement of abdominal organs due to respiratory motion was investigated.<sup>88</sup> The displacement of the organs was measured under different acquisition paradigms, and it was observed that the organs under breath-holding in expiration showed the least displacement. MRE under free-breathing had the shortest examination time.<sup>88</sup> Stiffness of the liver, kidneys, pancreas, and spleen were independent of respiratory motion and acquisition paradigm.<sup>88</sup> Rigid body image registration corrected organ displacement in all acquisition paradigms, which was already visible to the naked eye.<sup>88</sup> Based on the fact that MRE under free-breathing is by far the fastest acquisition method and organ stiffness was not affected by breathing or acquisition paradigm, this

study recommends performing abdominal MRE under free breathing followed by motion correction by image registration.<sup>88</sup> This procedure offers the best compromise between rapid MRE examination and good image quality for future studies.<sup>88</sup>

The third study demonstrated the feasibility of multifrequency MRE in a clinical hybrid PET/MRI scanner in rabbits.<sup>89</sup> This lays the foundation for future preclinical studies using a clinical scanner and demonstrates that PET measurements can be performed simultaneously with MRE measurements, allowing for the investigation of the relationship between metabolic functions and mechanical tissue properties.<sup>89</sup> It has been shown that even healthy livers differ in their metabolic and viscoelastic properties and soft livers have decreased cholesterol synthesis, whereas tag content, gluconeogenesis, and cholesterol synthesis are increased.<sup>89</sup> This study demonstrates relationships between the mechanical properties of the liver and its metabolic functions and highlights the possibility of noninvasive determination of liver metabolic capacity using multifrequency MRE.<sup>89</sup>

Overall, technical improvements have been achieved in both clinical and preclinical applications of multifrequency MRE and reliable maps of biomechanical tissue parameters with high spatial resolution could be generated.<sup>87-89</sup> The results of this work can be followed up in future studies to histologically investigate the relationship between tissue architecture and mechanical properties. For this purpose, clinical and preclinical studies can be performed in a clinical PET/MRI scanner. The usefulness of mechanical parameters measured by multifrequency MRE, such as tissue fluidity indicating solid-fluid tissue properties, has been demonstrated in liver tumors.<sup>87,89</sup> Therefore, this work makes an important contribution to the application of multifrequency MRE as a noninvasive *in vivo* imaging method providing quantitative mechanical biomarkers for clinical use in abdominal tissues and pathologies.<sup>87-89</sup>

## References

1. Ferguson, C.M. Inspection, Auscultation, Palpation, and Percussion of the Abdomen. in *Clinical Methods: The History, Physical, and Laboratory Examinations* (eds. Walker, H.K., Hall, W.D. & Hurst, J.W.) (Butterworth Publishers, a division of Reed Publishing, Boston, 1990).
2. Friedrich-Rust, M., Ong, M.F., Martens, S., Sarrazin, C., Bojunga, J., Zeuzem, S. & Herrmann, E. Performance of transient elastography for the staging of liver fibrosis: a meta-analysis. *Gastroenterology* 134, 960-974 (2008).
3. Lauer, G.M. & Walker, B.D. Hepatitis C virus infection. *N Engl J Med* 345, 41-52 (2001).
4. Tsochatzis, E.A., Bosch, J. & Burroughs, A.K. Liver cirrhosis. *Lancet* 383, 1749-1761 (2014).
5. Singh, S., Venkatesh, S.K., Wang, Z., Miller, F.H., Motosugi, U., Low, R.N., Hassanein, T., Asbach, P., Godfrey, E.M., Yin, M., Chen, J., Keaveny, A.P., Bridges, M., Bohte, A., Murad, M.H., Lomas, D.J., Talwalkar, J.A. & Ehman, R.L. Diagnostic performance of magnetic resonance elastography in staging liver fibrosis: a systematic review and meta-analysis of individual participant data. *Clin Gastroenterol Hepatol* 13, 440-451 e446 (2015).
6. Wang, Q.B., Zhu, H., Liu, H.L. & Zhang, B. Performance of magnetic resonance elastography and diffusion-weighted imaging for the staging of hepatic fibrosis: A meta-analysis. *Hepatology* 56, 239-247 (2012).
7. Manning, D.S. & Afdhal, N.H. Diagnosis and quantitation of fibrosis. *Gastroenterology* 134, 1670-1681 (2008).
8. Selvaraj, E.A., Mozes, F.E., Jayaswal, A.N.A., Zafarmand, M.H., Vali, Y., Lee, J.A., Levick, C.K., Young, L.A.J., Palaniyappan, N., Liu, C.H., Aithal, G.P., Romero-Gomez, M., Brosnan, M.J., Tuthill, T.A., Anstee, Q.M., Neubauer, S., Harrison, S.A., Bossuyt, P.M., Pavlides, M. & Investigators, L. Diagnostic accuracy of elastography and magnetic resonance imaging in patients with NAFLD: A systematic review and meta-analysis. *J Hepatol* 75, 770-785 (2021).
9. Huwart, L., Sempoux, C., Vicaut, E., Salameh, N., Annet, L., Danse, E., Peeters, F., ter Beek, L.C., Rahier, J., Sinkus, R., Horsmans, Y. & Van Beers, B.E. Magnetic resonance elastography for the noninvasive staging of liver fibrosis. *Gastroenterology* 135, 32-40 (2008).
10. Nia, H.T., Munn, L.L. & Jain, R.K. Physical traits of cancer. *Science* 370, eaaz0868 (2020).
11. Rimsten, A., Stenkvist, B., Johnson, H. & Lindgren, A. The Diagnostic Accuracy of Palpation and Fine-needle Biopsy and an Evaluation of their Combined Use in the Diagnosis of Breast Lesions. *Annals of Surgery* 182(1975).
12. Leitlinienprogramm Onkologie (Deutsche Krebsgesellschaft, Deutsche Krebshilfe, AWMF): S3-Leitlinie Früherkennung, Diagnose, Therapie und Nachsorge des Mammakarzinoms, Version 4.4, 2021, AWMF Registernummer: 032-045OL, <http://www.leitlinienprogramm-onkologie.de/leitlinien/mammakarzinom/> (Accessed May 11, 2022).
13. Leitlinienprogramm Onkologie (Deutsche Krebsgesellschaft, Deutsche Krebshilfe, AWMF): S3-Leitlinie Prostatakarzinom, Langversion 6.2, 2021, AWMF Registernummer: 043/022OL, <http://www.leitlinienprogramm-onkologie.de/leitlinien/prostatakarzinom/> (Accessed May 11, 2022).

14. Konert, J., Sentker, L., August, C. & Hatzinger, M. [The long journey from palpation to biopsy : The history of diagnosing prostate cancer]. *Urologe A* 60, 943-949 (2021).
15. Ngan, T.T., Nguyen, N.T.Q., Van Minh, H., Donnelly, M. & O'Neill, C. Effectiveness of clinical breast examination as a 'stand-alone' screening modality: an overview of systematic reviews. *BMC Cancer* 20, 1070 (2020).
16. Barr, R.G., Bam, A., Bortolotto, C., Bruno, C., Calliada, F., Cantisani, V., Catalano, C., Chaubal, N.G., Ciaravino, V., Correas, J.-M., Cosgrove, D., Crosara, S., D'ambrosio, F., David, E., Robertis, R.D., Leo, N.D., DiSegni, M., D'Onofrio, M., Dzyubak, B., Ferraioli, G., Filice, C., Gennari, A.G., Grazhdani, H., Hager, N.A., Hélénon, O., Isidori, A.M., Khadtare, K., Lex, A.M., Lissandrin, R., Masciotra, A., Mucelli, R.P., Pontello, M., Quايا, E., Schillizzi, G., Wilson, S.R. & Zicchetti, M. *Elastography: A Practical Approach*, (Thieme, New York, USA, 2016).
17. Sigrist, R.M.S., Liau, J., Kaffas, A.E., Chammas, M.C. & Willmann, J.K. Ultrasound Elastography: Review of Techniques and Clinical Applications. *Theranostics* 7, 1303-1329 (2017).
18. Sandrin, L., Catheline, S., Tanter, M., Hennequin, X. & Fink, M. Time-resolved pulsed elastography with ultrafast ultrasonic imaging. *Ultrason Imaging* 21, 259-272 (1999).
19. Sack, I. Magnetic resonance elastography from fundamental soft-tissue mechanics to diagnostic imaging. *Nature Reviews Physics* 5, 25-42 (2022).
20. Vuppalachchi, R., Siddiqui, M.S., Van Natta, M.L., Hallinan, E., Brandman, D., Kowdley, K., Neuschwander-Tetri, B.A., Loomba, R., Dasarathy, S., Abdelmalek, M., Doo, E., Tonascia, J.A., Kleiner, D.E., Sanyal, A.J., Chalasani, N. & Network, N.C.R. Performance characteristics of vibration-controlled transient elastography for evaluation of nonalcoholic fatty liver disease. *Hepatology* 67, 134-144 (2018).
21. Obara, N., Ueno, Y., Fukushima, K., Nakagome, Y., Kakazu, E., Kimura, O., Wakui, Y., Kido, O., Ninomiya, M., Kogure, T., Inoue, J., Kondo, Y., Shiina, M., Iwasaki, T., Yamamoto, T. & Shimosegawa, T. Transient elastography for measurement of liver stiffness measurement can detect early significant hepatic fibrosis in Japanese patients with viral and nonviral liver diseases. *J Gastroenterol* 43, 720-728 (2008).
22. Hirsch, S., Braun, J. & Sack, I. *Magnetic Resonance Elastography: Physical Background and Medical Applications*, (Wiley-VCHs, Weinheim, Germany, 2017).
23. Manduca, A., Bayly, P.J., Ehman, R.L., Kolipaka, A., Royston, T.J., Sack, I., Sinkus, R. & Van Beers, B.E. MR elastography: Principles, guidelines, and terminology. *Magn Reson Med* 85, 2377-2390 (2021).
24. Muthupillai, R., Lomas, D.J., Rossman, P.J., Greenleaf, J.F., Manduca, A. & Ehman, R.L. Magnetic resonance elastography by direct visualization of propagating acoustic strain waves. *Science* 269, 1854-1857 (1995).
25. Low, G., Owen, N.E., Joubert, I., Patterson, A.J., Graves, M.J., Alexander, G.J. & Lomas, D.J. Magnetic resonance elastography in the detection of hepatorenal syndrome in patients with cirrhosis and ascites. *Eur Radiol* 25, 2851-2858 (2015).
26. Prezzi, D., Neji, R., Kelly-Morland, C., Verma, H., O'Brien, T., Challacombe, B., Fernando, A., Chandra, A., Sinkus, R. & Goh, V. Characterization of Small Renal Tumors With Magnetic Resonance Elastography: A Feasibility Study. *Invest Radiol* 53, 344-351 (2018).
27. Garteiser, P., Doblaz, S. & Van Beers, B.E. Magnetic resonance elastography of liver and spleen: Methods and applications. *NMR Biomed* 31, e3891 (2018).

28. Venkatesh, S.K. & Ehman, R.L. Magnetic resonance elastography of abdomen. *Abdom Imaging* 40, 745-759 (2015).
29. Pepin, K.M., Ehman, R.L. & McGee, K.P. Magnetic resonance elastography (MRE) in cancer: Technique, analysis, and applications. *Prog Nucl Magn Reson Spectrosc* 90-91, 32-48 (2015).
30. Steinkohl, E., Bertoli, D., Hansen, T.M., Olesen, S.S., Drewes, A.M. & Frokjaer, J.B. Practical and clinical applications of pancreatic magnetic resonance elastography: a systematic review. *Abdom Radiol (NY)* 46, 4744-4764 (2021).
31. Bookwalter, C.A., Venkatesh, S.K., Eaton, J.E., Smyrk, T.D. & Ehman, R.L. MR elastography in primary sclerosing cholangitis: correlating liver stiffness with bile duct strictures and parenchymal changes. *Abdom Radiol (NY)* 43, 3260-3270 (2018).
32. European Association for the Study of the Liver. Electronic address, e.e.e., Clinical Practice Guideline, P., Chair, representative, E.G.B. & Panel, m. EASL Clinical Practice Guidelines on non-invasive tests for evaluation of liver disease severity and prognosis - 2021 update. *J Hepatol* 75, 659-689 (2021).
33. Xiao, G., Zhu, S., Xiao, X., Yan, L., Yang, J. & Wu, G. Comparison of laboratory tests, ultrasound, or magnetic resonance elastography to detect fibrosis in patients with nonalcoholic fatty liver disease: A meta-analysis. *Hepatology* 66, 1486-1501 (2017).
34. Aponte Ortiz, J.A., Konik, E., Eckert, E.C., Pepin, K.M. & Greenberg-Worisek, A. Premarket Approval Through the 510(k) Process: Lessons from the Translation Process of Magnetic Resonance Elastography. *Clin Transl Sci* 11, 447-449 (2018).
35. QIBA MR Biomarker Committee. MR Elastography of the Liver, Quantitative Imaging Biomarkers Alliance. Profile Stage: Technically Confirmed. February 14, 2022. Available from: <http://qibawiki.rsna.org/index.php/Profiles> (Accessed May 11, 2022).
36. Reiter, R., Shahryari, M., Tzschatzsch, H., Klatt, D., Siegmund, B., Hamm, B., Braun, J., Sack, I. & Asbach, P. Spatial heterogeneity of hepatic fibrosis in primary sclerosing cholangitis vs. viral hepatitis assessed by MR elastography. *Sci Rep* 11, 9820 (2021).
37. Yiyi, M., Xiaoqin, Q. & Lei, Z. Spleen Stiffness on Magnetic Resonance Elastography for the Detection of Portal Hypertension: A Systematic Review and Meta-Analysis. *Iran J Public Health* 51, 1925-1935 (2022).
38. Kennedy, P., Stocker, D., Carbonell, G., Said, D., Bane, O., Hectors, S., Abboud, G., Cuevas, J., Bolster, B.D., Jr., Friedman, S.L., Lewis, S., Schiano, T., Bhattacharya, D., Fischman, A., Thung, S. & Taouli, B. MR elastography outperforms shear wave elastography for the diagnosis of clinically significant portal hypertension. *Eur Radiol* 32, 8339-8349 (2022).
39. Jhang, Z.E., Wu, K.L., Chen, C.B., Chen, Y.L., Lin, P.Y. & Chou, C.T. Diagnostic value of spleen stiffness by magnetic resonance elastography for prediction of esophageal varices in cirrhotic patients. *Abdom Radiol (NY)* 46, 526-533 (2021).
40. Abe, H., Midorikawa, Y., Matsumoto, N., Moriyama, M., Shibutani, K., Okada, M., Udagawa, S., Tsuji, S. & Takayama, T. Prediction of esophageal varices by liver and spleen MR elastography. *Eur Radiol* 29, 6611-6619 (2019).
41. Wang, M., Gao, F., Wang, X., Liu, Y., Ji, R., Cang, L. & Shi, Y. Magnetic resonance elastography and T(1) mapping for early diagnosis and classification of chronic pancreatitis. *J Magn Reson Imaging* 48, 837-845 (2018).
42. Shi, Y., Cang, L., Zhang, X., Cai, X., Wang, X., Ji, R., Wang, M. & Hong, Y. The use of magnetic resonance elastography in differentiating autoimmune pancreatitis

- from pancreatic ductal adenocarcinoma: A preliminary study. *Eur J Radiol* 108, 13-20 (2018).
43. Steinkohl, E., Olesen, S.S., Hansen, T.M., Drewes, A.M. & Frokjaer, J.B. T1 relaxation times and MR elastography-derived stiffness: new potential imaging biomarkers for the assessment of chronic pancreatitis. *Abdom Radiol (NY)* 46, 5598-5608 (2021).
  44. Marticorena Garcia, S.R., Grossmann, M., Bruns, A., Durr, M., Tzschatzsch, H., Hamm, B., Braun, J., Sack, I. & Guo, J. Tomoelastography Paired With T2\* Magnetic Resonance Imaging Detects Lupus Nephritis With Normal Renal Function. *Invest Radiol* 54, 89-97 (2019).
  45. Kim, B., Kim, S.S., Cho, S.W., Cheong, J.Y., Huh, J., Kim, J.K., Lee, J.H., Ahn, H.R. & Cho, H.J. Liver stiffness in magnetic resonance elastography is prognostic for sorafenib-treated advanced hepatocellular carcinoma. *Eur Radiol* 31, 2507-2517 (2021).
  46. Allen, A.M., Shah, V.H., Therneau, T.M., Venkatesh, S.K., Mounajjed, T., Larson, J.J., Mara, K.C., Schulte, P.J., Kellogg, T.A., Kendrick, M.L., McKenzie, T.J., Greiner, S.M., Li, J., Glaser, K.J., Wells, M.L., Chen, J., Ehman, R.L. & Yin, M. The Role of Three-Dimensional Magnetic Resonance Elastography in the Diagnosis of Nonalcoholic Steatohepatitis in Obese Patients Undergoing Bariatric Surgery. *Hepatology* 71, 510-521 (2020).
  47. Chuaypen, N., Chittmittrapap, S., Avihingsanon, A., Siripongsakun, S., Wongpiyabovorn, J., Tanpowpong, N., Tanaka, Y. & Tangkijvanich, P. Liver fibrosis improvement assessed by magnetic resonance elastography and Mac-2-binding protein glycosylation isomer in patients with hepatitis C virus infection receiving direct-acting antivirals. *Hepatol Res* 51, 528-537 (2021).
  48. Zhang, X., Zhu, X., Ferguson, C.M., Jiang, K., Burningham, T., Lerman, A. & Lerman, L.O. Magnetic resonance elastography can monitor changes in medullary stiffness in response to treatment in the swine ischemic kidney. *MAGMA* 31, 375-382 (2018).
  49. Gidener, T., Ahmed, O.T., Larson, J.J., Mara, K.C., Therneau, T.M., Venkatesh, S.K., Ehman, R.L., Yin, M. & Allen, A.M. Liver Stiffness by Magnetic Resonance Elastography Predicts Future Cirrhosis, Decompensation, and Death in NAFLD. *Clin Gastroenterol Hepatol* 19, 1915-1924 e1916 (2021).
  50. Gidener, T., Yin, M., Dierkhising, R.A., Allen, A.M., Ehman, R.L. & Venkatesh, S.K. Magnetic resonance elastography for prediction of long-term progression and outcome in chronic liver disease: A retrospective study. *Hepatology* 75, 379-390 (2022).
  51. Eaton, J.E., Sen, A., Hoodeshenas, S., Schleck, C.D., Harmsen, W.S., Gores, G.J., LaRusso, N.F., Gossard, A.A., Lazaridis, K.N. & Venkatesh, S.K. Changes in Liver Stiffness, Measured by Magnetic Resonance Elastography, Associated With Hepatic Decompensation in Patients With Primary Sclerosing Cholangitis. *Clin Gastroenterol Hepatol* 18, 1576-1583 e1571 (2020).
  52. Lee, D.H., Lee, J.M., Chang, W., Yoon, J.H., Kim, Y.J., Lee, J.H., Yu, S.J. & Han, J.K. Prognostic Role of Liver Stiffness Measurements Using Magnetic Resonance Elastography in Patients with Compensated Chronic Liver Disease. *Eur Radiol* 28, 3513-3521 (2018).
  53. Idilman, I.S., Low, H.M., Bakhshi, Z., Eaton, J. & Venkatesh, S.K. Comparison of liver stiffness measurement with MRE and liver and spleen volumetry for prediction of disease severity and hepatic decompensation in patients with primary sclerosing cholangitis. *Abdom Radiol (NY)* 45, 701-709 (2020).

54. Singh, S., Fujii, L.L., Murad, M.H., Wang, Z., Asrani, S.K., Ehman, R.L., Kamath, P.S. & Talwalkar, J.A. Liver stiffness is associated with risk of decompensation, liver cancer, and death in patients with chronic liver diseases: a systematic review and meta-analysis. *Clin Gastroenterol Hepatol* 11, 1573-1584 e1571-1572; quiz e1588-1579 (2013).
55. Hanahan, D. & Weinberg, R.A. Hallmarks of cancer: the next generation. *Cell* 144, 646-674 (2011).
56. Levental, K.R., Yu, H., Kass, L., Lakins, J.N., Egeblad, M., Erler, J.T., Fong, S.F., Csiszar, K., Giaccia, A., Wenginger, W., Yamauchi, M., Gasser, D.L. & Weaver, V.M. Matrix crosslinking forces tumor progression by enhancing integrin signaling. *Cell* 139, 891-906 (2009).
57. Netti, P.A., Berk, D.A., Swartz, M.A., Grodzinsky, A.J. & Jain, R.K. Role of Extracellular Matrix Assembly in Interstitial Transport in Solid Tumors<sup>1</sup>. *Cancer Research* 60, 2497-2503 (2000).
58. Hashizume, H., Baluk, P., Morikawa, S., McLean, J.W., Thurston, G., Roberge, S., Jain, R.K. & McDonald, D.M. Openings between defective endothelial cells explain tumor vessel leakiness. *Am J Pathol* 156, 1363-1380 (2000).
59. Jamin, Y., Boulton, J.K.R., Li, J., Popov, S., Garteiser, P., Ulloa, J.L., Cummings, C., Box, G., Eccles, S.A., Jones, C., Waterton, J.C., Bamber, J.C., Sinkus, R. & Robinson, S.P. Exploring the biomechanical properties of brain malignancies and their pathologic determinants in vivo with magnetic resonance elastography. *Cancer Res* 75, 1216-1224 (2015).
60. Carmeliet, P. & Jain, R.K. Angiogenesis in cancer and other diseases. *Nature* 407, 249-257 (2000).
61. Jiao, Y., Dong, F., Wang, H., Zhang, L., Xu, J., Zheng, J., Fan, H., Gan, H., Chen, L. & Li, M. Shear wave elastography imaging for detecting malignant lesions of the liver: a systematic review and pooled meta-analysis. *Med Ultrason* 19, 16-22 (2017).
62. Shi, Y., Gao, F., Li, Y., Tao, S., Yu, B., Liu, Z., Liu, Y., Glaser, K.J., Ehman, R.L. & Guo, Q. Differentiation of benign and malignant solid pancreatic masses using magnetic resonance elastography with spin-echo echo planar imaging and three-dimensional inversion reconstruction: a prospective study. *Eur Radiol* 28, 936-945 (2018).
63. Gültekin, E., Wetz, C., Braun, J., Geisel, D., Furth, C., Hamm, B., Sack, I. & Marticorena Garcia, S.R. Added Value of Tomoelastography for Characterization of Pancreatic Neuroendocrine Tumor Aggressiveness Based on Stiffness. in *Cancers*, Vol. 13 (2021).
64. Liu, Y., Wang, M., Ji, R., Cang, L., Gao, F. & Shi, Y. Differentiation of pancreatic ductal adenocarcinoma from inflammatory mass: added value of magnetic resonance elastography. *Clin Radiol* 73, 865-872 (2018).
65. Zhao, X.G., Zheng, Y., Liang, J.M., Chan, Q.C.C., Yang, X.F., Li, G. & Yang, E.S. In vivo tumor detection on rabbit with biopsy needle as MRE driver. in *2008 30th Annual International Conference of the IEEE Engineering in Medicine and Biology Society* 121-124 (2008).
66. Page, G., Tardieu, M., Besret, L., Blot, L., Lopes, J., Sinkus, R., Van Beers, B.E. & Garteiser, P. Assessing Tumor Mechanics by MR Elastography at Different Strain Levels. *J Magn Reson Imaging* 50, 1982-1989 (2019).
67. Schregel, K., Nowicki, M.O., Palotai, M., Nazari, N., Zane, R., Sinkus, R., Lawler, S.E. & Patz, S. Magnetic Resonance Elastography reveals effects of anti-

- angiogenic glioblastoma treatment on tumor stiffness and captures progression in an orthotopic mouse model. *Cancer Imaging* 20, 35 (2020).
68. Schregel, K., Nazari, N., Nowicki, M.O., Palotai, M., Lawler, S.E., Sinkus, R., Barbone, P.E. & Patz, S. Characterization of glioblastoma in an orthotopic mouse model with magnetic resonance elastography. *NMR Biomed* 31, e3840 (2018).
  69. Chen, J., Woodrum, D.A., Glaser, K.J., Murphy, M.C., Gorny, K. & Ehman, R. Assessment of in vivo laser ablation using MR elastography with an inertial driver. *Magn Reson Med* 72, 59-67 (2014).
  70. Li, J., Jamin, Y., Boulton, J.K., Cummings, C., Waterton, J.C., Ulloa, J., Sinkus, R., Bamber, J.C. & Robinson, S.P. Tumour biomechanical response to the vascular disrupting agent ZD6126 in vivo assessed by magnetic resonance elastography. *Br J Cancer* 110, 1727-1732 (2014).
  71. Yin, M., Talwalkar, J.A., Glaser, K.J., Venkatesh, S.K., Chen, J., Manduca, A. & Ehman, R.L. Dynamic postprandial hepatic stiffness augmentation assessed with MR elastography in patients with chronic liver disease. *AJR Am J Roentgenol* 197, 64-70 (2011).
  72. Jajamovich, G.H., Dyvorne, H., Donnerhack, C. & Taouli, B. Quantitative liver MRI combining phase contrast imaging, elastography, and DWI: assessment of reproducibility and postprandial effect at 3.0 T. *PLoS One* 9, e97355 (2014).
  73. Petzold, G., Porsche, M., Ellenrieder, V., Kunsch, S. & Neesse, A. Impact of Food Intake on Liver Stiffness Determined by 2-D Shear Wave Elastography: Prospective Interventional Study in 100 Healthy Patients. *Ultrasound Med Biol* 45, 402-410 (2019).
  74. Obrzut, M., Atamaniuk, V., Chen, J., Obrzut, B., Ehman, R.L., Cholewa, M., Palusinska, A. & Gutkowski, K. Postprandial hepatic stiffness changes on magnetic resonance elastography in healthy volunteers. *Sci Rep* 11, 19786 (2021).
  75. Ipek-Ugay, S., Tzschatzsch, H., Hudert, C., Marticorena Garcia, S.R., Fischer, T., Braun, J., Althoff, C. & Sack, I. Time Harmonic Elastography Reveals Sensitivity of Liver Stiffness to Water Ingestion. *Ultrasound Med Biol* 42, 1289-1294 (2016).
  76. Dittmann, F., Tzschatzsch, H., Hirsch, S., Barnhill, E., Braun, J., Sack, I. & Guo, J. Tomoelastography of the abdomen: Tissue mechanical properties of the liver, spleen, kidney, and pancreas from single MR elastography scans at different hydration states. *Magn Reson Med* 78, 976-983 (2017).
  77. Garczynska, K., Tzschatzsch, H., Kuhl, A.A., Morr, A.S., Lilaj, L., Hackel, A., Schellenberger, E., Berndt, N., Holzhutter, H.G., Braun, J., Sack, I. & Guo, J. Changes in Liver Mechanical Properties and Water Diffusivity During Normal Pregnancy Are Driven by Cellular Hypertrophy. *Front Physiol* 11, 605205 (2020).
  78. Hines, C.D., Bley, T.A., Lindstrom, M.J. & Reeder, S.B. Repeatability of magnetic resonance elastography for quantification of hepatic stiffness. *J Magn Reson Imaging* 31, 725-731 (2010).
  79. Kim, H.J., Kim, B., Yu, H.J., Huh, J., Lee, J.H., Lee, S.S., Kim, K.W. & Kim, J.K. Reproducibility of hepatic MR elastography across field strengths, pulse sequences, scan intervals, and readers. *Abdom Radiol (NY)* 45, 107-115 (2020).
  80. Song, Q., Shi, Y., Gao, F., Yin, M., Yang, R., Liu, Y., Zhong, S. & Hong, Y. Feasibility and Reproducibility of Multifrequency Magnetic Resonance Elastography in Healthy and Diseased Pancreases. *J Magn Reson Imaging* 56, 1769-1780 (2022).

81. Lee, D.H., Lee, J.M., Han, J.K. & Choi, B.I. MR elastography of healthy liver parenchyma: Normal value and reliability of the liver stiffness value measurement. *J Magn Reson Imaging* 38, 1215-1223 (2013).
82. Wang, K., Manning, P., Szeverenyi, N., Wolfson, T., Hamilton, G., Middleton, M.S., Vaida, F., Yin, M., Glaser, K., Ehman, R.L. & Sirlin, C.B. Repeatability and reproducibility of 2D and 3D hepatic MR elastography with rigid and flexible drivers at end-expiration and end-inspiration in healthy volunteers. *Abdom Radiol (NY)* 42, 2843-2854 (2017).
83. Wang, J., Deng, Y., Jondal, D., Woodrum, D.M., Shi, Y., Yin, M. & Venkatesh, S.K. New and Emerging Applications of Magnetic Resonance Elastography of Other Abdominal Organs. *Top Magn Reson Imaging* 27, 335-352 (2018).
84. Fehlner, A., Hirsch, S., Weygandt, M., Christophel, T., Barnhill, E., Kadobianskyi, M., Braun, J., Bernarding, J., Lutzkendorf, R., Sack, I. & Hetzer, S. Increasing the spatial resolution and sensitivity of magnetic resonance elastography by correcting for subject motion and susceptibility-induced image distortions. *J Magn Reson Imaging* 46, 134-141 (2017).
85. Johnson, C.L., Holtrop, J.L., McGarry, M.D., Weaver, J.B., Paulsen, K.D., Georgiadis, J.G. & Sutton, B.P. 3D multislab, multishot acquisition for fast, whole-brain MR elastography with high signal-to-noise efficiency. *Magn Reson Med* 71, 477-485 (2014).
86. Murphy, I.G., Graves, M.J., Reid, S., Patterson, A.J., Patterson, I., Priest, A.N. & Lomas, D.J. Comparison of breath-hold, respiratory navigated and free-breathing MR elastography of the liver. *Magn Reson Imaging* 37, 46-50 (2017).
87. Shahryari, M., Tzschatzsch, H., Guo, J., Marticorena Garcia, S.R., Boning, G., Fehrenbach, U., Stencel, L., Asbach, P., Hamm, B., Kas, J.A., Braun, J., Denecke, T. & Sack, I. Tomoelastography Distinguishes Noninvasively between Benign and Malignant Liver Lesions. *Cancer Res* 79, 5704-5710 (2019).
88. Shahryari, M., Meyer, T., Warmuth, C., Herthum, H., Bertalan, G., Tzschatzsch, H., Stencel, L., Lukas, S., Lilaj, L., Braun, J. & Sack, I. Reduction of breathing artifacts in multifrequency magnetic resonance elastography of the abdomen. *Magn Reson Med* 85, 1962-1973 (2021).
89. Shahryari, M., Keller, S., Meierhofer, D., Wallach, I., Safraou, Y., Guo, J., Garcia, S.M., Braun, J., Makowski, M.R., Sack, I. & Berndt, N. On the relationship between metabolic capacities and in vivo viscoelastic properties of the liver. *Frontiers in Bioengineering and Biotechnology* 10(2023).
90. Tzschatzsch, H., Guo, J., Dittmann, F., Hirsch, S., Barnhill, E., Johrens, K., Braun, J. & Sack, I. Tomoelastography by multifrequency wave number recovery from time-harmonic propagating shear waves. *Med Image Anal* 30, 1-10 (2016).
91. Runggay, H., Arnold, M., Ferlay, J., Lesi, O., Cabasag, C.J., Vignat, J., Laversanne, M., McGlynn, K.A. & Soerjomataram, I. Global burden of primary liver cancer in 2020 and predictions to 2040. *J Hepatol* 77, 1598-1606 (2022).
92. Tsai, W.C., Kung, P.T., Wang, Y.H., Kuo, W.Y. & Li, Y.H. Influence of the time interval from diagnosis to treatment on survival for early-stage liver cancer. *PLoS One* 13, e0199532 (2018).
93. Huo, T.I., Huang, Y.H., Chiang, J.H., Wu, J.C., Lee, P.C., Chi, C.W. & Lee, S.D. Survival impact of delayed treatment in patients with hepatocellular carcinoma undergoing locoregional therapy: is there a lead-time bias? *Scand J Gastroenterol* 42, 485-492 (2007).

94. Singal, A.G., Waljee, A.K., Patel, N., Chen, E.Y., Tiro, J.A., Marrero, J.A. & Yopp, A.C. Therapeutic delays lead to worse survival among patients with hepatocellular carcinoma. *J Natl Compr Canc Netw* 11, 1101-1108 (2013).
95. Forner, A., Reig, M.E., de Lope, C.R. & Bruix, J. Current strategy for staging and treatment: the BCLC update and future prospects. *Semin Liver Dis* 30, 61-74 (2010).
96. Marrero, J.A., Kulik, L.M., Sirlin, C.B., Zhu, A.X., Finn, R.S., Abecassis, M.M., Roberts, L.R. & Heimbach, J.K. Diagnosis, Staging, and Management of Hepatocellular Carcinoma: 2018 Practice Guidance by the American Association for the Study of Liver Diseases. *Hepatology* 68, 723-750 (2018).
97. Garteiser, P., Doblaz, S., Daire, J.L., Wagner, M., Leitao, H., Vilgrain, V., Sinkus, R. & Van Beers, B.E. MR elastography of liver tumours: value of viscoelastic properties for tumour characterisation. *Eur Radiol* 22, 2169-2177 (2012).
98. Henedige, T.P., Hallinan, J.T., Leung, F.P., Teo, L.L., Iyer, S., Wang, G., Chang, S., Madhavan, K.K., Wee, A. & Venkatesh, S.K. Comparison of magnetic resonance elastography and diffusion-weighted imaging for differentiating benign and malignant liver lesions. *Eur Radiol* 26, 398-406 (2016).
99. Venkatesh, S.K., Yin, M., Glockner, J.F., Takahashi, N., Araoz, P.A., Talwalkar, J.A. & Ehman, R.L. MR elastography of liver tumors: preliminary results. *AJR Am J Roentgenol* 190, 1534-1540 (2008).
100. Koumoutsakos, P., Pivkin, I. & Milde, F. The Fluid Mechanics of Cancer and Its Therapy. *Annual Review of Fluid Mechanics, Vol 45* 45, 325-355 (2013).
101. Axel, L., Summers, R.M., Kressel, H.Y. & Charles, C. Respiratory effects in two-dimensional Fourier transform MR imaging. *Radiology* 160, 795-801 (1986).
102. Zhuo, J. & Gullapalli, R.P. AAPM/RSNA physics tutorial for residents: MR artifacts, safety, and quality control. *Radiographics* 26, 275-297 (2006).
103. Millonig, G., Friedrich, S., Adolf, S., Fonouni, H., Golriz, M., Mehrabi, A., Stiefel, P., Poschl, G., Buchler, M.W., Seitz, H.K. & Mueller, S. Liver stiffness is directly influenced by central venous pressure. *J Hepatol* 52, 206-210 (2010).
104. Ipek-Ugay, S., Tzschatzsch, H., Braun, J., Fischer, T. & Sack, I. Physiologic Reduction of Hepatic Venous Blood Flow by the Valsalva Maneuver Decreases Liver Stiffness. *J Ultrasound Med* 36, 1305-1311 (2017).
105. Hirsch, S., Guo, J., Reiter, R., Papazoglou, S., Kroencke, T., Braun, J. & Sack, I. MR elastography of the liver and the spleen using a piezoelectric driver, single-shot wave-field acquisition, and multifrequency dual parameter reconstruction. *Magn Reson Med* 71, 267-277 (2014).
106. Marticorena Garcia, S.R., Fischer, T., Durr, M., Gultekin, E., Braun, J., Sack, I. & Guo, J. Multifrequency Magnetic Resonance Elastography for the Assessment of Renal Allograft Function. *Invest Radiol* 51, 591-595 (2016).
107. Hudert, C.A., Tzschatzsch, H., Rudolph, B., Blaker, H., Loddenkemper, C., Muller, H.P., Henning, S., Bufler, P., Hamm, B., Braun, J., Holzhutter, H.G., Wiegand, S., Sack, I. & Guo, J. Tomoelastography for the Evaluation of Pediatric Nonalcoholic Fatty Liver Disease. *Invest Radiol* 54, 198-203 (2019).
108. Marticorena Garcia, S.R., Grossmann, M., Lang, S.T., Tzschatzsch, H., Dittmann, F., Hamm, B., Braun, J., Guo, J. & Sack, I. Tomoelastography of the native kidney: Regional variation and physiological effects on in vivo renal stiffness. *Magn Reson Med* 79, 2126-2134 (2018).
109. Capussotti, L., Vigano, L., Giuliani, F., Ferrero, A., Giovannini, I. & Nuzzo, G. Liver dysfunction and sepsis determine operative mortality after liver resection. *Br J Surg* 96, 88-94 (2009).

110. Mullen, J.T., Ribero, D., Reddy, S.K., Donadon, M., Zorzi, D., Gautam, S., Abdalla, E.K., Curley, S.A., Capussotti, L., Clary, B.M. & Vauthey, J.N. Hepatic insufficiency and mortality in 1,059 noncirrhotic patients undergoing major hepatectomy. *J Am Coll Surg* 204, 854-862; discussion 862-854 (2007).
111. Dokmak, S., Fteriche, F.S., Borscheid, R., Cauchy, F., Farges, O. & Belghiti, J. 2012 Liver resections in the 21st century: we are far from zero mortality. *HPB (Oxford)* 15, 908-915 (2013).
112. Kubota, K., Makuuchi, M., Kusaka, K., Kobayashi, T., Miki, K., Hasegawa, K., Harihara, Y. & Takayama, T. Measurement of liver volume and hepatic functional reserve as a guide to decision-making in resectional surgery for hepatic tumors. *Hepatology* 26, 1176-1181 (1997).
113. Wang, J., Zheng, T., Liao, Y., Geng, S., Li, J., Zhang, Z., Shang, D., Liu, C., Yu, P., Huang, Y., Liu, C., Liu, Y., Liu, S., Wang, M., Liu, D., Miao, H., Li, S., Zhang, B., Huang, A., Zhang, Y., Qi, X. & Chen, S. Machine learning prediction model for post-hepatectomy liver failure in hepatocellular carcinoma: A multicenter study. *Front Oncol* 12, 986867 (2022).
114. Ding, C., Jia, J., Bai, G., Zhou, W. & Shan, W. Predictive value of Gd-EOB-DTPA-enhanced magnetic resonance imaging for post-hepatectomy liver failure: a systematic review and meta-analysis. *Acta Radiol*, 2841851221134485 (2022).
115. Ding, C., Jia, J., Han, L., Zhou, W., Liu, Z., Bai, G. & Wang, Q. Developing and validating a nomogram based on skeletal muscle index and clinical scoring system for prediction of liver failure after hepatectomy. *Front Oncol* 13, 1036921 (2023).
116. Riauka, R., Ignatavicius, P. & Barauskas, G. Hypophosphatemia as a prognostic tool for post-hepatectomy liver failure: A systematic review. *World Journal of Gastrointestinal Surgery* 15, 249 (2023).
117. Zhang, D., Pan, Y., Yang, Z., Zeng, H., Wang, X., Chen, J., Wang, J., Zhang, Y., Zhou, Z., Chen, M. & Hu, D. A Nomogram Based on Preoperative Lab Tests, BMI, ICG-R15, and EHBF for the Prediction of Post-Hepatectomy Liver Failure in Patients with Hepatocellular Carcinoma. in *Journal of Clinical Medicine*, Vol. 12 (2023).
118. Bussler, S., Penke, M., Flemming, G., Elhassan, Y.S., Kratzsch, J., Sergejev, E., Lipek, T., Vogel, M., Spielau, U., Korner, A., de Giorgis, T. & Kiess, W. Novel Insights in the Metabolic Syndrome in Childhood and Adolescence. *Horm Res Paediatr* 88, 181-193 (2017).
119. Lonardo, A., Ballestri, S., Marchesini, G., Angulo, P. & Loria, P. Nonalcoholic fatty liver disease: a precursor of the metabolic syndrome. *Dig Liver Dis* 47, 181-190 (2015).
120. Caldwell, S. & Argo, C. The natural history of non-alcoholic fatty liver disease. *Dig Dis* 28, 162-168 (2010).
121. Wanless, I.R. & Lentz, J.S. Fatty liver hepatitis (steatohepatitis) and obesity: an autopsy study with analysis of risk factors. *Hepatology* 12, 1106-1110 (1990).
122. Marchesini, G., Bugianesi, E., Forlani, G., Cerrelli, F., Lenzi, M., Manini, R., Natale, S., Vanni, E., Villanova, N., Melchionda, N. & Rizzetto, M. Nonalcoholic fatty liver, steatohepatitis, and the metabolic syndrome. *Hepatology* 37, 917-923 (2003).
123. Ruf, A., Dirchwolf, M. & Freeman, R.B. From Child-Pugh to MELD score and beyond: Taking a walk down memory lane. *Ann Hepatol* 27, 100535 (2022).
124. Angermayr, B., Cejna, M., Karnel, F., Gschwantler, M., Koenig, F., Pidlich, J., Mendel, H., Pichler, L., Wichlas, M., Kreil, A., Schmid, M., Ferlitsch, A., Lipinski, E., Brunner, H., Lammer, J., Ferenci, P., Gangl, A. & Peck-Radosavljevic, M. Child-

- Pugh versus MELD score in predicting survival in patients undergoing transjugular intrahepatic portosystemic shunt. *Gut* 52, 879-885 (2003).
125. Cholongitas, E., Papatheodoridis, G.V., Vangeli, M., Terreni, N., Patch, D. & Burroughs, A.K. Systematic review: The model for end-stage liver disease--should it replace Child-Pugh's classification for assessing prognosis in cirrhosis? *Aliment Pharmacol Ther* 22, 1079-1089 (2005).
  126. Pugh, R.N., Murray-Lyon, I.M., Dawson, J.L., Pietroni, M.C. & Williams, R. Transection of the oesophagus for bleeding oesophageal varices. *Br J Surg* 60, 646-649 (1973).
  127. Stockmann, M., Lock, J.F., Riecke, B., Heyne, K., Martus, P., Fricke, M., Lehmann, S., Niehues, S.M., Schwabe, M., Lemke, A.J. & Neuhaus, P. Prediction of postoperative outcome after hepatectomy with a new bedside test for maximal liver function capacity. *Ann Surg* 250, 119-125 (2009).
  128. Lalazar, G., Pappo, O., Hershcovici, T., Hadjaj, T., Shubi, M., Ohana, H., Hemed, N. & Ilan, Y. A continuous <sup>13</sup>C methacetin breath test for noninvasive assessment of intrahepatic inflammation and fibrosis in patients with chronic HCV infection and normal ALT. *J Viral Hepat* 15, 716-728 (2008).
  129. Gambhir, S.S. Molecular imaging of cancer with positron emission tomography. *Nat Rev Cancer* 2, 683-693 (2002).
  130. Bodini, B., Tonietto, M., Airas, L. & Stankoff, B. Positron emission tomography in multiple sclerosis - straight to the target. *Nat Rev Neurol* 17, 663-675 (2021).
  131. Langen, K.J., Galldiks, N., Hattingen, E. & Shah, N.J. Advances in neuro-oncology imaging. *Nat Rev Neurol* 13, 279-289 (2017).
  132. Juweid, M.E. & Cheson, B.D. Positron-emission tomography and assessment of cancer therapy. *N Engl J Med* 354, 496-507 (2006).
  133. Aldin, A., Umlauff, L., Estcourt, L.J., Collins, G., Moons, K.G., Engert, A., Kobe, C., von Tresckow, B., Haque, M., Foroutan, F., Kreuzberger, N., Trivella, M. & Skoetz, N. Interim PET-results for prognosis in adults with Hodgkin lymphoma: a systematic review and meta-analysis of prognostic factor studies. *Cochrane Database Syst Rev* 1, CD012643 (2020).
  134. Kelloff, G.J., Hoffman, J.M., Johnson, B., Scher, H.I., Siegel, B.A., Cheng, E.Y., Cheson, B.D., O'Shaughnessy, J., Guyton, K.Z., Mankoff, D.A., Shankar, L., Larson, S.M., Sigman, C.C., Schilsky, R.L. & Sullivan, D.C. Progress and promise of FDG-PET imaging for cancer patient management and oncologic drug development. *Clin Cancer Res* 11, 2785-2808 (2005).
  135. Vaquero, J.J. & Kinahan, P. Positron Emission Tomography: Current Challenges and Opportunities for Technological Advances in Clinical and Preclinical Imaging Systems. *Annu Rev Biomed Eng* 17, 385-414 (2015).
  136. Wahl, R.L., Herman, J.M. & Ford, E. The promise and pitfalls of positron emission tomography and single-photon emission computed tomography molecular imaging-guided radiation therapy. *Semin Radiat Oncol* 21, 88-100 (2011).
  137. Nievelstein, R.A., Quarles van Ufford, H.M., Kwee, T.C., Bierings, M.B., Ludwig, I., Beek, F.J., de Klerk, J.M., Mali, W.P., de Bruin, P.W. & Geleijns, J. Radiation exposure and mortality risk from CT and PET imaging of patients with malignant lymphoma. *Eur Radiol* 22, 1946-1954 (2012).
  138. Kespohl, M., Bredow, C., Klingel, K., Voss, M., Paeschke, A., Zickler, M., Poller, W., Kaya, Z., Eckstein, J., Fechner, H., Spranger, J., Fahling, M., Wirth, E.K., Radoshevich, L., Thery, F., Impens, F., Berndt, N., Knobeloch, K.P. & Beling, A. Protein modification with ISG15 blocks coxsackievirus pathology by antiviral and metabolic reprogramming. *Sci Adv* 6, eaay1109 (2020).

139. Berndt, N., Eckstein, J., Heucke, N., Wuensch, T., Gajowski, R., Stockmann, M., Meierhofer, D. & Holzhutter, H.G. Metabolic heterogeneity of human hepatocellular carcinoma: implications for personalized pharmacological treatment. *FEBS J* 288, 2332-2346 (2021).
140. Berndt, N., Hudert, C.A., Eckstein, J., Loddenkemper, C., Henning, S., Bufler, P., Meierhofer, D., Sack, I., Wiegand, S., Wallach, I. & Holzhütter, H.-G. Alterations of Central Liver Metabolism of Pediatric Patients with Non-Alcoholic Fatty Liver Disease. in *International Journal of Molecular Sciences*, Vol. 23 (2022).
141. Berndt, N., Horger, M.S., Bulik, S. & Holzhutter, H.G. A multiscale modelling approach to assess the impact of metabolic zonation and microperfusion on the hepatic carbohydrate metabolism. *PLoS Comput Biol* 14, e1006005 (2018).
142. Berndt, N., Egners, A., Mastrobuoni, G., Vvedenskaya, O., Fragoulis, A., Dugourd, A., Bulik, S., Pietzke, M., Bielow, C., van Gassel, R., Damink, S.W.O., Erdem, M., Saez-Rodriguez, J., Holzhutter, H.G., Kempa, S. & Cramer, T. Kinetic modelling of quantitative proteome data predicts metabolic reprogramming of liver cancer. *Br J Cancer* 122, 233-244 (2020).
143. Berndt, N., Kolbe, E., Gajowski, R., Eckstein, J., Ott, F., Meierhofer, D., Holzhutter, H.G. & Matz-Soja, M. Functional Consequences of Metabolic Zonation in Murine Livers: Insights for an Old Story. *Hepatology* 73, 795-810 (2021).
144. Reichert, C.M., Weisenthal, L.M. & Klein, H.G. Delayed hemorrhage after percutaneous liver biopsy. *J Clin Gastroenterol* 5, 263-266 (1983).
145. Riley, T.R., 3rd. Predictors of pain medication use after percutaneous liver biopsy. *Dig Dis Sci* 47, 2151-2153 (2002).
146. Hirsch, S., Schaeffter, T. & Sack, I. The Fundamentals of Transport in Living Tissues Quantified by Medical Imaging Technologies. in *Quantification of Biophysical Parameters in Medical Imaging* (eds. Sack, I. & Schaeffter, T.) 9-43 (Springer International Publishing, Cham, 2018).
147. Wang, Y.H., Guo, J., Ma, D., Zhou, J.H., Yang, Y.C., Chen, Y.J., Wang, H.F., Sack, I., Li, R.K. & Yan, F.H. Reduced tumor stiffness quantified by tomoelastography as a predicative marker for glypican-3-positive hepatocellular carcinoma. *Frontiers in Oncology* 12(2022).
148. Hu, X., Zhou, J., Li, Y., Wang, Y., Guo, J., Sack, I., Chen, W., Yan, F., Li, R. & Wang, C. Added Value of Viscoelasticity for MRI-Based Prediction of Ki-67 Expression of Hepatocellular Carcinoma Using a Deep Learning Combined Radiomics (DLCR) Model. in *Cancers*, Vol. 14 (2022).
149. Lilaj, L., Herthum, H., Meyer, T., Shahryari, M., Bertalan, G., Caiazzo, A., Braun, J., Fischer, T., Hirsch, S. & Sack, I. Inversion-recovery MR elastography of the human brain for improved stiffness quantification near fluid-solid boundaries. *Magn Reson Med* 86, 2552-2561 (2021).
150. Herthum, H., Hetzer, S., Scheel, M., Shahryari, M., Braun, J., Paul, F. & Sack, I. In vivo stiffness of multiple sclerosis lesions is similar to that of normal-appearing white matter. *Acta Biomater* 138, 410-421 (2022).
151. Herthum, H., Shahryari, M., Tzschatsch, H., Schrank, F., Warmuth, C., Goner, S., Hetzer, S., Neubauer, H., Pfeuffer, J., Braun, J. & Sack, I. Real-Time Multifrequency MR Elastography of the Human Brain Reveals Rapid Changes in Viscoelasticity in Response to the Valsalva Maneuver. *Front Bioeng Biotechnol* 9, 666456 (2021).
152. Rump, J., Klatt, D., Braun, J., Warmuth, C. & Sack, I. Fractional encoding of harmonic motions in MR elastography. *Magnetic Resonance in Medicine* 57, 388-395 (2007).

153. Herthum, H., Carrillo, H., Osses, A., Uribe, S., Sack, I. & Bertoglio, C. Multiple motion encoding in phase-contrast MRI: A general theory and application to elastography imaging. *Med Image Anal* 78, 102416 (2022).
154. Flynn, T.J. Two-dimensional phase unwrapping with minimum weighted discontinuity. *Journal of the Optical Society of America a-Optics Image Science and Vision* 14, 2692-2701 (1997).
155. Sack, I., Rump, J., Elgeti, T., Samani, A. & Braun, J. MR elastography of the human heart: noninvasive assessment of myocardial elasticity changes by shear wave amplitude variations. *Magn Reson Med* 61, 668-677 (2009).
156. European Association for the Study of the L. EASL Clinical Practice Guidelines on the management of benign liver tumours. *J Hepatol* 65, 386-398 (2016).
157. Haring, M.P.D., Cuperus, F.J.C., Duiker, E.W., de Haas, R.J. & de Meijer, V.E. Scoping review of clinical practice guidelines on the management of benign liver tumours. *BMJ Open Gastroenterol* 8, e000592 (2021).
158. Henningsson, M. & Botnar, R.M. Advanced Respiratory Motion Compensation for Coronary MR Angiography. in *Sensors*, Vol. 13 6882-6899 (2013).
159. Dixon, W.T. Simple proton spectroscopic imaging. *Radiology* 153, 189-194 (1984).
160. Ma, J. Dixon techniques for water and fat imaging. *J Magn Reson Imaging* 28, 543-558 (2008).
161. Qi, J. & Leahy, R.M. Iterative reconstruction techniques in emission computed tomography. *Phys Med Biol* 51, R541-578 (2006).
162. Hudson, H.M. & Larkin, R.S. Accelerated image reconstruction using ordered subsets of projection data. *IEEE Trans Med Imaging* 13, 601-609 (1994).
163. Keereman, V., Fierens, Y., Broux, T., De Deene, Y., Lonneux, M. & Vandenberghe, S. MRI-based attenuation correction for PET/MRI using ultrashort echo time sequences. *J Nucl Med* 51, 812-818 (2010).
164. Gielisch, I. & Meierhofer, D. Metabolome and proteome profiling of complex I deficiency induced by rotenone. *J Proteome Res* 14, 224-235 (2015).
165. The MathWorks Inc. (2022). MATLAB versions: 9.5.0 (R2018a), 9.8.0 (R2020a), 9.10.0 (R2021a), Natick, Massachusetts: The MathWorks Inc. <https://www.mathworks.com>.
166. Klein, S., Staring, M., Murphy, K., Viergever, M.A. & Pluim, J.P. elastix: a toolbox for intensity-based medical image registration. *IEEE Trans Med Imaging* 29, 196-205 (2010).
167. Pech-Pacheco, J.L., Cristobal, G., Chamorro-Martinez, J. & Fernandez-Valdivia, J. Diatom autofocusing in brightfield microscopy: a comparative study. in *Proceedings 15th International Conference on Pattern Recognition. ICPR-2000*, Vol. 3 314-317 vol.313 (2000).
168. Yushkevich, P.A., Piven, J., Hazlett, H.C., Smith, R.G., Ho, S., Gee, J.C. & Gerig, G. User-guided 3D active contour segmentation of anatomical structures: significantly improved efficiency and reliability. *Neuroimage* 31, 1116-1128 (2006).
169. Berndt, N., Bulik, S., Wallach, I., Wunsch, T., Konig, M., Stockmann, M., Meierhofer, D. & Holzhutter, H.G. HEPATOKIN1 is a biochemistry-based model of liver metabolism for applications in medicine and pharmacology. *Nat Commun* 9, 2386 (2018).
170. Berndt, N., Kann, O. & Holzhutter, H.G. Physiology-based kinetic modeling of neuronal energy metabolism unravels the molecular basis of NAD(P)H fluorescence transients. *J Cereb Blood Flow Metab* 35, 1494-1506 (2015).
171. Bulik, S., Holzhutter, H.G. & Berndt, N. The relative importance of kinetic mechanisms and variable enzyme abundances for the regulation of hepatic

- glucose metabolism--insights from mathematical modeling. *BMC Biol* 14, 15 (2016).
172. Wallstab, C., Eleftheriadou, D., Schulz, T., Damm, G., Seehofer, D., Borlak, J., Holzhutter, H.G. & Berndt, N. A unifying mathematical model of lipid droplet metabolism reveals key molecular players in the development of hepatic steatosis. *FEBS J* 284, 3245-3261 (2017).
  173. Berndt, N., Eckstein, J., Heucke, N., Gajowski, R., Stockmann, M., Meierhofer, D. & Holzhütter, H.-G. Characterization of Lipid and Lipid Droplet Metabolism in Human HCC. in *Cells*, Vol. 8 (2019).
  174. R Core Team (2022). R: A language and environment for statistical computing. R Foundation for Statistical Computing, version 3.4.3, 3.6.2 and 4.0.2, Vienna, Austria. <https://www.R-project.org/>.
  175. Liu, H. & Wu, T. Estimating the Area Under a Receiver Operating Characteristic Curve For Repeated Measures Design. *Journal of Statistical Software* 8, 1 - 18 (2003).
  176. DeLong, E.R., DeLong, D.M. & Clarke-Pearson, D.L. Comparing the areas under two or more correlated receiver operating characteristic curves: a nonparametric approach. *Biometrics* 44, 837-845 (1988).
  177. McFarland, E.G., Mayo-Smith, W.W., Saini, S., Hahn, P.F., Goldberg, M.A. & Lee, M.J. Hepatic hemangiomas and malignant tumors: improved differentiation with heavily T2-weighted conventional spin-echo MR imaging. *Radiology* 193, 43-47 (1994).
  178. Youden, W.J. Index for rating diagnostic tests. *Cancer* 3, 32-35 (1950).
  179. Wang, J., Shan, Q., Liu, Y., Yang, H., Kuang, S., He, B., Zhang, Y., Chen, J., Zhang, T., Glaser, K.J., Zhu, C., Chen, J., Yin, M., Venkatesh, S.K. & Ehman, R.L. 3D MR Elastography of Hepatocellular Carcinomas as a Potential Biomarker for Predicting Tumor Recurrence. *J Magn Reson Imaging* 49, 719-730 (2019).
  180. Boucher, Y., Leunig, M. & Jain, R.K. Tumor Angiogenesis and Interstitial Hypertension1. *Cancer Research* 56, 4264-4266 (1996).
  181. Haak, V.M., Huang, S. & Panigrahy, D. Debris-stimulated tumor growth: a Pandora's box? *Cancer Metastasis Rev* 40, 791-801 (2021).
  182. Sauer, F., Oswald, L., Ariza de Schellenberger, A., Tzschatzsch, H., Schrank, F., Fischer, T., Braun, J., Mierke, C.T., Valiullin, R., Sack, I. & Kas, J.A. Collagen networks determine viscoelastic properties of connective tissues yet do not hinder diffusion of the aqueous solvent. *Soft Matter* 15, 3055-3064 (2019).
  183. Juge, L., Doan, B.T., Seguin, J., Albuquerque, M., Larrat, B., Mignet, N., Chabot, G.G., Scherman, D., Paradis, V., Vilgrain, V., Van Beers, B.E. & Sinkus, R. Colon tumor growth and antivascular treatment in mice: complementary assessment with MR elastography and diffusion-weighted MR imaging. *Radiology* 264, 436-444 (2012).
  184. Lin, J. & Westerhoff, M. Vascular Neoplasms of the Liver. *Clin Liver Dis (Hoboken)* 17, 261-266 (2021).
  185. Asbach, P., Klatt, D., Schlosser, B., Biermer, M., Mucbe, M., Rieger, A., Loddenkemper, C., Somasundaram, R., Berg, T., Hamm, B., Braun, J. & Sack, I. Viscoelasticity-based staging of hepatic fibrosis with multifrequency MR elastography. *Radiology* 257, 80-86 (2010).
  186. Morin, C.E., Dillman, J.R., Serai, S.D., Trout, A.T., Tkach, J.A. & Wang, H. Comparison of Standard Breath-Held, Free-Breathing, and Compressed Sensing 2D Gradient-Recalled Echo MR Elastography Techniques for Evaluating Liver Stiffness. *AJR Am J Roentgenol* 211, W279-W287 (2018).

187. Qiu, T., Wang, H., Song, J., Guo, G., Shi, Y., Luo, Y. & Liu, J. Could Ultrasound Elastography Reflect Liver Function? *Ultrasound Med Biol* 44, 779-785 (2018).
188. Morr, A.S., Herthum, H., Schrank, F., Gorner, S., Anders, M.S., Lerchbaumer, M., Muller, H.P., Fischer, T., Jenderka, K.V., Hansen, H.H.G., Janmey, P.A., Braun, J., Sack, I. & Tzschatzsch, H. Liquid-Liver Phantom: Mimicking the Viscoelastic Dispersion of Human Liver for Ultrasound- and MRI-Based Elastography. *Invest Radiol* 57, 502-509 (2022).
189. Abuhattum, S., Kotzbeck, P., Schlussler, R., Harger, A., Ariza de Schellenberger, A., Kim, K., Escolano, J.C., Muller, T., Braun, J., Wabitsch, M., Tschop, M., Sack, I., Brankatschk, M., Guck, J., Stemmer, K. & Taubenberger, A.V. Adipose cells and tissues soften with lipid accumulation while in diabetes adipose tissue stiffens. *Sci Rep* 12, 10325 (2022).
190. Heucke, N., Wuensch, T., Mohr, J., Kaffarnik, M., Arsenic, R., Sinn, B., Muller, T., Pratschke, J., Stockmann, M., Sack, I. & Tzschatzsch, H. Non-invasive structure-function assessment of the liver by 2D time-harmonic elastography and the dynamic Liver MAXimum capacity (LiMAX) test. *J Gastroenterol Hepatol* 34, 1611-1619 (2019).
191. Lin, H., Wang, Y., Zhou, J., Yang, Y., Xu, X., Ma, D., Chen, Y., Yang, C., Sack, I., Guo, J., Li, R. & Yan, F. Tomoelastography based on multifrequency MR elastography predicts liver function reserve in patients with hepatocellular carcinoma: a prospective study. *Insights Imaging* 13, 95 (2022).
192. Fung, J., Poon, R.T., Yu, W.C., Chan, S.C., Chan, A.C., Chok, K.S., Cheung, T.T., Seto, W.K., Lo, C.M., Lai, C.L. & Yuen, M.F. Use of liver stiffness measurement for liver resection surgery: correlation with indocyanine green clearance testing and post-operative outcome. *PLoS One* 8, e72306 (2013).
193. Sun, X.L., Liang, L.W., Cao, H., Men, Q., Hou, K.Z., Chen, Z. & Zhao, Y.E. Liver reserve function assessment by acoustic radiation force impulse imaging. *World J Gastroenterol* 21, 9648-9655 (2015).
194. Berumen, J., Baglieri, J., Kisseleva, T. & Mekeel, K. Liver fibrosis: Pathophysiology and clinical implications. *WIREs Mech Dis* 13, e1499 (2021).
195. Nault, J.C., Couchy, G., Balabaud, C., Morcrette, G., Caruso, S., Blanc, J.F., Bacq, Y., Calderaro, J., Paradis, V., Ramos, J., Scoazec, J.Y., Gnemmi, V., Sturm, N., Guettier, C., Fabre, M., Savier, E., Chiche, L., Labrune, P., Selves, J., Wendum, D., Pilati, C., Laurent, A., De Muret, A., Le Bail, B., Rebouissou, S., Imbeaud, S., Investigators, G., Bioulac-Sage, P., Letouze, E. & Zucman-Rossi, J. Molecular Classification of Hepatocellular Adenoma Associates With Risk Factors, Bleeding, and Malignant Transformation. *Gastroenterology* 152, 880-894 e886 (2017).
196. Bioulac-Sage, P., Rebouissou, S., Thomas, C., Blanc, J.F., Saric, J., Sa Cunha, A., Rullier, A., Cubel, G., Couchy, G., Imbeaud, S., Balabaud, C. & Zucman-Rossi, J. Hepatocellular adenoma subtype classification using molecular markers and immunohistochemistry. *Hepatology* 46, 740-748 (2007).
197. Zucman-Rossi, J., Jeannot, E., Nhieu, J.T., Scoazec, J.Y., Guettier, C., Rebouissou, S., Bacq, Y., Leteurtre, E., Paradis, V., Michalak, S., Wendum, D., Chiche, L., Fabre, M., Mellottee, L., Laurent, C., Partensky, C., Castaing, D., Zafrani, E.S., Laurent-Puig, P., Balabaud, C. & Bioulac-Sage, P. Genotype-phenotype correlation in hepatocellular adenoma: new classification and relationship with HCC. *Hepatology* 43, 515-524 (2006).
198. Brandner, E.D., Wu, A., Chen, H., Heron, D., Kalnicki, S., Komanduri, K., Gerszten, K., Burton, S., Ahmed, I. & Shou, Z. Abdominal organ motion measured using 4D CT. *Int J Radiat Oncol Biol Phys* 65, 554-560 (2006).

199. Cohen, J.F., Korevaar, D.A., Altman, D.G., Bruns, D.E., Gatsonis, C.A., Hooft, L., Irwig, L., Levine, D., Reitsma, J.B., de Vet, H.C. & Bossuyt, P.M. STARD 2015 guidelines for reporting diagnostic accuracy studies: explanation and elaboration. *BMJ Open* 6, e012799 (2016).
200. Murad, M.H., Katabi, A., Benkhadra, R. & Montori, V.M. External validity, generalisability, applicability and directness: a brief primer. *BMJ Evid Based Med* 23, 17-19 (2018).
201. Streitberger, K.J., Lilaj, L., Schrank, F., Braun, J., Hoffmann, K.T., Reiss-Zimmermann, M., Kas, J.A. & Sack, I. How tissue fluidity influences brain tumor progression. *Proc Natl Acad Sci U S A* 117, 128-134 (2020).
202. Asbach, P., Ro, S.R., Aldoj, N., Snellings, J., Reiter, R., Lenk, J., Kohlitz, T., Haas, M., Guo, J., Hamm, B., Braun, J. & Sack, I. In Vivo Quantification of Water Diffusion, Stiffness, and Tissue Fluidity in Benign Prostatic Hyperplasia and Prostate Cancer. *Invest Radiol* 55, 524-530 (2020).
203. Liu, G., Ma, D., Wang, H., Zhou, J., Shen, Z., Yang, Y., Chen, Y., Sack, I., Guo, J., Li, R. & Yan, F. Three-dimensional multifrequency magnetic resonance elastography improves preoperative assessment of proliferative hepatocellular carcinoma. *Insights Imaging* 14, 89 (2023).
204. van Mierlo, K.M., Schaap, F.G., Dejong, C.H. & Olde Damink, S.W. Liver resection for cancer: New developments in prediction, prevention and management of postresectional liver failure. *J Hepatol* 65, 1217-1231 (2016).



## Statutory declaration

“I, Mehrgan Shahryari, by personally signing this document in lieu of an oath, hereby affirm that I prepared the submitted dissertation on the topic “Entwicklung und Anwendung der *in vivo* abdominellen Magnetresonanzelastographie” / “Development and application of *in vivo* abdominal magnetic resonance elastography”, independently and without the support of third parties, and that I used no other sources and aids than those stated.

All parts which are based on the publications or presentations of other authors, either in letter or in spirit, are specified as such in accordance with the citing guidelines. The sections on methodology (in particular regarding practical work, laboratory regulations, statistical processing) and results (in particular regarding figures, charts and tables) are exclusively my responsibility.

Furthermore, I declare that I have correctly marked all of the data, the analyses, and the conclusions generated from data obtained in collaboration with other persons, and that I have correctly marked my own contribution and the contributions of other persons (cf. declaration of contribution). I have correctly marked all texts or parts of texts that were generated in collaboration with other persons.

My contributions to any publications to this dissertation correspond to those stated in the below joint declaration made together with the supervisor. All publications created within the scope of the dissertation comply with the guidelines of the ICMJE (International Committee of Medical Journal Editors; [www.icmje.org](http://www.icmje.org)) on authorship. In addition, I declare that I shall comply with the regulations of Charité – Universitätsmedizin Berlin on ensuring good scientific practice.

I declare that I have not yet submitted this dissertation in identical or similar form to another Faculty.

The significance of this statutory declaration and the consequences of a false statutory declaration under criminal law (Sections 156, 161 of the German Criminal Code) are known to me.”

---

Date

---

Signature

---

## Declaration of contribution to the publications

I made significant and diverse contributions throughout the study, including ideation and formulation of research questions, design and development of methodology, implementation and execution of the study, and communication of results. The following section presents a comprehensive description of my contributions to all three studies.

Publication 1: **Shahryari, M.**, H. Tzschätzsch, J. Guo, S. R. Marticorena Garcia, G. Böning, U. Fehrenbach, L. Stencel, P. Asbach, B. Hamm, J. A. Kas, J. Braun, T. Denecke and I. Sack (2019). "Tomoelastography Distinguishes Noninvasively between Benign and Malignant Liver Lesions." *Cancer Res* 79(22): 5704-5710.

Contributions: Dr. Fehrenbach, Prof. Denecke, Prof. Sack, and I collaborated on the conception and design of the study. I performed a comprehensive literature review. Together with Dr. Braun, I installed MRE hardware at the Magnetom Aera MRI Scanner at Charité – Campus Virchow Klinikum. I installed the MRE sequence on the MRI scanner and optimized the MRE sequence parameters with guidance from Prof. Sack and Dr. Braun. I conducted the first test measurements prior to subject recruitment. Dr. Böning, Dr. Fehrenbach, Prof. Denecke, and I enrolled patients. I informed all patients about the study's purpose and benefits, performed imaging measurements for all patients, post-processed the imaging data, generated mechanical maps, drew volumes of interest for liver and tumor to generate all quantitative values, and created a database for the study. Using programming languages MATLAB and R, I conducted post-processing and analysis, statistical analysis, and generated all tables and figures. Dr. Tzschätzsch, Dr. Guo, Dr. Marticorena Garcia, Ms. Stencel, Prof. Asbach, Prof. Käs, and Prof. Sack provided expert advice and guidance on the analysis of medical and physical aspects of the data and assisted in interpreting the findings. Prof. Sack and I wrote the first draft of the manuscript together, which was reviewed and revised by all co-authors. I submitted the manuscript and performed necessary editing with valuable contributions from all co-authors. Prof. Sack and Prof. Denecke provided administrative, technical, and material support and supervised the study.

---

Publication 2: **Shahryari, M.**, T. Meyer, C. Warmuth, H. Herthum, G. Bertalan, H. Tzschätzsch, L. Stencel, S. Lukas, L. Lilaj, J. Braun and I. Sack (2021). "Reduction of breathing artifacts in multifrequency magnetic resonance elastography of the abdomen." *Magn Reson Med* 85(4): 1962-1973.

Prof. Sack and I formulated the idea to investigate breathing motion artifacts in MRE measurements through an assessment of free-breathing, breath-hold, and navigator-based MRE measurements, as well as utilizing rigid body image registration in post-processing for motion correction. To support this idea, I performed an extensive literature review. Dr. Warmuth implemented the breathing-navigator into the MRE sequence, while I optimized the MRE sequence parameters with guidance from Prof. Sack, Dr. Braun, and Dr. Warmuth. Prior to subject recruitment, I conducted the first test measurements and enrolled all participants, providing them with information about the study's purpose and benefits. Mr. Meyer, in consultation with Dr. Lukas, implemented image registration in the MRE post-processing pipeline. I then performed and evaluated various image registration methods and parameters and decided on using Elastix in discussion with Mr. Meyer. With Mr. Meyer's support, I conducted sharpness analysis based on the Laplacian operator. For all imaging paradigms and patients, I conducted the post-processing analysis, generated mechanical maps and sharpness maps, and drew regions of interest for the liver, kidney, spleen, and pancreas to generate all quantitative values. Additionally, I created a database for the study and utilized programming languages MATLAB and R for post-processing and statistical analysis, as well as generating all tables and figures. Dr. Warmuth, Mr. Meyer, Dr. Herthum, Dr. Tzschätzsch, Dr. Bertalan, Ms. Stencel and Dr. Lilaj provided expert advice and guidance on the analysis of medical and physical aspects of the data and assisted in interpreting the findings. Prof. Sack and I jointly wrote the first draft of the manuscript which was subsequently reviewed and revised by all co-authors. Following manuscript submission, I performed necessary editing incorporating valuable contributions from all co-authors. Prof. Sack provided administrative support throughout the study and supervised the research.

---

Publication 3: **Shahryari, M.**, S. Keller, D. Meierhofer, I. Wallach, Y. Safraou, J. Guo, S. M. Garcia, J. Braun, M. R. Makowski, I. Sack and N. Berndt (2023). "On the relationship between metabolic capacities and in vivo viscoelastic properties of the liver." *Frontiers in Bioengineering and Biotechnology* 10.

Contributions: Dr. Berndt, Prof. Makowski, Prof. Sack, Dr. Keller, and I engaged in the conceptualization of investigating the correlation between metabolic liver function and metabolic liver viscoelasticity. Subsequently, in collaboration with Dr. Braun, I facilitated the installation of the MRE hardware on the PET/MRI scanner at Charité – Campus Virchow Klinikum. Following the installation, I adjusted and optimized the MRE sequence by conducting initial test measurements of phantom and liver tissue samples to ensure applicability in small animals like rabbits. I conducted MRE imaging for all rabbits, while Dr. Keller handled animal handling and PET imaging. Subsequent proteomics analysis was performed by Dr. Meierhofer after liver sample preparation by me. Dr. Berndt and Dr. Wallach undertook metabolic modeling based on the proteomics data and cluster analysis of liver metabolism. For post-processing of MRE and PET imaging data, I utilized MATLAB programming languages to create mechanical maps based on MRE and SUV maps based on PET imaging. Furthermore, I performed all statistical analysis and clustering based on mechanical properties using R. In addition, I generated Figures 1, 3, 4, 5, 6, and 7 and the Table while Dr. Berndt generated Figure 2. The initial manuscript draft was jointly written by Prof. Sack, Dr. Berndt, and me and was reviewed and revised by all co-authors. Following manuscript submission, I performed necessary editing incorporating valuable contributions from all co-authors. Administrative and financial support throughout the study were provided by Prof. Sack, Dr. Berndt, and Prof. Makowski who also supervised the research.

---

Signature, date and stamp of first supervising university professor / lecturer

---

Signature of doctoral candidate

## **Publications**

### **Publication 1: Tomoelastography Distinguishes Noninvasively between Benign and Malignant Liver Lesions**

**Shahryari, M.**, Tzschatzsch, H., Guo, J., Marticorena Garcia, S. R., Boning, G., Fehrenbach, U., Stencel, L., Asbach, P., Hamm, B., Kas, J. A., Braun, J., Denecke, T., & Sack, I. (2019). Tomoelastography Distinguishes Noninvasively between Benign and Malignant Liver Lesions. *Cancer Res*, 79(22), 5704-5710. <https://doi.org/10.1158/0008-5472.CAN-19-2150>

## Priority Report

Cancer  
Research

## Tomoelastography Distinguishes Noninvasively between Benign and Malignant Liver Lesions

Mehrgan Shahryari<sup>1</sup>, Heiko Tzschätzsch<sup>1</sup>, Jing Guo<sup>1</sup>, Stephan R. Marticorena Garcia<sup>1</sup>, Georg Böning<sup>1</sup>, Uli Fehrenbach<sup>1</sup>, Lisa Stencel<sup>1</sup>, Patrick Asbach<sup>1</sup>, Bernd Hamm<sup>1</sup>, Joseph A. Käs<sup>2</sup>, Jürgen Braun<sup>3</sup>, Timm Denecke<sup>4</sup>, and Ingolf Sack<sup>1</sup>



### Abstract

Patients with increased liver stiffness have a higher risk of developing cancer, however, the role of fluid–solid tissue interactions and their contribution to liver tumor malignancy remains elusive. Tomoelastography is a novel imaging method for mapping quantitatively the solid–fluid tissue properties of soft tissues *in vivo*. It provides high resolution and thus has clear clinical applications. In this work we used tomoelastography in 77 participants, with a total of 141 focal liver lesions of different etiologies, to investigate the contributions of tissue stiffness and fluidity to the malignancy of liver tumors. Shear-wave speed ( $c$ ) as surrogate for tissue stiffness and phase-angle ( $\phi$ ) of the complex shear modulus reflecting tissue fluidity were abnormally high in malignant tumors and allowed them to be distinguished from nontumorous liver tissue with high accuracy [ $c$ : AUC = 0.88 with 95% confidence interval (CI) = 0.83–0.94;  $\phi$ : AUC = 0.95, 95% CI = 0.92–0.98]. Benign focal nodular hyperplasia and hepatocellular adenoma could be distinguished from malignant lesions on the basis of tumor stiffness

(AUC = 0.85, 95% CI = 0.72–0.98; sensitivity = 94%, 95% CI = 89–100; and specificity = 85%, 95% CI = 62–100), tumor fluidity (AUC = 0.86, 95% CI = 0.77–0.96; sensitivity = 83%, 95% CI = 72–93; and specificity = 92%, 95% CI = 77–100) and liver stiffness (AUC = 0.84, 95% CI = 0.74–0.94; sensitivity = 72%, 95% CI = 59–83; and specificity = 88%, 95% CI = 69–100), but not on the basis of liver fluidity. Together, hepatic malignancies are characterized by stiff, yet fluid tissue properties, whereas surrounding nontumorous tissue is dominated by solid properties. Tomoelastography can inform noninvasively on the malignancy of suspicious liver lesions by differentiating between benign and malignant lesions with high sensitivity based on stiffness and with high specificity based on fluidity.

**Significance:** Solid–fluid tissue properties measured by tomoelastography can distinguish malignant from benign masses with high accuracy and provide quantitative noninvasive imaging biomarkers for liver tumors.

### Introduction

Liver mechanical properties affect mass formation and treatment outcome (1–3). Specifically, each 1-kilopascal increase in liver stiffness increases the probability of hepatocellular carcinoma (HCC) by 4% (2) and the risk of tumor recurrence after hepatic resection by 16.3% (3). This is the rationale for using elastography to measure mechanical tissue properties of the liver as predictive markers of tumor progression (4).

<sup>1</sup>Department of Radiology, Charité - Universitätsmedizin Berlin, corporate member of Freie Universität Berlin, Humboldt-Universität zu Berlin, and Berlin Institute of Health, Berlin, Germany. <sup>2</sup>Faculty of Physics and Earth Sciences, Peter Debye Institute, Leipzig University, Leipzig, Germany. <sup>3</sup>Institute of Medical Informatics, Charité - Universitätsmedizin Berlin, corporate member of Freie Universität Berlin, Humboldt-Universität zu Berlin, and Berlin Institute of Health, Berlin, Germany. <sup>4</sup>Department of Diagnostic and Interventional Radiology, University Hospital of Leipzig, Leipzig, Germany.

**Note:** Supplementary data for this article are available at Cancer Research Online (<http://cancerres.aacrjournals.org/>).

**Corresponding Author:** Ingolf Sack, Department of Radiology, Charité - Universitätsmedizin Berlin, Berlin 10117, Germany. Phone: 4930-4505-39058; Fax: 49-30-450-539988; E-mail: [ingolf.sack@charite.de](mailto:ingolf.sack@charite.de)

Cancer Res 2019;79:5704–10

doi: 10.1158/0008-5472.CAN-19-2150

©2019 American Association for Cancer Research.

Complex shear modulus  $G^*$  measured by magnetic resonance elastography (MRE) provides a basic description of mechanical tissue properties. Stiffness is usually characterized by magnitude modulus ( $|G^*|$ ), while elasticity and viscosity are quantified by storage (real part of  $G^*$ ) and loss modulus (imaginary part of  $G^*$ ), respectively. Phase angle  $\phi$  of the complex modulus indicates fluidity, equaling zero for pure solids and  $\pi/2$  radians (rad) for pure fluids. Thus, fluidity is conceptually signifying the conversion of a solid into a fluid over a continuous range from 0 to  $\pi/2$ . Materials with  $\phi < \pi/4$  have predominantly solid and materials with  $\phi > \pi/4$  have predominantly fluid properties (5).

Fluidity is currently under investigation as a mechanical property defining the metastatic potential and aggressiveness of tumors (6). Despite many reports on the stiffness of liver tumors (4), little is known about how disease alters the solid–fluid properties of liver tissue. Multifrequency MRE shows that a power-law coefficient related to  $\phi$  does not change with progression of hepatic fibrosis, while tissue stiffness increases (7). Interestingly, Garteiser and colleagues reported a changed ratio of loss-to-storage properties for liver tumors, suggesting increased fluidity due to carcinogenesis (8). MRE without considering solid–fluid tissue properties is moderately sensitive to malignancy in the liver (8, 9). Given (i) the altered loss modulus in liver tumors (8), (ii) the insensitivity of fluidity to liver fibrosis (7), and (iii) a moderate diagnostic performance of stiffness in identifying liver

tumors (9), we hypothesize that fluidity may be a promising imaging biomarker unaffected by the stiffness of nontumorous liver tissue, which is normally altered by fibrosis. However, fluidity has never been explored in liver tumors; specifically, novel high-resolution multifrequency MRE with tomoelastographic data processing (10, 11) has never been used for this.

Here we use tomoelastography to investigate whether solid-fluid properties can differentiate hepatic tumors from nontumorous liver tissue and malignant from benign lesions. This study was performed to quantify the solid-fluid properties of both tumor and nontumorous liver by tomoelastography.

## Patients and Methods

### Study design and patients

The study protocol conforms with the Declaration of Helsinki and was approved by the institutional ethics review board (EA1/261/12 and EA1/076/17). All patients gave written informed consent.

From March 2015 to August 2017, the electronic scheduling systems of the departments of liver surgery and radiology were screened for patients with focal liver lesions detected by previous imaging and without contraindications to MRI. Patients with prior treatment of the respective lesion were excluded. The final study cohort included 70 patients with a total of 105 malignant and 36 benign lesions, and 7 healthy volunteers. Diagnoses were 22 HCC, 12 cholangiocarcinoma, 71 metastasis, 11 hemangioma, 10 focal nodular hyperplasia (FNH), and 15 hepatic adenoma. Details are provided in Table 1 and Supplementary Fig. S1.

### MRI and MRE

MRI was performed on a 1.5-Tesla Clinical Scanner (Magnetom Aera, Siemens) with a 12-channel phased-array surface coil and the spine-array coils integrated into the table. The MRE sequence and set-up are described in detail elsewhere (11). In brief, mechanical vibrations of 30, 40, 50, and 60 Hz harmonic frequency were induced with two posterior (0.6 bar) and two anterior-pneumatic actuators (0.4 bar) near the liver region (Supplementary Fig. S2). The three-dimensional wave field was acquired by using a single-shot, spin-echo echo-planar imaging sequence with flow-compensated motion-encoding gradients (MEG). Eight phase offsets over a full vibration period were recorded for all three Cartesian-motion field directions. Fifteen consecutive transverse slices with a field-of-view of  $384 \times 312 \text{ mm}^2$  (matrix size  $128 \times 104$ ) and  $3 \times 3 \times 5 \text{ mm}^3$  resolution were acquired during free breathing. Further imaging parameters: echo time = 59 ms; repetition time = 2,050 ms; parallel imaging with GRAPPA-factor 2; MEG frequency of 43.48 Hz for 30, 40, and 50 Hz vibration frequencies and 44.88 Hz for 60 Hz vibration frequency; and MEG amplitude of 30 mT/m. Total MRE measurement time was approximately 3.5 minutes. More details about the tomoelastography setup are provided in Supplementary Fig. S2.

### MRE data processing

MRE data were processed with the tomoelastography pipeline based on multifrequency wavenumber recovery providing maps of shear-wave speed  $c$  (in m/s; ref. 10). Because  $c$  is deduced

Tumor entities	Participant numbers	Sex female	Age in years (range)	BMI (kg/m <sup>2</sup> )	Number of tumors	Tumor diameter in mm (range)	Tumor VOI in cm <sup>3</sup> (IQR)	Tumor $c$ in m/s	Tumor $\phi$ in rad	Liver VOI in cm <sup>3</sup> (IQR)	Liver $c$ in m/s	Liver $\phi$ in rad
HCC	17	4	67 (43-81)	26.1 $\pm$ 3.4	22	30 (12-150)	9.0 (1.7-33.8)	2.54 $\pm$ 0.64	1.20 $\pm$ 0.29	180 (100-344)	1.97 $\pm$ 0.49	0.81 $\pm$ 0.16
CCA	10	5	70 (56-76)	25.9 $\pm$ 4.1	12	53 (6-124)	11.3 (3.9-164.4)	2.57 $\pm$ 0.90	1.24 $\pm$ 0.25	252 (156-453)	1.72 $\pm$ 0.29	0.66 $\pm$ 0.10
MET	27	10	61 (30-85)	25.2 $\pm$ 4.0	71	25 (9-175)	5.7 (2.0-12.1)	2.34 $\pm$ 0.48	1.14 $\pm$ 0.28	210 (104-508)	1.61 $\pm$ 0.23	0.65 $\pm$ 0.08
HEM	5	5	52 (38-74)	24.0 $\pm$ 4.2	11	23 (12-87)	1.8 (1.0-3.6)	1.97 $\pm$ 0.45	0.95 $\pm$ 0.30	260 (241-329)	1.37 $\pm$ 0.13	0.60 $\pm$ 0.03
FNH	5	3	38 (29-66)	25.2 $\pm$ 5.2	10	21 (9-95)	2.9 (1.5-7.6)	2.08 $\pm$ 0.96	0.78 $\pm$ 0.24	372 (329-497)	1.40 $\pm$ 0.12	0.66 $\pm$ 0.04
HCA	8	8	39 (22-52)	25.0 $\pm$ 5.0	15	30 (14-90)	5.3 (2.3-22.8)	1.41 $\pm$ 0.21	0.66 $\pm$ 0.12	226 (143-316)	1.38 $\pm$ 0.12	0.66 $\pm$ 0.06
Healthy	7	1	35 (28-46)	22.8 $\pm$ 3.2	1	—	—	—	—	360 (324-456)	1.39 $\pm$ 0.04	0.61 $\pm$ 0.03

NOTE: Means are given with  $\pm$  SD, range or IQR as shown. Abbreviations:  $c$ , shear-wave speed (stiffness);  $\phi$ , phase angle of the complex shear modulus (fluidity); BMI, body mass index; CCA, cholangiocellular carcinoma; HCA, hepatocellular adenoma; HEM, hemangioma; MET, metastasis; IQR, interquartile range.

Shahryari et al.

from the real part of wave numbers, it can be considered a surrogate of stiffness. Furthermore, we recovered the phase angle of the complex shear modulus,  $\varphi$  (range:  $0-\pi/2$ ).  $\varphi > \pi/4$  indicates that loss modulus dominates over storage modulus (12). Both parameters,  $c$  and  $\varphi$ , were retrieved by multifrequency dual elastovisco inversion programs publicly available at <https://bioqic-apps.charite.de/downloads>. Volumes of interest (VOI), drawn manually, were based on all MRE magnitude images covering tumor or liver and using the information of the lesion's anatomic location obtained by routine MRI. For nontumorous liver tissue VOIs were drawn excluding visible blood vessels.

#### Statistical analysis

Means were calculated for tumor and liver tissue. Group values were reported as mean  $\pm$  SD. Different tumor entities in two subjects were considered as independent lesions. Statistical differences between tumor entities were analyzed by the Kruskal-Wallis test. A *post hoc* test with Bonferroni correction for multiple testing was performed. For separation of lesions and nontumorous liver tissue, ROCs were calculated from probabilities predicted by a general linear mixed-effect model (GLMM; ref. 13). The outcome variable was labeled as "liver" or "tumor." We accounted for fixed effects ( $\beta$ ) for either  $c$  or  $\varphi$  and for nonindependence of multiple tumors within one subject. ROC measures were compared by DeLong method (14).

ROC analysis was performed for characterization (distinguishing malignant from benign lesions). Youden index was calculated to derive optimal cut-off values of  $\varphi$  or  $c$ . Sensitivity, specificity, positive predictive value, and negative predictive value were calculated. ROC analysis was repeated without hemangioma because this is easily detected by its strong T2-hyperintensity in MRI (15). Correlation of mechanical properties of tumor and liver was analyzed by Spearman rank correlation coefficient. Statistical analysis was performed in R (version 3.4.3; R-Foundation) using "lme4," "pROC," and "ggplot2" packages.  $P < 0.05$  was considered statistically significant. All confidence intervals (CI) stated are for 95%.

#### Results

Tomoelastography was successful in all participants, that is, there was no drop out due to technical failure. Participant characteristics and group-mean values of  $c$  and  $\varphi$  of tumors and liver tissue are summarized in Table 1. MRE results of four representative cases of malignant lesions including two metastasis, one HCC, and one cholangiocarcinoma are shown in Fig. 1A–D. Figure 2A–D shows four representative cases of benign lesions including two hepatic adenoma, one FNH, and one hemangioma. More cases and additional imaging data are presented in Supplementary Figs. S3A–S3D and S4A and S4B.

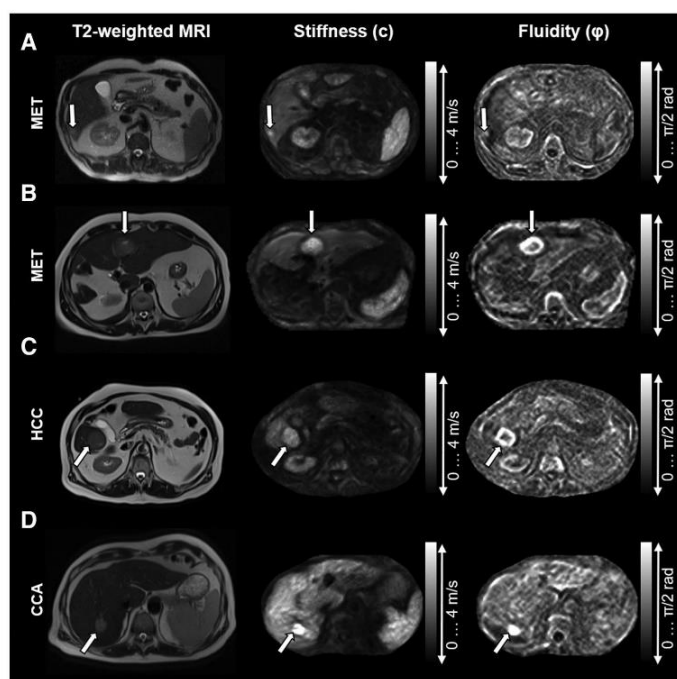
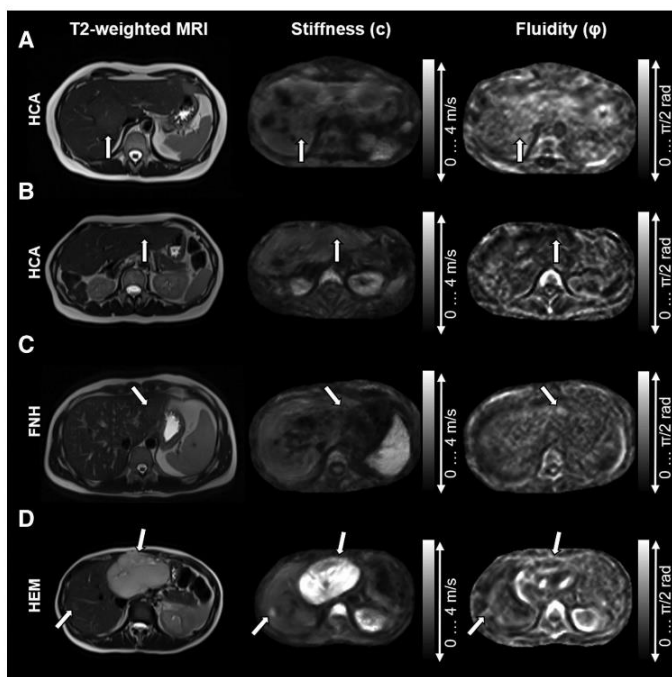


**Figure 1.**

Tomoelastography results in four representative cases of malignant liver tumors. Shown are maps of shear-wave speed  $c$  (stiffness) and phase angle  $\varphi$  (fluidity) along with T2-weighted MR images for anatomic orientation. **A**, Malignant urothelial metastasis (arrow) with 9-mm diameter in a 66-year-old man showing higher  $c$  and  $\varphi$  than nontumorous liver tissue. **B**, Fifty-year-old man with hepatic metastasis (MET) of a neuroendocrine tumor (arrow) in the left liver lobe after right hemihepatectomy. The tumor shows high  $c$  and  $\varphi$  compared with surrounding liver tissue. **C**, HCC (arrow) in liver segment VI in a 78-year-old man showing high  $c$  and  $\varphi$  surrounded by liver tissue stiffened by fibrosis. **D**, Seventy-two-year-old man with a cholangiocarcinoma (CCA; arrow) with larger  $c$  than nontumorous liver tissue, although stiffness is increased by fibrosis.  $\varphi$  in cholangiocarcinoma is larger than in nontumorous liver tissue.

**Figure 2.**

Tomoeleostography results in four representative cases of benign liver tumors. Maps of shear wave speed  $c$  (stiffness) and phase angle  $\phi$  (fluidity) are shown, along with T2-weighted MR images for anatomic orientation. **A**, Benign hepatocellular adenoma (HCA; arrow) in a 40-year-old woman shows similar  $c$  and  $\phi$  to normal, nontumorous liver tissue, making it difficult to separate hepatic adenoma from surrounding liver tissue in tomoeleostography maps. **B**, Fifty-two-year-old woman after right partial hepatic resection with hepatic adenoma (arrow), which shows a shear-wave speed and phase angle of the complex shear modulus similar to those in nontumorous liver. **C**, Twenty-two-year-old man with FNH. While FNH (arrow) shows a  $c$  similar to that of the surrounding liver, its  $\phi$  value is slightly above that of the liver. **D**, Two hepatic hemangiomas (HEM) in one slice in a 42-year-old woman. Both hemangioma (arrows) have high T2 signal intensity as well as a high shear-wave speed ( $c$ ) compared with surrounding liver tissue. Hemangiomas have rather high heterogeneous  $\phi$  values.



#### Separation of malignant and benign tumors

Overall,  $c$  and  $\phi$  were significantly larger in malignant lesions (including metastasis, HCC, and cholangiocarcinoma) than in nontumorous liver tissue (respectively,  $\beta = 3.62$ , 95% CI = 2.41–5.73,  $P < 0.001$  and  $\beta = 10.64$ , 95% CI = 7.02–16.35,  $P < 0.001$ ). GLMM-based ROC analysis showed a significantly larger area under the ROC curve (AUC) of 0.95 (95% CI = 0.92–0.98) for  $\phi$ , compared with 0.88 (95% CI = 0.83–0.94) for  $c$  ( $P < 0.01$ ). Separation of malignant lesions and liver by  $c$  was feasible, with a sensitivity of 91% (95% CI = 86–96) and specificity of 70% (95% CI = 59–81), while separation of malignant lesions and liver by  $\phi$  revealed 92% sensitivity (95% CI = 87–97) and 85% specificity (95% CI = 76–93). Detailed GLMM results for tumor and liver separation based on  $c$  and  $\phi$  are shown in Supplementary Table S1.

Benign lesions (including hemangioma, FNH, and hepatic adenoma) separated from nontumorous liver based on  $c$  ( $P = 0.03$ ), while  $\phi$  was not significantly different ( $P = 0.051$ ). Corresponding AUC values were 0.71 (95% CI = 0.57–0.84) and 0.66 (95% CI = 0.51–0.80) for  $c$  and  $\phi$ , respectively. However, ROC curves of  $c$  and  $\phi$  did not differ statistically ( $P = 0.57$ ).

Results of GLMM-based ROC analysis for separation are shown in Fig. 3A and Supplementary Table S2.

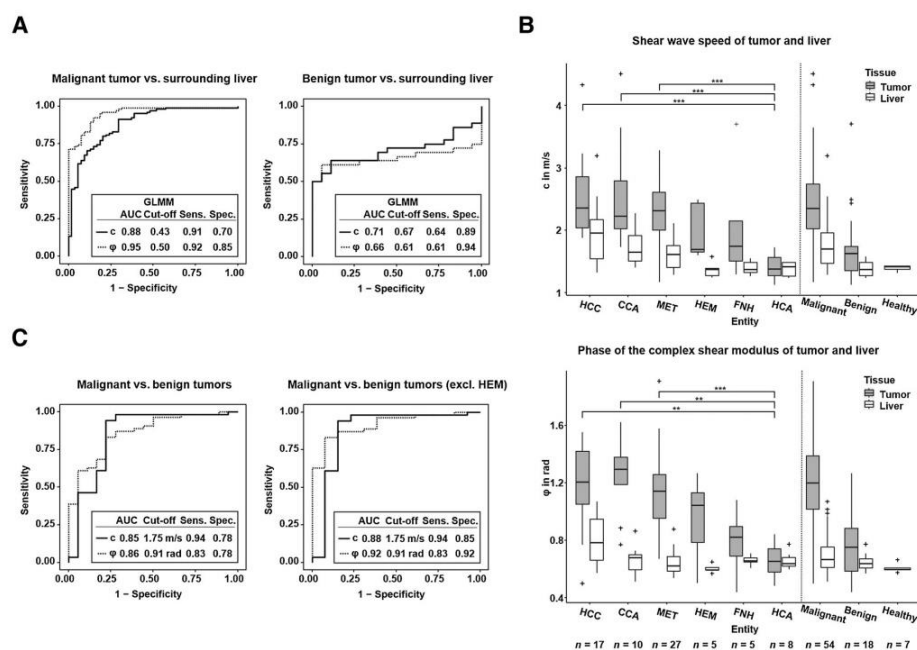
#### Characterization based on tumor properties

Tumor entities varied significantly in their  $c$  and  $\phi$  properties (both  $P < 0.001$ ). *Post hoc* tests revealed smaller  $c$  values for hepatic adenoma than for all malignant tumor entities ( $P < 0.001$ ), but not compared with other benign entities (Fig. 3B). In addition, hepatic adenoma showed smaller  $\phi$  values than malignant tumors did ( $P < 0.01$  vs. HCC and cholangiocarcinoma,  $P < 0.001$  vs. metastasis). Two patients with large FNH showed high  $c$  and  $\phi$  values. Additional information can be found in Supplementary Fig. S4A and S4B. Statistical plots of group mean  $c$  and  $\phi$  are shown in Fig. 3B.

A lesion- $c$  threshold of 1.75 m/s allowed distinction between benign and malignant lesions with a very good sensitivity of 94% (95% CI = 87–100) and moderate specificity of 78% (95% CI = 56–94; AUC = 0.85, 95% CI = 0.72–0.98). Similarly, lesion- $\phi$  of 0.91 rad, which indicates fluid tissue properties, distinguished benign from malignant lesions with a good sensitivity of 83% (95% CI = 72–93) and moderate specificity of 78% (95% CI = 56–94; AUC = 0.86, 95% CI = 0.77–0.96).

In a total of 13 patients, excluding patients with hemangioma of vascular origin ( $n = 5$ ) from our analysis, diagnostic accuracy increased when the same lesion thresholds of  $c = 1.75$  m/s and  $\phi = 0.91$  rad were used. Without hemangioma, sensitivity and specificity of  $c$  were very good, at 94% (95% CI = 89–100), and

Shahryari et al.

**Figure 3.**

**A**, ROC curves based on predictions of GLMM. Left, AUC ROC curve based on model  $c$  and  $\phi$  for separation of malignant lesions and normal liver. Significance for differentiating between the ROC curves was  $P < 0.01$  according to DeLong test. Right, ROC based on model  $c$  and  $\phi$  values for separating benign lesions and liver. Here, the two ROC curves are not statistically significantly different ( $P = 0.057$ ). **B**, Boxplot of group shear-wave speed  $c$  (top) and fluidity  $\phi$  (bottom) of tumor and nontumorous liver tissue, for 70 patients and 7 healthy volunteers.  $P$  values were obtained by the Kruskal-Wallis test, followed by Bonferroni corrected, *post hoc* test for comparison between different tumor entities. Bonferroni, \*,  $P < 0.05$ ; \*\*,  $P < 0.01$ ; \*\*\*,  $P < 0.001$ . Means and SDs are given in Table 1. **C**, Left, ROC based on tumor- $c$  and tumor- $\phi$  for distinguishing patients with malignant from patients with benign tumors. Right, ROC based on tumor- $c$  and tumor- $\phi$  for distinguishing malignant and benign tumors, excluding participants with hepatic hemangioma. Detailed information is provided in Supplementary Tables S3 and S4. Sens, sensitivity; spec, specificity.

good, at 85% (95% CI = 62–100; AUC = 0.88, 95% CI = 0.73–1.00), respectively, while those of  $\phi$  were good, at 83% (95% CI = 72–93) and very good, at 92% (95% CI = 77–100; AUC = 0.88, 95% CI = 0.73–1.00). These results show that diagnostic performance increases when benign tumors of vascular origin are excluded from the characterization of hepatic lesions based on their mechanical properties.

#### Characterization based on liver properties

We also characterized liver lesions on the basis of nontumorous liver tissue. Liver properties in patients with benign lesions were not different from those of healthy volunteers (all  $P > 0.05$ ). Optimum cutoffs for discrimination of embedded benign tumors from embedded malignant tumors were  $c = 1.5$  m/s and  $\phi = 0.60$  rad, the latter being in the range indicating solid tissue properties. Sensitivity and specificity for liver- $c$  were, respectively, moderate, 72% (95% CI = 59–83), and good, at 88% (95% CI = 71–100; AUC = 0.84, 95% CI = 0.75–0.94), while results for liver- $\phi$  were poor, at

46% (95% CI = 33–59) and moderate, at 82% (95% CI = 65–100; AUC = 0.60, 95% CI = 0.47–0.73). The inferior diagnostic power of liver- $\phi$  compared with tumor- $\phi$  indicates noncorrelated fluid properties of liver and embedded lesions. Liver- $c$  of the healthy volunteers showed a stiffness below the cut-off value ( $1.39 \pm 0.04$  m/s). Results of ROC analysis for characterization with  $c$  and  $\phi$  are shown in Fig. 3C and Supplementary Table S3.

Liver- $c$  correlated with tumor- $c$  ( $P < 0.001$ ;  $r = 0.74$ ), indicating that tumors preferentially grow in stiff livers, while liver- $\phi$  correlated only moderately with tumor- $\phi$  ( $P < 0.01$ ;  $r = 0.34$ ) in agreement with the aforementioned insensitivity of liver fluidity to fibrosis.

#### Discussion

To the best of our knowledge, this is the first study generating fluidity maps for the characterization of liver tumors. We believe that whole-organ tomographic mapping of stiffness

and fluidity with high spatial resolution to depict multiple lesions in the same liver, including lesions smaller than 10 millimeters, is important for quantitative biomechanics-based diagnosis of liver tumors.

#### Factors contributing to stiffness and fluidity

For further discussion, it is important to note the contributions of elasticity (the tissue's ability to store mechanical energy) and viscosity (its ability to convert mechanical energy into heat) to our parameters. Because  $c$  is related to magnitude shear modulus  $|G^*|$  by  $c^2 = 2 \cdot |G^*| / (\rho \cdot [1 + \cos \phi])$ , it mixes contributions from elasticity and viscosity. Garteiser and colleagues found the loss modulus to be significantly larger in HCCs than in benign hepatocellular tumors, while storage modulus did not differ between these lesion entities (8). Those authors also reported larger  $|G^*|$  values for malignant than for benign tumors, probably caused by an increase in loss properties. The sensitivity of the loss modulus to tumor malignancy might be explained by an increase in fluidity due to vascularization or the presence of necrotic tissue. Furthermore, malignant tumors can accumulate hydrophobic, disorganized proteins, which increase tissue stiffness and mechanical friction. This could explain why malignant lesions present as stiff, yet fluid, masses with  $\phi$  values above the limit of solid-fluid transitions ( $\pi/4 = 0.78$  rad). Other mechanisms potentially decrease  $\phi$  as sketched in Supplementary Fig. S5A–S5C. For example, large organized networks such as portal-to-portal bridges in liver fibrosis or polar water-binding ECM components could reduce  $\phi$ . In liver fibrosis, the mechanisms that either drive or inhibit fluidity seem to be balanced, rendering the overall fluid-solid behavior of liver tissue insensitive to the progression of fibrosis (7). Similarly, our parameter  $\phi$  in tumor surrounding liver tissue was not sensitive to malignancy. The apparent insensitivity of  $\phi$  to liver fibrosis makes fluidity a promising biomechanical marker, with a large difference between tumors and surrounding collagen-rich liver tissues regardless of present fibrosis. Furthermore, in our cohort, abnormal fluidity was specific for malignancy (ruling out solid, benign lesions) while tumor stiffness was sensitive to malignancy (detecting stiff, malignant lesions), thus rendering the combination of the two MRE-based parameters useful for tumor characterization.

#### Solid-fluid properties in hemangioma

Although fluidity was greater in malignant than benign tumors, we observed high  $\phi$  values in hemangioma, which can be explained by their vascularity and fluid structure. Vascularity has been reported to increase liver stiffness and viscosity (16). The diagnosis of hemangioma is well established through the European Association for the Study of the Liver guidelines (17). In contrast, hepatic adenoma and FNH can be misinterpreted as malignant tumors when classified by contrast-enhanced MRI alone (18). To address this radiological ambiguity, we performed a second analysis without hemangioma and identified hepatic adenoma and FNH versus malignant masses. In this analysis, overall diagnostic power further increased to 94% sensitivity for  $c$  and 92% specificity for  $\phi$ . It should be noted that in 2 patients with large FNH we observed stiffer and more fluid mechanical properties, similar to those of malignant masses. In those cases, presented in Supplementary Fig. S4A and S4B, hypervascularization due to hyperplastic response to portal tract injury (19, 20) may have been responsible for elevated  $\phi$  values, while collagen deposition due to scarring could explain higher  $c$  values.

Although encouraging, our study has limitations. First of all, by nature of its design, only patients with known liver lesions who needed further diagnostic MRI workup or treatment were enrolled. On the one hand, the distribution of tumor entities in our cohort is typical for a tertiary-care liver center. On the other hand, patient selection is therefore biased toward malignant lesions, as individuals with benign liver tumors (except hepatic adenoma) rarely undergo treatment. For this reason, our study cohort includes a relatively small number of patients with benign liver tumors. Second, not all patients with benign lesions had histopathologic confirmation, but were diagnosed by established imaging criteria in contrast-enhanced MRI. Similarly, not all patients with stiff livers obtained biopsy for confirmation of liver fibrosis or cirrhosis, precluding a correlation analysis of tomoelastography and fibrosis grade. Finally, tomoelastography requires specialized hardware, making set-up and clinical dissemination of the method more difficult than for other innovative MRI methods. Nevertheless, prospective multicenter studies in larger cohorts are planned.

In conclusion, solid-fluid parameters measured by tomoelastography are a promising source of additional diagnostic information in patients with liver tumors including small lesions below 10 mm in diameter. Our results indicate that changes in liver stiffness are related to changes in solid-tissue properties, while changes in tumor stiffness are related to fluid-tissue properties. We propose fluidity as a new imaging marker that holds great promise for tumor detection, irrespective of the stage of liver fibrosis; in conjunction with tissue stiffness, it may allow highly sensitive and specific characterization of liver tumors.

#### Disclosure of Potential Conflicts of Interest

T. Denecke reports receiving commercial research support and honoraria from Speakers Bureau from Siemens. No potential conflicts of interest were disclosed by the other authors.

#### Authors' Contributions

Conception and design: M. Shahryari, U. Fehrenbach, T. Denecke, I. Sack  
Development of methodology: M. Shahryari, J. Braun, I. Sack  
Acquisition of data (provided animals, acquired and managed patients, provided facilities, etc.): M. Shahryari, G. Böning, U. Fehrenbach, T. Denecke  
Analysis and interpretation of data (e.g., statistical analysis, biostatistics, computational analysis): M. Shahryari, H. Tzschätzsch, J. Guo, S.R. Marticorena Garcia, P. Asbach, J.A. Käs, I. Sack  
Writing, review, and/or revision of the manuscript: M. Shahryari, J. Guo, S.R. Marticorena Garcia, G. Böning, U. Fehrenbach, L. Stencel, P. Asbach, B. Hamm, J. Braun, T. Denecke, I. Sack  
Administrative, technical, or material support (i.e., reporting or organizing data, constructing databases): M. Shahryari, S.R. Marticorena Garcia, G. Böning, U. Fehrenbach, L. Stencel, P. Asbach, B. Hamm, J. Braun, T. Denecke, I. Sack  
Study supervision: T. Denecke, I. Sack

#### Acknowledgments

Support of the German Research Foundation (SFB1340 "Matrix in Vision", GRK2260 BIOQIC to I. Sack, J. Braun, J. Guo, P. Asbach, and B. Hamm) and the German Federal Ministry of Education and Research (LiSyM 031L0057 to I. Sack) is gratefully acknowledged.

The costs of publication of this article were defrayed in part by the payment of page charges. This article must therefore be hereby marked *advertisement* in accordance with 18 U.S.C. Section 1734 solely to indicate this fact.

Received July 12, 2019; revised August 31, 2019; accepted September 18, 2019; published first September 24, 2019.

Shahryari et al.

## References

1. Ichikawa S, Motosugi U, Enomoto N, Onishi H. Magnetic resonance elastography can predict development of hepatocellular carcinoma with longitudinally acquired two-point data. *Eur Radiol* 2019;29:1013–21.
2. Singh S, Fujii LL, Murad MH, Wang Z, Asrani SK, Ehman RL, et al. Liver stiffness is associated with risk of decompensation, liver cancer, and death in patients with chronic liver diseases: a systematic review and meta-analysis. *Clin Gastroenterol Hepatol* 2013;11:1573–84.
3. Wang J, Shan Q, Liu Y, Yang H, Kuang S, He B, et al. 3D MR elastography of hepatocellular carcinomas as a potential biomarker for predicting tumor recurrence. *J Magn Reson Imaging* 2019;49:719–30.
4. Jiao Y, Dong F, Wang H, Zhang L, Xu J, Zheng J, et al. Shear wave elastography imaging for detecting malignant lesions of the liver: a systematic review and pooled meta-analysis. *Med Ultrason* 2017;19:16–22.
5. Hirsch S, Braun J, Sack I. Magnetic resonance elastography: physical background and medical applications. Weinheim, Germany: Wiley-VCH; 2017.
6. Koumoutsakos P, Pivkin I, Milde F. The fluid mechanics of cancer and its therapy. *Ann Rev Fluid Mechanics* 2013;45:325–55.
7. Asbach P, Klatt D, Schlosser B, Biermer M, Muche M, Rieger A, et al. Viscoelasticity-based staging of hepatic fibrosis with multifrequency MR elastography. *Radiology* 2010;257:80–6.
8. Garteiser P, Doblas S, Daire JL, Wagner M, Leitao H, Vilgrain V, et al. MR elastography of liver tumours: value of viscoelastic properties for tumour characterisation. *Eur Radiol* 2012;22:2169–77.
9. Venkatesh SK, Yin M, Glockner JF, Takahashi N, Araoz PA, Talwalkar JA, et al. MR elastography of liver tumors: preliminary results. *AJR Am J Roentgenol* 2008;190:1534–40.
10. Tszchatzsch H, Guo J, Dittmann F, Hirsch S, Barnhill E, Jöhrens K, et al. Tomoelastography by multifrequency wave number recovery from time-harmonic propagating shear waves. *Med Image Anal* 2016;30:1–10.
11. Dittmann F, Tszchatzsch H, Hirsch S, Barnhill E, Braun J, Sack I, et al. Tomoelastography of the abdomen: tissue mechanical properties of the liver, spleen, kidney, and pancreas from single MR elastography scans at different hydration states. *Magn Reson Med* 2017;78:976–83.
12. Hirsch S, Guo J, Reiter R, Papazoglou S, Kroencke T, Braun J, et al. MR elastography of the liver and the spleen using a piezoelectric driver, single-shot wave-field acquisition, and multifrequency dual parameter reconstruction. *Magn Reson Med* 2014;71:267–77.
13. Liu H, Wu T. Estimating the area under a receiver operating characteristic curve for repeated measures design. *J Statistical Software* 2003;8:18.
14. DeLong ER, DeLong DM, Clarke-Pearson DL. Comparing the areas under two or more correlated receiver operating characteristic curves: a nonparametric approach. *Biometrics* 1988;44:837–45.
15. McFarland EG, Mayo-Smith WW, Saini S, Hahn PF, Goldberg MA, Lee MJ. Hepatic hemangiomas and malignant tumors: improved differentiation with heavily T2-weighted conventional spin-echo MR imaging. *Radiology* 1994;193:43–7.
16. Jamin Y, Boulton JK, Li J, Popov S, Garteiser P, Ullola JL, et al. Exploring the biomechanical properties of brain malignancies and their pathologic determinants in vivo with magnetic resonance elastography. *Cancer Res* 2015;75:1216–24.
17. European Association for the Study of the Liver (EASL). EASL Clinical Practice Guidelines on the management of benign liver tumours. *J Hepatol* 2016;65:386–98.
18. Semelka RC, Nimojan N, Chandana S, Ramalho M, Palmer SL, DeMulder D, et al. MRI features of primary rare malignancies of the liver: a report from four university centres. *Eur Radiol* 2018;28:1529–39.
19. Wanless IR, Mawdsley C, Adams R. On the pathogenesis of focal nodular hyperplasia of the liver. *Hepatology* 1985;5:1194–200.
20. Nault JC, Bioulac-Sage P, Zucman-Rossi J. Hepatocellular benign tumors—from molecular classification to personalized clinical care. *Gastroenterology* 2013;144:888–902.

# Cancer Research

The Journal of Cancer Research (1916-1930) | The American Journal of Cancer (1931-1940)

**AACR** American Association  
for Cancer Research

## Tomoelelastography Distinguishes Noninvasively between Benign and Malignant Liver Lesions

Mehrgan Shahryari, Heiko Tzschätzsch, Jing Guo, et al.

*Cancer Res* 2019;79:5704-5710. Published OnlineFirst September 24, 2019.

<b>Updated version</b>	Access the most recent version of this article at: doi: <a href="https://doi.org/10.1158/0008-5472.CAN-19-2150">10.1158/0008-5472.CAN-19-2150</a>
<b>Supplementary Material</b>	Access the most recent supplemental material at: <a href="http://cancerres.aacrjournals.org/content/suppl/2019/09/24/0008-5472.CAN-19-2150.DC1">http://cancerres.aacrjournals.org/content/suppl/2019/09/24/0008-5472.CAN-19-2150.DC1</a>
<b>Cited articles</b>	This article cites 19 articles, 1 of which you can access for free at: <a href="http://cancerres.aacrjournals.org/content/79/22/5704.full#ref-list-1">http://cancerres.aacrjournals.org/content/79/22/5704.full#ref-list-1</a>
<b>Citing articles</b>	This article has been cited by 2 HighWire-hosted articles. Access the articles at: <a href="http://cancerres.aacrjournals.org/content/79/22/5704.full#related-urls">http://cancerres.aacrjournals.org/content/79/22/5704.full#related-urls</a>
<b>E-mail alerts</b>	<a href="#">Sign up to receive free email-alerts</a> related to this article or journal.
<b>Reprints and Subscriptions</b>	To order reprints of this article or to subscribe to the journal, contact the AACR Publications Department at <a href="mailto:pubs@aacr.org">pubs@aacr.org</a> .
<b>Permissions</b>	To request permission to re-use all or part of this article, use this link <a href="http://cancerres.aacrjournals.org/content/79/22/5704">http://cancerres.aacrjournals.org/content/79/22/5704</a> . Click on "Request Permissions" which will take you to the Copyright Clearance Center's (CCC) Rightslink site.



**Publication 2: Reduction of breathing artifacts in multifrequency magnetic resonance elastography of the abdomen**

**Shahryari, M.**, Meyer, T., Warmuth, C., Herthum, H., Bertalan, G., Tzschatzsch, H., Stencel, L., Lukas, S., Lilaj, L., Braun, J., & Sack, I. (2021). Reduction of breathing artifacts in multifrequency magnetic resonance elastography of the abdomen. *Magn Reson Med*, 85(4), 1962-1973. <https://doi.org/10.1002/mrm.28558>

## Reduction of breathing artifacts in multifrequency magnetic resonance elastography of the abdomen

Mehrgan Shahryari<sup>1</sup>  | Tom Meyer<sup>1</sup> | Carsten Warmuth<sup>1</sup> | Helge Herthum<sup>1</sup>  |  
Gergely Bertalan<sup>1</sup> | Heiko Tzschätzsch<sup>1</sup> | Lisa Stencel<sup>1</sup> | Steffen Lukas<sup>1</sup> | Ledia Lilaj<sup>1</sup>  |  
Jürgen Braun<sup>2</sup>  | Ingolf Sack<sup>1</sup> 

<sup>1</sup>Department of Radiology, Charité–Universitätsmedizin Berlin, Berlin, Germany

<sup>2</sup>Institute of Medical Informatics, Charité–Universitätsmedizin Berlin, Berlin, Germany

### Correspondence

Ingolf Sack, Department of Radiology,  
Charité–Universitätsmedizin Berlin,  
Charitéplatz 1, 10117 Berlin, Germany.  
Email: ingolf.sack@charite.de

**Funding information** The German Federal  
Ministry of Education and Research  
(LiSyM 031L0057) and the German  
Research Foundation (SFB1340 “Matrix in  
Vision” and GRK2260 BIOQIC)

**Purpose:** With abdominal magnetic resonance elastography (MRE) often suffering from breathing artifacts, it is recommended to perform MRE during breath-hold. However, breath-hold acquisition prohibits extended multifrequency MRE examinations and yields inconsistent results when patients cannot hold their breath. The purpose of this work was to analyze free-breathing strategies in multifrequency MRE of abdominal organs.

**Methods:** Abdominal MRE with 30, 40, 50, and 60 Hz vibration frequencies and single-shot, multislice, full wave-field acquisition was performed four times in 11 healthy volunteers: once with multiple breath-holds and three times during free breathing with ungated, gated, and navigated slice adjustment. Shear wave speed maps were generated by tomoelastography inversion. Image registration was applied for correction of intrascan misregistration of image slices. Sharpness of features was quantified by the variance of the Laplacian.

**Results:** Total scan times ranged from 120 seconds for ungated free-breathing MRE to 376 seconds for breath-hold examinations. As expected, free-breathing MRE resulted in larger organ displacements (liver,  $4.7 \pm 1.5$  mm; kidneys,  $2.4 \pm 2.2$  mm; spleen,  $3.1 \pm 2.4$  mm; pancreas,  $3.4 \pm 1.4$  mm) than breath-hold MRE (liver,  $0.7 \pm 0.2$  mm; kidneys,  $0.4 \pm 0.2$  mm; spleen,  $0.5 \pm 0.2$  mm; pancreas,  $0.7 \pm 0.5$  mm). Nonetheless, breathing-related displacement did not affect mean shear wave speed, which was consistent across all protocols (liver,  $1.43 \pm 0.07$  m/s; kidneys,  $2.35 \pm 0.21$  m/s; spleen,  $2.02 \pm 0.15$  m/s; pancreas,  $1.39 \pm 0.15$  m/s). Image registration before inversion improved the quality of free-breathing examinations, yielding no differences in image sharpness to uncorrected breath-hold MRE in most organs ( $P > .05$ ).

**Conclusion:** Overall, multifrequency MRE is robust to breathing when considering whole-organ values. Respiration-related blurring can readily be corrected using image registration. Consequently, ungated free-breathing MRE combined with image registration is recommended for multifrequency MRE of abdominal organs.

This is an open access article under the terms of the Creative Commons Attribution License, which permits use, distribution and reproduction in any medium, provided the original work is properly cited.

© 2020 The Authors. *Magnetic Resonance in Medicine* published by Wiley Periodicals LLC on behalf of International Society for Magnetic Resonance in Medicine

## KEYWORDS

abdomen, breathing artifacts, image registration, multifrequency MRE, navigator, stiffness

## 1 | INTRODUCTION

Abdominal magnetic resonance elastography (MRE) is gaining in importance for the clinical diagnosis of a large variety of diseases that alter the mechanical properties of tissues such as liver fibrosis,<sup>1-5</sup> portal hypertension,<sup>6,7</sup> renal dysfunction,<sup>8-10</sup> and tumors.<sup>11-14</sup> Since the introduction of MRE in 1995 by Muthupillai et al.,<sup>15</sup> various MRE methods tailored for clinical examinations of the abdomen have been proposed.<sup>16</sup> A general challenge for abdominal MRE is to cope with respiratory motion during data acquisition, which potentially degrades the consistency of MRE-encoded vibration data.<sup>17</sup> Therefore, the Quantitative Imaging Biomarkers Alliance of RSNA (Radiological Society of North America) recommends MRE of the liver to be performed during breath-holds after expiration.<sup>18</sup> Standard MRE of the liver consists of acquisitions of four slices squeezed into multiple breath-holds of 12 to 20 seconds<sup>2</sup> or into a single breath-hold using rapid single-shot sequences or simultaneous multislice MRE.<sup>19,20</sup> However, there are several reasons to avoid breath-holds in abdominal MRE. First, patients with chronic liver diseases often suffer from comorbidities that limit their ability to hold their breath after expiration during the acquisition of MRE data.<sup>17</sup> Second, patients cannot always follow breathing commands, resulting in motion during scans or inconsistent organ positions.<sup>21</sup> Furthermore, breath-holds might alter abdominal pressure and hepatic perfusion, which in turn affect liver stiffness.<sup>22,23</sup> Finally, paused data acquisition to permit intermittent respiration prolongs total acquisition time beyond the clinically acceptable limit if rich data are acquired as in multifrequency, 3D MRE.

Published studies report multifrequency 3D MRE of abdominal organs with up to eight wave dynamics consecutively acquired at up to seven frequencies, resulting in total acquisition times exceeding 5 minutes, during which patients are allowed to breathe freely.<sup>8-10,24,25</sup> The same protocol with breath-hold acquisition would exceed 20 minutes.<sup>26</sup> Nevertheless, there are good reasons for multifrequency MRE of abdominal organs, including measurement of viscoelastic dispersion or improved detail resolution.<sup>25,27,28</sup> For example, tomoelastography, a multifrequency MRE technique for abdominal organs, was applied during free breathing for detecting small hepatic lesions<sup>14</sup> or fine renal structures,<sup>25</sup> despite the risk of breathing artifacts. Although individual images from rapid single-shot MRE scans may have minimal motion artifacts in the organs of interest, intrascan misregistration may degrade the resulting elastograms. This study

addresses strategies to avoid and correct intrascan misregistration in single-shot MRE of abdominal organs. Our hypothesis is that detail resolution in multifrequency MRE can be further improved by suppression of motion artifacts either during image acquisition using respiratory navigators or with postprocessing using image registration before MRE wave inversion.

Experimental strategies include one-dimensional breathing navigators for either defining acquisition windows or for adapting slice positions following inspiration and expiration. Additionally, motion is corrected in raw MRI signals during postprocessing. These strategies will be compared with the current gold standard, which is breath-hold MRE. The overall aim of our study is to recommend strategies for efficiently suppressing breathing artifacts in abdominal multifrequency MRE toward time-efficient, highly resolved stiffness mapping of the liver, spleen, pancreas, and kidneys without the need for restricting breathing during the examination.

## 2 | METHODS

## 2.1 | Subjects and paradigms

Eleven healthy male participants (age,  $28 \pm 4$  years; range, 23-38 years; body mass index,  $23 \pm 2$  kg/m<sup>2</sup>) were included after approval by the institutional ethics review board of the Charité-Universitätsmedizin Berlin in accordance with the World Medical Association Declaration of Helsinki (Ethical Principles for Medical Research Involving Human Subjects). Written, informed consent was obtained. Volunteers reported no history of abdominal or respiratory diseases. Multifrequency MRE was conducted four times in each volunteer to investigate and compare the displacement of the liver, kidneys, spleen, and pancreas with use of different MRE protocols:

- (i) Block acquisitions during repeat breath-holds in expiration (BH-MRE);
- (ii) Continuous acquisitions during free breathing (FB-MRE);
- (iii) Continuous RF excitation (to maintain a steady state of magnetization) and gated block acquisition within an acquisition window (defined by the navigator signals through the diaphragm, G-MRE); and
- (iv) Continuous acquisitions during automated adjustments of image slice positions using a respiratory navigator within an acquisition window (gating and following, GF-MRE).

## 2.2 | Magnetic resonance imaging and MRE acquisition techniques

All MRI and MRE acquisitions were performed on a 1.5T clinical MRI scanner (Magnetom Sonata; Siemens, Erlangen, Germany) using a 12-channel phased-array surface coil and the spine-array coils integrated into the examination table. For anatomical orientation, localizer,  $T_1$ -weighted and  $T_2$ -weighted axial, as well as  $T_2$ -weighted coronal MRI sequences were acquired before MRE. The MRE sequences and driver setups were similar to Shahryari et al.<sup>14</sup> In brief, the driver setups consisted of four pressurized air drivers that were attached to the body surface with a Velcro belt at the position of the transpyloric plane. Two of the drivers were attached ventrally on the midclavicular line, while the remaining two were placed dorsally on the scapular line. Mechanical vibrations of 30, 40, 50, and 60 Hz frequency were induced in the abdomen with 0.4 bar air pressure for the ventral drivers and 0.6 bar air pressure for the dorsal drivers. Neither position nor air pressure of the actuators was individually adapted to the body shape of the volunteer. A single-shot spin-echo EPI sequence with flow-compensated motion-encoding gradients was used to acquire the 3D wave field.<sup>29</sup> Eight phase offsets over a full vibration period were recorded for all three Cartesian motion field directions. Nine contiguous slices of 5 mm thickness and placed in a coronal view through the liver, spleen, pancreas, and both kidneys were acquired, covering a FOV of  $284 \times 350 \text{ mm}^2$ . Further imaging parameters were as follows: matrix size =  $104 \times 128$ , pixel resolution =  $2.7 \times 2.7 \times 5 \text{ mm}^3$ , TR = 1200 ms, TE = 55 ms, parallel imaging with GRAPPA factor 2, motion-encoding gradient frequency = 43.48 Hz for 30, 40, and 50 Hz vibration frequencies and 44.88 Hz for 60 Hz vibration frequency, and motion-encoding gradient amplitude = 30 mT/m.

For BH-MRE (i), single-component, single-frequency MRE data of each of the three Cartesian wave field components and four drive frequencies were acquired block-wise. Therefore, separate scans were performed during 12 single breath-holds in expiration of approximately 10 seconds duration. Data were merged afterward to full six-dimensional data arrays of sizes  $104 \times 128 \times 9 \times 8 \times 3 \times 4$ , depicting 3D spatial-resolved displacement data ( $104 \times 128 \times 9$ ) at multiple time steps (8), components (3), and frequencies (4) resulting in  $N = 96$  consecutively acquired slice blocks. The magnitude images of the 96 acquired slice blocks were averaged to a mean magnitude image (M). For FB-MRE (ii), all data were continuously acquired without account of respiratory motion.

For G-MRE (iii) and GF-MRE (iv), we integrated a navigator echo into the EPI-MRE sequence before slice block acquisition, to monitor the respiratory position based on the method described in Henningson and Botnar.<sup>30</sup> In brief, a pencil beam RF pulse with  $30^\circ$  flip angle and 20 mm diameter was positioned craniocaudally through the right

diaphragm with the readout axis parallel to the long axis of the beam. The acquired navigator data were then Fourier-transformed in real time, generating a one-dimensional line image illustrating respiratory motion. An acceptance window of 5 mm has been defined for G-MRE to interrupt the acquisition of data outside this window. In GF-MRE, the acceptance window was 20 mm, within which the position of the full image slice block was continuously moved along the head-to-foot axis, to follow the position of the right diaphragm depicted by the navigator signal. As in G-MRE, data acquisition was interrupted if a very deep breathing motion exceeded the 20 mm window detected by the navigator. Of note, image slices were continuously excited in G-MRE and GF-MRE, similar to FB-MRE but with paused data acquisition whenever the navigator signal was outside the acceptance window. Because TR in all protocols was identical (1.2 seconds), a similar steady state of magnetization was established during FB-MRE, G-MRE, and GF-MRE. Only in BH-MRE did the steady-state magnetization have to be re-established for each single breath-hold, potentially inducing MRI intensity fluctuations. However, as analyzed later, these fluctuations did not affect the sharpness of averaged magnitude images M. All protocols are illustrated in Figure 1.

## 2.3 | Magnetic resonance elastography data processing

Organ displacement and motion artifacts were quantified by 2D rigid-body image registration using the open-source *Elastix* toolbox.<sup>31</sup> Therefore, a presegmentation region of interest (ROI) was manually delineated for each organ, covering the full organ with a tolerance margin of approximately 5 pixels that covers organ displacements caused by motion. Presegmentation ROIs for image registration are demarcated in Supporting Information Figure S1. The mean MRE magnitude images (M) displaying a mixed  $T_2$  and  $T_2^*$  contrast were registered to the first of  $8 \times 3 \times 4 = 96$  slice blocks acquired during a multifrequency MRE scan using (1) advanced Mattes mutual information with 32 histogram bins as a similarity metric<sup>32</sup> and (2) stochastic gradient descent as an optimizer implemented in *Elastix*. The registration was performed with a pyramid resampling scheme at three different resolutions. The optimizer was set to a maximum of 100 iterations, and at each iteration, 2000 random coordinates were sampled for the computation of the similarity metric. As a result,  $N = 95$  in-plane relative displacements  $x$  (horizontally) and  $y$  (vertically) were generated for each organ. Mean displacement  $U$  was then calculated by taking the mean of the magnitude displacements  $u_n = \sqrt{(\bar{x} - x_n)^2 + (\bar{y} - y_n)^2}$ , with the bar denoting time-averaged displacements  $x$  and  $y$ . For motion correction, third-order B-spline interpolation was

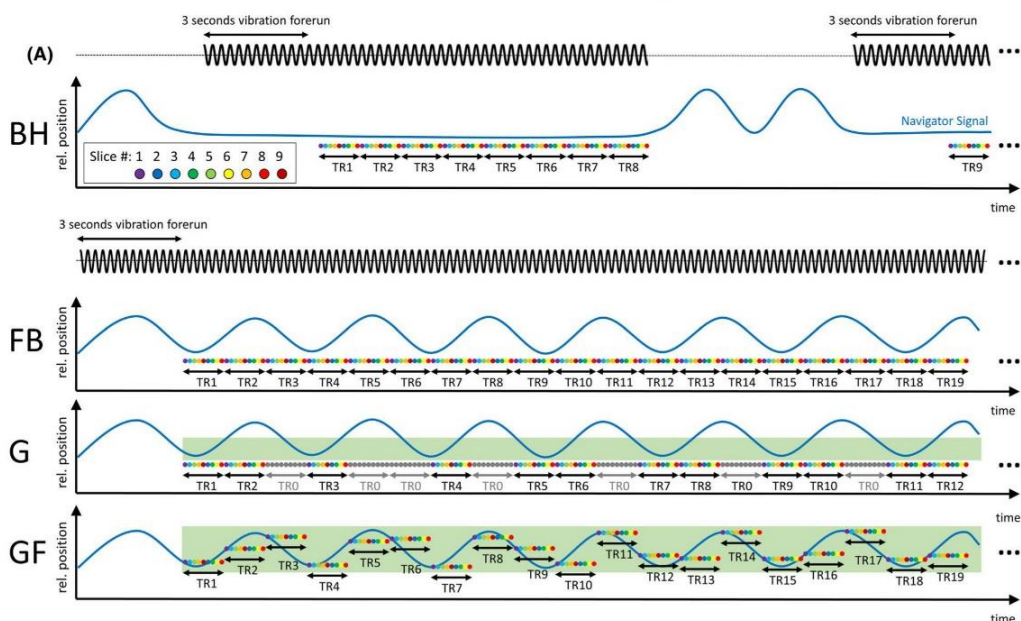


**FIGURE 1** Schematic timing of magnetic resonance elastography (MRE) protocols tested in this study. A, Breath-hold MRE (BH) with acquisition of slice blocks during repeat breath-holds in expiration. B, Continuous free-breathing MRE: ungated (FB), gated by respiratory navigator signals (G), and with automated adjustment of image slice positions according to the navigator signal (GF). Shown is the relative timing of vibration along with the relative position (rel. position) of navigator signals along the craniocaudal axis through the diaphragm. The timing of slice acquisition and slice positions (on rel. position axis) are indicated by colored circles. Vibrations were induced 3 seconds before data acquisition, to establish a steady-state flux of shear waves throughout the abdomen. Note that slices are acquired in an interleaved manner in the following order: 1, 3, 5, 7, 9, 2, 4, 6, 8. TR1, TR2, and so on, denote the TRs of each block of nine image slices. The gray circles during TR0 indicate that the data acquisition was interrupted (due to the respiration detected by the navigator), whereas the RF stimulation was performed continuously. After measuring TR1-TR8 with the first motion-encoding gradient (MEG) component, the following 16 TRs are measured with the second and third MEG, respectively

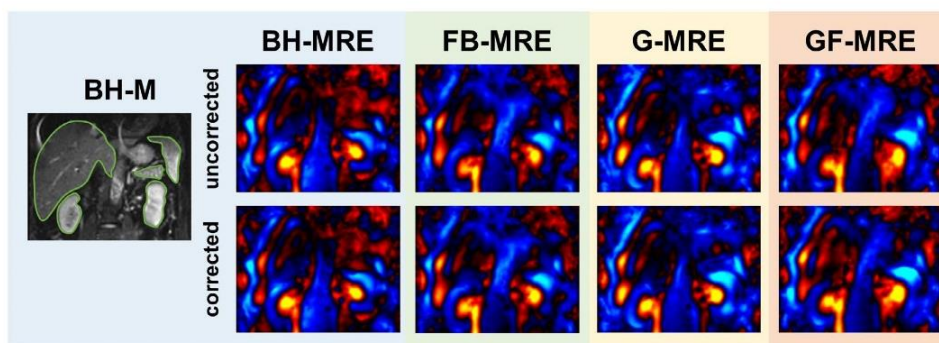


**FIGURE 2** Wave images acquired in a volunteer in a coronal view through the liver, pancreas, spleen, and kidneys with 40 Hz excitation frequency (left–right deflection component) after unwrapping and temporal Fourier transformation, uncorrected and corrected for motion using image registration. Blue to yellow colors scale the deflections from left to right with amplitudes of 20  $\mu\text{m}$ . A magnitude image (gray scale) from breath-hold MRE (BH-MRE) is shown for anatomical orientation and display of organ-specific regions of interest (green lines). Abbreviations: FB-MRE, ungated free-breathing MRE; G-MRE, gated free-breathing MRE; GF-MRE, gated, slice-following, free-breathing MRE

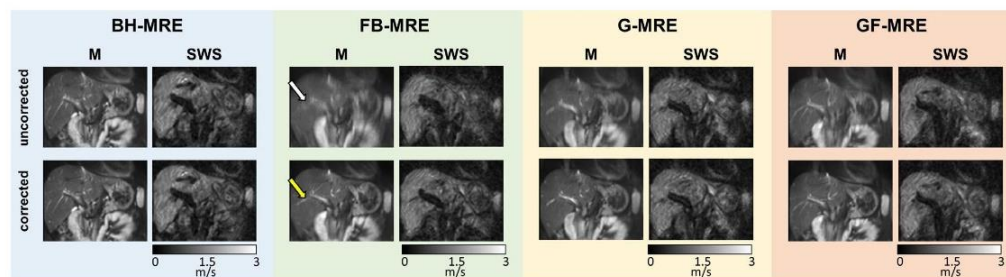


**FIGURE 3** Representative magnitude MRE images (magnitude [M],  $T_2$ , and  $T_2^*$  weighted) and stiffness maps (shear wave speed [SWS]) of the liver of a healthy subject obtained with different MRE protocols. Shown are averaged images with and without correction for breathing artifact by 2D in-plane rigid registration. Open arrow indicates blurred features, and yellow arrow indicates improved anatomical representations

used to apply the transformations to the real and imaginary parts of the complex MRI data, the phases of which were further processed for MRE parameter recovery. Although no explicit smoothing step was implemented in the registration process, a slight smoothing may have occurred due to the B-spline interpolation.

Figure 2 shows representative 40 Hz waves (left-to-right component) in a slice covering the liver, kidneys, spleen, and pancreas acquired with all MRE protocols, uncorrected and corrected. More material on animated waves is presented in Supporting Information Video S1. All MRE wave data were processed using wave number-based multifrequency dual elasto-visco inversion (k-MDEV), which provides maps of the shear wave speed (SWS) in meters per second.<sup>33</sup> Because SWS is derived from the real part of wave numbers, it is virtually not influenced by viscosity and can be considered a surrogate of stiffness. The inversion pipeline is publicly available at <https://bioqic-apps.charite.de>.<sup>34</sup> For parameter quantification, organ-specific ROIs were manually drawn based on time-averaged magnitude MRE (M) images and accounting for whole-organ boundaries, as illustrated in Figure 2. Furthermore, these ROIs were refined by empirical thresholds of 1 m/s for softer organs (liver and pancreas) and 1.5 m/s for stiffer organs (spleen and kidneys), to remove blood vessels that appear enlarged in SWS maps.<sup>24,35</sup> Without motion, both M (MRE magnitude averaged over 96 consecutively acquired image slice blocks) and SWS maps are expected to display sharp edges at tissue interfaces, which is reflected in the Laplacian  $\Delta$  of the images. Therefore, image sharpness was quantified by computing the variance ( $\sigma$ ) of the Laplacian  $\Delta$  of MRE images as described in Pech-Pacheco et al.<sup>36</sup> A Laplacian derivative kernel of size  $3 \times 3$  was applied to both the mean magnitude M (averaged over 96 image slice blocks) and SWS maps. The value of  $\sigma$  was then derived by computing the variance of  $\Delta M$  and  $\Delta SWS$  within presegmented ROIs of each organ and protocol.

## 2.4 | Statistical analysis

The mean U, SWS, and sharpness ( $\sigma$ ) were calculated for all four breathing paradigms and organs. All values are tabulated as mean  $\pm$  SD, unless otherwise stated. Statistical significance of differences in displacement and stiffness across all abdominal organs and motion-reduction strategies (protocols) were analyzed using linear mixed-effect models. Linear mixed-effect models accounted for U and SWS as dependent variables, whereas organs and protocols, as well as their interactions, were taken as independent variables. Statistical differences of the dependent variables were tested by Tukey's post hoc test with Bonferroni correction for multiple comparisons. A paired Student t-test was used to test for differences between uncorrected and motion-corrected MRE data based on SWS values. A Wilcoxon signed-rank test was used to test for differences between uncorrected and motion-corrected  $\sigma$  in all organs and protocols. Furthermore, the same test was applied to test for differences between uncorrected BH-MRE and motion-corrected FB-MRE, as well as motion-corrected BH-MRE and motion-corrected FB-MRE in all organs.

The significance level was set to 5%. Statistical analysis was performed in R (version 3.6.2; R-Foundation, Vienne, Austria) using "lme4," "lsmeans," and "ggplot2" packages.

## 3 | RESULTS

Figures 3-6 illustrate the effects of breathing motion and artifact-reduction strategies in different organs of 1 representative volunteer. Participant characteristics and group mean values of U, SWS, and  $\sigma$  of  $\Delta M$  and SWS of all abdominal organs and protocols are summarized in Table 1. Scan times were  $376 \pm 68$  seconds for BH-MRE, 120 seconds for FB-MRE,  $166 \pm 117$  seconds for G-MRE, and  $128 \pm 17$  seconds for GF-MRE. In addition to total acquisition time, it took 168 seconds on average (range, 18-413 seconds) to set up the respiratory navigators for G-MRE and GF-MRE.

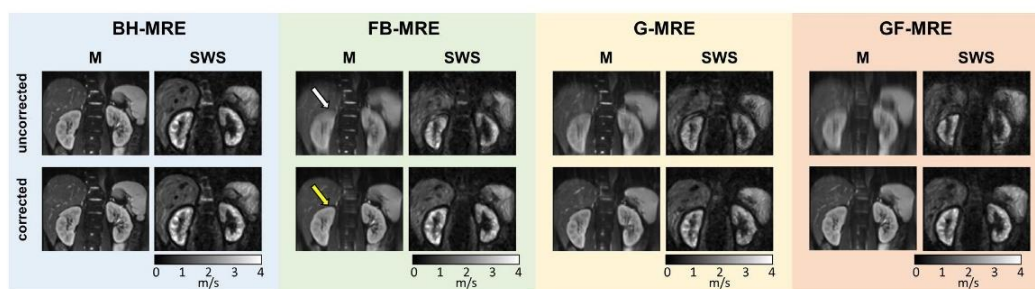


**FIGURE 4** Representative magnitude MRE images (M,  $T_2$ , and  $T_2^*$  weighted) and stiffness maps (SWS) of the kidneys of a healthy subject obtained with different MRE protocols. Shown are averaged images with and without correction for breathing artifact by 2D in-plane rigid registration. Open arrow indicates blurred features, and yellow arrow indicates improved anatomical representations

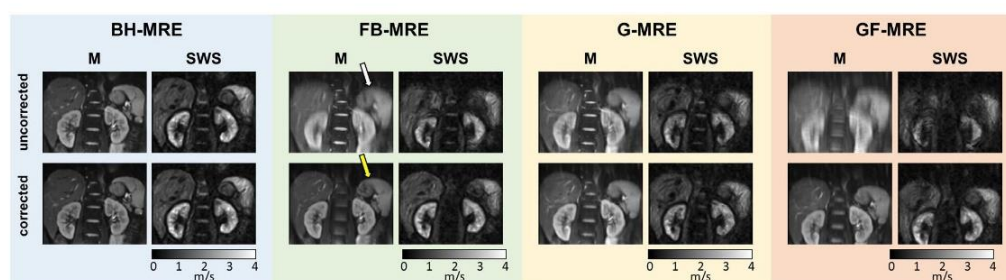


**FIGURE 5** Representative magnitude MRE images (M,  $T_2$ , and  $T_2^*$  weighted) and stiffness maps (SWS) of the spleen of a healthy subject obtained with different MRE protocols. Shown are averaged images with and without correction for breathing artifact by 2D in-plane rigid registration. Open arrow indicates blurred features, and yellow arrow indicates improved anatomical representations

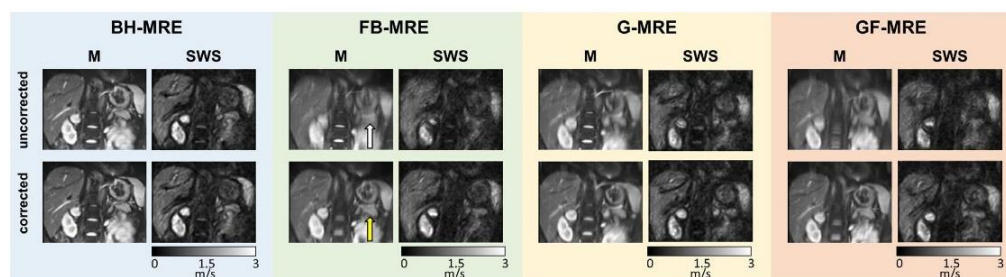


**FIGURE 6** Representative magnitude MRE images (M,  $T_2$ , and  $T_2^*$  weighted) and stiffness maps (SWS) of the pancreas of a healthy subject obtained with different MRE protocols. Shown are averaged images with and without correction for breathing artifact by 2D in-plane rigid registration. Open arrow indicates blurred features, and yellow arrow indicates improved anatomical representations

### 3.1 | Displacement

The BH-MRE protocol was used as reference standard for the four abdominal organs investigated by multifrequency MRE. There were only minor displacements of these organs (liver,  $0.7 \pm 0.2$  mm; kidneys,  $0.4 \pm 0.2$  mm; spleen,

$0.5 \pm 0.2$  mm; pancreas,  $0.7 \pm 0.5$  mm) without significant differences among them (all  $P > .05$ ). In FB-MRE, the liver was most severely affected by displacement (liver,  $4.7 \pm 1.5$  mm; kidneys,  $2.4 \pm 2.2$  mm; spleen,  $3.1 \pm 2.4$  mm; pancreas,  $3.4 \pm 1.4$  mm) with significantly larger displacement amplitudes than the kidneys ( $P < .01$ ). Navigated GF-MRE

**TABLE 1** Group mean values of organ displacement, sharpness, and stiffness obtained with different multifrequency MRE protocols (mean value  $\pm$  SD)

Organ	Protocol	U (mm)	$\sigma$ of $\Delta M$		P-Values	SWS (m/s)		P-Values	$\sigma \cdot 10^{-2}$ of $\Delta SWS$		P-Values
			Uncorrected	Corrected		Uncorrected	Corrected		Uncorrected	Corrected	
Liver	BH-MRE	0.7 $\pm$ 0.2	45.9 $\pm$ 30.7	51.5 $\pm$ 26.0	ns	1.49 $\pm$ 0.11	1.49 $\pm$ 0.12	ns	1.05 $\pm$ 0.16	1.06 $\pm$ 0.16	ns
	FB-MRE	4.7 $\pm$ 1.5	24.3 $\pm$ 14.1	37.8 $\pm$ 23.7	<.001	1.44 $\pm$ 0.07	1.43 $\pm$ 0.07	ns	0.99 $\pm$ 0.13	0.97 $\pm$ 0.09	ns
	G-MRE	3.5 $\pm$ 1.4	29.4 $\pm$ 17.6	45.7 $\pm$ 27.6	.003	1.46 $\pm$ 0.09	1.46 $\pm$ 0.09	ns	0.99 $\pm$ 0.13	1.03 $\pm$ 0.18	ns
	GF-MRE	2.6 $\pm$ 1.4	40.2 $\pm$ 29.8	42.3 $\pm$ 30.4	ns	1.45 $\pm$ 0.07	1.45 $\pm$ 0.07	ns	0.98 $\pm$ 0.15	0.99 $\pm$ 0.15	ns
Kidneys	BH-MRE	0.4 $\pm$ 0.2	372.1 $\pm$ 149.2	430.7 $\pm$ 149.8	<.001	2.46 $\pm$ 0.25	2.46 $\pm$ 0.24	ns	4.04 $\pm$ 1.11	4.19 $\pm$ 1.23	.042
	FB-MRE	2.4 $\pm$ 2.2	174.7 $\pm$ 62.2	231.8 $\pm$ 96.9	.014	2.33 $\pm$ 0.22	2.35 $\pm$ 0.21	ns	3.26 $\pm$ 0.79	3.42 $\pm$ 0.76	ns
	G-MRE	2.0 $\pm$ 1.7	213.4 $\pm$ 125.9	262.6 $\pm$ 145.7	.002	2.34 $\pm$ 0.20	2.35 $\pm$ 0.20	ns	3.27 $\pm$ 0.87	3.37 $\pm$ 0.90	ns
	GF-MRE	5.6 $\pm$ 2.6	136.1 $\pm$ 98.9	255.6 $\pm$ 138.6	.002	2.34 $\pm$ 0.18	2.36 $\pm$ 0.17	ns	3.06 $\pm$ 0.53	3.34 $\pm$ 0.55	.003
Spleen	BH-MRE	0.5 $\pm$ 0.2	465.0 $\pm$ 350.6	539.5 $\pm$ 400.1	ns	2.02 $\pm$ 0.18	2.03 $\pm$ 0.18	ns	7.12 $\pm$ 3.98	7.49 $\pm$ 3.92	ns
	FB-MRE	3.1 $\pm$ 2.4	314.9 $\pm$ 354.1	438.1 $\pm$ 459.4	.005	2.01 $\pm$ 0.17	2.02 $\pm$ 0.15	ns	5.99 $\pm$ 3.17	6.56 $\pm$ 4.03	ns
	G-MRE	3.0 $\pm$ 1.8	417.0 $\pm$ 474.0	530.0 $\pm$ 573.6	<.001	2.02 $\pm$ 0.17	2.00 $\pm$ 0.17	ns	6.84 $\pm$ 3.98	7.22 $\pm$ 4.44	.042
	GF-MRE	5.9 $\pm$ 3.8	349.8 $\pm$ 380.6	509.5 $\pm$ 509.9	.003	2.01 $\pm$ 0.20	2.02 $\pm$ 0.20	ns	6.51 $\pm$ 3.76	6.85 $\pm$ 4.19	ns
Pancreas	BH-MRE	0.7 $\pm$ 0.5	642.4 $\pm$ 265.2	839.8 $\pm$ 518.3	.042	1.38 $\pm$ 0.15	1.41 $\pm$ 0.16	ns	6.97 $\pm$ 3.01	6.94 $\pm$ 2.95	ns
	FB-MRE	3.4 $\pm$ 1.4	310.1 $\pm$ 224.2	548.6 $\pm$ 390.2	<.001	1.36 $\pm$ 0.14	1.39 $\pm$ 0.15	ns	5.33 $\pm$ 2.24	5.81 $\pm$ 2.41	.007
	G-MRE	3.0 $\pm$ 1.3	338.4 $\pm$ 251.3	491.3 $\pm$ 326.5	.019	1.38 $\pm$ 0.14	1.37 $\pm$ 0.12	ns	5.31 $\pm$ 1.81	5.74 $\pm$ 2.29	ns
	GF-MRE	5.0 $\pm$ 2.6	280.6 $\pm$ 280.4	519.0 $\pm$ 507.3	.014	1.37 $\pm$ 0.12	1.39 $\pm$ 0.13	ns	6.09 $\pm$ 2.34	5.95 $\pm$ 1.61	ns

Note: P-values refer to tests uncorrected versus corrected.

Abbreviation: ns, not significant.

reduced liver displacement relative to FB-MRE to  $2.6 \pm 1.4$  mm ( $P = .011$ ), while displacement of the other organs remained unchanged or even increased (kidneys,  $5.6 \pm 2.6$  mm,  $P < .001$ ; spleen,  $5.9 \pm 3.8$  mm,  $P < .001$ ; pancreas,  $5.0 \pm 2.6$  mm,  $P = .063$ ;  $P$ -values relative to FB-MRE). Larger displacement amplitudes in these organs compared with the liver were consistent with an increased latency between navigator scans and more posterior slices (eg, slice 7, 400 ms; slice 9, 533 ms; slice 6, 933 ms; and slice 8, 1067 ms, in the interleaved multislice acquisition scheme illustrated in Figure 1). Displacement was slightly better for G-MRE, which acquired data during relatively quiet phases of breathing only. Here, displacement improved relative to GF-MRE for three organs (kidneys,  $2.0 \pm 1.7$  mm,  $P < .001$ ; spleen,  $3.0 \text{ mm} \pm 1.8$ ,  $P < .001$ ; pancreas,  $3.0 \pm 1.3$  mm,  $P = .013$ ), whereas liver displacement did not significantly change ( $3.5 \pm 1.4$  mm,  $P = .538$ ) despite significantly longer acquisition. The results are summarized in Table 1. Statistical plots of  $U$  for all organs and protocols are shown in Figure 7.

### 3.2 | Stiffness

Figure 8 presents organ-specific differences in SWS with mean values of  $1.43 \pm 0.07$  m/s (liver),  $2.35 \pm 0.21$  m/s (kidneys),  $2.02 \pm 0.15$  m/s (spleen), and  $1.39 \pm 0.15$  m/s

(pancreas) obtained during free breathing (all  $P < .001$ , except for liver vs. pancreas:  $P > .05$ ). Interestingly, SWS did not differ across protocols despite the aforementioned differences in  $U$  (all  $P > .05$ ).

### 3.3 | Sharpness

Sharpness was improved by image registration as revealed to the naked eye when looking at both MRE magnitude images (M) and SWS maps (Figure 3-6). Accordingly,  $\sigma$  of  $\Delta M$  showed a significant reduction of blurring after registration in all organs investigated for FB-MRE and G-MRE (all  $P < .05$ ). Registration improved the GF-MRE data obtained in the kidneys, spleen, and pancreas (all  $P < .05$ ), whereas the liver, analyzed based on the first slice, had lower displacement amplitudes in GF-MRE and did not benefit from registration. Interestingly, sharpness even improved in BH-MRE examinations for the kidneys and pancreas, indicating the susceptibility of these organs to unconscious motion during breath-holds (Figure 9). After motion correction of FB-MRE,  $\sigma$  was indistinguishable from uncorrected BH-MRE in the liver, spleen, and pancreas (all  $P > .05$ ), while corrected FB-MRE in the kidneys had still lower  $\sigma$ -values than uncorrected BH-MRE ( $P < .01$ ) despite visual improvements. Motion-corrected BH-MRE shows significantly higher

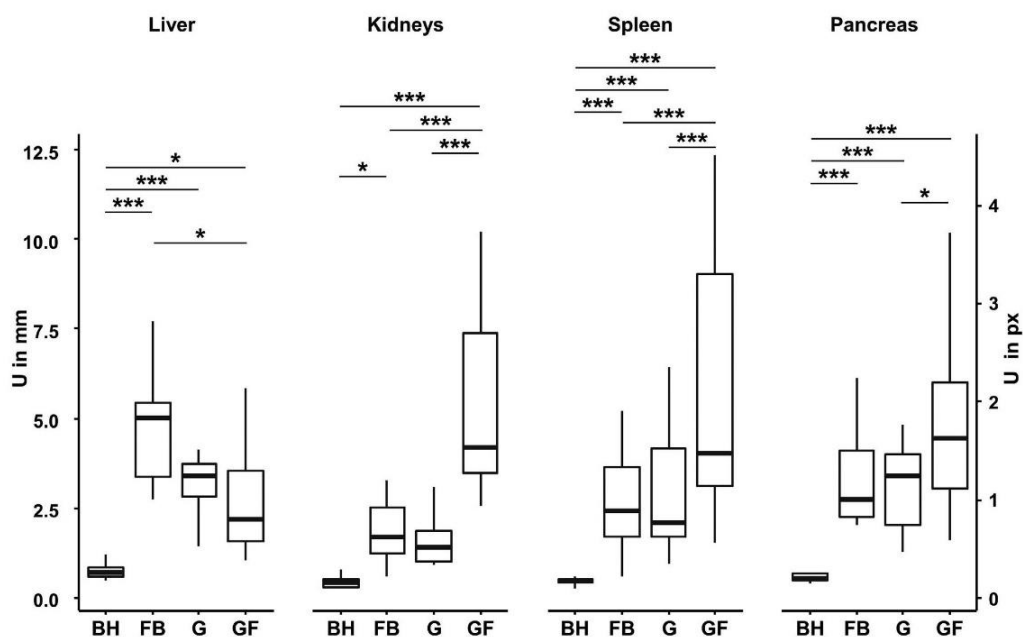
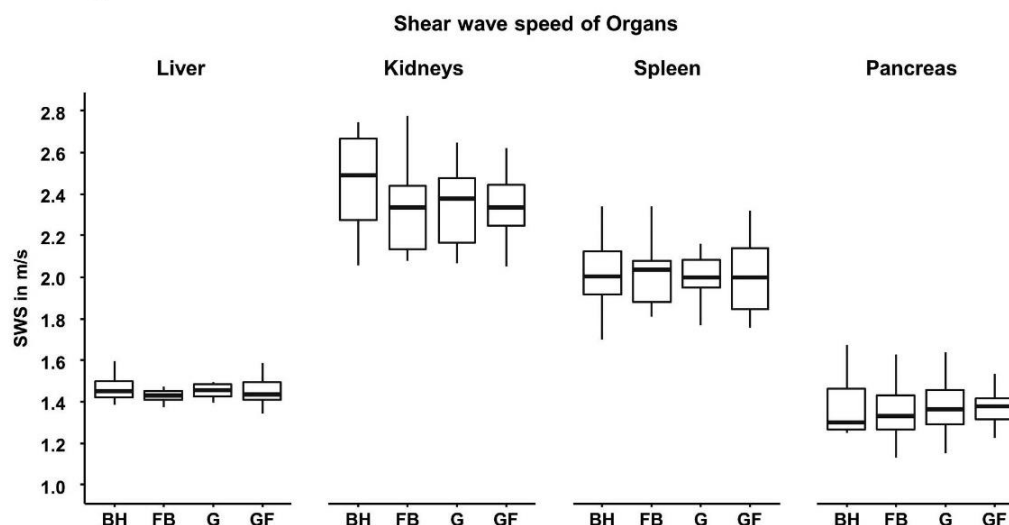
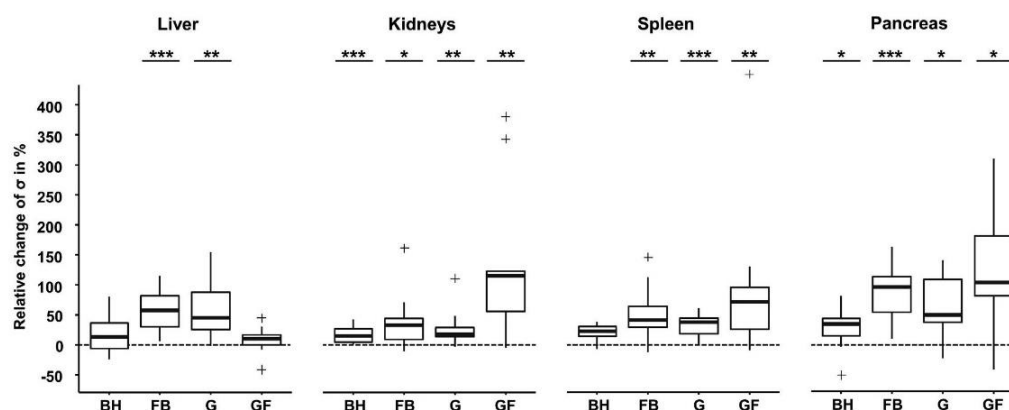


FIGURE 7 Group statistical plots of displacement amplitudes  $U$  (in millimeters and in pixels) of the liver, kidneys, spleen, and pancreas for different MRE protocols (\* $P < .05$ , \*\* $P < .01$ , \*\*\* $P < .001$ )



**FIGURE 8** Group statistical plots of stiffness SWS (in meters per second) of the liver, kidneys, spleen, and pancreas for different MRE protocols



**FIGURE 9** Box plot of relative changes of image sharpness (in percentages) indicated by the sharpness variance  $\sigma$  ( $[\sigma(\text{corrected}) - \sigma(\text{uncorrected})]/\sigma[\text{uncorrected}] \cdot 100$ ) of the Laplacian  $\Delta$  of MRE magnitude ( $*P < .05$ ,  $**P < .01$ ,  $***P < .001$ )

$\sigma$  values compared with motion-corrected FB-MRE in the liver, kidneys, and pancreas (all  $P < .05$ ), whereas no such difference to the spleen was observed. Representative  $\Delta M$  and  $\Delta SWS$  images are shown in Supporting Information Figure S1. It is apparent from the examples shown that  $\Delta SWS$  improved primarily at organ boundaries, indicating sharper edges while within organs, and higher-frequency  $\Delta SWS$  patterns are seemingly unaffected by the image registration.

All relevant parameters are summarized in Table 1.

## 4 | DISCUSSION AND CONCLUSIONS

This study of breathing-induced artifacts in multifrequency MRE presents three key findings. First, this is the first study providing systematic quantitative motion data for different abdominal organs when asymptomatic subjects freely breathe during MRE data acquisition with different protocols. Second, our results demonstrate that averaged MRE values are surprisingly stable, regardless of whether

MRE is performed during free breathing or breath-holds. Finally, we show that unnavigated free-breathing MRE combined with motion correction by image registration represents the optimal trade-off in terms of scan time and detail resolution. In the following, we will briefly discuss each of these three points.

- (i) Breath-hold MRE results in the smallest displacement amplitudes of abdominal organs compared with free-breathing MRE and navigator-triggered gating MRE techniques. The liver and pancreas are the abdominal organs most severely affected by breathing, whereas the kidneys show the smallest displacement amplitudes. An earlier study of our group shows that multifrequency MRE of the kidneys is improved when omitting any breathing command compared with breath-hold MRE.<sup>25</sup> However, this case-specific finding from a single subject was never reproduced or compared with other abdominal organs, as done in the present study.
- (ii) All protocols provided values in the range of published values of abdominal MRE (converting SWS to shear modulus by  $\mu = \text{SWS}^2 \cdot 1000 \text{ kg/m}^3$ )<sup>37-39</sup> or directly agreed with reported SWS values in that region.<sup>25,40</sup> The visible blurring of the magnitude images in free-breathing MRE (see Figures 3-6) suggests that stiffness values are strongly affected by breathing motion, which, however, is not the case. This observation is remarkable because it indicates the intrinsic stability of MRE to respiration.<sup>41,42</sup> We attribute this stability to two main effects. First, MRE analyzes parameters that refer to local wavelengths, which in turn are unaffected by boundary conditions to a certain extent. Although actuator position, wave amplitudes, and wave patterns can change with breathing, the resulting parameter maps do not necessarily reflect these changes. Second, local wavelengths are calculated from time-harmonic tissue displacements selected from the fundamental frequency in the Fourier spectrum.<sup>16</sup> This is temporal filtering, which efficiently suppresses breathing-related signals as long as they do not overlap with the timing of the fundamental oscillation. For these reasons, MRE might be more robust to breathing-induced artifact than other MRI techniques. Because the MRE magnitude signals presented in Figures 3-6 are time-averaged across 96 consecutive acquisitions, similar blurring would occur in any MRI data acquired over the same time during free breathing.
- (iii) Nonetheless, blurring can sufficiently be corrected by image registration. The resulting improvement in sharpness  $\sigma$  was seen primarily in magnitude images, and to a lesser extent in stiffness maps. The SWS maps predominantly suffered from distorted boundaries,

which became sharper after correction, although without significant changes in  $\sigma$ . Therefore, we may conclude that  $\sigma$  of SWS maps tends to exaggerate degradation of images by possible artifacts. For example, breathing-related organ displacement causes high-frequency SWS changes, which are spuriously interpreted by  $\sigma$  as sharpness. Despite the inappropriateness of  $\sigma$  to reflect improvements in stiffness maps, the facts that MRE magnitude images are significantly improved (as correctly quantified by  $\sigma$ ) and that anatomical organ boundaries are more conspicuous in SWS maps after image registration (as revealed to the eye when looking at the SWS maps in Figures 3-6) suggest image registration to be a feasible way of reducing motion artifacts in multifrequency MRE.

In essence, we recommend free-breathing multifrequency MRE in conjunction with retrospective rigid-body image registration for abdominal tomoelastography, as it combines the shortest acquisition times with preserved sharpness of organ boundaries and tissue interfaces.

Our study has limitations. First, our displacement analysis was essentially 2D. Given that major breathing motion occurred along the craniocaudal axis,<sup>43</sup> which is covered by coronal view, our 2D in-plane motion correction was effective. However, through-plane motion occurring in transverse orientation needs to be addressed by rigid 3D image registration. Second, our navigator-based motion-correction technique uses single navigators in conjunction with subsequent full-slice block acquisition. For that reason, early slices acquired immediately after the navigators are more reliable than late slices due to the latency between navigator signal and slice acquisition. In our setup, liver motion was evaluated in the first slice, which was well addressed by GF-MRE. However, GF-MRE was less efficient in organs other than the liver, which were covered by images slices acquired at later time points. Although adaptation of slice positions is possible to focus on other organs, we do not recommend GF-MRE but rather FB-MRE combined with image registration. Third, as mentioned previously, Laplacian  $\Delta$  and variance  $\sigma$  are limited in assessing sharpness of stiffness (SWS) maps. A suitable parameter for the future assessment of detail resolution in MRE should quantify the sharpness of tissue boundaries rather than higher frequency features in SWS maps. Future research in MRE is warranted to identify such a measure of sharpness of elastograms. Ideally, such a measure should afford quantitative assessment of image quality in MRE and ultimately allow automated detection of reliable maps<sup>44</sup> and reduction of technical failures.<sup>45</sup> Finally, we focused here on SWS as a surrogate of stiffness but did not analyze viscosity-related parameters such as wave penetration,<sup>33</sup> damping ratio,<sup>46</sup> loss modulus,<sup>11</sup> and loss angle or fluidity.<sup>14</sup> However, we assume that our analysis of breathing

artifacts can also be applied to other mechanical parameters attainable by MRE.

In summary, we have introduced and compared different motion-artifact reduction strategies in multifrequency MRE with the aims of testing the susceptibility of MRE to breathing motion and proposing a time-efficient multifrequency MRE protocol that generates reliable stiffness maps. Our findings indicate that larger displacement amplitudes due to respiratory motion do not significantly affect averaged MRE values and that breathing motion can readily be corrected by image registration, which improves both the sharpness and detail resolution of MRE magnitude images and parameter maps. Consequently, the shortest free-breathing protocol is recommended for 3D multifrequency MRE of the abdomen and allows stiffness mapping without breathing commands in approximately 2 minutes.

#### ACKNOWLEDGMENTS

We gratefully acknowledge the support of the German Federal Ministry of Education and Research (LiSyM 031L0057) and the German Research Foundation (SFB1340 "Matrix in Vision" and GRK2260 BIOQIC). Open access funding enabled and organized by Projekt DEAL.

#### ORCID

Mehrgan Shahryari  <https://orcid.org/0000-0002-3981-1711>

Helge Herthum  <https://orcid.org/0000-0001-6494-0833>

Ledia Lilaj  <https://orcid.org/0000-0001-8222-0397>

Jürgen Braun  <https://orcid.org/0000-0001-5183-7546>

Ingolff Sack  <https://orcid.org/0000-0003-2460-1444>

#### REFERENCES

- Venkatesh SK, Yin M, Ehman RL. Magnetic resonance elastography of liver: Technique, analysis, and clinical applications. *J Magn Reson Imaging*. 2013;37:544-555.
- Venkatesh SK, Ehman RL. Magnetic resonance elastography of abdomen. *Abdom Imaging*. 2015;40:745-759.
- Garteiser P, Doblus S, Van Beers BE. Magnetic resonance elastography of liver and spleen: Methods and applications. *NMR Biomed*. 2018;31:e3891.
- Huwart L, Sempoux C, Salameh N, et al. Liver fibrosis: Noninvasive assessment with MR elastography versus aspartate aminotransferase-to-platelet ratio index. *Radiology*. 2007;245:458-466.
- Yin M, Talwalkar JA, Glaser KJ, et al. Assessment of hepatic fibrosis with magnetic resonance elastography. *Clin Gastroenterol Hepatol*. 2007;5:1207-1213.e1202.
- Guo J, Buening C, Schott E, et al. In vivo abdominal MR elastography for the assessment of portal hypertension before and after transjugular intrahepatic portosystemic shunt (TIPS) implantation. *Investigative Radiology*. 2015;50:347-351.
- Navin PJ, Gidener T, Allen AM, et al. The role of magnetic resonance elastography in the diagnosis of noncirrhotic portal hypertension. *Clin Gastroenterol Hepatol*. 2019;17:1542-1546.
- Martcorena Garcia SR, Fischer T, Durr M, et al. Multifrequency magnetic resonance elastography for the assessment of renal allograft function. *Invest Radiol*. 2016;51:591-595.
- Lang ST, Guo J, Bruns A, et al. Multiparametric quantitative MRI for the detection of IgA nephropathy using tomoelastography, DWI, and BOLD imaging. *Invest Radiol*. 2019;54:669-674.
- Martcorena Garcia SR, Grossmann M, Bruns A, et al. Tomoelastography paired with T2\* magnetic resonance imaging detects lupus nephritis with normal renal function. *Invest Radiol*. 2019;54:89-97.
- Garteiser P, Doblus S, Daire JL, et al. MR elastography of liver tumours: Value of viscoelastic properties for tumour characterisation. *Eur Radiol*. 2012;22:2169-2177.
- Shi Y, Gao F, Li Y, et al. Differentiation of benign and malignant solid pancreatic masses using magnetic resonance elastography with spin-echo echo planar imaging and three-dimensional inversion reconstruction: A prospective study. *Eur Radiol*. 2018;28:936-945.
- Gordic S, Ayache JB, Kennedy P, et al. Value of tumor stiffness measured with MR elastography for assessment of response of hepatocellular carcinoma to locoregional therapy. *Abdom Radiol (NY)*. 2017;42:1685-1694.
- Shahryari M, Tzschatzsch H, Guo J, et al. Tomoelastography distinguishes noninvasively between benign and malignant liver lesions. *Cancer Res*. 2019;79:5704-5710.
- Muthupillai R, Lomas DJ, Rossman PJ, Greenleaf JF, Manduca A, Ehman RL. Magnetic resonance elastography by direct visualization of propagating acoustic strain waves. *Science*. 1995;269:1854-1857.
- Hirsch S, Braun J, Sack I. *Magnetic Resonance Elastography: Physical Background and Medical Applications*. Weinheim, Germany: Wiley-VCH; 2017:456.
- Murphy IG, Graves MJ, Reid S, et al. Comparison of breath-hold, respiratory navigated and free-breathing MR elastography of the liver. *Magn Reson Imaging*. 2017;37:46-50.
- QIBA MR Elastography Biomarker Committee. Magnetic Resonance Elastography of the Liver, Quantitative Imaging Biomarkers Alliance. 2. Profile Stage: Consensus. QIBA, June 6, 2019. <http://qibawiki.rsna.org/index.php/Profiles>. Accessed January 4, 2020.
- Majeed W, Kalra P, Kolipaka A. Simultaneous multislice rapid magnetic resonance elastography of the liver. *NMR Biomed*. 2020;33:e4252.
- Ebersole C, Ahmad R, Rich AV, Potter LC, Dong H, Kolipaka A. A Bayesian method for accelerated magnetic resonance elastography of the liver. *Magn Reson Med*. 2018;80:1178-1188.
- Kennedy P, Wagner M, Castera L, et al. Quantitative elastography methods in liver disease: Current evidence and future directions. *Radiology*. 2018;286:738-763.
- Ipek-Ugay S, Tzschatzsch H, Braun J, Fischer T, Sack I. Physiologic reduction of hepatic venous blood flow by the Valsalva Maneuver decreases liver stiffness. *J Ultrasound Med*. 2017;36:1305-1311.
- Millonig G, Friedrich S, Adolf S, et al. Liver stiffness is directly influenced by central venous pressure. *J Hepatol*. 2010;52:206-210.
- Hudert CA, Tzschatzsch H, Rudolph B, et al. Tomoelastography for the evaluation of pediatric nonalcoholic fatty liver disease. *Invest Radiol*. 2019;54:198-203.
- Martcorena Garcia SR, Grossmann M, Lang ST, et al. Tomoelastography of the native kidney: Regional variation and physiological effects on in vivo renal stiffness. *Magn Reson Med*. 2018;79:2126-2134.
- Hirsch S, Guo J, Reiter R, et al. MR elastography of the liver and the spleen using a piezoelectric driver, single-shot wave-field

- acquisition, and multifrequency dual parameter reconstruction. *Magn Reson Med.* 2014;71:267-277.
27. Asbach P, Klatt D, Schlosser B, et al. Viscoelasticity-based staging of hepatic fibrosis with multifrequency MR elastography. *Radiology.* 2010;257:80-86.
  28. Etchell E, Juge L, Hatt A, Sinkus R, Bilston LE. Liver stiffness values are lower in pediatric subjects than in adults and increase with age: A multifrequency MR elastography study. *Radiology.* 2017;283:222-230.
  29. Dittmann F, Reiter R, Guo J, et al. Tomoelastography of the prostate using multifrequency MR elastography and externally placed pressurized-air drivers. *Magn Reson Med.* 2018;79:1325-1333.
  30. Henningson M, Botnar RM. Advanced respiratory motion compensation for coronary MR angiography. *Sensors (Basel).* 2013;13:6882-6899.
  31. Klein S, Staring M, Murphy K, Viergever MA, Pluim JP. elastix: A toolbox for intensity-based medical image registration. *IEEE Trans Med Imaging.* 2010;29:196-205.
  32. Mattes D, Haynor DR, Vesselle H, Lewellen TK, Eubank W. PET-CT image registration in the chest using free-form deformations. *IEEE Trans Med Imaging.* 2003;22:120-128.
  33. Tzschätzsch H, Guo J, Dittmann F, et al. Tomoelastography by multifrequency wave number recovery from time-harmonic propagating shear waves. *Med Image Anal.* 2016;30:1-10.
  34. Meyer T, Tzschätzsch H, Braun J, Kalra P, Kolipaka A, Sack I. Online platform for extendable server-based processing of magnetic resonance elastography data. In: Proceedings of the 27th Annual Meeting of ISMRM, Montreal, Canada, 2019. Abstract. 3966.
  35. Reiter R, Tzschätzsch H, Schwahofer F, et al. Diagnostic performance of tomoelastography of the liver and spleen for staging hepatic fibrosis. *Eur Radiol.* 2020;30:1719-1729.
  36. Pech-Pacheco JL, Cristobal G, Chamorro-Martinez J, Fernandez-Valdivia J. Diatom autofocusing in brightfield microscopy: a comparative study. In: Proceedings of the 15th International Conference on Pattern Recognition, Barcelona, Spain, 2000. pp 314-317.
  37. Gandhi D, Kalra P, Raterman B, Mo X, Dong H, Kolipaka A. Magnetic resonance elastography of kidneys: SE-EPI MRE reproducibility and its comparison to GRE MRE. *NMR Biomed.* 2019;32:e4141.
  38. Gandhi D, Kalra P, Raterman B, Mo X, Dong H, Kolipaka A. Magnetic resonance elastography-derived stiffness of the kidneys and its correlation with water perfusion. *NMR Biomed.* 2020;33:e4237.
  39. Kolipaka A, Schroeder S, Mo X, Shah Z, Hart PA, Conwell DL. Magnetic resonance elastography of the pancreas: Measurement reproducibility and relationship with age. *Magn Reson Imaging.* 2017;42:1-7.
  40. Dittmann F, Tzschätzsch H, Hirsch S, et al. Tomoelastography of the abdomen: Tissue mechanical properties of the liver, spleen, kidney, and pancreas from single MR elastography scans at different hydration states. *Magn Reson Med.* 2017;78:976-983.
  41. Glaser KJ, Chen J, Ehman RL. Fast 2D hepatic MR elastography for free-breathing and short breath hold applications. In: Proceedings of the 24th Annual Meeting of ISMRM, Singapore, 2015. Abstract 2522.
  42. Li J, Dzyubak B, Glaser KJ, et al. Repeatability and clinical performance of non-gated, free-breathing, MR elastography (MRE) of the liver. In: Proceedings of the 27th Annual Meeting of ISMRM, Montreal, Canada, 2019. Abstract 3972.
  43. Brandner ED, Wu A, Chen H, et al. Abdominal organ motion measured using 4D CT. *Int J Radiat Oncol Biol Phys.* 2006;65:554-560.
  44. Dzyubak B, Venkatesh SK, Manduca A, Glaser KJ, Ehman RL. Automated liver elasticity calculation for MR elastography. *J Magn Reson Imaging.* 2016;43:1055-1063.
  45. Kim DW, Kim SY, Yoon HM, Kim KW, Byun JH. Comparison of technical failure of MR elastography for measuring liver stiffness between gradient-recalled echo and spin-echo echo-planar imaging: A systematic review and meta-analysis. *J Magn Reson Imaging.* 2020;51:1086-1102.
  46. Yin M, Glaser KJ, Manduca A, et al. Distinguishing between hepatic inflammation and fibrosis with MR elastography. *Radiology.* 2017;284:694-705.

## SUPPORTING INFORMATION

Additional supporting information may be found online in the Supporting Information section.

**FIGURE S1** Representative Laplacian images of magnetic resonance elastography (MRE) magnitude ( $\Delta M$ ) and shear wave speed ( $\Delta SWS$ ) of the liver, kidneys, spleen, and pancreas of a healthy subject obtained with different MRE protocols. Shown are images with and without correction for breathing artifacts by 2D in-plane rigid registration. Green contours show the presegmented region of interest used for image registration. Arrows indicate blurred features (open arrows) and improved anatomical representations (yellow arrows) in each organ. Note that improved feature sharpness is better seen in  $\Delta M$  than in  $\Delta SWS$ . The  $\Delta SWS$  maps reveal high-frequency patterns (eg, red arrows) that do not change with correction and therefore hinder quantification of sharpness by  $\sigma$ . Abbreviations: BH-MRE, breath-hold MRE; FB-MRE, ungated free-breathing MRE; G-MRE, gated free-breathing MRE; GF-MRE, gated, slice-following, free-breathing MRE

**VIDEO S1** Animated wave images acquired in a volunteer in a coronal view through the liver, pancreas, spleen, and kidneys for all excitation frequencies (30-60 Hz) and deflection components (left-right, head-feet, through-plane) after unwrapping and temporal Fourier transformation, uncorrected and corrected for motion using image registration. Blue to yellow colors scale deflections with amplitudes of 30 and 20  $\mu m$  for 30 and 40 Hz, respectively, and 15  $\mu m$  for 50 and 60 Hz. Mean magnitude images (M) in gray scale of the respective mechanical frequency are shown for anatomical orientation and display of organ-specific regions of interest (green lines). In the shown cases, image registration for motion correction was applied to the spleen

**How to cite this article:** Shahryari M, Meyer T, Warmuth C, et al. Reduction of breathing artifacts in multifrequency magnetic resonance elastography of the abdomen. *Magn Reson Med.* 2021;85:1962-1973. <https://doi.org/10.1002/mrm.28558>



**Publication 3: On the relationship between metabolic capacities and *in vivo* viscoelastic properties of the liver**

**Shahryari, M.**, Keller, S., Meierhofer, D., Wallach, I., Safraou, Y., Guo, J., Garcia, S. M., Braun, J., Makowski, M. R., Sack, I., & Berndt, N. (2023). On the relationship between metabolic capacities and *in vivo* viscoelastic properties of the liver. *Frontiers in Bioengineering and Biotechnology*, 10. <https://doi.org/10.3389/fbioe.2022.1042711>



## OPEN ACCESS

EDITED BY  
Salavat Aglyamov,  
University of Houston, United States

REVIEWED BY  
Meng Yin,  
Mayo Clinic, United States  
Mohsin Rahim,  
Vanderbilt University, United States

\*CORRESPONDENCE  
Nikolaus Berndt,  
✉ Nikolaus.berndt@charite.de

SPECIALTY SECTION  
This article was submitted to  
Biomechanics,  
a section of the journal  
Frontiers in Bioengineering and  
Biotechnology

RECEIVED 12 September 2022  
ACCEPTED 21 December 2022  
PUBLISHED 09 January 2023

CITATION  
Shahryari M, Keller S, Meierhofer D,  
Wallach I, Safraou Y, Guo J,  
Marticorena Garcia SR, Braun J,  
Makowski MR, Sack I and Berndt N (2023),  
On the relationship between metabolic  
capacities and *in vivo* viscoelastic  
properties of the liver.  
*Front. Bioeng. Biotechnol.* 10:1042711.  
doi: 10.3389/fbioe.2022.1042711

COPYRIGHT  
© 2023 Shahryari, Keller, Meierhofer,  
Wallach, Safraou, Guo, Marticorena Garcia,  
Braun, Makowski, Sack and Berndt. This is  
an open-access article distributed under  
the terms of the Creative Commons  
Attribution License (CC BY). The use,  
distribution or reproduction in other  
forums is permitted, provided the original  
author(s) and the copyright owner(s) are  
credited and that the original publication in  
this journal is cited, in accordance with  
accepted academic practice. No use,  
distribution or reproduction is permitted  
which does not comply with these terms.

# On the relationship between metabolic capacities and *in vivo* viscoelastic properties of the liver

Mehrgan Shahryari<sup>1</sup>, Sarah Keller<sup>1</sup>, David Meierhofer<sup>2</sup>,  
Iwona Wallach<sup>3</sup>, Yasmine Safraou<sup>1</sup>, Jing Guo<sup>1</sup>,  
Stephan R. Marticorena Garcia<sup>1</sup>, Jürgen Braun<sup>4</sup>,  
Marcus R. Makowski<sup>5</sup>, Ingolf Sack<sup>1</sup> and Nikolaus Berndt<sup>3\*</sup>

<sup>1</sup>Department of Radiology, Charité—Universitätsmedizin Berlin, Corporate Member of Freie Universität Berlin and Humboldt-Universität zu Berlin, Berlin, Germany, <sup>2</sup>Mass Spectrometry Facility, Max Planck Institute for Molecular Genetics, Berlin, Germany, <sup>3</sup>Institute of Computer-Assisted Cardiovascular Medicine, Charité—Universitätsmedizin Berlin, Corporate Member of Freie Universität Berlin and Humboldt-Universität zu Berlin, Berlin, Germany, <sup>4</sup>Institute of Medical Informatics, Charité—Universitätsmedizin Berlin, Corporate Member of Freie Universität Berlin and Humboldt-Universität zu Berlin, Berlin, Germany, <sup>5</sup>Department of Diagnostic and Interventional Radiology, Technical University of Munich, Faculty of Medicine, Munich, Germany

The liver is the central metabolic organ. It constantly adapts its metabolic capacity to current physiological requirements. However, the relationship between tissue structure and hepatic function is incompletely understood; this results in a lack of diagnostic markers in medical imaging that can provide information about the liver's metabolic capacity. Therefore, using normal rabbit livers, we combined magnetic resonance elastography (MRE) with proteomics-based kinetic modeling of central liver metabolism to investigate the potential role of MRE for predicting the liver's metabolic function *in vivo*. Nineteen New Zealand white rabbits were investigated by multifrequency MRE and positron emission tomography (PET). This yielded maps of shear wave speed (SWS), penetration rate (PR) and standardized uptake value (SUV). Proteomic analysis was performed after the scans. Hepatic metabolic functions were assessed on the basis of the HEPATOKIN1 model in combination with a model of hepatic lipid-droplet metabolism using liquid chromatography–mass spectrometry. Our results showed marked differences between individual livers in both metabolic functions and stiffness properties, though not in SUV. When livers were divided into 'stiff' and 'soft' subgroups (cutoff SWS = 1.6 m/s), stiff livers showed a lower capacity for triacylglycerol storage, while at the same time showing an increased capacity for gluconeogenesis and cholesterol synthesis. Furthermore, SWS was correlated with gluconeogenesis and PR with urea production and glutamine exchange. In conclusion, our study indicates a close relationship between the viscoelastic properties of the liver and metabolic function. This could be used in future studies to predict non-invasively the functional reserve capacity of the liver in patients.

## KEYWORDS

viscoelasticity, MRE, PET, stiffness, liver metabolism, proteomics, reserve capacity, hepatic function model

## 1 Introduction

The liver is the key metabolic organ of the human body. It has a wide range of metabolic functions including homeostatic regulation of numerous plasma metabolites (glucose, amino acids and lipoproteins), detoxification of endogenously formed metabolic end products (e.g., ammonia, urea), and storage of nutrients in the form of glycogen or triacylglycerol. It continuously adapts its metabolic capacities to the current physiological status of the individual. For example, after a carbohydrate-rich meal, the liver takes up a substantial amount of glucose from the plasma; this is then transiently converted into glycogen and triacylglycerol. Conversely, under fasting conditions the liver produces glucose by phosphorylation of glycogen and synthesis *de novo* from amino acids, lactate and glycerol to prevent a potentially life-threatening drop in plasma glucose below 55 mg/dl (Mathew et al., 2022). Metabolic alterations become permanent as a result of long-term life habits such as overnutrition, as in metabolic syndrome (MetS). MetS—with its hallmarks of obesity, insulin resistance and dyslipidaemia (Bussler et al., 2017)—is an epidemic disease that is often triggered by childhood overnutrition. Non-alcoholic fatty liver disease (NAFLD) is recognized as the hepatic manifestation of MetS (Lonardo et al., 2015) and can progress silently into liver fibrosis and cirrhosis without apparent clinical symptoms (Sivell, 2019). Today, non-alcoholic steatohepatitis is the most common etiology among waiting-list candidates for liver transplantation (Wong and Singal, 2020). Nevertheless, early diagnosis and differentiation of liver diseases remains a major challenge. While cirrhosis and liver tumors represent the end-stage of liver pathology, with life-threatening complications and clear clinical manifestation, most patients with NAFLD have a stable and relatively benign fatty liver for a long time (Caldwell and Argo, 2010).

Evaluation of liver function is a diagnostic challenge because there are only few techniques that can directly quantify metabolic functions *in vivo*. Quantitative liver function test, which use specific metabolites, such as indocyanine green clearance test or methacetin breath-test are complex and costly, and they entail considerable discomfort for the subject (Lalazar et al., 2008; Seyama and Kokudo, 2009). Furthermore, they assess only very specific pathways under very restricted conditions and cannot be used for a general evaluation of metabolic capacities (Vos et al., 2014; De Gasperi et al., 2016; Gorowska-Kowolik et al., 2017). New computational methods such as proteomics-based evaluation of metabolic liver function by large-scale kinetic modelling allows the assessment of metabolic capacities under a wide range of physiological and pathological conditions (Berndt et al., 2018a; Berndt et al., 2019; Berndt et al., 2020; Kespohl et al., 2020; Berndt et al., 2021a; Berndt et al., 2021b). However, these require biopsies, which are limited in follow-up examinations owing to pain, risk of bleeding and sampling errors (Ratziu et al., 2005; Boyd et al., 2020). Despite advances in quantitative medical imaging, there is still no reliable non-invasive imaging marker that can detect metabolic changes occurring in seemingly healthy livers during the 'silent progression' phase of NAFLD (Chalasani et al., 2018). Positron emission tomography (PET) is a versatile technique for the assessment of glucose metabolism in lesions or neurodegenerative diseases, where it can be used to investigate changes in various neurotransmitter systems, neuroinflammation, and protein aggregates that characterize the disease. However, PET scans are expensive, they result in exposure of the patient to ionizing

radiation and they address only specific metabolic pathways that are not necessarily fully suited for assessment of the liver's metabolic capacity. Ultrasound-based elastography and magnetic resonance elastography (MRE) have become successful in addressing structural changes such as like degree of fibrosis and steatosis, and they therefore have the potential to replace biopsy-based histological evaluation of structural alteration (Singh et al., 2015; Castera et al., 2019; Hudert et al., 2021; Qu et al., 2021; Selvaraj et al., 2021). Liver fibrosis increases liver stiffness through accumulation and cross-linking of matrix proteins (Huwart et al., 2008; Singh et al., 2015; Reiter et al., 2020). However, beyond fibrosis, the liver's biomechanical properties are also affected by non-fibrotic alterations such as prandial states (Yin et al., 2011; Jajamovich et al., 2014; Petzold et al., 2019; Obrzut et al., 2021), hydration (Ipek-Ugay et al., 2016; Dittmann et al., 2017), blood perfusion (Ipek-Ugay et al., 2016; Meyer et al., 2022a), cell hypertrophy (Garczyńska et al., 2020), fat accumulation (Hudert et al., 2019) or inflammation (Qu et al., 2021; Selvaraj et al., 2021), making elastography unspecifically sensitive to a variety of pathophysiological processes that occur in the course of NAFLD. Only little is known about the correlation between liver biomechanical parameters and liver metabolism. In cancer patients, liver function has been correlated with stiffness measured by ultrasound-based elastography (Heucke et al., 2019) and with viscoelastic parameters measured by MRE (Lin et al., 2022). However, it remains unclear which specific metabolic function may influence viscoelastic parameters in the liver and whether apparently normal livers display a range of biomechanical properties that are correlated with the variability of metabolic functions.

Therefore, in this study we used a comprehensive kinetic model of central liver metabolism (Berndt et al., 2018a) to characterize metabolic states and capacities of healthy rabbit livers on the basis of proteomic data. We performed *in vivo* MRE in a clinical hybrid PET/MRI scanner to investigate the relationship between viscoelasticity and liver metabolism. In addition, we analyzed the *in vivo* glucose metabolism using <sup>18</sup>F-fluorodesoxyglucose (FDG)-based PET to test the sensitivity of this imaging marker toward small variations in liver metabolism in correlation with MRE.

## 2 Materials and methods

### 2.1 Animal model

This study and all procedures involving animals were approved by the local authority (Landesamt für Gesundheit und Soziales Berlin, Reg. No. 0178/17). The experimental protocols were performed in accordance with the regulations and guidelines of the Federation of Laboratory Animal Science Association (FELASA) as well as our institutional guidelines.

Nineteen female New Zealand white rabbits (Charles River Laboratories, Sulzfeld, Germany) at the age of 11–15 weeks with a mean weight  $3.22 \pm .27$  kg were used for this study. All rabbits were housed in a pathogen-free animal facility, in rooms with laminar flow, constant temperature and constant humidity. Food and water were provided *ad libitum*. However, the rabbits were fasted 2 h before the measurements and blood glucose (BG) level, as well as animal weight was measured prior to MRI scans (Table 1). Imaging was performed at the same daytime under deep-sedation of rabbits by subcutaneous injections of medetomidin hydrochlorid (Cepetor, 200 mg/kg body

**TABLE 1** Descriptive data of rabbits. Parameters with group mean values given as mean  $\pm$  standard deviation for all 19 rabbits, including weight, BG, SWS, PR, SUV. BG, blood glucose; SWS, shear wave speed; PR, penetration rate; SUV, standardized uptake value.

ID	Weight in kg	BG in mg/dl	SWS in m/s	PR in m/s	SUV
3	3.6	107	1.45 $\pm$ .11	1.04 $\pm$ .33	2.50 $\pm$ .21
1	2.6	178	1.65 $\pm$ .16	1.16 $\pm$ .26	2.26 $\pm$ .36
15	3.5	168	1.60 $\pm$ .15	.99 $\pm$ .31	3.06 $\pm$ .28
4	3.0	139	1.51 $\pm$ .14	.96 $\pm$ .23	2.34 $\pm$ .37
9	3.5	154	1.70 $\pm$ .17	1.01 $\pm$ .35	3.00 $\pm$ .36
16	3.3	187	1.56 $\pm$ .13	.87 $\pm$ .24	2.88 $\pm$ .21
4	3.4	140	1.39 $\pm$ .10	.84 $\pm$ .22	2.73 $\pm$ .18
5	3.4	158	1.41 $\pm$ .13	.88 $\pm$ .28	2.74 $\pm$ .16
2	3.1	184	1.70 $\pm$ .12	1.21 $\pm$ .39	2.82 $\pm$ .10
22	3.2	132	1.65 $\pm$ .14	1.06 $\pm$ .29	2.89 $\pm$ .18
13	3.6	191	1.64 $\pm$ .16	1.03 $\pm$ .28	
7	3.2	150	1.69 $\pm$ .12	1.03 $\pm$ .30	
6	3.5	135	1.57 $\pm$ .15	1.09 $\pm$ .44	
14	2.9	159	1.56 $\pm$ .11	1.03 $\pm$ .38	
12	3.1	123	1.64 $\pm$ .12	1.02 $\pm$ .29	
8	2.9	144	1.55 $\pm$ .16	.83 $\pm$ .29	
18	3.2		1.68 $\pm$ .11	.99 $\pm$ .35	
17	3.2		1.71 $\pm$ .16	1.00 $\pm$ .44	
19	3.2		1.51 $\pm$ .14	.80 $\pm$ .18	
Mean	3.23 $\pm$ .26	153.06 $\pm$ 24.1	1.59 $\pm$ .1	.99 $\pm$ .11	2.72 $\pm$ .27

weight) and Ketamin (Anesketin, 300 mg/kg body weight). Immediately after experimental imaging, euthanasia was performed by intravenous injection of pentobarbital sodium (Narcoren, 300 mg/kg body weight) and liver explantation was conducted. Tissues were dissected and snap frozen in liquid nitrogen for further proteomics analysis.

## 2.2 Imaging

### 2.2.1 MRI

All experiments were performed on a clinical 3-Tesla hybrid PET/MR scanner (Magnetom Biograph mMR, Siemens Healthineers, Erlangen, Germany) with a 20-channel head coil. Rabbits were positioned head first in prone position. For anatomic orientation, a transversal T1-weighted fat-saturated Dixon sequence (repetition time [TR] 4.76, echo time [TE] 1.49 ms, matrix 512  $\times$  512 mm, voxel size .5  $\times$  .5  $\times$  2.0 mm<sup>3</sup> and coverage of the complete liver) was performed in the abdominal region of the rabbits before MRE and PET scans.

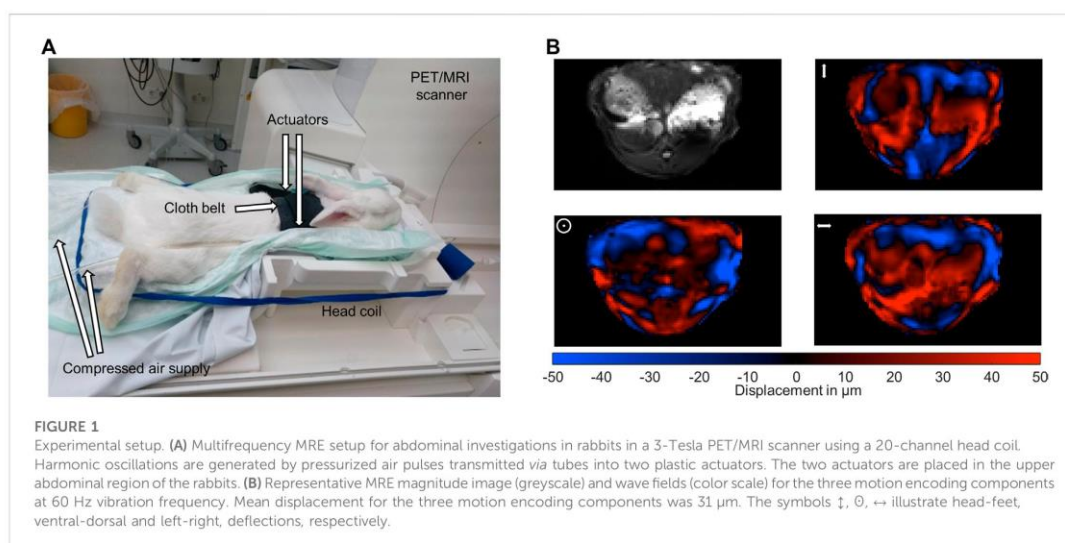
### 2.2.2 Multifrequency MRE

The used multifrequency MRE setup was similar to previous *in vivo* studies in patients with driver fixation adapted to rabbits (Shahryari et al., 2019; Shahryari et al., 2021). 8 phase offsets equally distributed over full vibration cycle of 40 Hz, 50 Hz, 60 Hz, 70 Hz and 80 Hz mechanical

vibrations were recorded for all three Cartesian-motion field directions in a transversal plane using a single-shot spin-echo echo-planar-imaging (EPI) sequence (Tzschätzsch et al., 2016; Dittmann et al., 2017). Oscillations were induced by two pressurized air drivers attached onto the upper abdominal region of the rabbits. The drivers were powered by air pulses of .2 bar maximum amplitude. A cloth belt around the abdomen was used to improve the contact of the drivers to the rabbits and the efficiency of shear wave excitation. Vibrations were started 2 s prior to image acquisition to ensure a steady-state flux of harmonic shear wave energy. Imaging parameters were: TE 40 ms, TR 1000 ms, matrix 104  $\times$  60, voxel size 1.55  $\times$  1.55  $\times$  5 mm<sup>3</sup>, 6 contiguous slices in a transversal view, 4 averages, parallel imaging with GRAPPA-factor 2, motion encoding gradient (MEG) frequency 78.61 Hz for all vibration frequencies, MEG amplitude 42 mT/m with first order moment nulling. Total MRE acquisition time was approximately 8 min. Cloth belt and actuators were removed prior to PET image acquisition. Figures 1A, B show the experimental MRE setup along with wave field components at 60 Hz vibration frequency.

### 2.2.3 PET

PET measurement was conducted in a subgroup of 10 rabbits injecting <sup>18</sup>F-FDG as radiotracer intravenously (mean 75.88  $\pm$  14.35 MBq, min 38.59 MBq, max 91.42 MBq). The PET scan was performed, covering the entire thorax and abdomen. PET image reconstruction was conducted by ordered-subset expectation maximization (OSEM) algorithm with 3 iterations and 21 subsets, 512  $\times$  512  $\times$  127 image matrix and 1  $\times$  1  $\times$



2 mm<sup>3</sup> voxel size. Ultrashort echo-time sequence (UTE) implemented by the vendor was used for attenuation and scatter correction (AC).

### 2.2.4 Image processing

MRE data were processed in MATLAB Release 2021a (The Mathworks Inc. Natick, MN, United States) using wavenumber-based inversion method (k-MDEV) (Tzschätzsch et al., 2016) publicly available at <https://bioqic-apps.charite.de> (Meyer et al., 2022b). A Butterworth low-pass filter of order 3 with a threshold of 250 m<sup>-1</sup> was used to suppress noise prior to image unwrapping (Herthum et al., 2022) while a spatial bandpass Butterworth filter of order 3 with thresholds of 15 m<sup>-1</sup> and 300 m<sup>-1</sup> was used for directional filtering (Herthum et al., 2022). Frequency-compound maps of shear wave speed (SWS in m/s) and penetration rate (PR in m/s) were computed as surrogates for tissue stiffness and inverse viscosity (Reiter et al., 2020). MRE magnitude images, SWS-, PR- and attenuation-corrected PET maps were further analyzed and used for manually drawing 3D regions of interest (ROIs) covering the liver. Mean liver SWS and PR values were calculated for each rabbit. Mean standardized uptake values (SUV) was calculated for 10 rabbits based on activity concentration (A(t)) in kBq/mL, body weight (W) in kg, injected dose (ID) in MBq, dose and decay correction factor d derived by the half-life of the radiotracer <sup>18</sup>F-FDG and the time delay between injection and start of the measurement:

$$SUV_{VOI} = \frac{A(t) \cdot W}{ID \cdot d}$$

## 2.3 Shotgun proteome profiling and data analysis

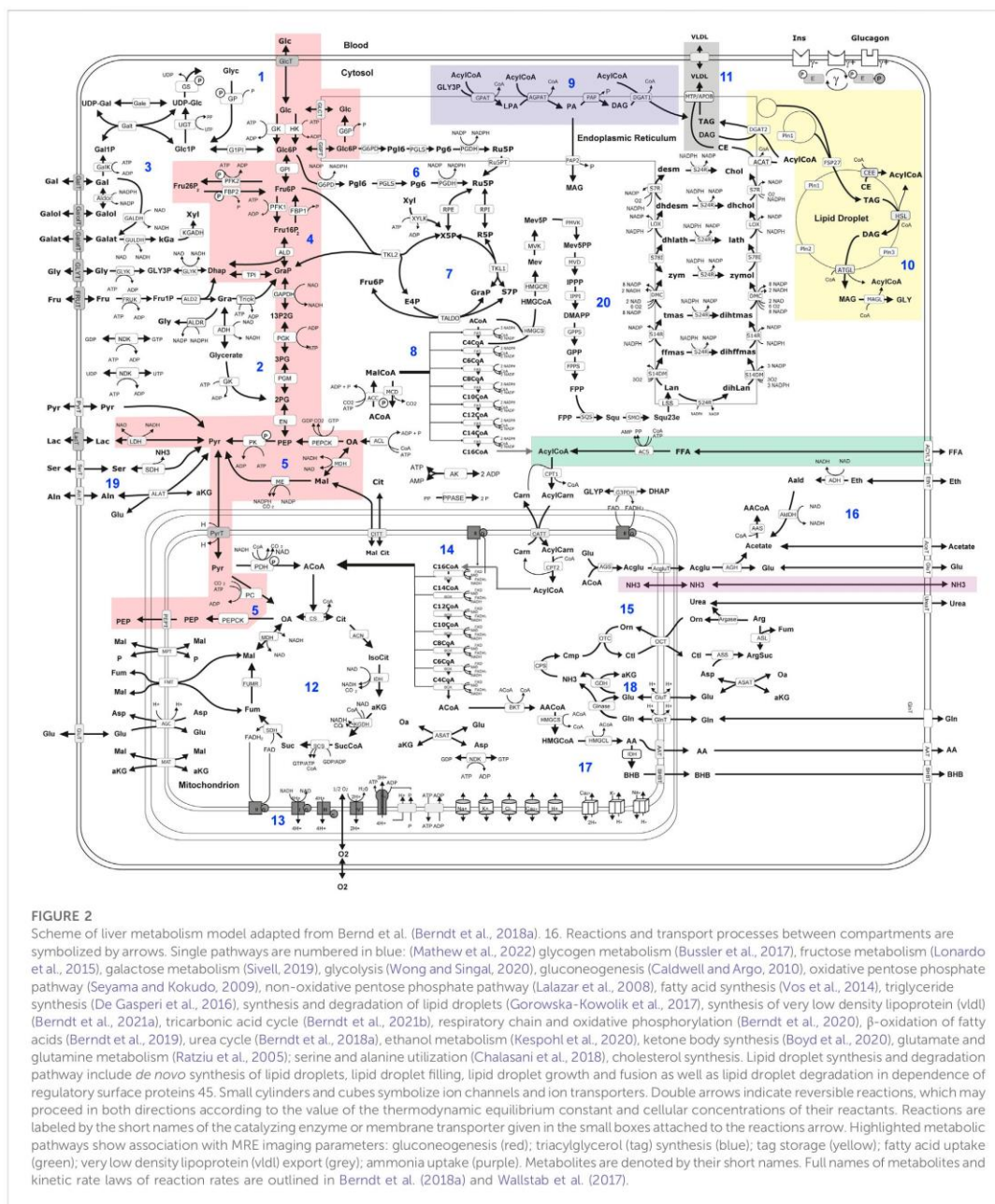
### 2.3.1 Proteomics sample preparation with label-free quantification (LFQ)

Between 11 and 100 mg of each liver tissue were homogenized under denaturing conditions with a FastPrep (two times for 60 s, 6.5 m × s<sup>-1</sup>) in 1 mL of a fresh buffer containing 3 M guanidinium chloride

(GdmCl), 10 mM Tris (2-carboxyethyl)phosphine, 20 mM chloroacetamide and 100 mM Tris-HCl pH 8.5. Lysates were boiled at 95°C for 10 min in a thermal shaker, followed by sonication for 10 min and centrifuged at 10,000 rcf for 5 min at 4°C. The supernatant was transferred into new protein low binding tubes (Eppendorf, Germany). 30  $\mu\text{g}$  protein per sample were diluted to 1 M GdmCl by adding 10% acetonitrile and 25 mM Tris, 8.5<sup>o</sup>pH, followed by a Lys C digestion (Roche, Basel, Switzerland; enzyme to protein ratio 1:50, MS-grade) at 37°C for 2 h. This was followed by another dilution to .5 M GdmCl and a tryptic digestion (Roche, 1:50) at 37°C, at 800 rpm, and overnight. Subsequently, peptides were desalted with C18 columns and reconstituted in 2% formic acid in water and further separated into five fractions by strong cation exchange chromatography (SCX, 3 M Purification, Meriden, CT). Eluates were first dried in a SpeedVac, then dissolved in 5% acetonitrile and 2% formic acid in water, briefly vortexed, and sonicated in a water bath for 30 s prior to injection to nano-Liquid chromatography–mass spectrometry (LC-MS).

### 2.3.2 LC-MS/MS instrument settings for shotgun proteome profiling and data analysis

LC-MS/MS was carried out by nanoflow reverse-phase liquid chromatography (Dionex Ultimate 3000, Thermo Scientific) coupled online to a Q-Exactive HF Orbitrap mass spectrometer (Thermo Scientific), as reported previously (Gielisch and Meierhofer, 2015). Briefly, the LC separation was performed using a PicoFrit analytical column (75  $\mu\text{m}$  ID × 50 cm long, 15  $\mu\text{m}$  Tip ID; New Objectives, Woburn, MA) in-house packed with 3  $\mu\text{m}$  C18 resin (Reprosil-AQ Pur, Dr. Maisch, Ammerbuch, Germany). Peptides were eluted using a gradient from 3.8% to 38% solvent B in solvent A over 120 min at a 266 nL per minute flow rate. Solvent A was .1% formic acid and solvent B was 79.9% acetonitrile, 20% H<sub>2</sub>O, and .1% formic acid. For the IP samples, a 1-h gradient was used. Nanoelectrospray was generated by applying 3.5 kV. A cycle of one full Fourier transformation scan mass spectrum (300–1750 m/z, resolution of



60,000 at  $m/z$  200, automatic gain control (AGC) target  $1 \times 10^6$  was followed by 12 data-dependent MS/MS scans (resolution of 30,000, AGC target  $5 \times 10^5$ ) with a normalized collision energy of 25 eV.

Raw MS data were processed with MaxQuant software (v 1.6.1.43) and searched against the *Oryctolagus cuniculus* (rabbit) proteome

database UniProtKB (UP000001811) with 21,178 entries, released in September 2019. Parameters of MaxQuant database searching were a false discovery rate (FDR) of .01 for proteins and peptides, cysteine carbamidomethylation was set as fixed modification, while N-terminal acetylation and methionine oxidation were set as variable

modifications. The mass spectrometry proteomics data have been deposited to the ProteomeXchange Consortium via the PRIDE (Perez-Riverol et al., 2022) partner repository with the dataset identifier PXD036659.

## 2.4 Assessment of metabolic capacities

Hepatic metabolic capacities were assessed using HEPATOKIN1 (Berndt et al., 2018a) in combination with a molecular-resolution model of hepatic lipid droplet metabolism (Wallstab et al., 2017). It comprises the major metabolic pathways of carbohydrate, lipid and amino-acid metabolism in hepatocytes (see Figure 2). Electrophysiological processes at the inner mitochondrial membrane describing the generation and utilization of the proton motive force were modelled by kinetic equations of the Goldman-Hodgkin-Katz type (Berndt et al., 2015). Hormone-dependent regulation of the liver metabolism by reversible enzyme phosphorylation was taken into account by a phenomenological transfer function (Bulik et al., 2016). Individual model instantiations were generated based on proteomic profiles as described in Berndt et al. (2019).

Physiological metabolic functions were defined as maximal fluxes obtained under a wide range of physiological conditions (3–12 mM plasma glucose), where plasma metabolite concentrations are not independent from each other. The interdependence between plasma glucose, plasma hormone and plasma fatty acid concentration was taken into account by using experimentally determined transfer functions (Bulik et al., 2016; Berndt et al., 2018a).

## 2.5 Statistical analysis

Statistical analysis and cluster analysis were done MATLAB Release 2021a (The MathWorks, Inc., Natick, MA, United States) with the bioinformatics toolbox. Group values were checked for normality based on quantile-quantile plots (qqPlots) with a 95% confidence interval margins. For normal distributed grouped values, unpaired two-sided students' *t*-test was used to calculate group differences. Otherwise, Wilcoxon signed-ranked test was used. Statistical analysis was performed using R version 4.0.2 (R-Foundation, Vienna, Austria). The level of significance was  $p < .05$ . Cluster analysis was performed using clustergram function. Row-wise normalization was used transforming values so that the mean of each metabolic function is 0 and the standard deviation is 1.

## 3 Results

### 3.1 Metabolic modelling

For the assessment of metabolic capabilities, we used personalized kinetic models to compute steady-state load characteristics describing the metabolic functions under a wide range of physiological conditions ranging from fasted state (low glucose, high fatty acids, low insulin and high glucagon) to a fed state (high glucose, low fatty acids, high insulin,

low glucagon). The remaining plasma nutrients (e.g., lactate, amino acids, ketone bodies, ammonia) were kept fixed at mean diurnal values (see Section 2.4 for more details).

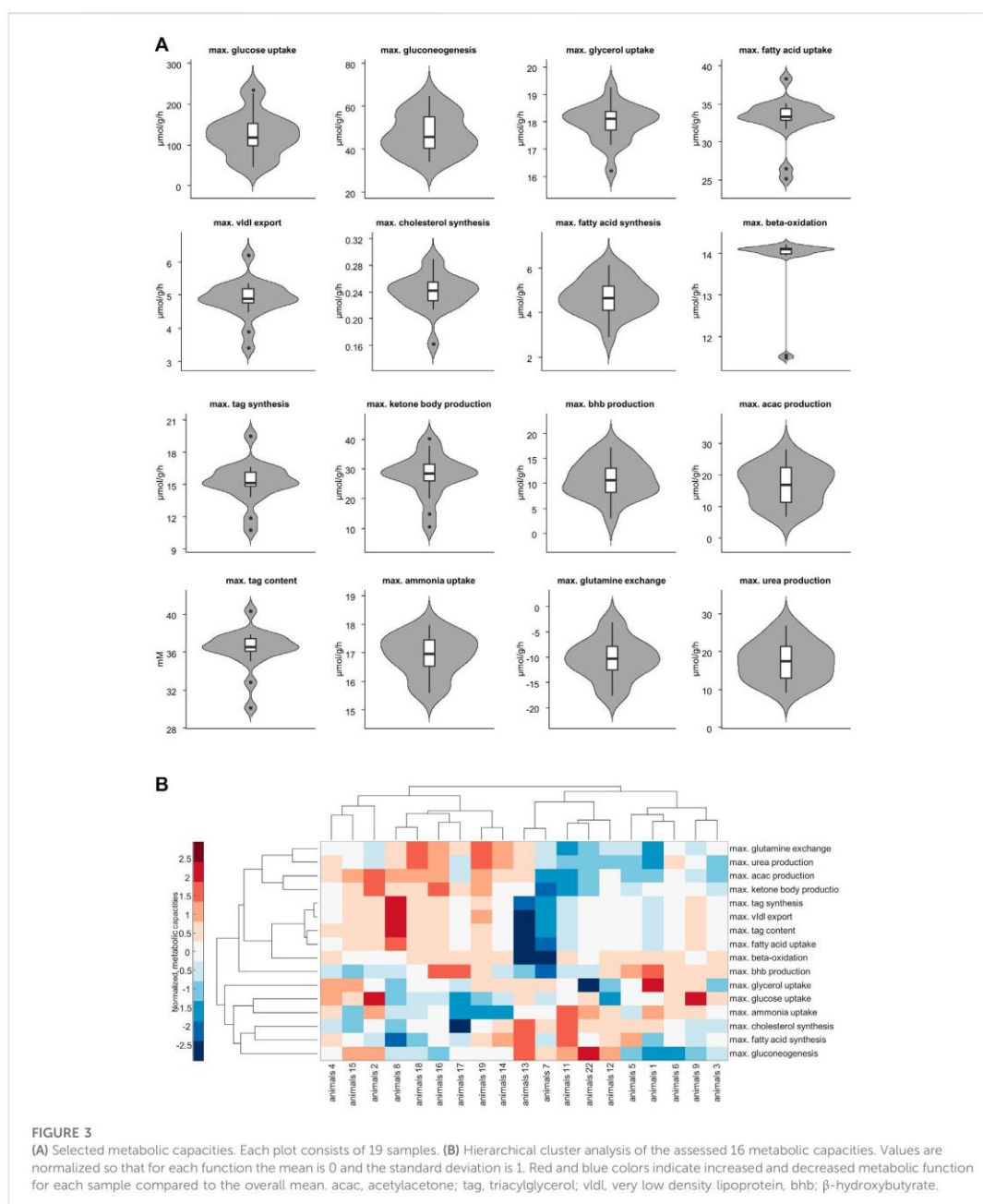
Figure 3A shows the panel of investigated metabolic capacities. Our analysis revealed strong metabolic differences among the individual livers. Individual livers differed in metabolic functions regarding carbohydrate metabolism, including glycolysis and gluconeogenesis, ketone body synthesis and fatty acid metabolism such as fatty acid uptake, lipoproteins production, triacylglycerol (tag) storage and fatty acid synthesis. We performed an unbiased cluster analysis to group the livers according to similarities in their metabolic functions. The cluster analysis depicted in Figure 3B shows that two main groups could be identified. Compared with the mean of all livers, metabolic cluster 2 is characterized by a less active metabolism of fatty acids, including reduced fatty acid uptake, reduced tag synthesis and storage as well as reduced ketone body synthesis. Instead, it has a higher synthetic capacity for glucose, fatty acids and cholesterol. Complementary, the metabolic cluster 1 has a more pronounced fatty acid metabolism and reduced biosynthetic activity than the mean of all livers.

We used the two metabolic clusters to define subgroups and investigated whether metabolic functions differ significantly between the two clusters. Cluster 1 consisted of 9 samples, whereas cluster 2 consisted of 10 samples. Figure 4 shows that the two groups differed significantly with respect to fatty acid uptake ( $34.7 \pm 1.54$  vs.  $31.51 \pm 3.1$   $\mu\text{mol/g/h}$ ,  $p = .001$ ), very low density lipoprotein (vldl) export ( $5.22 \pm 0.42$  vs.  $4.56 \pm .54$   $\mu\text{mol/g/h}$ ,  $p = .002$ ), cholesterol synthesis ( $.22 \pm 0.03$  vs.  $.25 \pm .02$   $\mu\text{mol/g/h}$ ,  $p = .01$ ), tag synthesis ( $16.32 \pm 1.35$  vs.  $14.15 \pm 1.67$   $\mu\text{mol/g/h}$ ,  $p = .001$ ), ketone body production ( $32.91 \pm 4.04$  vs.  $23.23 \pm 6.31$   $\mu\text{mol/g/h}$ ,  $p = .001$ ), acetylacetone (acac) production ( $21.95 \pm 3.6$  vs.  $12.53 \pm 4.28$ ,  $p < .001$   $\mu\text{mol/g/h}$ ), tag content ( $37.48 \pm 1.24$  vs.  $35.31 \pm 2.24$  mM,  $p = .01$ ), ammonia uptake ( $16.49 \pm .73$  vs.  $17.3 \pm .46$   $\mu\text{mol/g/h}$ ,  $p = .013$ ), glutamine exchange ( $-7.54 \pm 2.94$  vs.  $-12.98 \pm 3.12$   $\mu\text{mol/g/h}$ ,  $p = .001$ ), and urea production ( $20.96 \pm 3.93$  vs.  $14.26 \pm 3.88$   $\mu\text{mol/g/h}$ ,  $p = .002$ ).

We also checked whether the metabolic subgroups are characterized by significant differences in imaging markers. Figure 5 shows a representative slice of MRE and PET imaging parameters of rabbit's liver. SWS, PR and SUV values are given in Table 1. While no significant differences could be detected, PR shows a tendency to be lower in the livers with increased fatty acid metabolism and decreased biosynthetic capacities, hinting at a connection between non-invasive imaging markers and metabolic functionality.

Another approach to investigate the association of liver metabolism to liver mechanics was the clustering based on liver mechanics. Therefore, we divided the livers into two groups according to liver stiffness. Stiff livers were defined by SWS  $>1.6$  m/s ( $n = 10$ ), while soft livers were defined by a SWS  $<1.6$  m/s ( $n = 9$ ), corresponding to the median of all SWS values of the rabbits. Using this classification, we again compared metabolic functions and non-invasive imaging markers between these two groups to see, whether liver stiffness can be used to differentiate hepatic metabolic functionality.

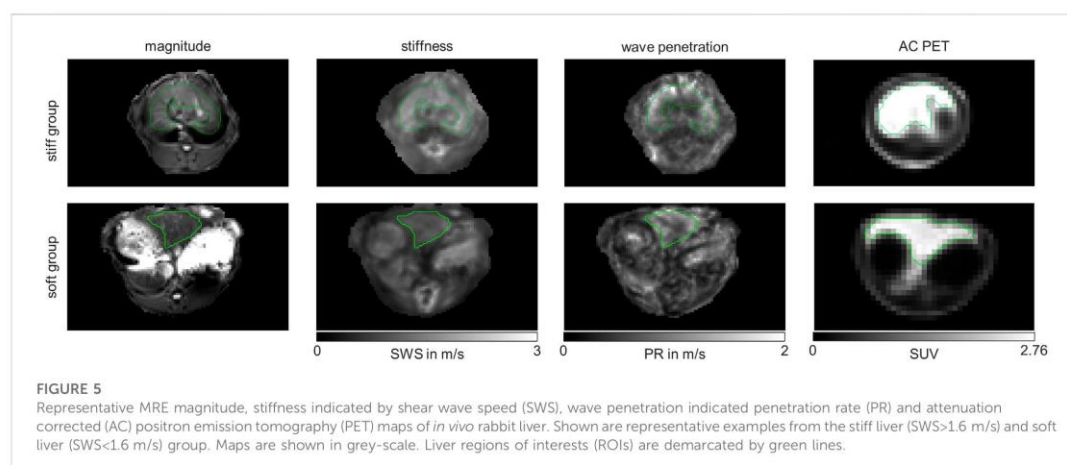
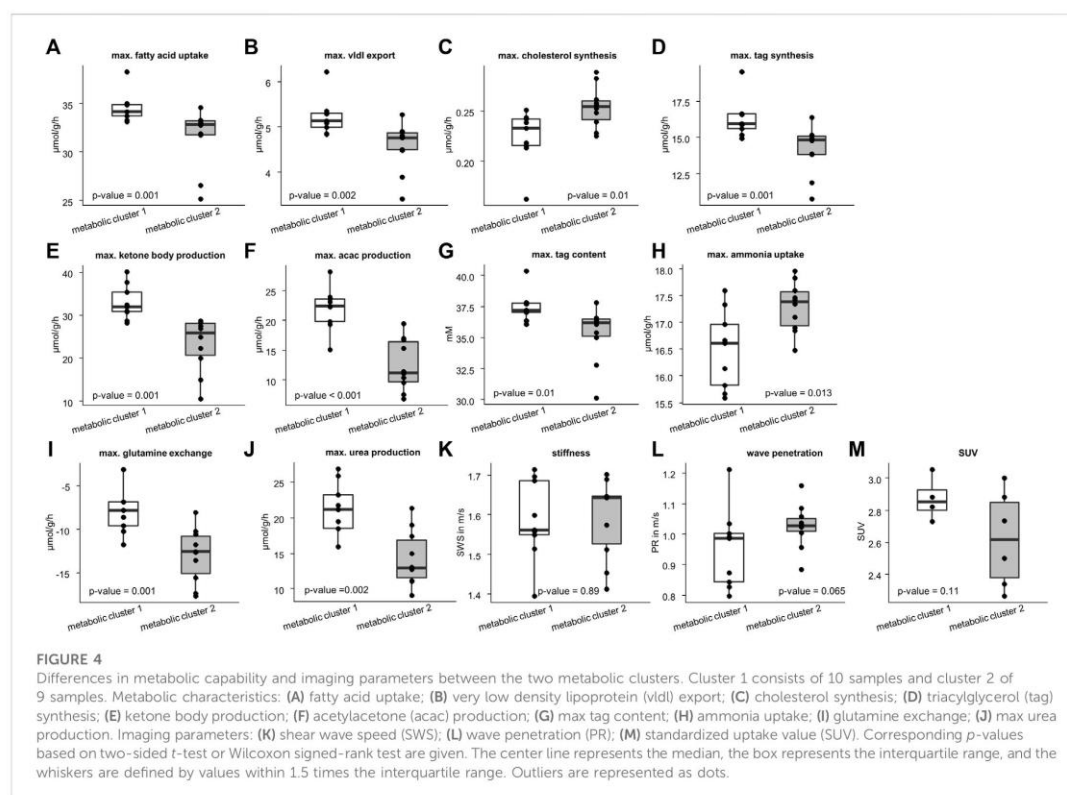
Figure 6 shows that stiff livers had a significantly higher capacity for gluconeogenesis ( $-52.81 \pm 9.48$  vs.  $-42.55 \pm 6.17$   $\mu\text{mol/g/h}$ ,  $p = .016$ ), cholesterol synthesis ( $.25 \pm .04$  vs.  $.23 \pm .01$   $\mu\text{mol/g/h}$ ,  $p = .035$ ),



and tag content ( $35.32 \pm 2.45$  vs.  $37.26 \pm 1.25$  mM,  $p = .043$ ). Besides increased SWS, the parameter PR was also significantly higher in stiff livers than in soft livers ( $1.06 \pm .08$  vs.  $.93 \pm .1$  m/s,  $p = .02$ ) and a linear correlation between SWS and PR was observed ( $r = .59$ ,  $p = .008$ , Figure 7A).

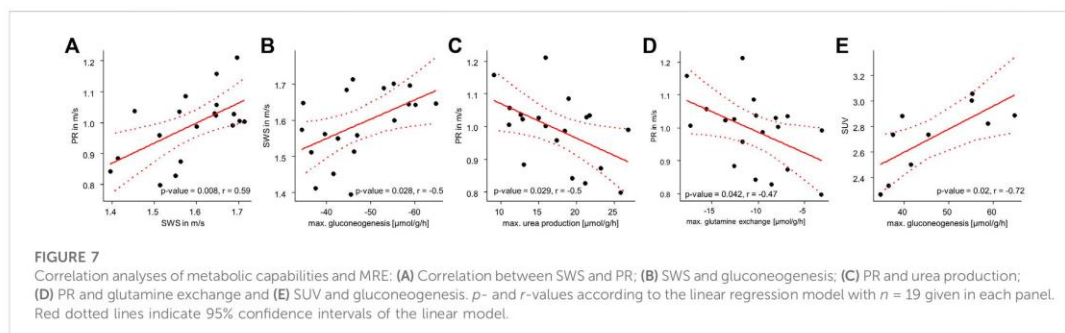
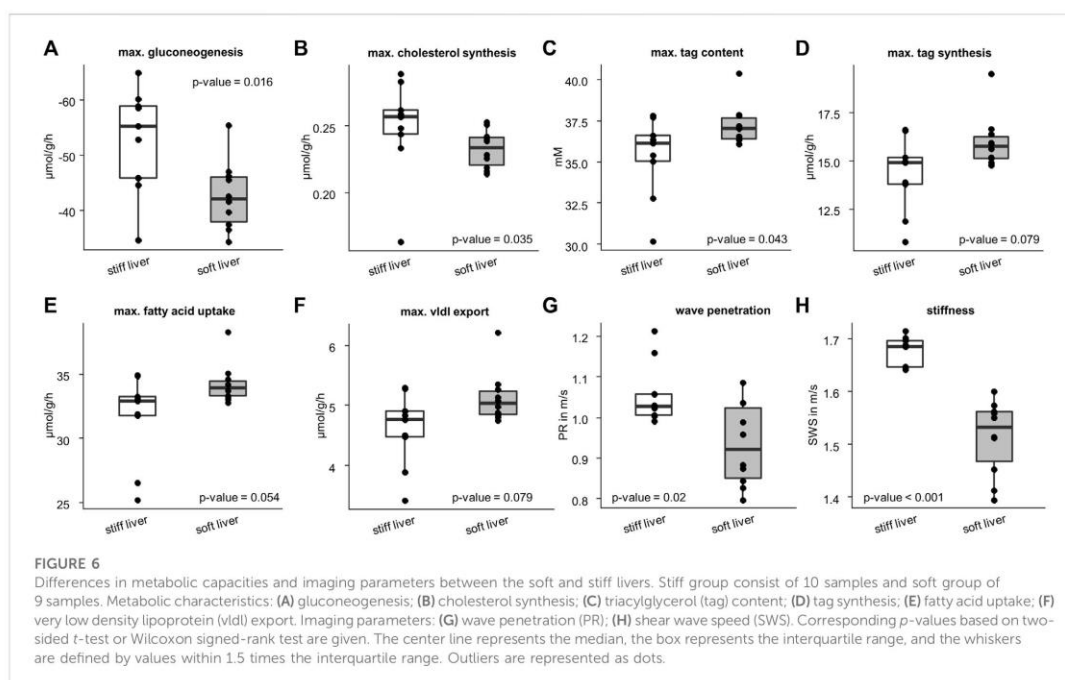
### 3.2 Correlations of metabolic functions with MRE parameters

So far, we have shown, that metabolic functionality can be used to define metabolic subclasses in healthy livers and that these subclasses



can be detected by MRE based on liver viscosity. Vice versa we showed, that differentiating between stiff and soft livers allows classification of metabolic functionality. While subgroups enable the metabolic and biomechanical classification of livers, the question remains, whether individual metabolic functions can possibly be assessed by MRE. To

answer this question, we correlated individual metabolic liver functions with liver SWS and PR. SWS was significantly correlated with gluconeogenesis ( $r = -.5, p = .028$ , Figure 7B), while PR was correlated with urea production ( $r = -.5, p = .029$ , Figure 7C) and glutamine exchange ( $r = -.47, p = .042$ , Figure 7D). Interestingly, SUV



was correlated with gluconeogenesis ( $r = -0.72$ ,  $p = .02$ , Figure 7E), although not with glucose uptake.

## 4 Discussion

In this study, we demonstrated for the first time the feasibility of MRE in small animals using a clinical hybrid PET/MRI scanner. This PET/MRE system allowed us to generate maps related to stiffness and viscosity, as well as  $^{18}\text{F}$ -FDG uptake simultaneously; this allowed the first-ever investigation of the correlation between metabolism and viscoelasticity. Furthermore, we harvested liver tissue after euthanasia for

modeling liver metabolism of key metabolic markers for each individual rabbit.

The first important finding of our study was a surprisingly large heterogeneity in metabolic capacities among the healthy rabbit livers. Although all the rabbits were genetically identical and received the same nutrition, there were clear differences in fatty-acid metabolism, ketone-body synthesis and urea metabolism. While this is the first time we studied rabbit liver, variability in metabolic capacities were also shown in healthy mouse liver as well as human pediatric patients with moderate liver fibrosis (Berndt et al., 2021b; Berndt et al., 2022).

Direct evaluation of metabolic fluxes *in vivo* remains an expensive experimental challenge. Estimation of *in vivo* fluxes by measuring time series of labelled nutrients (Hasenour et al., 2015; Hui et al., 2020;

Rahim et al., 2021) is restricted to the analysis of very few pathways and gives the average flux rate during the time of measurement, but it is not suited for monitoring metabolic fluxes over a longer period of varying physical activity and plasma profiles of nutrients. Furthermore, metabolic flux rates depend not only on the availability of the substrate of interest but also on the overall plasma nutrient and hormone composition making it hard to assess all the information necessary to define the observed metabolic state.

In our approach we assessed metabolic capacities rather than actual fluxes. We evaluated 16 different metabolic capacities under a wide range of physiological conditions ranging from fasted state (low glucose, high fatty acids, low insulin, and high glucagon) to a fed state (high glucose, low fatty acids, high insulin, low glucagon). The remaining plasma nutrients (e.g., lactate, amino acids, ketone bodies, ammonia) were kept fixed at mean diurnal values (see Berndt et al., 2018a for more details).

In this study, we circumvented these problems by evaluation of metabolic capacities based on protein abundances under pre-described conditions rather than actual fluxes. This allowed us to robustly assess the metabolic differences which are not prone to short-term variations due to varying metabolic conditions because metabolic enzymes are stable for hours (see Berndt and Holzthutter, 2018 and references within). It is important to note that the metabolic capacities assessed in this way do not themselves form a consistent metabolic state, since conditions under which they are realized are not the same. For example, maximal gluconeogenesis is reached under low glucose conditions, while maximal glycolysis is reached under high glucose conditions.

The differences in metabolic capacities allowed a rough classification of the livers into two clusters. Cluster 2 was characterized by reduced fatty-acid metabolism and increased biosynthetic capacity, while cluster 1 displayed the opposite metabolic characteristics. While statistically not significant, probably owing to the low sample number, a similar trend was seen in  $^{18}\text{F}$ -FDG uptake as measured by PET ( $p = .11$ ). Importantly, the two metabolic clusters showed a clear distinction in mechanical properties: cluster 1 was more viscous (lower PR) than cluster 2, albeit again without statistical significance ( $p = .065$ ).

Alternatively, classification of livers according to their biomechanical properties may provide an indication of metabolic functions. Therefore, we classified livers according to their mechanical properties. The clustering in two groups based on the cutoff value of 1.6 m/s for the liver SWS agrees with SWS values of a healthy human liver, i.e., approximately 1.4 m/s for 30–60 Hz when considering the dispersion of SWS in the liver as analyzed by Morr et al. (2022). This biomechanical classification revealed that stiff livers differ significantly from soft livers in their metabolic capacities. Specifically, stiff livers have a markedly reduced tag content, while showing increased capacity for gluconeogenesis and cholesterol synthesis. This observation agrees with recent findings in adipose tissue, where a decrease in stiffness was associated with excessive accumulation of lipids (Abuhattum et al., 2022). In future studies, it would be interesting to investigate whether increased gluconeogenesis activity associated with increased liver stiffness is an early marker of pathologically altered metabolism toward NAFLD.

We also studied which liver functions are directly associated with mechanical parameters. Figure 7 shows that PR is

significantly correlated with hepatic capacities of urea production and glutamine exchange. It is noteworthy that these metabolic capacities are not independent of one another, as ammonia detoxification can take place either by urea production or by glutamine synthesis.

One may speculate whether the observed correlations indicate a causal relationship between liver biomechanics and metabolic function. However, it is important to note that short-term physiological changes such as prandial state or perfusion rate induce acute changes in the liver's mechanical properties within seconds or minutes (Yin et al., 2011; Jajamovich et al., 2014; Dittmann et al., 2017; Manduca et al., 2021; Obrzut et al., 2021). In contrast, alterations in metabolic capacities due to variable protein abundance represent long-term adaptations taking place over hours or days (Berndt and Holzthutter, 2018). To reduce the confounding influence of physiological fluctuations on the mechanical properties of the liver, rabbits were fasted before the measurements. Sedation of rabbits reduced heart rate and breathing frequency while physiological short-term effects should have averaged out during the 8 min MRE examination time. Overall, the coefficient of variation of liver stiffness was 6% which is lower than in other MRE studies in healthy rabbit livers (14%–42%, [Zou et al., 2016; Zou et al., 2020; Zou et al., 2022]), suggesting a minor effect of physiological fluctuations on the measured mechanical properties.

Long-term architectural changes related to metabolism are conceivable when one considers ultrastructural liver properties such as extracellular collagen deposition or cellular fat accumulation. As discussed earlier, these structural changes directly affect mechanical properties but could also be associated with metabolic capacities (Sasso et al., 2016; Hudert et al., 2019). For example, excessive storage of tag might indicate an increased capacity for fatty-acid uptake and concomitant production of lipoproteins from these fatty acids. Collagen deposition and liver fibrosis, on the other hand, might alter substrate availability by alterations in hepatic blood flow and perfusion pressure, and thereby alter the capacities of glucose metabolism that respond directly to glucose availability (Berndt et al., 2018b). Hence, a close interaction between liver structure and metabolism would result in a correlation between viscoelastic properties and clusters of metabolic markers, as indeed observed in this study.

It should be emphasized that our results were obtained from healthy rabbit livers. We anticipate larger effects in livers with diseases such as NAFLD, and would expect such diseases to be readily detectable by *in vivo* MRE. For example, PR was shown by MRE to correlate negatively with the degree of hepatic steatosis in children with NAFLD at the same time that liver stiffness increased (Hudert et al., 2019). This is consistent with our analysis, in which stiffer livers were associated with reduced fatty-acid metabolism and increased biosynthetic capacity. Hence, the results of our study may explain findings in the literature, and they put MRE forward as a potentially sensitive tool for further studies on the relationship between liver function and viscoelastic properties.

Although encouraging, our study has limitations. First, only a small portion of the liver was used for proteomic analysis, whereas the MRE investigation covered most of the liver. Regional heterogeneity or different fractions of portal and central liver regions could affect proteomics-based metabolic capacities (Berndt et al., 2021b). Because healthy livers were used, we

assume no regional heterogeneity. Secondly, MRE measurements were performed under free breathing, which could have led to respiratory artifacts. However, the rabbits in our study were under deep sedation to minimize any respiration-induced distortions. Furthermore, in earlier work we showed that MRE performed under free breathing yields values similar to those obtained by MRE under breath hold (Shahryari et al., 2021). Thirdly, this pilot study included only 19 healthy rabbits. Future studies with more animals and disease models such as NASH are needed to further investigate the association of liver mechanical parameters with metabolism. Furthermore, PET measurements were performed only in a subset of rabbits for cost reasons. Therefore, metabolic cluster group 1 consists of only four data points, which does not allow statistical conclusions.

In summary, this study has revealed the relationship between liver metabolism analyzed by proteomics-based modeling and viscoelastic parameters measured with MRE *in vivo*. We demonstrate for the first time the feasibility of MRE in small animals using a clinical hybrid PET/MRI scanner. A surprisingly large heterogeneity of metabolic capacities was found in healthy rabbit livers, manifested by marked differences in carbohydrate metabolism, ketone body synthesis and fatty-acid metabolism. Biomechanical classification revealed that stiff livers are distinctly different from soft livers in that they have a lower capacity for triacylglycerol storage, while at the same time showing an increased capacity for gluconeogenesis and cholesterol synthesis. The sensitivity of MRE parameters to key metabolic functions in the liver suggests that MRE holds promise as a potentially useful noninvasive method for the assessment of liver function capacity in the future.

## Data availability statement

The mass spectrometry proteomics dataset presented in this study can be found in an online repository. The name of the repository and accession number can be found below: <https://www.ebi.ac.uk/pride/archive/>, PXD036659. The raw imaging dataset presented in this study will be made available by the authors upon reasonable request.

## References

- Abuhattum, S., Kotzbeck, P., Schlüßler, R., Harger, A., Ariza de Schellenberger, A., Kim, K., et al. (2022). Adipose cells and tissues soften with lipid accumulation while in diabetes adipose tissue stiffens. *Sci. Rep.* 12 (1), 10325. doi:10.1038/s41598-022-13324-9
- Berndt, N., and Holzthutter, H. G. (2018). Dynamic metabolic zonation of the hepatic glucose metabolism is accomplished by sinusoidal plasma gradients of nutrients and hormones. *Front. Physiol.* 9, 1786. doi:10.3389/fphys.2018.01786
- Berndt, N., Kann, O., and Holzthutter, H. G. (2015). Physiology-based kinetic modeling of neuronal energy metabolism unravels the molecular basis of NAD(P)H fluorescence transients. *J. Cereb. Blood Flow. Metab.* 35 (9), 1494–1506. doi:10.1038/jcbfm.2015.70
- Berndt, N., Bulik, S., Wallach, I., Wünsch, T., König, M., Stockmann, M., et al. (2018a). HEPATOKIN1 is a biochemistry-based model of liver metabolism for applications in medicine and pharmacology. *Nat. Commun.* 9 (1), 2386. doi:10.1038/s41467-018-04720-9
- Berndt, N., Horger, M. S., Bulik, S., and Holzthutter, H. G. (2018b). A multiscale modelling approach to assess the impact of metabolic zonation and microperfusion on the hepatic carbohydrate metabolism. *PLoS Comput. Biol.* 14 (2), e1006005. doi:10.1371/journal.pcbi.1006005
- Berndt, N., Eckstein, J., Heucke, N., Gajowski, R., Stockmann, M., Meierhofer, D., et al. (2019). Characterization of lipid and lipid droplet metabolism in human HCC. *Cells* 8 (5), 512. doi:10.3390/cells8050512
- Berndt, N., Egners, A., Mastrobuoni, G., Vvedenskaya, O., Fragoulis, A., Dugourd, A., et al. (2020). Kinetic modelling of quantitative proteome data predicts metabolic reprogramming of liver cancer. *Br. J. Cancer* 122 (2), 233–244. doi:10.1038/s41416-019-0659-3
- Berndt, N., Kolbe, E., Gajowski, R., Eckstein, J., Ott, F., Meierhofer, D., et al. (2021a). Functional consequences of metabolic zonation in murine livers: Insights from an old story. *Hepatology* 73 (2), 795–810. doi:10.1002/hep.31274
- Berndt, N., Eckstein, J., Heucke, N., Wuensch, T., Gajowski, R., Stockmann, M., et al. (2021b). Metabolic heterogeneity of human hepatocellular carcinoma: implications for personalized pharmacological treatment. *FEBS J.* 288 (7), 2332–2346. doi:10.1111/febs.15587
- Berndt, N., Hudert, C. A., Eckstein, J., Lodenkemper, C., Henning, S., Bufler, P., et al. (2022). Alterations of central liver metabolism of pediatric patients with non-alcoholic fatty liver disease. *Int. J. Mol. Sci.* 23 (19), 11072. doi:10.3390/ijms231911072
- Boyd, A., Cain, O., Chauhan, A., and Webb, G. J. (2020). Medical liver biopsy: Background, indications, procedure and histopathology. *Frontline Gastroenterol.* 11 (1), 40–47. doi:10.1136/flgastro-2018-101139
- Bulik, S., Holzthutter, H.-G., and Berndt, N. (2016). The relative importance of kinetic mechanisms and variable enzyme abundances for the regulation of hepatic glucose metabolism – insights from mathematical modeling. *BMC Biol.* 14 (1), 15. doi:10.1186/s12915-016-0237-6

## Ethics statement

The animal study was reviewed and approved by Landesamt für Gesundheit und Soziales Berlin (Reg. No. 0178/17).

## Author contributions

Conceptualization: MS, SK, MM, IS and NB; methodology: MS, SK, DM, IW, JB, NB and IS; software: MS, IW and NB; validation: MS, IW and NB; formal analysis: MS, IW and NB; investigation: MS, SK, DM, IW, NB and IS; resources: MS, SK, DM, IW, JB, MM, IS and NB; data curation: MS, IW, DM and NB; writing—original draft: MS, IS and NB; writing—review and editing: MS, SK, DM, IW, YS, JG, SRMG, JB, MM, IS and NB; visualization: MS, NB; supervision: MM, IS and NB; funding acquisition: JB, MM and IS.

## Acknowledgments

We acknowledge financial support from the Open Access Publication Fund of Charité—Universitätsmedizin Berlin and the German Research Foundation (DFG, SFB1340 Matrix in Vision, GRK2260 BIOQIC).

## Conflict of interest

The authors declare that the research was conducted in the absence of any commercial or financial relationships that could be construed as a potential conflict of interest.

## Publisher's note

All claims expressed in this article are solely those of the authors and do not necessarily represent those of their affiliated organizations, or those of the publisher, the editors and the reviewers. Any product that may be evaluated in this article, or claim that may be made by its manufacturer, is not guaranteed or endorsed by the publisher.

- Bussler, S., Penke, M., Flemming, G., Elhassan, Y. S., Kratzsch, J., Sergejev, E., et al. (2017). Novel insights in the metabolic syndrome in childhood and adolescence. *Horm. Res. Paediatr.* 88 (3–4), 181–193. doi:10.1159/000479510
- Caldwell, S., and Argo, C. (2010). The natural history of non-alcoholic fatty liver disease. *Dig. Dis.* 28 (1), 162–168. doi:10.1159/000282081
- Castera, L., Friedrich-Rust, M., and Loomba, R. (2019). Noninvasive assessment of liver disease in patients with nonalcoholic fatty liver disease. *Gastroenterology* 156 (5), 1264–1281.e4. doi:10.1053/j.gastro.2018.12.036
- Chalasani, N., Younossi, Z., Lavine, J. E., Charlton, M., Cusi, K., Rinella, M., et al. (2018). The diagnosis and management of nonalcoholic fatty liver disease: Practice guidance from the American Association for the Study of Liver Diseases. *Hepatology* 67 (1), 328–357. doi:10.1002/hep.29367
- De Gasperi, A., Mazza, E., and Prosperi, M. (2016). Indocyanine green kinetics to assess liver function: Ready for a clinical dynamic assessment in major liver surgery? *World J. Hepatol.* 8, 355. doi:10.4254/wjh.v8.i7.355
- Dittmann, F., Tzschätzsch, H., Hirsch, S., Barnhill, E., Braun, J., Sack, L., et al. (2017). Tomoelastography of the abdomen: Tissue mechanical properties of the liver, spleen, kidney, and pancreas from single MR elastography scans at different hydration states. *Magnetic Reson. Med.* 78 (3), 976–983. doi:10.1002/mrm.26484
- Garczynska, K., Tzschätzsch, H., Kühl, A. A., Morr, A. S., Lilaj, L., Häckel, A., et al. (2020). Changes in liver mechanical properties and water diffusivity during normal pregnancy are driven by cellular hypertrophy. *Front. Physiol.* 11, 605205. doi:10.3389/fphys.2020.605205
- Gielisch, I., and Meierhofer, D. (2015). Metabolome and proteome profiling of complex I deficiency induced by rotenone. *J. Proteome Res.* 14 (1), 224–235. doi:10.1021/pr500894v
- Gorowska-Kowolik, K., Chobot, A., and Kwicien, J. (2017). <sup>13</sup>C methacetin breath test for assessment of microsomal liver function: Methodology and clinical application. *Gastroenterol. Res. Pract.* 2017, 1–5. doi:10.1155/2017/7397840
- Hasenour, C. M., Wall, M. L., Ridley, D. E., Hughey, C. C., James, F. D., Wasserman, D. H., et al. (2015). Mass spectrometry-based microarray of 2H and 13C plasma glucose labeling to quantify liver metabolic fluxes in vivo. *Am. J. Physiol.-Endocrinol. Metab.* 309 (2), E191–E203. doi:10.1152/ajpendo.00003.2015
- Herthum, H., Hetzer, S., Scheel, M., Shahryari, M., Braun, J., Paul, F., et al. (2022). In vivo stiffness of multiple sclerosis lesions is similar to that of normal-appearing white matter. *Acta Biomater.* 138, 410–421. doi:10.1016/j.actbio.2021.10.038
- Heucke, N., Wuensch, T., Mohr, J., Kaffarnik, M., Arsenic, R., Sinn, B., et al. (2019). Non-invasive structure–function assessment of the liver by 2D time-harmonic elastography and the dynamic Liver MAXimum capacity (LIMAX) test. *J. Gastroenterol. Hepatol.* 34 (9), 1611–1619. doi:10.1111/jgh.14629
- Hudert, C. A., Tzschätzsch, H., Rudolph, B., Bläker, H., Loddenkemper, C., Müller, H.-P., et al. (2019). Tomoelastography for the evaluation of pediatric nonalcoholic fatty liver disease. *Investig. Radiol.* 54 (4), 198–203. doi:10.1097/rli.0000000000000529
- Hudert, C. A., Tzschätzsch, H., Rudolph, B., Loddenkemper, C., Holzhütter, H.-G., Kalveram, L., et al. (2021). How histopathologic changes in pediatric nonalcoholic fatty liver disease influence in vivo liver stiffness. *Acta Biomater.* 123, 178–186. doi:10.1016/j.actbio.2021.01.019
- Hui, S., Cowan, A. J., Zeng, X., Yang, L., TeSlaa, T., Li, X., et al. (2020). Quantitative fluxomics of circulating metabolites. *Cell Metab.* 32 (4), 676–688.e4. doi:10.1016/j.cmet.2020.07.013
- Huwart, L., Sempoux, C., Vicaat, E., Salameh, N., Annet, L., Danse, E., et al. (2008). Magnetic resonance elastography for the noninvasive staging of liver fibrosis. *Gastroenterology* 135 (1), 32–40. doi:10.1053/j.gastro.2008.03.076
- Ipek-Ugay, S., Tzschätzsch, H., Hudert, C., Marticorena Garcia, S. R., Fischer, T., Braun, J., et al. (2016). Time harmonic elastography reveals sensitivity of liver stiffness to water ingestion. *Ultrasound Med. Biol.* 42 (6), 1289–1294. doi:10.1016/j.ultrasmedbio.2015.12.026
- Jajamovich, G. H., Dyvorne, H., Donnerhack, C., and Taouli, B. (2014). Quantitative liver MRI combining phase contrast imaging, elastography, and DWI: Assessment of reproducibility and postprandial effect at 3.0 T. *PLOS ONE* 9 (5), e97355. doi:10.1371/journal.pone.0097355
- Kespoli, M., Bredow, C., Klingel, K., Voss, M., Paeschke, A., Zickler, M., et al. (2020). Protein modification with ISG15 blocks coxsackievirus pathology by antiviral and metabolic reprogramming. *Sci. Adv.* 6 (11), eaay1109. doi:10.1126/sciadv.aay1109
- Lalazar, G., Pappo, O., Hershovici, T., Hadjaj, T., Shubi, M., Ohana, H., et al. (2008). A continuous 13C methacetin breath test for noninvasive assessment of intrahepatic inflammation and fibrosis in patients with chronic HCV infection and normal ALT. *J. Viral Hepat.* 15 (10), 716–728. doi:10.1111/j.1365-2893.2008.01007.x
- Lin, H., Wang, Y., Zhou, J., Yang, Y., Xu, X., Ma, D., et al. (2022). Tomoelastography based on multifrequency MR elastography predicts liver function reserve in patients with hepatocellular carcinoma: a prospective study. *Insights into Imaging* 13 (1), 95. doi:10.1186/s13244-022-01232-5
- Lonardo, A., Ballestri, S., Marchesini, G., Angulo, P., and Loria, P. (2015). Nonalcoholic fatty liver disease: a precursor of the metabolic syndrome. *Dig. Liver Dis.* 47 (3), 181–190. doi:10.1016/j.dld.2014.09.020
- Manduca, A., Bayly, P. J., Ehman, R. L., Kolipaka, A., Royston, T. J., Sack, L., et al. (2021). MR elastography: Principles, guidelines, and terminology. *Magnetic Reson. Med.* 85 (5), 2377–2390. doi:10.1002/mrm.28627
- Mathew, P., and Thoppil, D. Hypoglycemia (2022). *StatPearls*. Treasure Island (FL): StatPearls Publishing LLC. StatPearls Publishing Copyright © 2022.
- Meyer, T., Tzschätzsch, H., Wellge, B., Sack, L., Kröncke, T., and Martl, A. (2022a). Valsalva maneuver decreases liver and spleen stiffness measured by time-harmonic ultrasound elastography. *Front. Bioeng. Biotechnol.* 10, 886363. doi:10.3389/fbioe.2022.886363
- Meyer, T., Marticorena Garcia, S., Tzschätzsch, H., Herthum, H., Shahryari, M., Stencil, L., et al. (2022b). Comparison of inversion methods in MR elastography: An open-access pipeline for processing multifrequency shear-wave data and demonstration in a phantom, human kidneys, and brain. *Magn. Reson. Med.* 88, 1840–1850. doi:10.1002/mrm.29320
- Morr, A. S., Herthum, H., Schrank, F., Görner, S., Anders, M. S., Lerchbaumer, M., et al. (2022). Liquid-liver phantom: Mimicking the viscoelastic dispersion of human liver for ultrasound- and MRI-based elastography. *Investig. Radiol.* 57 (8), 502–509. doi:10.1097/rli.0000000000000862
- Obrzut, M., Atamaniuk, V., Chen, J., Obrzut, B., Ehman, R. L., Cholewa, M., et al. (2021). Postprandial hepatic stiffness changes on magnetic resonance elastography in healthy volunteers. *Sci. Rep.* 11 (1), 19786. doi:10.1038/s41598-021-99243-7
- Perez-Riverol, Y., Bai, J., Bandla, C., García-Seisdedos, D., Hewapathirana, S., Kamatchinathan, S., et al. (2022). The PRIDE database resources in 2022: a hub for mass spectrometry-based proteomics evidences. *Nucleic Acids Res.* 50 (D1), D543–D552. doi:10.1093/nar/gkab1038
- Petzold, G., Porsche, M., Ellenrieder, V., Kunsch, S., and Neesse, A. (2019). Impact of food intake on liver stiffness determined by 2-D shear wave elastography: Prospective interventional study in 100 healthy patients. *Ultrasound Med. Biol.* 45 (2), 402–410. doi:10.1016/j.ultrasmedbio.2018.09.021
- Qu, Y., Middleton, M. S., Loomba, R., Glaser, K. J., Chen, J., Hooker, J. C., et al. (2021). Magnetic resonance elastography biomarkers for detection of histologic alterations in nonalcoholic fatty liver disease in the absence of fibrosis. *Eur. Radiol.* 31 (11), 8408–8419. doi:10.1007/s00330-021-07988-6
- Rahim, M., Hasenour, C. M., Bednarski, T. K., Hughey, C. C., Wasserman, D. H., and Young, J. D. (2021). Multitissue 2H/13C flux analysis reveals reciprocal upregulation of renal gluconeogenesis in hepatic PEPCK-C-knockout mice. *JCI Insight* 6 (12), e149278. doi:10.1172/jci.insight.149278
- Ratzliff, V., Charlotte, F., Heurtier, A., Gombert, S., Giral, P., Bruckert, E., et al. (2005). Sampling variability of liver biopsy in nonalcoholic fatty liver disease. *Gastroenterology* 128 (7), 1898–1906. doi:10.1053/j.gastro.2005.03.084
- Reiter, R., Tzschätzsch, H., Schwahof, F., Haas, M., Bayerl, C., Muehe, M., et al. (2020). Diagnostic performance of tomoeelastography of the liver and spleen for staging hepatic fibrosis. *Eur. Radiol.* 30 (3), 1719–1729. doi:10.1007/s00330-019-06471-7
- Sasso, M., Audière, S., Kemgang, A., Gaouar, F., Corpechot, C., Chazouillères, O., et al. (2016). Liver steatosis assessed by controlled attenuation parameter (CAP) measured with the XL probe of the FibroScan: A pilot study assessing diagnostic accuracy. *Ultrasound Med. Biol.* 42 (1), 92–103. doi:10.1016/j.ultrasmedbio.2015.08.008
- Selvaraj, E. A., Mózes, F. E., Jayaswal, A. N. A., Zafarmand, M. H., Vali, Y., Lee, J. A., et al. (2021). Diagnostic accuracy of elastography and magnetic resonance imaging in staging liver fibrosis: A systematic review and meta-analysis. *J. Hepatol.* 75 (4), 770–785. doi:10.1016/j.jhep.2021.04.044
- Seyama, Y., and Kokudo, N. (2009). Assessment of liver function for safe hepatic resection. *Hepatol. Res.* 39 (2), 107–116. doi:10.1111/j.1872-034x.2008.00441.x
- Shahryari, M., Tzschätzsch, H., Guo, J., Marticorena Garcia, S. R., Böning, G., Fehrenbach, U., et al. (2019). Tomoelastography distinguishes noninvasively between benign and malignant liver lesions. *Cancer Res.* 79 (22), 5704–5710. doi:10.1158/0008-5472.can-19-2150
- Shahryari, M., Meyer, T., Warmuth, C., Herthum, H., Bertalan, G., Tzschätzsch, H., et al. (2021). Reduction of breathing artifacts in multifrequency magnetic resonance elastography of the abdomen. *Magn. Reson. Med.* 85 (4), 1962–1973. doi:10.1002/mrm.28558
- Singh, S., Venkatesh, S. K., Wang, Z., Miller, F. H., Motosugi, U., Low, R. N., et al. (2015). Diagnostic performance of magnetic resonance elastography in staging liver fibrosis: A systematic review and meta-analysis of individual participant data. *Clin. Gastroenterol. Hepatol.* 13 (3), 440–451.e6. doi:10.1016/j.cgh.2014.09.046
- Sivell, C. (2019). Nonalcoholic fatty liver disease: A silent epidemic. *Gastroenterol. Nurs.* 42 (5), 428–434. doi:10.1097/sga.0000000000000443
- Tzschätzsch, H., Guo, J., Dittmann, F., Hirsch, S., Barnhill, E., Jöhrens, K., et al. (2016). Tomoelastography by multifrequency wave number recovery from time-harmonic propagating shear waves. *Med. Image Anal.* 30, 1–10. doi:10.1016/j.media.2016.01.001
- Vos, J. J., Wietasch, J. K. G., Absalom, A. R., Hendriks, H. G. D., and Scheeren, T. W. L. (2014). Green light for liver function monitoring using indocyanine green? An overview of current clinical applications. *Anaesthesia* 69 (12), 1364–1376. doi:10.1111/anae.12755
- Wallstab, C., Eleftheriadou, D., Schulz, T., Damm, G., Seehofer, D., Borlak, J., et al. (2017). A unifying mathematical model of lipid droplet metabolism reveals key molecular players in the development of hepatic steatosis. *FEBS J.* 284, 3245–3261. doi:10.1111/febs.14189
- Wong, R. J., and Singal, A. K. (2020). Trends in liver disease etiology among adults awaiting liver transplantation in the United States, 2014–2019. *JAMA Netw. Open* 3 (2), e1920294–e. doi:10.1001/jamanetworkopen.2019.20294
- Yin, M., Talwalkar, J. A., Glaser, K. J., Venkatesh, S. K., Chen, J., Manduca, A., et al. (2011). Dynamic postprandial hepatic stiffness augmentation assessed with MR elastography in patients with chronic liver disease. *Am. J. Roentgenol.* 197 (1), 64–70. doi:10.2214/ajr.10.5989
- Zou, L., Jiang, J., Zhong, W., Wang, C., Xing, W., and Zhang, Z. (2016). Magnetic resonance elastography in a rabbit model of liver fibrosis: a 3-T longitudinal validation for clinical translation. *Am. J. Transl. Res.* 8 (11), 4922–4931.
- Zou, L.-Q., Zhao, F., Zhang, H., Zhang, K., and Xing, W. (2020). Staging liver fibrosis on multiparametric MRI in a rabbit model with elastography, susceptibility-weighted imaging and T1p imaging: a preliminary study. *Acta Radiol.* 62 (2), 155–163. doi:10.1177/0284185120917117
- Zou, L., Jiang, J., Zhang, H., Zhong, W., Xiao, M., Xin, S., et al. (2022). Comparing and combining MRE, T1p, SWI, IVIM, and DCE-MRI for the staging of liver fibrosis in rabbits: Assessment of a predictive model based on multiparametric MRI. *Magn. Reson. Med.* 87 (5), 2424–2435. doi:10.1002/mrm.29126



## **Curriculum vitae**

My curriculum vitae does not appear in the electronic version of my thesis for reasons of data protection.

My curriculum vitae does not appear in the electronic version of my thesis for reasons of data protection.

## Publication list

**Shahryari, M.**, Tzschatzsch, H., Guo, J., Marticorena Garcia, S. R., Boning, G., Fehrenbach, U., Stencel, L., Asbach, P., Hamm, B., Kas, J. A., Braun, J., Denecke, T., & Sack, I. (2019). Tomoelastography Distinguishes Noninvasively between Benign and Malignant Liver Lesions. *Cancer Res*, 79(22), 5704-5710. <https://doi.org/10.1158/0008-5472.CAN-19-2150>

Journal impact factor: 9.727 (JCR 2019)

Marticorena Garcia, S. R., Zhu, L., Gultekin, E., Schmuck, R., Burkhardt, C., Bahra, M., Geisel, D., **Shahryari, M.**, Braun, J., Hamm, B., Jin, Z. Y., Sack, I., & Guo, J. (2020). Tomoelastography for Measurement of Tumor Volume Related to Tissue Stiffness in Pancreatic Ductal Adenocarcinomas. *Invest Radiol*, 55(12), 769-774. <https://doi.org/10.1097/RLI.0000000000000704>

Journal impact factor: 6.016 (JCR 2020)

Reiter, R., **Shahryari, M.**, Tzschatzsch, H., Klatt, D., Siegmund, B., Hamm, B., Braun, J., Sack, I., & Asbach, P. (2021). Spatial heterogeneity of hepatic fibrosis in primary sclerosing cholangitis vs. viral hepatitis assessed by MR elastography. *Sci Rep*, 11(1), 9820. <https://doi.org/10.1038/s41598-021-89372-4>

Journal impact factor: 4.997 (JCR 2021)

Herthum, H., **Shahryari, M.**, Tzschatzsch, H., Schrank, F., Warmuth, C., Gerner, S., Hetzer, S., Neubauer, H., Pfeuffer, J., Braun, J., & Sack, I. (2021). Real-Time Multifrequency MR Elastography of the Human Brain Reveals Rapid Changes in Viscoelasticity in Response to the Valsalva Maneuver. *Front Bioeng Biotechnol*, 9, 666456. <https://doi.org/10.3389/fbioe.2021.666456>

Journal impact factor: 6.064 (JCR 2021)

---

Lilaj, L., Herthum, H., Meyer, T., **Shahryari, M.**, Bertalan, G., Caiazzo, A., Braun, J., Fischer, T., Hirsch, S., & Sack, I. (2021). Inversion-recovery MR elastography of the human brain for improved stiffness quantification near fluid-solid boundaries. *Magn Reson Med*, 86(5), 2552-2561. <https://doi.org/10.1002/mrm.28898>

Journal impact factor: 3.737 (JCR 2021)

**Shahryari, M.**, Meyer, T., Warmuth, C., Herthum, H., Bertalan, G., Tzschätzsch, H., Stencel, L., Lukas, S., Lilaj, L., Braun, J., & Sack, I. (2021). Reduction of breathing artifacts in multifrequency magnetic resonance elastography of the abdomen. *Magn Reson Med*, 85(4), 1962-1973. <https://doi.org/10.1002/mrm.28558>

Journal impact factor: 3.737 (JCR 2021)

Kreft, B., Bergs, J., **Shahryari, M.**, Danyel, L. A., Hetzer, S., Braun, J., Sack, I., & Tzschätzsch, H. (2021). Cerebral Ultrasound Time-Harmonic Elastography Reveals Softening of the Human Brain Due to Dehydration. *Frontiers in Physiology*, 11. <https://www.frontiersin.org/articles/10.3389/fphys.2020.616984>

Journal impact factor: 4.755 (2021)

Sauer, F., Fritsch, A., Grosser, S., Pawlizak, S., Kiessling, T., Reiss-Zimmermann, M., **Shahryari, M.**, Muller, W. C., Hoffmann, K. T., Kas, J. A., & Sack, I. (2021). Whole tissue and single cell mechanics are correlated in human brain tumors. *Soft Matter*, 17(47), 10744-10752. <https://doi.org/10.1039/d1sm01291f>

Journal impact factor: 4.046 (JCR 2021)

Herthum, H., Dempsey, S. C. H., Samani, A., Schrank, F., **Shahryari, M.**, Warmuth, C., Tzschätzsch, H., Braun, J., & Sack, I. (2021). Superviscous properties of the in vivo brain at large scales. *Acta Biomater*, 121, 393-404. <https://doi.org/10.1016/j.actbio.2020.12.027>

Journal impact factor: 10.633 (JCR 2021)

---

Reiter, R., **Shahryari, M.**, Tzschatzsch, H., Haas, M., Bayerl, C., Siegmund, B., Hamm, B., Asbach, P., Braun, J., & Sack, I. (2021). Influence of fibrosis progression on the viscous properties of in vivo liver tissue elucidated by shear wave dispersion in multifrequency MR elastography. *J Mech Behav Biomed Mater*, 121, 104645. <https://doi.org/10.1016/j.jmbbm.2021.104645>

Journal impact factor: 4.042 (JCR 2021)

Herthum, H., Hetzer, S., Scheel, M., **Shahryari, M.**, Braun, J., Paul, F., & Sack, I. (2022). In vivo stiffness of multiple sclerosis lesions is similar to that of normal-appearing white matter. *Acta Biomater*, 138, 410-421. <https://doi.org/10.1016/j.actbio.2021.10.038>

Journal impact factor: 10.633 (JCR 2021)

Herthum, H., Hetzer, S., Kreft, B., Tzschatzsch, H., **Shahryari, M.**, Meyer, T., Gerner, S., Neubauer, H., Guo, J., Braun, J., & Sack, I. (2022). Cerebral tomoelastography based on multifrequency MR elastography in two and three dimensions. *Front Bioeng Biotechnol*, 10, 1056131. <https://doi.org/10.3389/fbioe.2022.1056131>

Journal impact factor: 6.064 (JCR 2021)

Kreft, B., Tzschatzsch, H., **Shahryari, M.**, Haffner, P., Braun, J., Sack, I., & Streitberger, K. J. (2022). Noninvasive Detection of Intracranial Hypertension by Novel Ultrasound Time-Harmonic Elastography. *Invest Radiol*, 57(2), 77-84. <https://doi.org/10.1097/RLI.0000000000000817>

Journal impact factor: 10.065 (JCR 2021)

Meyer, T., Marticorena Garcia, S., Tzschatzsch, H., Herthum, H., **Shahryari, M.**, Stencel, L., Braun, J., Kalra, P., Kolipaka, A., & Sack, I. (2022). Comparison of inversion methods in MR elastography: An open-access pipeline for processing multifrequency shear-wave data and demonstration in a phantom, human kidneys, and brain. *Magn Reson Med*, 88(4), 1840-1850. <https://doi.org/10.1002/mrm.29320#>

---

Journal impact factor: 3.737 (JCR 2021)

**Shahryari, M.**, Keller, S., Meierhofer, D., Wallach, I., Safrou, Y., Guo, J., Garcia, S. M., Braun, J., Makowski, M. R., Sack, I., & Berndt, N. (2023). On the relationship between metabolic capacities and in vivo viscoelastic properties of the liver. *Frontiers in Bioengineering and Biotechnology*, 10. <https://doi.org/10.3389/fbioe.2022.1042711>

Journal impact factor: 6.064 (JCR 2021)

Bertalan, G., Becker, J., Tzschatzsch, H., Morr, A., Herthum, H., **Shahryari, M.**, Greenhalgh, R. D., Guo, J., Schroder, L., Alzheimer, C., Budday, S., Franze, K., Braun, J., & Sack, I. (2023). Mechanical behavior of the hippocampus and corpus callosum: An attempt to reconcile ex vivo with in vivo and micro with macro properties. *J Mech Behav Biomed Mater*, 138, 105613. <https://doi.org/10.1016/j.jmbbm.2022.105613>

Journal impact factor: 4.042 (JCR 2021)

## Acknowledgment

First of all, I would like to thank my doctoral advisors Prof. Dr. Ingolf Sack and PD Dr. Jürgen Braun for the time I spent in the Elastography research group. The extensive discussions, joint experiments, and critical feedback motivated me as a young student to pursue scientific work and provided me with deep insights into magnetic resonance imaging. I am sincerely grateful for the privilege of pursuing my PhD as part of the BioQic graduate program and the CRC "Matrix in Vision," as well as for the exceptional supervision I received throughout this period.

I am sincerely grateful to Dr. Carsten Warmuth, Dr. Helge Herthum, Dr. Jing Guo, Dr. Heiko Tzschätzsch, and Tom Meyer for their invaluable collaboration and expert guidance in the fields of magnetic resonance imaging, biophysics and medical informatics. Their expertise has enabled me to gain valuable knowledge that I have effectively applied in my professional endeavors.

Furthermore, I would like to convey my appreciation to the dedicated colleagues of the Elastography research group and our external partners for their exceptional teamwork, which has significantly contributed to our collective achievements.

I am also deeply grateful for the unwavering support and motivation provided by my friends and family throughout this journey.

Lastly, I would like to express my sincere thanks to Lisa for her unwavering technical and emotional support.

I am genuinely thankful for the remarkable years we have shared together, filled with growth, collaboration, and memorable experiences.